

# Sheffield Hallam University

*Quantification of swelling clays in mineral mixtures and rocks using infrared spectroscopy.*

GEDDES, Jill.

Available from the Sheffield Hallam University Research Archive (SHURA) at:

<http://shura.shu.ac.uk/19682/>

## A Sheffield Hallam University thesis

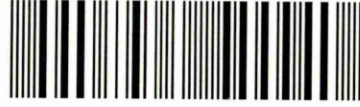
This thesis is protected by copyright which belongs to the author.

The content must not be changed in any way or sold commercially in any format or medium without the formal permission of the author.

When referring to this work, full bibliographic details including the author, title, awarding institution and date of the thesis must be given.

Please visit <http://shura.shu.ac.uk/19682/> and <http://shura.shu.ac.uk/information.html> for further details about copyright and re-use permissions.

101 835 365 8



~~Return to Learning Centre or local~~  
Fines are charged at 50p per hour

**REFERENCE**

ProQuest Number: 10696981

All rights reserved

INFORMATION TO ALL USERS

The quality of this reproduction is dependent upon the quality of the copy submitted.

In the unlikely event that the author did not send a complete manuscript and there are missing pages, these will be noted. Also, if material had to be removed, a note will indicate the deletion.



ProQuest 10696981

Published by ProQuest LLC (2017). Copyright of the Dissertation is held by the Author.

All rights reserved.

This work is protected against unauthorized copying under Title 17, United States Code  
Microform Edition © ProQuest LLC.

ProQuest LLC.  
789 East Eisenhower Parkway  
P.O. Box 1346  
Ann Arbor, MI 48106 – 1346

# **Quantification of Swelling Clays in Mineral Mixtures and Rocks using Infrared Spectroscopy**

**Jill Geddes**

**A thesis submitted in partial fulfilment of the requirement of Sheffield Hallam University for the degree of Doctor of Philosophy.**

**June 2006**



## **Acknowledgements**

Special thanks go to my supervisor, Professor Chris Breen, for all his help, support, and guidance throughout the last few years. I am truly grateful for all the effort he has made to support me.

I'd also like to thank the staff at Schlumberger Cambridge Research, in particular Trevor Hughes for his guidance, constant support, and enthusiasm, and also Alex Wilson for his time and expertise.

Many thanks also to the staff and students at Sheffield Hallam University for their assistance, in particular Francis Clegg for his expertise and relentless patience.

To the MERI staff and students who have become friends over the years, and also friends and family outside MERI, I'd like to say a big thank you for all the jokes and distractions but also for the support and understanding.

## Abstract

The use of a chemometric method, partial least squares (PLS) regression and the infrared technique, diffuse reflectance infrared Fourier transform spectroscopy (DRIFTS) was developed for the quantification of minerals in synthetic mixtures and sandstone rocks. Particular emphasis was directed towards quantifying swelling clays since the proportion of swelling minerals present in a reservoir rock influence the composition of fluids injected into the rock to enhance oil recovery.

In the first study, the capability of PLS with DRIFTS was demonstrated when low quantities of swelling mineral, smectite, were determined in synthetic mixtures with the non-swelling mineral, kaolinite, and an additional mineral, calcite. A substantial improvement in the detection limit of smectite was found using this method since lower quantities could be determined (with a maximum error of 3.8 wt%) than had been determined by previous workers using a peak fitting technique.

An initial investigation of seven different types of sandstone rocks was carried out by visual inspection of XRD traces of powder and rock samples. In this work mineralogical heterogeneity was found along the length of the different sandstone cores investigated. Ideally a representative sample would be one collected from a ball milled sample of a large portion of a core.

The main programme of research was the development of a PLS model consisting of eleven mineral components, to resemble the composition of a real sandstone. This PLS model was used for the quantification of components in synthetic mineral mixtures using their DRIFTS spectra. The maximum error for predicting all the components was  $\pm 2.8$  wt%. This was in the same order as errors reported by other workers for quantification of minerals using XRD.

The same PLS model was used to quantify components in seven different types of sandstone and the results have been compared with studies by independent investigators using different techniques. The PLS model predicted components in the sandstones which contained relatively high concentrations of feldspars and clays, accurately, with all components predicted within  $\pm 2.8$  wt%. PLS model was optimized in order to obtain more accurate quantification of components in the sandstones, in particular for the "cleaner" sandstones, i.e. those which contained low concentrations of feldspars and clays. Some improvement in accuracy was found. The PLS model developed in this thesis, however, was most accurate for prediction of components in sandstones which contained higher concentrations of feldspars and clays.

<b>1. Introduction</b> .....	5
1.1 Aims and Objectives .....	5
1.2 The Importance of Surface Mineralogy.....	6
1.3 Reservoir Rocks .....	7
1.3.1 Sandstone Rocks .....	7
1.3.2 Carbonate Rocks .....	11
1.3.3 Porosity and Permeability in Reservoir Rocks.....	16
1.3.4 Wettability in Reservoir Rocks .....	18
1.4 Classification of Minerals.....	19
1.4.1 Tectosilicates (Quartz and Feldspars).....	19
1.4.2 Phyllosilicates (Clay Minerals and Mica) .....	21
1.4.3 Carbonates.....	26
<b>2. Theory of Techniques used in this thesis</b> .....	28
2.1 Infrared Spectroscopy .....	28
2.1.1 Introduction .....	28
2.1.2 Absorption of Infrared Radiation.....	28
2.1.3 Use of Infrared Spectroscopy for Clay Mineral Analysis .....	30
2.1.4 Fourier Transform Infrared Spectroscopy (FTIR).....	31
2.1.5 Diffuse Reflectance Infrared Fourier Transform Spectroscopy (DRIFTS).....	34
2.1.5.5 Reproducing Physical Characteristics of Samples.....	37
2.1.6 Other Infrared Techniques.....	42
2.2 Thermogravimetric Analysis .....	43
2.3 X-ray Diffraction (XRD).....	45
2.4 X-ray Fluorescence (XRF) Spectroscopy .....	46
2.5 Chemometrics.....	46
2.5.1 Classical Quantification Methods.....	47
2.5.2 Eigenvector Quantification Methods.....	48
<b>3. Literature Survey</b> .....	55
3.1 Identifying Minerals.....	55
3.1.1 Identifying Minerals using FTIR .....	55
3.1.2 Identifying Minerals using TGA.....	58
3.1.3 Identifying Minerals using XRD.....	59
3.2 Clay Organic Interactions .....	59
3.2.1 Kaolinite-Organic Interactions.....	60
3.2.2 Montmorillonite Organic Interactions .....	61
3.3 Quantitative Analysis of Minerals.....	62
3.3.1 Quantitative Analysis using FTIR .....	62
3.3.2 Quantitative Analysis using XRD.....	63
3.3.3 Other Techniques .....	68
3.4 Quantitative Analysis of Rocks.....	68
3.5 Chemometrics.....	72
3.5.1 Partial Least Squares (PLS) Regression .....	72

<b>4. Results - Quantification of small amounts of swelling mineral, smectite, in synthetic mixtures using Diffuse Reflectance Infrared Fourier Transform Spectroscopy (DRIFTS)</b> .....	77
4.1 Determining low amounts of smectite .....	77
4.2 Experimental.....	77
4.2.1 Equipment.....	77
4.2.2 Spectral Collection.....	78
4.2.3 OMNIC and GRAMS Software .....	79
4.3 Reproducibility Studies.....	79
4.3.1 Introduction .....	79
4.3.2 Turning Sample Cup.....	80
4.3.3 Compaction in Sample Cup.....	80
4.3.4 Differentiating Sample Concentration by Peak Intensity .....	81
4.3.5 Altering Grinding Time of Sample and KBr.....	82
4.4 Use of PLS.....	84
4.5 Standard Preparation .....	85
4.6 Sample Preparation .....	87
4.7 Standard Exposure to Dimethylformamide (DMF) .....	87
4.8 Results and Discussion .....	88
4.8.1 Visual Examination of Spectra from Standards.....	88
4.8.2 Visual Detection of Components .....	91
4.8.3 Results obtained using OMNIC and GRAMS Software .....	92
4.8.4 Results from Chemical Probe Treated Standards .....	100
4.8.5 Results from Ball Milled and Compacted Standards.....	109
4.8.6 Comparing the Precision of Calibrations .....	115
4.8.7 Comparing the Accuracy of Predictions.....	116
4.8.8 Comparing the Precision of Predictions .....	118
4.8.9 Comparing Results with Literature.....	119
4.9 Conclusion .....	121
<b>5. Results - Heterogeneity of Sandstone Rock Cores</b> .....	122
5.1 Introduction.....	122
5.2 Experimental Strategy.....	122
5.3 Coarse Survey of Rock Cores.....	123
5.3.1 Introduction .....	123
5.3.2 Experimental .....	124
5.3.3 Reproducibility of XRD traces.....	125
5.4 Mineralogical Variation along Core Length.....	128
5.4.1 Introduction .....	128
5.4.2 Experimental .....	129
5.4.3 Results and Discussion .....	130
5.5 Conclusion .....	153

<b>6. Results - Sandstone Absolute PLS Model</b> .....	155
6.1 Introduction.....	155
6.2 Experimental.....	156
6.2.1 Equipment.....	156
6.2.2 Spectral Collection.....	156
6.3 Training Set Components.....	157
6.3.1 Components Structural Formula and Source.....	157
6.3.2 DRIFTS Spectra of the Pure Components used in the Training Set.....	158
6.4 Standard Preparation.....	163
6.5 Sample Preparation.....	165
6.6 Results and Discussion.....	166
6.6.1 Visual Examination of Spectra from Standards.....	166
6.6.2 Pre-processing Studies.....	168
6.6.3 Absolute PLS Model.....	175
6.7 Comparing Results with Literature.....	191
6.8 Conclusion.....	195
<b>7. Results – Quantification of Sandstone Rocks</b> .....	197
7.1 Introduction.....	197
7.2 Experimental.....	198
7.2.1 Preparation of Powders.....	198
7.2.2 Equipment.....	199
7.2.3 Sample Preparation.....	199
7.2.4 Spectral Collection.....	199
7.3 Qualitative DRIFTS study of Sandstones.....	200
7.3 Predicting the Mineral Composition of Powders from Sandstone Rocks using the Absolute PLS Model.....	205
7.3.1 Introduction.....	205
7.3.2 Comparing Predictions of Powder from Cutting, Ground Slices, and Ball milled Slices.....	205
7.3.3 Comparing the Particle Size of Powders.....	224
7.4 Comparing Absolute PLS Model and Other Model Predictions.....	232
7.4.1 Introduction.....	232
7.4.2 Comparing Predictions by the Different Models.....	233
7.4.3 XRF of Ball milled Slices.....	244
7.5 Forming the Pragmatic PLS Model.....	247
7.5.1 Introduction.....	247
7.5.2 Altering the Number of Factors.....	248
7.5.3 Comparing Absolute PLS Model, Pragmatic PLS Model, and XRD-Hillier Model Predictions.....	252
7.6 Absolute and Pragmatic PLS Model Errors.....	260
7.6.1 Maximum Errors of Absolute and Pragmatic PLS Models.....	260
7.6.2 Maximum Reproducibility Errors.....	261
7.7 Reasons for Quartz Predictions.....	274
7.7.1 Over-Prediction of Quartz in Sandstones.....	274
7.7.2 Impurities in the Training Set Components.....	280

7.7.3 Summary.....	285
7.8 Comparing Results with Literature.....	288
7.9 Conclusion.....	291
<b>8. Conclusions.....</b>	<b>294</b>
8.1 Use of DRIFTS and PLS to quantify small amounts of swelling mineral, smectite, in synthetic mixtures.....	294
8.2 Heterogeneity of Sandstone Rock Cores.....	295
8.3 Sandstone Absolute PLS Model.....	295
8.4 Quantification of Sandstone Rocks.....	297
8.5 Considerations for Future Work.....	299
8.5.1 Improving the Training Set and PLS Models.....	299
8.5.2 Other Techniques.....	302
8.5.3 Quantification of Carbonate Rocks.....	302
<b>9. Conferences Attended.....</b>	<b>303</b>
<b>10. References.....</b>	<b>304</b>

# **1. Introduction**

## **1.1 Aims and Objectives**

The research in this PhD thesis has been undertaken in collaboration with Schlumberger Cambridge Research (SCR) and involved a study of sandstone heterogeneity, and the use of a chemometric method, partial least squares (PLS) and the infrared technique, diffuse reflectance infrared spectroscopy (DRIFTS), for the quantification of minerals present in sandstone rocks.

Reservoir rocks have been traditionally studied and quantified using the X-ray diffraction (XRD) technique. Although XRD was used in the research included in this thesis to visually detect mineralogical variations within a sandstone core and also to confirm the purity of components, it was not used for quantification purposes. The main technique used in this thesis was diffuse reflectance Fourier transform infrared spectroscopy (DRIFTS). Partial least squares regression, a program of mathematical calculations, was used with the DRIFTS spectra to quantify mineral components present in a sample. DRIFTS was used since it is a fast and relatively inexpensive technique compared to XRD.

In the first study, the capability of PLS with DRIFTS was demonstrated when low quantities of swelling mineral, smectite, were determined in synthetic mixtures with the non-swelling mineral, kaolinite. Industrially this is important since the presence of clays with different surface areas can cause problems in the coatings industry and also for reservoir rock analysis in the oil industry. The proportion of swelling minerals present in a reservoir rock would influence the composition of treatment fluid injected into the rock to enhance oil recovery.

An initial investigation of seven different types of sandstone rocks has been carried out by visual inspection of XRD traces of powder and rock samples. The aim of this work was to investigate the gross mineralogical heterogeneity along the length of the different sandstones and to determine a representative sample size.

The main programme of research has been the development of a PLS model consisting of eleven mineral components, chosen to resemble the composition of a real sandstone.

This PLS model was used for the quantification of components in synthetic mineral mixtures using their DRIFTS spectra. The same PLS model has been used to quantify components in seven different types of sandstone and the results have been compared to studies by independent investigators using different techniques. The objective of further optimisation of the PLS model was to obtain more accurate quantification of components in the sandstones, in particular for the “cleaner” sandstones, i.e. those which contained low concentrations of feldspars and clays.

## **1.2 The Importance of Surface Mineralogy**

This project quantitatively investigated the bulk mineralogy of sandstone rocks and their heterogeneity with a view to quantitatively determining the mineralogy on the surface of pores in oil-bearing rocks.

It is important to increase knowledge of reservoir rock mineralogy and in particular pore surface mineralogy since the presence of clay minerals in a sandstone reservoir rock can significantly affect fluid flow, cation-exchange capacity, adsorption characteristics and swelling behaviour. Clay minerals lining the pores can greatly reduce the permeability of the rock by blocking the pore throats. In the oil industry, treatment fluids are pumped into reservoir rocks to increase well productivity and interactions of this treatment fluid with swelling minerals on the pore surface may also catastrophically alter the fluid composition. Therefore, the type of reservoir rocks better suited to this enhanced oil recovery process are those with high permeability and porosity, low clay mineral content (of which more is non-swelling kaolinite than swelling smectite) and weak quartz cement [1, 2].

## **1.3 Reservoir Rocks**

Of the rocks at the Earth's surface, 70% are sedimentary in origin. Sedimentary rocks form from sediment, produced from the weathering of pre-existing rocks or from chemical and/or biochemical processes. The sediment is compacted by the weight or pressure of overlying sediments and cemented, where minerals are deposited in pore spaces from water carrying ions. Precipitation of minerals from solution in lakes, or the sea for example, can also produce sedimentary rocks. Sedimentary rocks can be categorised into four main groups. Terrigenous clastic sediments (or siliciclastic deposits) are one group and these consist of fragments (or clasts) of pre-existing rocks which have been transported and deposited by physical processes. Sandstones and shale belong to this first group. Carbonate rocks belong to the second group, which are formed from sediments of biochemical and organic origin. The third group includes the evaporites, which are of chemical origin, and form mostly by direct precipitation. Volcaniclastic deposits consisting of lava and rock fragments from volcanic activity make up the fourth group [1]. This thesis focuses on sandstone rocks.

A reservoir rock is formed when organic matter, which has matured in sediments, migrates to porous sedimentary rocks. A reservoir rock is therefore defined as one that has the ability to contain and yield oil, gas or both in commercial quantities. The most common reservoir rock types are sandstones and carbonates, while a less common type is shale. For successful oil/gas exploration, the distinct compositional and structural differences between these reservoir rock types must be understood.

### **1.3.1 Sandstone Rocks**

#### **1.3.1.1 Introduction**

Terrigenous sand and sandstone cover about 30% of the world's sedimentary cover. They are often highly porous, frequently making them appropriate hydrocarbon reservoirs [2].

### **1.3.1.2 Sandstone Formation**

Sandstone is formed through inorganic and clastic processes. Sediments are composed mostly of fragments derived from the erosion of pre-existing igneous, metamorphic and sedimentary rocks. The grains are released by mechanical and chemical weathering processes, and are then transported to the depositional site. The grains may be rock fragments, but the majority are individual crystals, mostly quartz and feldspar. Finer breakdown products formed during weathering, such as clay minerals, form the matrix of some sandstones. Sandstones are therefore an accumulation of particles of broken rock generally held together by silica. The exact composition of the sandstone depends largely on the weathering processes, determined by the climate and geography of the area. Other things that affect the composition are the distance of sediment transport and diagenetic processes, described in section 1.3.1.5 [2].

### **1.3.1.3 Sandstone Rock Components**

Clastic sedimentary rocks such as sandstone and shale have a fragmental texture consisting of clasts, matrix and cement. Clasts are the larger fragment grains such as sand or gravel which form the framework of the sediments. Some minerals and rock types are more stable than others. In decreasing stability order, these minerals include quartz, chert, muscovite and feldspars. A matrix, consisting of mud or fine-grained sediment, surrounds these larger grains. The cement holds the structure together, and may be calcite, iron oxide, silica, or clay. The cement is precipitated after the sediment is deposited, during diagenesis [1]. Characteristics of the sandstone such as its strength and durability are affected by the type of cementing material present since even a sandstone composed only of quartz grains may be relatively soft if the grains are loosely cemented. Silica cement is the most durable, producing a very hard sandstone, while iron oxide is a slightly less strong cement. Calcite and clay cements are softer than silica and iron oxide cements and an excess of clay cement also means that more water will be present in the sandstone.

### **1.3.1.4 Sandstone Classification**

There are four principal types of sandstone, classified according to their composition:

- (i) dominated by quartz grains (quartz sandstone),
- (ii) dominated by unweathered feldspar (arkose),
- (iii) dominated by sand-sized rock fragments (lithic sandstone),
- (iv) containing high contents of clay minerals (shale).

While quartz sandstone contains 100% quartz, shale contains the lowest concentration of quartz, at around 65% and the highest concentration of clay minerals, at 1-20%. The concentration of feldspars is around 1-25% in both arkose and shale.

### **1.3.1.5 Diagenesis**

The resulting sandstone, composed of a network of various structures, is constantly modified by diagenetic processes. These processes include compaction, dissolution and replacement and result in either an introduction of material into the pore space or removal of material, creating pore space. This obviously has an affect on rock porosity and permeability and therefore the rock's potential as an oil/gas reservoir.

Compaction arises from the weight of overlying sediment, which produces fracturing and grain reshaping, resulting in closer packing of grains. Dissolution of unstable quartz grains or, more commonly, of chemically less stable feldspar grains, can result in the release of ions and formation of clay minerals and carbonates, which can replace dissolved grains within the structure. Ions may alternatively be carried in solution until chemical and physical conditions favour their precipitation.

### **1.3.1.6 Composition**

#### **1.3.1.6.1 Rock Fragments**

The rock fragments found in sandstones can be described as being, (i) fine grained sedimentary rock such as mudstone and shale, (ii) siliceous sedimentary rock such as chert and siltstone, or (iii) igneous rocks. Fragments of shale and igneous rocks can be compacted and undergo diagenetic alteration, becoming indistinguishable from a fine

grained muddy matrix. Igneous rock fragments may be replaced by chlorite and zeolites [1].

#### 1.3.1.6.2 Quartz

Sand particles are the largest found in a sandstone, and are between 62.5  $\mu\text{m}$  and 2 mm. Quartz is the most common and stable mineral in sandstone, and commonly makes up 65-100% of the sandstone composition [1].

#### 1.3.1.6.3 Feldspars

Feldspars make up between 10 and 15% of a sandstone's content. Feldspar grains can be found mixed with quartz grains but are less stable, and feldspar crystals can disintegrate during transportation, or undergo chemical alteration to clay minerals [1].

#### 1.3.1.6.4 Other Minerals

Clay minerals, carbonates, and iron oxides that are present can act as a cement, binding the quartz and feldspar grains together. Mica is also a common silicate mineral found in sedimentary rock. Where clay minerals are present in a rock, the most commonly occurring are kaolinite, montmorillonite, illite and chlorite. Clays in sandstones can be either allogenic or authigenic. Allogenic clays originate outside of the rock and then, once formed, mix with the sand fraction during deposition. Authigenic clay minerals, however, form within the rock after burial. Authigenic clays tend to have a higher degree of purity, are more crystalline, and less susceptible to deformation by compaction than allogenic clays [3]. In sandstones, kaolinite can be found most commonly as discrete particles attached to pore walls and can reduce the intergranular pore volume. Illite, chlorite and montmorillonite can, however, form on pore walls as a continuous clay mineral coating and are referred to as pore-lining clays. These pore-lining clays can also become pore-bridging, if the continuous coating extends completely across a pore or pore throat [4].

### **1.3.1.7 Sandstone Maturity**

A sandstone containing many unstable rock fragments and minerals, and a high concentration of feldspar, is considered compositionally immature. Mature sandstone contains more stable rock fragments, some feldspar but a high concentration of quartz.

[1]

The performance of a sandstone as a reservoir rock depends upon its porosity and permeability which in turn depends upon the grain size and size distribution. The sandstone reservoirs which give maximum oil recovery are those that are composed of sand-sized quartz grains, silica cement and minimal fragmented particles.

## **1.3.2 Carbonate Rocks**

### **1.3.2.1 Introduction**

Carbonates make up about 20% of the world's sedimentary rocks and understanding carbonate reservoirs has become more important in industry since they account for 40% of today's hydrocarbon production and are expected to dominate production through the next century [5]. Carbonate formations, in fact, hold about one half of oil reserves in the USA, so improving oil recovery in these formations is very important. Carbonate rocks are, however, highly complex and heterogeneous even at the core scale [6]. They are much less uniform than sandstones and it is more difficult to predict their geometry and reservoir performance [2]. Carbonate reservoirs can be large but contain microscopic pores and can have low matrix permeability.

Carbonate sedimentary rocks differ greatly from siliciclastic sedimentary rocks in their formation processes, composition, stability, classification, and porosity.

### **1.3.2.2 Carbonate Formation**

Carbonate rocks consist mainly of only two minerals, calcite ( $\text{CaCO}_3$ ) and dolomite ( $\text{CaMg}(\text{CO}_3)_2$ ), and remain near their point of origin compared with the longer distances travelled by silica based grains to form siliciclastic rocks. Carbonate rocks can form in

many environments. Most mature carbonate rocks formed in shallow marine settings, while the most common type of modern carbonate rock is formed in deep water. Biological activity and the accumulation of organism remains on the seafloor form biogenic sediments from which most carbonate rocks develop. Other carbonate rocks form as water evaporates from shallow onshore basins or as precipitates from seawater [7].

### **1.3.2.3 Carbonate Rock Components**

Like siliciclastic rocks, a typical carbonate rock is made of grains, matrix and cement.

Grains are either skeletal fragments of small organisms or non-skeletal particles precipitated from calcium-rich water. Skeletal grains are identified by their size, shape, microstructure and original mineralogy. Non-skeletal grains can be produced abiotically, by non-living physical and chemical factors, or biotically, by living organisms [8].

The matrix fills most of the space not occupied by grains and is lithified mud of deposition. The fine mud can be formed by chemical precipitation (associated with high temperatures and salinities or changes in partial pressure of  $\text{CO}_2$ ), or by the breaking of skeletal material into finer material [8]. Many limestone matrices were originally composed of unstable aragonite ( $\text{CaCO}_3$ ) and high-Mg calcite, but were replaced by more stable, low-Mg, calcite during diagenesis [8].

Sediments can be considered either matrix supported or grain supported. In matrix supported systems, matrix materials are generally too small to be distinguished as a grain, i.e. they consist of microcrystalline carbonate sediments. Grain supported carbonate rocks, on the other hand, have a dominance of visible sedimentary grains over microcrystalline grains.

In most of the space remaining between grains and matrix, or between grains themselves, precipitates a crystalline material called cement. Depending on the cement composition, the conditions of crystallisation, and the spaces to be filled, cements can have a variety of

crystal sizes [9]. Aragonite, high Mg calcite, low-Mg calcite, and dolomite are the most common carbonate cements in limestones. Less common cements are ankerite ( $\text{CaFe}(\text{CO}_3)_2$ ), siderite ( $\text{FeCO}_3$ ), kaolinite, anhydrite ( $\text{CaSO}_4$ ), gypsum ( $\text{Ca}(\text{SO}_4) \cdot 2\text{H}_2\text{O}$ ) and halite. The actual mineralogy depends on the composition of the pore-fluids, the carbonate supply rate and on the rate of precipitation. Sparite, which consists of coarsely crystalline clear calcite crystals more than 10  $\mu\text{m}$  in size [10], is the dominant pore-filling cement in limestones [8].

### 1.3.2.4 Classification

Carbonate rocks are classified by a completely different system from that used for clastic rocks. While clastic rocks are distinguished by grain composition and size, carbonate rocks are distinguished by factors such as depositional texture, grain or pore types, rock fabric or diagenesis [7].

There are numerous ways in which matrix and grains can coexist and the Dunham classification (1962) is the most widely used and simplest classification based on the internal structure and texture of the rock. The classification of limestones is described in Table 1.1.

Mudstones	Matrix supported	< 10% suspended grains > 20 $\mu\text{m}$ in size.
Wackstones		> 10% suspended grains >20 $\mu\text{m}$ in size.
Packstones	Grain supported	Increasing amount of grains and progressively less Matrix. ↓
Grainstones		
Boundstones	Biologically bound	Supported during deposition by original material i.e. rocks formed mainly by binding of organisms.
Crystalline Limestone	Lost all original texture due to diagenetic recrystallisation.	

**Table 1.1: Classification of limestones [1, 9, 10].**

### **1.3.2.5 Diagenesis**

Diagenesis refers to the postdepositional chemical and physical changes that sediments undergo which transform them into solid rock. The diagenesis process can be divided into six main mechanisms; cementation, microbial micritisation, neomorphism, dissolution, compaction, and dolomitisation. The diagenesis a carbonate rock undergoes depends on the composition and mineralogy of the sediment, the pore-fluid chemistry and flow rates, geological history of the sediment, the influx of different pore-fluids, and climate. The three main environments in which carbonate diagenesis takes place are marine, near-surface meteoric and burial [1, 8, 10].

#### **1.3.2.5.1 Cementation**

Cements in carbonate rocks have been discussed in more detail in section 1.3.2.3. The precipitation of cements in carbonate sediments can take place provided no kinetic factors inhibit it.

#### **1.3.2.5.2 Microbial Micritisation**

While cementation is considered aggradation, microbial micritisation is degradation. This type of degradation occurs when bioclasts on the seafloor are altered by small organisms. The skeletal grains are bored and holes filled by fine-grained sediment or cement. With intense activity completely micritised grains are formed.

#### **1.3.2.5.3 Neomorphism**

Neomorphism refers to replacement and recrystallisation processes where there may have been a change in mineralogy. Neomorphic processes take place in the presence of water through dissolution-reprecipitation. In limestones, most neomorphism is of the aggrading type, leading to a general increase in crystal size, and occurs mostly in fine-grained limestones. Calcitisation is a common neomorphic process. During calcitisation, aragonite grains, cements, dolomite and evaporite minerals (halite, gypsum, anhydrite) can be replaced by calcite. The original mineral gradually undergoes dissolution and precipitation of calcite replaces it.

#### 1.3.2.5.4 Dissolution

It is the presence of the metastable minerals, aragonite and high-Mg calcite, in carbonate rocks that makes them much more likely to undergo dissolution than clastic rocks.

Grains in carbonate rocks can be dissolved to form new pore space and dissolution along fractures and bedding planes can produce large vugs and caves. This can restore higher porosity in deeply buried carbonate rocks.

#### 1.3.2.5.5 Compaction

Carbonate sediments buried, but not already cemented, become compacted under an increasing overburden and grain fracture can occur, resulting in a decrease in porosity due to closer packing. This mechanical compaction can also lead to chemical compaction when the grains begin to dissolve at point contacts. In previously compacted and cemented limestones, this chemical compaction can produce features such as stylolites and dissolution seams at depths of several thousand metres. Stylolites commonly appear as dark, jagged lines on exposed surfaces of carbonate rocks (and rarely on other sedimentary rock types) and are composed of insoluble residues. Dissolution seams are layers where minerals have dissolved as a result of the pressure of compaction. This can happen because minerals that are under pressure, or deformed due to stress, are more soluble than unstressed minerals.

#### 1.3.2.5.6 Dolomitisation

While clastic diagenesis does not normally involve a change in mineralogy, carbonate diagenesis commonly involves the replacement of calcite and aragonite with dolomite in a process called dolomitisation [7]. Dolomitisation can improve the hydrocarbon-producing characteristics because, while dolomites are normally less porous than limestones at shallow depths, they retain their porosity more effectively during burial and are less affected by compaction. Dolomites therefore tend to be better reservoir rocks because they contain more voids that hydrocarbons can fill.

### **1.3.2.6 Composition**

The most modern carbonate sediments are mainly composed of the two mineral forms, aragonite and calcite. There are two types of calcite, low magnesium calcite, with <4 mole% MgCO<sub>3</sub>, and high magnesium calcite, with >4 mole% MgCO<sub>3</sub>. Since low-Mg calcite is more stable than both high-Mg calcite and aragonite, these less stable forms are commonly replaced by it. Over time all three forms may be replaced by dolomite, particularly in the presence of magnesium rich ground waters with a significant amount of salinity. Most limestones are therefore composed of low-Mg calcite and/or dolomite [8]. Phosphate, and minerals such as glauconite can also be present in carbonate rocks but are less common. Secondary minerals (minerals that replace existing minerals during the diagenesis process) that may also be present are anhydrite, chert (a microcrystalline variety of quartz), quartz, clay minerals, pyrite (FeS<sub>2</sub>), ankerite and siderite [7].

### **1.3.3 Porosity and Permeability in Reservoir Rocks**

The porosity of a rock is determined by the shape and arrangement of sand grains and the amount of cementing material present, while the permeability depends upon the size of the pore openings and the degree and type of cementation between sand grains.

Carbonate rocks tend to be composed of more densely packed particles than sandstone rocks, so their porosity depends on void spaces formed by the movement of water, and on fractures. This causes porosity in carbonate rocks to be very irregular and more difficult to measure than in sandstone rocks.

The porosity, permeability, and wettability of a given reservoir rock determine its value since these factors affect the amount of oil or gas present in the rock and the ease at which it can be extracted.

Oil and gas can accumulate in the void space in reservoir rocks. Porosity is a measure of this void space and gives the rock its ability to absorb and hold fluids. Porosity in reservoir rocks can be primary or secondary. Primary porosity occurs where the pore spaces, in which oil and gas are found, originated when the formation was laid down, while secondary porosity refers to pore spaces formed through subsequent rock stresses

or ground water action. The porosity most common in sandstones is primary, while secondary porosity is most common in limestones and dolomites. Porosity can be classified into two categories, effective porosity (interconnected porosity), and non-effective porosity (isolated porosity). Only the effective porosity is useful for commercial oil and gas deposits since it is only from this type of porosity that fluids can be recovered.

The porosity of feldspars has been studied by David *et al.* [11] using scanning electron microscopy and transmission electron microscopy. Pores were found to range in size from  $<1 \mu\text{m}$  to around  $40 \mu\text{m}$  in alkali feldspars, and porosities were measured up to 2.3% by volume. However, the pores were often not evenly distributed. Micropores can form in feldspars contained in weathered rocks due to release of strain or dissolution of structure around dislocations. The micropores on weathered feldspar surfaces are, however, different to those in fresh feldspar. During weathering, micropores become more interconnected than in fresh feldspar due to dissolution [11].

Permeability is a measure of how easily fluid flows through a reservoir rock. Darcy's law is used to define the permeability, and has the equation,

$$Q = (K/\mu)(dp/dl),$$

where  $Q$  is the rate of fluid flow,  $K$  is the permeability,  $\mu$  is the fluid viscosity, and  $dp/dl$  is the pressure gradient in the direction of flow [1].

Fluids can flow either through a fracture in the rock or can work their way through the network of grains. Isolated pores (voids inaccessible to fluids) can form in rocks. There are various reasons for the presence of isolated pores, such as cement formation at a pore throat, and clay minerals blocking a pore throat. These isolated pores cause some highly cemented rocks with high concentrations of clay to have a low permeability despite having a high porosity.

### 1.3.4 Wettability in Reservoir Rocks

Wettability refers to a measure of the tendency for one immiscible fluid to preferentially spread on to a solid surface compared with another immiscible fluid. In reservoir rocks, oil and water are the immiscible fluids in question and most producing reservoirs are generally in a water-wet state, meaning that water preferentially adheres to the rock surface [12, 13]. Most carbonate reservoirs are, however, oil-wet or of mixed-wettability despite pure carbonate being water-wet. This means that it is difficult to predict oil extraction and profitability in carbonate rocks [14]. The way in which oil and water flow through the rock is governed by the wettability and the type of flow effects the fraction and yield of oil that can be recovered [15]. Wettability has a large effect on oil production in reservoirs so it is necessary to determine the preferential wettability of the reservoir. The contact angle between the fluid interface and the solid surface can be used to define wettability [12]. High contact angles ( $>90^\circ$ ) indicate oil wet conditions and low contact angles ( $<90^\circ$ ) indicate water wetness, when water is the wetting phase. Intermediate wetness is also possible, when the contact angle is around  $90^\circ$ , and all three states are shown in Figure 1.1. In Figure 1.1 a decrease in wettability of the surface with respect to water is shown from surface A to C. Conversely, the surfaces in Figure 1.1 would show an increase in wettability with respect to oil from surface A to C.

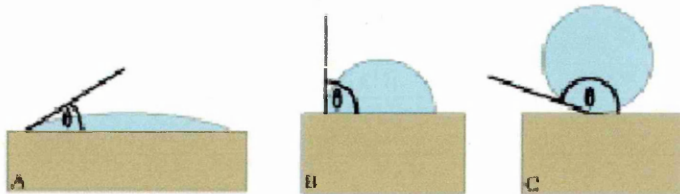


**Figure 1.1: Wettability conditions of water on a surface: A) water wet, B) intermediate wetness, C) not water wet [16].**

Porous media however, makes direct measurement of contact angles impractical, so core wettability tends to be measured, based on capillary pressure. In this method, non-wetting fluid is displaced from a sample by invasion of the wetting fluid [12]. Measuring the wettability of a reservoir rock is made more difficult due to the higher temperature of

reservoir rock in situ (in excess of 80 °C) compared to the temperature at which measurements take place. It is known that wettability increases with temperature. However, the relationship between wetness and pressure is less clear [16].

### 1.4 Classification of Minerals

The most commonly found minerals in sandstones are the silicates. Differences in the types of linkages between basic units are used to divide the silicates into sub-classes. In sandstones and sedimentary rocks, tectosilicate and phyllosilicate sub-classes are found. A summary of the classification of minerals is shown in Table 1.2.

Class	Subclass	Group	Subgroup
Silicates	Tectosilicates	silica	quartz
		feldspars	alkali series
			plagioclase series
Silicates	Phyllosilicates	smectites	
		kandites	
		illites	
		chlorites	
		micas	
Carbonates		calcite	
		aragonite	
		dolomite	

**Table 1.2: Classification of major minerals of relevance in this thesis.**

#### 1.4.1 Tectosilicates (Quartz and Feldspars)

Tectosilicates have a three-dimensional network of  $\text{SiO}_4^{4-}$  tetrahedra with a Si:O ratio of 1:2 (i.e. silica). The most common form of silica is quartz. In silica, substitution of  $\text{Al}^{3+}$  for  $\text{Si}^{4+}$  results in a negative charge which must be compensated for by additional positive ions. The most common group of these aluminosilicates is the feldspars.

### 1.4.1.1 Quartz

Quartz is the most common mineral on the face of the Earth. It is found in nearly every geological environment and is a component of almost every rock type, frequently the primary mineral, due to its stability.

### 1.4.1.2 Feldspars

Feldspars are second in abundance, after quartz, in arenaceous sediments (sediments containing sand sized particles). The general formula, for the common feldspars, is  $XAl_{(1-2)}Si_{(3-2)}O_8$ , where the X in the formula can be sodium and/or potassium and/or calcium.

The structure consists of interlinked tetrahedra of  $SiO_4^{4-}$  and  $AlO_4^{5-}$  with silicon and aluminium ions occupying the centres. The tetrahedra are connected at each corner to other tetrahedra forming an intricate, three dimensional, negatively charged framework. It is the presence of the aluminium (in up to one half of the units) that causes the resulting negative charge. The cations that represent the X in the formula sit within the voids in this structure and balance the charge.

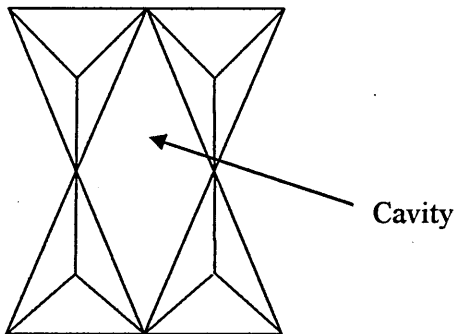


**Figure 1.2: Four membered ring of silica tetrahedral in feldspar.**

There are two sub-groups of feldspars, the alkali (or K-feldspar) and the plagioclase series. Isomorphism occurs between end-members (orthoclase, albite and anorthite) of these series, indicated in the triangular phase diagram in Figure 1.3. The alkali feldspars show a continuous composition series between end members orthoclase ( $KAlSi_3O_8$ ) and albite ( $NaAlSi_3O_8$ ), for feldspars stable at high temperatures. Intermediate members are

homogenous mixtures of the pure end members. The plagioclase series is, however, continuous between end members albite ( $\text{NaAlSi}_3\text{O}_8$ ) and anorthite ( $\text{CaAl}_2\text{Si}_2\text{O}_8$ ) at all temperatures. While alkali feldspars such as orthoclase are considered K-feldspars, albite is a Na-feldspar.

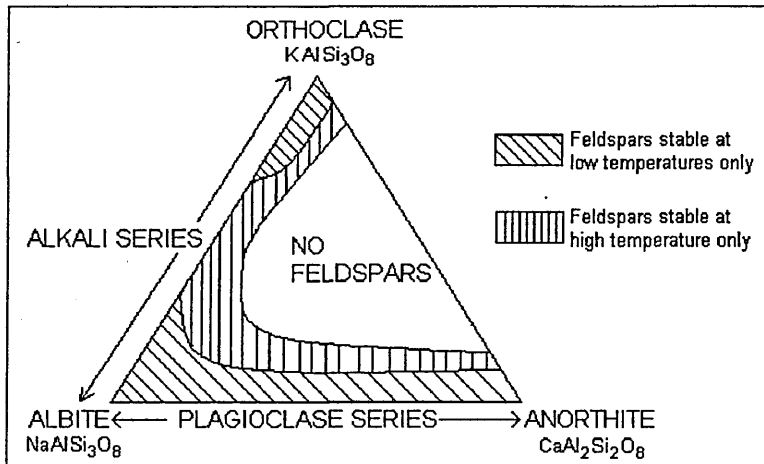


**Figure 1.3: Triangular phase diagram describing the compositions of the Feldspars.**

## 1.4.2 Phyllosilicates (Clay Minerals and Mica)

### 1.4.2.1 Clay Minerals

#### 1.4.2.1.1 Structure

Clay minerals are layer silicates, and are constructed from tetrahedral sheets, as shown in Figure 1.4, with a dominant  $\text{Si}^{4+}$  cation, and octahedral sheets, as shown in Figure 1.5, with a dominant  $\text{Al}^{3+}$  cation. When fitted together to form a 1:1 layer silicate, i.e. one tetrahedral and one octahedral sheet, two out of the three hydroxyl ions in the octahedral sheet are replaced by oxygens of the tetrahedra. An oxygen surface is exposed on the silica sheet and a hydroxyl surface is exposed on the alumina sheet. There is hydrogen bonding between the layers [17]. The hydroxyl groups located between the tetrahedral and octahedral sheets are called "inner-hydroxyls", while hydroxyls located on the interlayer side of the octahedral sheet are called "inner-surface hydroxyls".

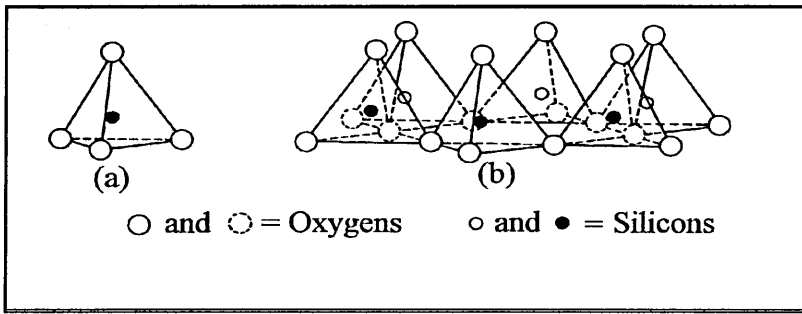


**Figure 1.4: Single silica tetrahedron (a), and a section of a silica tetrahedral sheet (b).**

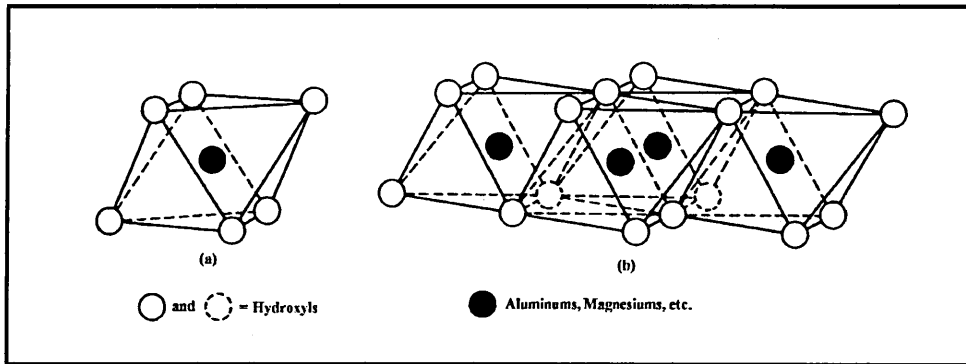


**Figure 1.5: Single octahedral unit (a), and a section of an octahedral sheet (b).**

Layer silicates can also form in a 2:1 arrangement, consisting of an octahedral sheet sandwiched between two tetrahedral sheets, so that a surface of oxygens is exposed on each surface. In this 2:1 arrangement, van der Waal's forces between oxygens on neighbouring sheets hold the layers together.

The sheet-like structures of kaolinite (1:1 layered mineral), montmorillonite and illite (2:1 layered minerals) and chlorite (2:1:1 layered mineral) are represented in Figure 1.6.

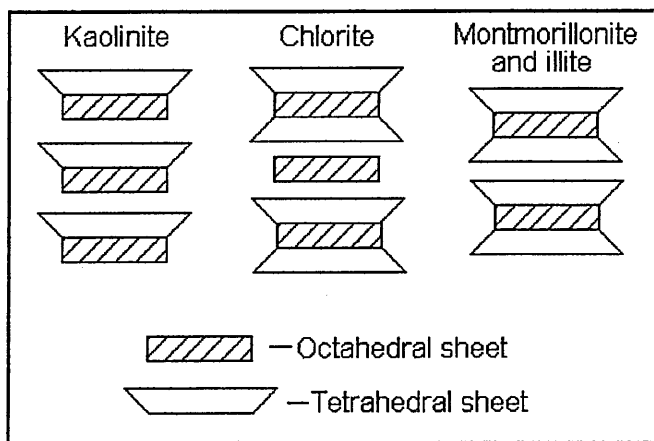


**Figure 1.6: Schematic representation of the sheet-like structures of clays.**

#### 1.4.2.1.2 Isomorphous Substitution

Isomorphous substitution is the replacement of ions in a sheet by ions of like size but lower charge. When  $\text{Si}^{4+}$  is substituted by  $\text{Al}^{3+}$  in the tetrahedral sheet, or when  $\text{Al}^{3+}$  is substituted by  $\text{Mg}^{2+}$  in the octahedral sheet, the layer obtains a net negative charge, which can be neutralised by introducing exchangeable cations into the interlayer space [18].

The clay layers are then bound together electrostatically by sharing these exchangeable cations. The number of these interlayer exchangeable cations in a clay is defined by the cation exchange capacity (CEC), measured in milliequivalents (meq) per 100 grams of clay, and is different for different mineral types. The CEC values for some clays are shown in Table 1.3. The cations can be exchanged by other cations such as Na, Ca, Mg, and K by placing the clay in a solution of the new ion.

#### 1.4.2.1.3 Swelling of Clay

Montmorillonite can swell with water and can intercalate polar organic molecules [18] as shown in Figure 1.7. The d spacing is  $12.5 \text{ \AA}$  with one layer of water and cations but can swell further to  $15.0 \text{ \AA}$  with two water layers, or can shrink to  $9.6 \text{ \AA}$  when dehydrated. It is possible to estimate the orientation of an intercalated organic molecule from the d spacing [19]. The amount of water in the interlayer is controlled by the humidity, the type of interlayer cation and by the charge density of the mineral [20].

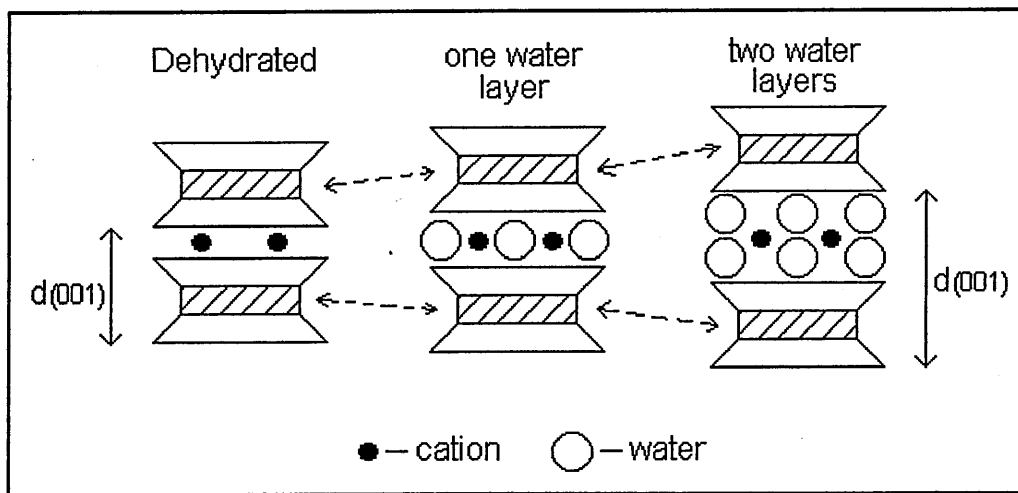


**Figure 1.7: Schematic representation of the swelling of a clay (e.g. montmorillonite) in water.**

#### 1.4.2.1.4 Clay Minerals of particular interest in this thesis

	Kaolinite	Montmorillonite	Illite	Chlorite
CEC (meq/100g)	3-15	80-150	10-40	10-40
Particle size (microns)	0.5-5	0.1-2	0.1-2	0.1-5
Surface area BET-N <sub>2</sub> (m <sup>2</sup> g <sup>-1</sup> )	15-25	30-80		140

**Table 1.3: Selected properties of Clay Minerals [21].**

#### Kaolinite

Kaolinite belongs to the kandite group of layer silicates. There are four polymorphs and kaolinite is the most common. The others are dickite (rare), nacrite (rare) and halloysite (moderately common). Kaolinite has the idealised formula  $Al_4Si_4O_{10}(OH)_8$ , although Fe, Ti, K, and Mg can also be present. It is a 1:1 layer silicate with d spacings being reported as 7.1 Å to 7.4 Å [22, 23, 24] where the d spacing is the distance between one sheet on a clay layer, and the equivalent sheet on the adjacent clay layer. Kaolinite has no interlayer cations since there is no charge on the lattice arising from isomorphous substitution. Kaolinite has not been found to swell in water but some organic molecules such as formamide can be intercalated between the kaolinite layers because it enters into the hydrogen bonding network.

### Montmorillonite

Montmorillonite has the idealised formula  $\text{Na}_{0.3}(\text{Al}_{1.7}\text{Mg}_{0.3})\text{Si}_4\text{O}_{10}(\text{OH})_2$  and is a dioctahedral smectite with a 2:1 layer structure. It can have a relatively high amount of isomorphous substitution so there are often deviations from the idealised formula. The surface of montmorillonite acts as a weak Lewis base since it can donate electrons to make a chemical bond. The surface is however quite unreactive since there is a strong bond between Si and O on the surface [25]. In contrast to kaolinite, the structure of montmorillonite allows water and polar molecules to enter between the layers easily. This is due to the weak electrostatic bonding between the layers and exchangeable cations present in the montmorillonite interlayer. Interaction with interlayer cations is an important feature of montmorillonite behaviour.

### Illite

The idealised structural formula for illite is  $\text{KAl}_2(\text{Si}_3\text{Al})\text{O}_{10}(\text{OH})_2$ , but Fe and Mg can also be present. The structure is the same as for montmorillonite except that some of the silicon ions are always replaced by aluminium ions and the deficiency balanced by potassium ions. Van der Waals attractive forces, caused by the small size of the non-hydrated potassium ions, combine with the electrostatic forces to produce stronger bonding between the layers. This strong bonding makes the illite structure very difficult to swell and difficult for cation exchange to occur.

### Chlorite

The idealised structural formula for chlorite is  $(\text{Mg, Fe, Al})_6(\text{Al, Si})_4\text{O}_{10}(\text{OH})_8$ , although some varieties contain high amounts of chromium, nickel, or manganese. Isomorphous substitution of silicon by iron or aluminium ions occurs in the tetrahedral sheet of chlorite, generating negative charges on the surface. A magnesium-hydroxide sheet with isomorphous substitution of aluminium ions for magnesium ions, neutralises these charges. Like montmorillonite, chlorite is a 2:1 layered mineral but has an extra sheet so is considered a 2:1:1 layered structure. Unlike montmorillonite which has a dioctahedral arrangement in the octahedral layer, the octahedral layer of chlorite has a trioctahedral arrangement. A dioctahedral arrangement means that there are two cations for each of

the six OH<sup>-</sup> anions on a sheet and a trioctahedral arrangement means that there are three cations for each of the six OH<sup>-</sup> anions on a sheet.

#### **1.4.2.2 Mica**

Muscovite is a common mineral found in sedimentary rock and is also found in igneous and metamorphic rock. It is the most common mineral of the mica group and is in the same silicate class and phyllosilicate subclass as the clay minerals. It therefore also has a layered structure of aluminosilicate sheets. These sheets are strongly bonded together by layers of unhydrated potassium ions [26, 17]. Bound nitrogen, mainly in the form of ammonium, is common in the Earth's crust and can be found in layer silicates and mica in particular. The charge and radius of the ammonium atom allows it to replace the interlayer potassium ions of mica, although the most common interlayer cation remains potassium [27].

#### **1.4.3 Carbonates**

The structure of carbonates is based on the fundamental anionic unit (CO<sub>3</sub>)<sup>2-</sup>, with carbon at the centre of an equilateral triangle of three oxygen ions. Carbonates are very common minerals, and calcite is one of the most common on Earth, comprising about 4 wt% of the Earth's crust. It is also widespread, being able to form in many different geological environments [26]

##### **1.4.3.1 Rhombohedral Carbonates**

###### **1.4.3.1.1 Calcite**

Calcite is the stable form of the widespread mineral CaCO<sub>3</sub>. Calcite is a rhombohedral carbonate with a central carbon ion and three oxygen ions lying in a single plane, giving it trigonal symmetry. The structure of calcite consists of alternating layers of these carbonate ions, and of calcium ions.

#### 1.4.3.1.2 Dolomite

Dolomite has the formula  $\text{CaMg}(\text{CO}_3)_2$ . In comparison to calcite, the dolomite structure has the addition of magnesium ions, which differ in size to calcium ions. In dolomite, the structure therefore has alternating layers of exclusively Mg ions, followed by carbonate ions, followed by exclusively Ca ions and so on. It is thought that having these alternating layers probably produces a more stable structure than one with layers of mixed Ca and Mg ions due to the size difference of the cations.

#### 1.4.3.1.3 Others

Ankerite is a member of the dolomite group and has the general formula  $\text{CaFe}(\text{CO}_3)_2$ . However, there is actually a significant amount of magnesium and manganese substitution for the iron. The structure of ankerite is similar to that of dolomite but has alternating layers of calcium and iron cations. The significant amount of cation substitution, however, lowers the symmetry compared with dolomite.

Siderite is another rhombohedral carbonate but has the formula  $\text{FeCO}_3$ . It has a similar structure to calcite but with iron replacing calcium.

### **1.4.3.2 Orthorhombic Carbonates**

#### 1.4.3.2.1 Aragonite

Aragonite is a common polymorph of calcite so also has the formula  $\text{CaCO}_3$ . It is less stable than calcite, though, and aragonite will convert to calcite over a long time period or at temperatures above 400 °C.

In comparison to the one plane structure of calcite, the structure of aragonite has the three oxygen ions lying in two planes pointing in different directions, giving it orthorhombic symmetry.

#### 1.4.3.2.2 Others

Vaterite is also a polymorph of calcite so has the formula  $\text{CaCO}_3$ , but it has hexagonal symmetry. It is a very rare mineral and is the least common of the three phases of  $\text{CaCO}_3$ .

Strontianite,  $\text{SrCO}_3$ , and witherite,  $\text{BaCO}_3$ , are other orthorhombic carbonates. However, both are rare.

## **2. Theory of Techniques used in this thesis**

### **2.1 Infrared Spectroscopy**

#### **2.1.1 Introduction**

Infrared radiation (IR) is electromagnetic radiation with a wavelength between approximately  $10^{-3}$  and  $10^{-6}$  m. When a sample is positioned in the path of an IR beam, polyatomic molecules absorb particular frequencies of this infrared radiation, creating a characteristic infrared spectrum. Different functional groups absorb characteristic frequencies of IR radiation making IR spectroscopy an important tool for determining the structure of molecules and identifying compounds. An infrared spectrum is generally presented as absorption intensity vs. wavenumber in  $\text{cm}^{-1}$  and in this thesis the mid IR region, between 4000 and  $400 \text{ cm}^{-1}$ , was used [28]. The infrared spectra of powdered samples can be measured using transmission spectroscopy, diffuse reflectance spectroscopy, emission spectroscopy, and photoacoustic spectroscopy. Diffuse reflectance spectroscopy has been applied in this thesis and will be discussed further in section 2.1.5 of this chapter.

#### **1.2.2 Absorption of Infrared Radiation**

The atoms in molecules are in continuous vibration with respect to each other at temperatures above absolute zero. A molecule absorbs radiation when the frequency of a specific vibration is equal to the frequency of the IR radiation directed at the molecule. A molecule must undergo a net change in dipole moment due to its vibrational motion to produce adsorption bands in the IR spectrum. The dipole moment describes the asymmetry of charge distribution, and is defined as the product of the total amount of positive or negative charge and the distance between the atoms.

The number of observed absorption bands is generally different from the number of fundamental vibrations. The number of fundamental vibrations is  $3N-6$  for non-linear molecules and  $3N-5$  for linear molecules, where  $N$  is the number of atoms. Fewer

absorption bands may be observed because some vibrations are not IR active, i.e. there is no net change in dipole moment, and because a single frequency can cause more than one type vibration to occur [29]. The number of observed absorption bands can, however, be increased by the appearance of overtones, combinations of fundamental frequencies, differences of fundamental frequencies and coupling interactions. Overtones are integral multiples of the fundamental absorption frequencies, and coupling interactions can be between two fundamental frequencies or between fundamental vibrations and overtones or combinations bands. The intensities of overtone, combination, and difference bands are less than those of the fundamental bands. All these factors combined, produces a unique IR spectrum for each compound [28].

In polyatomic molecules, there are two fundamental types of vibration:

- (i) stretching of the interatomic bonds, where the length of a bond changes, and
- (ii) bending, where the angle between two bonds changes.

The types of stretching and bending vibrations that occur in molecules are shown in Figure 2.1.

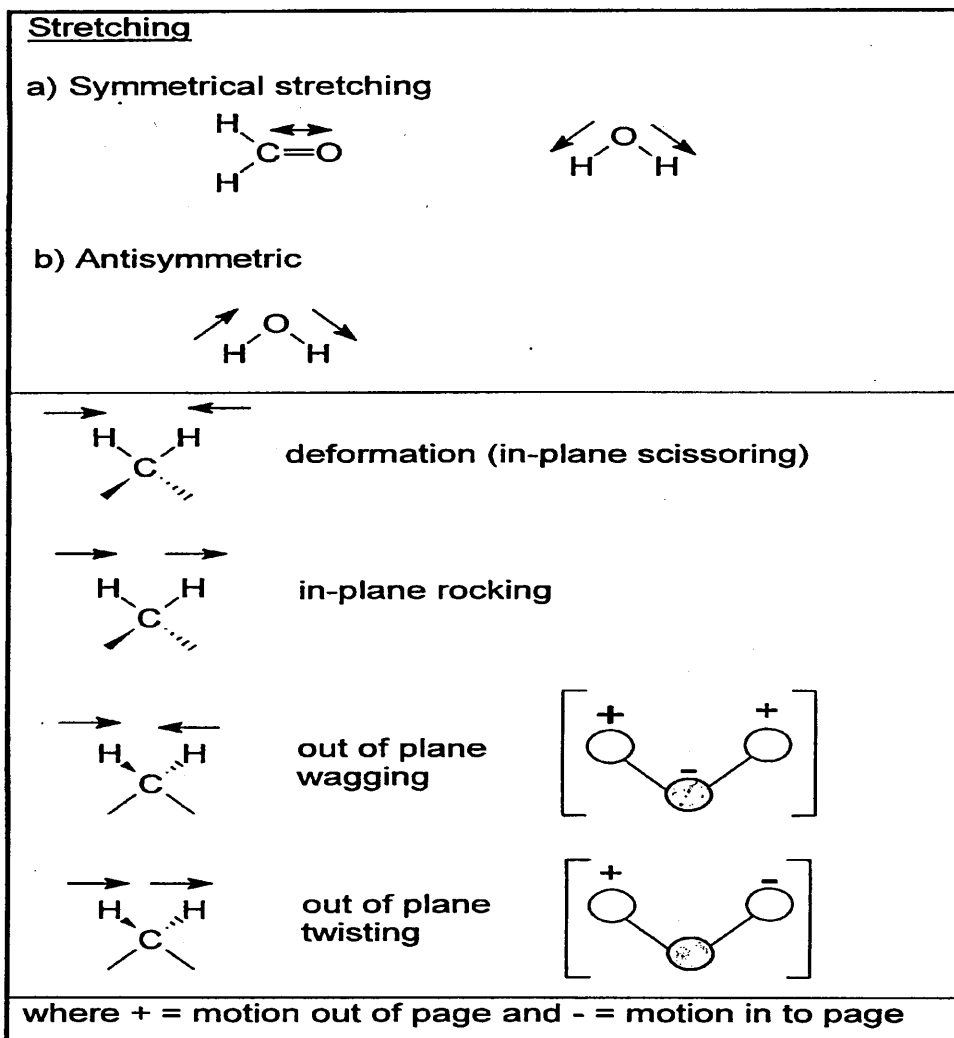


**Figure 2.1: Types of stretching and bending vibrations that occur in molecules.**

### 2.1.3 Use of Infrared Spectroscopy for Clay Mineral Analysis

For the investigation of clay organic complexes in particular, infrared spectroscopy has proved to be most effective since it can provide characteristic information regarding the molecular orientation of organic molecules in the interlayer space, mechanisms of interaction with the silicate surface, interlayer cations, residual water and interactions between the adsorbed molecules themselves. Changes in the chemical composition taking place in the interlayer space under the effect of heat, evacuation or changing humidity can be detected by infrared spectroscopy. It is therefore complementary to the

X-ray diffraction (XRD) technique which provides information regarding the modification of clay basal spacing due to packing and orientation.

#### **2.1.4 Fourier Transform Infrared Spectroscopy (FTIR)**

While the FTIR spectrometer was initially used as a high performance research tool in industry in the late 1970s, it is now the preferred method of infrared spectral analysis. Both FTIR spectrometers and dispersive spectrometers can be used for mid-infrared applications. A dispersive spectrometer uses a prism or grating to resolve the radiation into its separate components for successive measurement, while an FTIR spectrometer uses a Michelson interferometer. FTIR spectrometers have mostly replaced dispersive spectrometers for mid-infrared applications because the interferometer reduces the measuring time of the instrument by measuring all the spectral radiation simultaneously, and the FTIR spectrometer is more sensitive.

FTIR spectrometers have three basic components: radiation source, interferometer, and detector. While a dispersive IR spectrometer uses a monochromator, this is replaced with an interferometer in an FTIR spectrometer. The interferometer divides radiant beams, generating an optical path difference between the beams before recombining them to produce repetitive interference signals [28]. The layout of an FTIR spectrometer is shown in Figure 2.2.

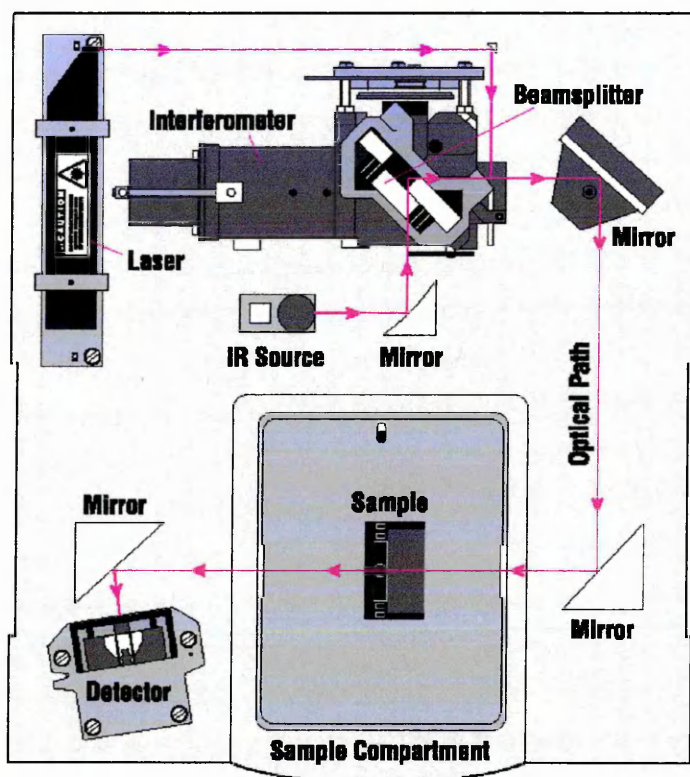


**Figure 2.2: Layout of an FTIR Spectrometer [30].**

A Michelson interferometer is the most common interferometer and it consists of three active components: a moving mirror (A), a fixed mirror (B), and a beamsplitter. The components of a Michelson interferometer are shown in Figure 2.3.

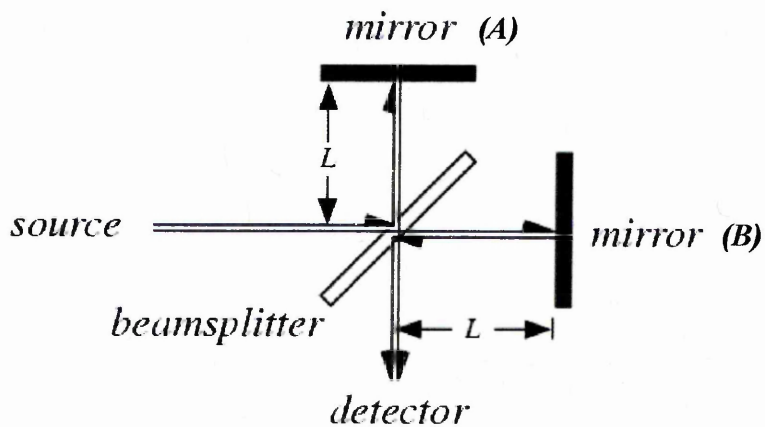


**Figure 2.3: Components of a Michelson interferometer [29].**

When collimated monochromatic radiation from the source reaches the beam-splitter, it is divided into two equal beams, one transmitted to each of the two mirrors. The two beams are then reflected back to the beam-splitter and recombined. The optical path difference between the two recombined beams varies due to the moving mirror. When the path difference is an integral number of wavelengths, then the beams will be in phase and constructive interference will occur. When the path difference is  $\lambda/2$ , destructive interference occurs. The changes in the relative position of the moving mirror to the fixed mirror, therefore generates an interference pattern. Of the recombined beam, 50% is sent to the detector via the sample, and the remaining 50% is lost as it is sent back towards the source.

Since the mirror is moved at a constant velocity, the intensity of radiation reaching the detector varies in a sinusoidal manner, producing an interferogram. An interferogram is a plot of the detector response, intensity in volts vs. the position of the moving mirror in cm. At a frequency at which the sample absorbs, the amplitude of the sinusoidal wave reduces by an amount related to the amount of sample in the beam. The concentration of the sample is proportional to absorbance. The absorbance is equal to  $\log I_0/I$ , where  $I_0$  is the intensity of the radiation incident on the sample and  $I$  is the amount of radiation transmitted by the sample. The interferogram, which contains information over the full IR region to which the detector is responsive, is converted to a frequency domain by a mathematical operation known as a Fourier transform. An apodisation function is used to truncate the interferogram, removing unnecessary data, and this function can also change both the resolution and signal to noise ratio of the spectrum.

There are two popular detectors that can be used in an FTIR spectrometer, a deuterated triglycine sulphate (DTGS), and a mercury cadmium telluride (MCT). The DTGS detector is a pyroelectric detector that can deliver rapid responses. The MCT detector also delivers fast responses but is a photon detector. DTGS detectors operate at room temperature while MCT detectors must be cooled to liquid nitrogen temperature (77 °K) to operate effectively. Generally, MCT detectors are faster and more sensitive than DTGS detectors [28].

## **2.1.5 Diffuse Reflectance Infrared Fourier Transform Spectroscopy (DRIFTS)**

### **2.1.5.1 Introduction and Theory**

The diffuse reflectance spectra of powders have been measured for many years to obtain qualitative results. DRIFTS is widely used because little sample preparation is required, it is a sensitive technique which allows qualitative and quantitative information to be obtained [31], and useful overtone and combination bands are observed [32].

In DRIFTS, incident radiation is reflected from the surface of a sample. A single reflectance spectrum of a sample is ratioed against a single reflectance spectrum of a good diffuse reflector reference to calculate a DRIFTS spectrum.

### **2.1.5.2 Types of Reflectance**

The main difficulty with DRIFTS is the presence of spectral distortions caused by the mixing of diffuse and specular reflectance, diffuse reflectance being that which has penetrated samples and therefore contains information about the absorptivity of the sample, and specular reflectance being that which is reflected from the surface of a particle without being absorbed [33]. Diffuse specular reflectance is the name given to radiation that has been reflected from the surface of multiple particles but, like specular reflectance, is not absorbed. True diffuse and diffuse specular reflections are indistinguishable, since in both the reflected beam can emerge at any angle relative to the incident radiation [33]. In specular reflectance, however, the angle of incidence is equal to the angle of reflectance. The three modes of reflection in a DRIFTS experiment are shown in Figure 2.4.

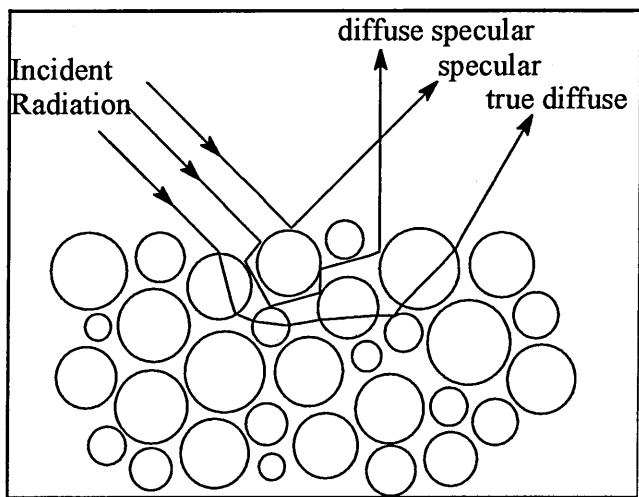


**Figure 2.4: Schematic illustration showing the three modes of reflection in a DRIFTS experiment.**

The optical arrangement of the accessory and the physical and chemical characteristics of the sample govern the amount of each type of reflectance collected in an experiment. For example, spectral distortions, such as peak inversion (Reststrahlen bands), can be reduced by diluting with a powdered material inactive to infrared [31, 33, 34] and a Blocker can be used to reduce spectral distortions. A Blocker is a blade which, when placed perpendicularly onto the sample surface, prevents the true specular reflectance from reaching the detector [33].

The amount of specular component in the spectrum is governed by the refractive index ( $n'$ ), which is described as the sum of the index of refraction ( $n$ ) and the absorption index ( $k'$ ) [21].

$$n' = n + ik'$$

Fresnel's equations describe specularly reflected light. The reflection of radiation at an interface is expressed as a function of the refractive indices of the two media that form the interface. The difference in the refractive indices leads to reflection.

The absorption index,  $k'$  is related to the absorption coefficient,  $K$ ,

$$k' = K/(4\pi\nu),$$

where  $\nu$  is the frequency of radiation ( $\text{cm}^{-1}$ ).

The absorption coefficient,  $K$ , is related to the absorptivity,  $a$ ,

$$K = 2.303ac,$$

where  $c$  is the concentration.

The larger the absorptivity of a sample, the greater the specular reflectance will affect the spectra. Specular reflectance can cause a sample with intermediate absorptivity to have spectra with derivative shaped features or a shift in peak position to higher wavenumbers. Samples with larger absorptivity, such as some minerals, can have large Reststrahlen bands present in their spectra.

Much of the non-linearity associated with DRIFTS is due to specular reflectance so all factors that produce specular reflectance must be minimised in experiments so that the maximum ratio of true diffuse to specular reflectance is collected.

### 2.1.5.3 Instrumentation

A schematic diagram of the type of DRIFTS accessory used for the studies in this thesis is shown in Figure 2.5.

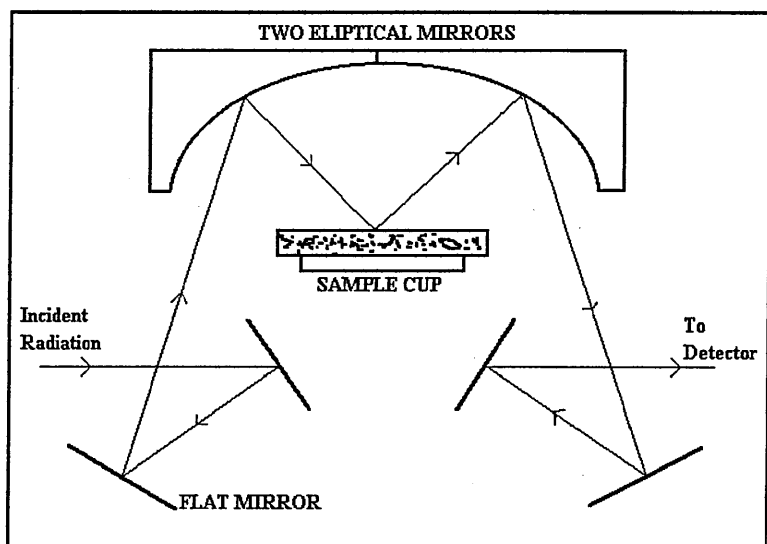


**Figure 2.5: Schematic diagram of the accessory used to collect DRIFTS spectra.**

The total reflectance is collected by two elliptical mirrors. Accessory alignment is critical because typically only 10 to 15% of the energy throughput is available for DRIFTS analysis. Two of the mirrors can be manually adjusted with Allen keys and the

sample height adjusted with a screw so that the sample surface is aligned at the focal point.

#### **2.1.5.4 Diffuse Reflectance as a Quantitative Technique**

For an analytical technique to be considered quantitative, the procedure must be reproducible. Concerns about using DRIFTS for quantitative work have been expressed for two main reasons. The first is the difficulty in preparing samples with reproducible physical characteristics since reproducibility of spectra is dependant on maintaining the same particle size, packing density, analyte concentration, homogeneity and position in the accessory between samples [31]. The second reason is the difficulty in converting spectra into a format where band intensities vary linearly with concentration over a wide concentration range. The second problem arises due to the presence of specular reflectance in a diffuse reflectance spectrum, making it difficult to correlate the amount of true diffuse reflectance to sample concentration.

#### **2.1.5.5 Reproducing Physical Characteristics of Samples**

##### 2.1.5.5.1 Reference Powder

The spectrum of a reference powder is used in a DRIFTS experiment as a background that the sample spectrum is ratioed against.

Ideal matrices for DRIFTS are hard, finely ground powders that will scatter radiation efficiently [35]. They should also be non-absorbing, nonhygroscopic, inert, nontoxic, and have a low refractive index [36]. A small particle size is required since large particle sizes are difficult to pack and level [37]. KBr is the most widely used material for the matrix and TeVrucht *et al.* [35] compared pure KBr to a mixture of CsI and KBr and found KBr alone to be better since the CsI mixture is softer.

The reference powder is also used to dilute the sample. This dilution reduces the specular component and increases the diffuse component in the reflected radiation. This is because around 95% of the surface is KBr and not sample, so only around 5% of the

incident beam is truly specularly reflected. The remainder of the beam penetrates into the sample and undergoes true diffuse and diffuse specular reflectance. Also, the sample is in contact with KBr as opposed to air, as would be the case in pure sample. This reduces the specular reflectance and increases the diffuse reflectance that will occur because the refractive index of the powdered sample is closer in value to KBr than it is to air [21]. The amount of dilution used throughout the majority of this thesis is 4 wt% powdered sample dispersed in KBr.

#### 2.1.5.5.2 Particle Size and Grinding Effects

The particle sizes of the reference powder and the sample affect the amount and type of reflectance that occurs in a DRIFTS experiment. With larger particle sizes, the specular reflectance increases, reducing the amount of spectral information which can be collected on the sample [21]. Also, in order for the Kubelka-Munk function, described in section 2.1.5.6.1, to be directly proportional to the concentration of sample, the particle size must be less than the wavelength of the radiation [38].

The general trend is that a decrease in particle size causes an increase in band height and a decrease in band width.

Some previous workers found that KCl was the best alkali halide to use as the diluent if ground to <10  $\mu\text{m}$ , giving the fewest interferences and highest reflectance [39, 40].

Azambre *et al.* [34] also suggested particle sizes of about 10  $\mu\text{m}$  for both the diluents and sample. However, they used KBr and not KCl. Xu *et al.* [41] proposed that the particle size must not be greater than 2.5  $\mu\text{m}$  for accurate quantitative analysis since above this the particle size would be larger than or equal to the wavelength of radiation, which would cause a decrease in band intensity, an increase in background, broad peaks and sloped backgrounds.

TeVrucht *et al.* [35] found the most reproducible spectra for a bituminous coal when diluent KBr was ground to a particle size range of 10-20  $\mu\text{m}$  in a ball mill. The coal was ground to match this particle size range then 1 wt% of coal was diluted with KBr before

measurement. Other workers, such as Azambre *et al.* [34] have used different procedures including grinding by hand.

Studies have been carried out on how grinding affects the structure of the clay mineral kaolin. During grinding local heat generated produces enough energy to break hydroxyl bonds and inner-surface hydroxyls are lost before inner hydroxyls [42]. The reduction in structural hydroxyls causes a lower dehydroxylation temperature. The amount of adsorbed water on the clay increases with more grinding as the clay becomes hygroscopic [37, 42, 43]. Up to a certain time, grinding increases the surface area of the powder, as clay layers are delaminated. After this grinding time however, the particles agglomerate and surface area begins to decrease [37, 43, 44, 45]. The cation exchange capacity of the clay also increases with grinding since protons that have migrated to the particle surface can be exchanged with other cations [37, 33, 44]. Grinding is said to be less destructive if carried out under water and the effect of grinding is less on trioctahedral clays than dioctahedral clays [43].

The effects of grinding on the spectra of clays were highlighted by Frost *et al.* [42] and Aglietti [44]. They reported that the OH stretching band at  $3670\text{ cm}^{-1}$  decreased with grinding while the OH bending band at  $1640\text{ cm}^{-1}$  and the band due to adsorbed water at  $3400\text{ cm}^{-1}$  increased. Clegg [21] reported that in general, as the particle size was reduced, band heights increased and band widths decreased. Frost *et al.* [42] and La Iglesia *et al.* [46] reported small changes in the  $1070\text{-}1150\text{ cm}^{-1}$  region when pressure was exerted on a sample, due to Si-O-Si in-plane deformation, i.e. structural disorder.

#### 2.1.5.5.3 Sample Packing

The method used to pack powdered samples into sample cups can affect the band intensities in collected spectra. Samples can be packed under different pressures, altering the degree of scattering that occurs, and therefore changing the band intensities.

A compaction device is likely to give more reproducible results since it would allow more control over the amount of sample in the cup and therefore provides reproducible depth of penetration of radiation into the matrix. Also, uniform packing across the

surface of the cup can be achieved with a packing device. Samples packed with even pressure on the whole surface produce a uniform scattering coefficient for the surface. This means that reproducible band intensities can be achieved [36, 47]. The duration of pressure on the sample during packing also affects the scattering coefficient and therefore band intensities, so this also must be controlled [47].

Conflicting reports about the effect of pressure on the scattering coefficient have been reported by Yeboah *et al.* [47] and by Krivácsy *et al.* [36]. The scattering coefficient determines the extent of interaction of the incident radiation with the sample before it emerges from the sample [47]. While Yeboah *et al.* reported that the pressure increase resulted in a decrease in the diffuse reflectance, band intensity and scattering, Krivácsy *et al.* reported an increase in scattering with pressure. The pressures investigated by Yeboah *et al.* [47] were in the range 10-80 MPa, while Krivácsy *et al.* investigated the much lower 0-1 MPa range. Krivácsy *et al.* [36] reported that applying a pressure of 1 MPa for 1 minute gave reproducible sample packing and fulfils the infinite thickness criteria of the Kubelka-Munk theory.

TeVrucht *et al.* [35] also used a compaction device to ensure repeatable packing density, as did Hřebičík *et al.* for various chemicals including hydroquinone and nicotinamide [48]. Azambre *et al.* [34] also used a concentration of only 2 wt% of an anthron-anthracen mixture, and did not pack the sample but, instead, simply levelled the sample with a blade.

#### 2.1.5.5.4 Sample Rotation

Velapoldi and Tvedt [49] devised an apparatus for rotating the sample during DRIFTS analysis to obtain more precise, representative spectra. They also highlight the time saving advantage of using this device since multiple spectra would not have to be collected and averaged to obtain a representative spectrum. With their device the sample is rotated through 360° in the time taken to collect a spectrum.

## 2.1.5.6 Relationship between Diffuse Reflectance and Sample Concentration

### 2.1.5.6.1 The Kubelka-Munk function

If the physical characteristics of a sample are reproducible then, as the sample concentration increases, the amount of specular reflectance increases, causing a decrease in diffuse reflectance.

Kubelka and Munk developed a theory regarding the relationship between the light absorbed in a diffuse reflectance experiment and the concentration of an absorbing component [50, 51]. The Kubelka-Munk (K-M) function,  $F(R_\infty)$ , is given by,

$$F(R_\infty) = (1 - R_\infty)^2 / (2R_\infty) = K/S,$$

where  $R_\infty$  is the diffuse reflectance spectrum of an infinitely thick sample ratioed against that of a non-absorbing reference.  $K$  is the absorption coefficient and  $S$  is the scattering coefficient.

The Kubelka-Munk (K-M) function gives a linear relationship between sample concentration and peak intensity in a DRIFTS spectrum provided that the scattering coefficient remains constant [31, 40], and the amount of specular reflectance is negligible, as the concentration is varied. Since the scattering coefficient depends on particle size and packing density, these must remain as consistent as possible between samples for quantitative measurements [40]. The K-M function is only useful when samples are small absorbers and the concentration range is small since deviations from linearity can be found with highly absorbing samples and with high sample concentrations [31, 40]. One reason for this deviation from linearity is that the penetration depth of the radiation is reduced when sample concentration increases. The K-M equation was derived for weakly absorbing samples, and so it was assumed that the penetration depth should remain constant. The K-M equation assumes infinite dilution of the sample in the non-absorbing matrix [33] and infinite thickness, relative to the depth of penetration of the infrared beam [31, 40]. Strong bands are exaggerated and weak bands diminished with the K-M function [31, 33].

## 2.1.6 Other Infrared Techniques

### 2.1.6.1 Transmission Spectroscopy

Transmission spectroscopy is the classical infrared spectroscopy method. Radiation passes completely through the sample and a plot of difference in energy between the incident and transmitted beams against wavelength/wavenumber is recorded. The amount of infrared radiation transmitted,  $T$ , by a sample is given by,

$$T = I/I_0$$

The intensity of infrared radiation incident on the sample and the amount of radiation transmitted by the sample are represented by  $I_0$  and  $I$  respectively. Sampling techniques include mulls, potassium bromide (KBr) disks, free standing films and sodium chloride (NaCl) plates. For the analysis of clay minerals using transmission spectroscopy, KBr disks, and free standing films are used [20]. A disadvantage of the KBr technique is that the pressure required to prepare the disks can cause structural damage to the sample, spectral distortions, and chemical reactions [21].

The amount of sample analysed using transmission spectroscopy is less than that analysed using DRIFTS since the penetration depth of the infrared beam in DRIFTS is about 200  $\mu\text{m}$ , approximately 10% of the total bed depth. The DRIFTS spectrum is therefore averaged over a larger, more representative mass of sample than the transmission spectrum is. The enhancement of absorbance bands in the DRIFTS spectrum, in comparison to the transmission spectrum, also makes DRIFTS a more useful technique [37].

### 2.1.6.2 Attenuated Total Reflectance (ATR) Spectroscopy

In ATR spectroscopy, a beam of radiation enters from a more-dense, higher refractive index medium such as zinc selenide or diamond, into the less-dense, lower refractive index medium of the sample. When the angle of incidence is greater than the critical angle (a function of refractive index) all incident radiation is completely reflected. Before complete reflection occurs, the beam penetrates a very short distance beyond the interface into the less-dense sample. The penetration is typically at a depth of a few micrometers and is called the evanescent wave. The sample must therefore be flush with

the surface. While the band positions in an ATR-IR spectrum are the same as in a transmission spectrum, the relative intensities of corresponding bands are different [28]. When using ATR to study clay minerals, a clay powder or paste must have good contact with the crystal. ATR would be a useful technique if the clay is already in a high water environment [20].

### **2.1.6.3 Photoacoustic Spectroscopy**

Photoacoustic spectroscopy is a suitable technique for analysing highly absorbing samples and requires minimal sample preparation. The modulated IR radiation from an FTIR interferometer is focused on a sample contained within a chamber filled with helium or nitrogen gas. IR radiation absorbed by the sample converts into heat inside the sample, which diffuses into the surrounding gas. Pressure waves are generated and a sensitive microphone is used to detect the resulting photoacoustic signal [28].

As an alternative technique to DRIFTS, photoacoustic spectrometry has the advantages of reduced distortions in the spectra and more reproducible band intensities. Also, this technique does not require a powdered sample, so preparation time is reduced. It does, however, have a poorer signal to noise ratio than DRIFTS [52].

## **2.2 Thermogravimetric Analysis**

Thermogravimetric analysis (TGA) is a technique whereby the mass of a sample is monitored over time and temperature. A refractory crucible suspended from a sensitive recording balance contains the sample. A sample can be heated from room temperature to 1000 °C and the TG curve produced shows a decrease (or increase) in weight as the sample is heated. The TG data can be represented as a negative derivative (DTG) curve where the maximum corresponds to the maximum rate of mass loss as shown in Figure 2.6. Information on the dehydration, i.e. loss of physisorbed water, and dehydroxylation of samples can be found and it can be used for the quantitative analysis of multicomponent mixtures [53]. TGA can differentiate between interlayer water and structural hydroxyl groups by the temperature at which the peaks appear. Since many minerals have constant mass loss over certain temperature ranges, amounts of mineral

components in a mixture can be determined provided the minerals do not have overlapping mass losses.

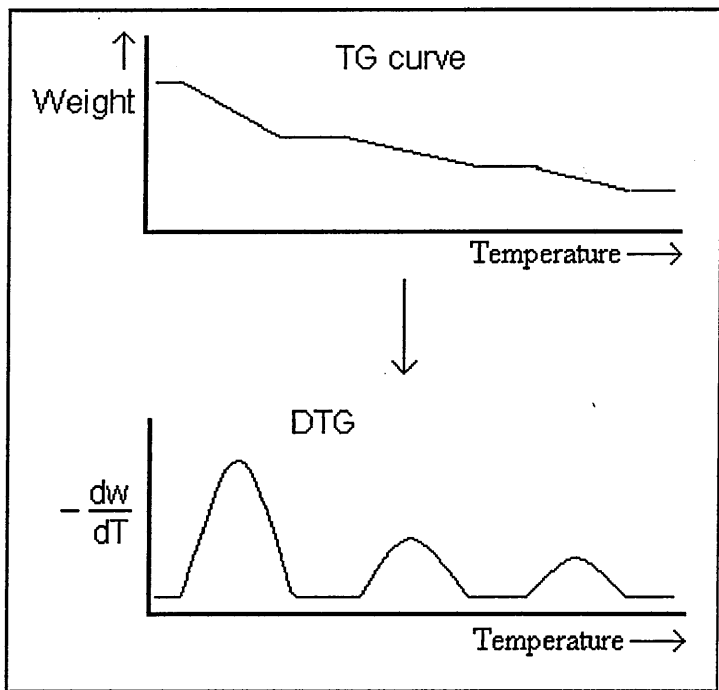


**Figure 2.6: A weight loss curve (upper plot) and the negative first derivative of this curve (lower plot) from TGA.**

Thermogravimetric data can be affected by the amount of sample, the depth of the sample bed, particle size distribution, and degree of order of the sample [53]. The heating rate also affects the shape of the DTG curve. With an increase in the heating rate, the resolution of the maxima decrease and maxima temperatures and size increase. These factors must therefore be taken into account in order to achieve reproducible data. Other factors that should be considered are the use of inert atmospheres and the type of sample holder. Nitrogen and/or helium atmospheres, for example, may be used to suppress the oxidation of organic materials in clays and the sample holder must enable efficient removal of product gases close to the sample.

### 2.3 X-ray Diffraction (XRD)

XRD is used to identify crystalline phases present in materials. The basic features of an XRD experiment are shown in Figure 2.7.

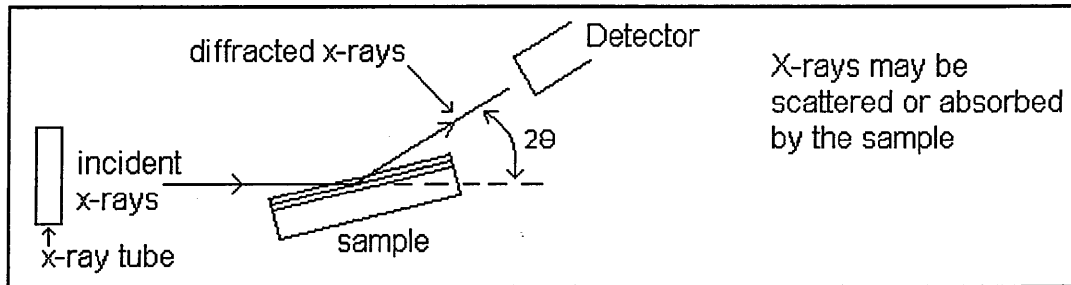


**Figure 2.7: Schematic illustration showing the basic features of an XRD experiment.**

X-rays are produced when high speed electrons strike the atoms of another substance. Inside the X-ray tube the electrons are generated by a heated tungsten filament (the cathode), under vacuum. The electrons are then accelerated in order to strike a target, such as Cu (the anode). The accelerated electrons strike the inner more tightly bound electrons of the target and knock them out of their orbital positions, producing electron vacancies, which are then filled by higher orbit electrons dropping inwards. The higher orbit electrons dropping inwards produces an X-ray photon, the energy of which is proportional to the difference between the energy levels of the orbitals. This energy difference is dependent on the number of protons in the nucleus attracting the electrons. The wavelength of Cu  $K\alpha$  radiation is 1.5418 Å.

When X-rays pass through sample matter, the radiation interacts with the electrons in the atoms, which results in scattering of the radiation. If the atoms are organised in planes (i.e. the matter is crystalline) and the distances between the atoms are of the same magnitude as the wavelength of the X-rays, constructive and destructive interference will occur [30].

Diffraction will occur if a beam of X-rays falls on a series of atom-bearing planes, each a distance  $d$  apart, at an angle  $\theta$ , if the Bragg Law:

$$n\lambda = 2d \sin \theta$$

(where  $\lambda$  is the wavelength of the rays and  $n$  is an integer), is obeyed.

By rearranging this equation, the  $d$  spacing of clays can be calculated.

During an experiment the detector is rotated by a goniometer in order to reach the required angle ranges (2-75°).

In this thesis the samples analysed were either rock core slices or powders. Powders were compacted into an aluminium sample holder by the back packing method.

## **2.4 X-ray Fluorescence (XRF) Spectroscopy**

The elemental composition of a sample can be determined by XRF spectroscopy. X-rays, produced from an X-ray tube, are directed towards a sample, where the x-ray is either absorbed by an atom or scattered through the material. When the X-ray is absorbed by an atom, electrons are ejected from the inner shells, creating vacancies which are then filled by electrons from the outer shells. In this process, a characteristic X-ray is produced, whose energy is the difference between the two energy levels, and this is called X-ray fluorescence. Since each element has a unique set of energy levels, each element produces X-rays at a unique set of energies. It is therefore possible to non-destructively measure the elemental composition of a sample. The amount of fluorescence at a specific wavelength is related to the concentration of that element in the sample.

## **2.5 Chemometrics**

Chemometrics is the use of calculations on spectral data to enhance quantitative analysis of samples. Due to the complexity of multicomponent spectra, peak overlap often means that univariate analysis, i.e. assigning an isolated peak to correspond to one component, will not give accurate results [55]. Multivariate analysis is used to give more accurate quantitative analysis, and linear calibration models are created by techniques such as classical least squares (CLS), inverse least squares (ILS), principal component regression (PCR) and partial least squares (PLS) regression. Using these models, the concentration of the individual components in the samples can be related to a measured response.

### 2.5.1 Classical Quantification Methods

Classical methods of quantitative analysis are relatively straightforward and use Beer's law,

$$A = abc,$$

where  $A$  is the sample's absorbance at a specific wavelength,  $a$  is the absorptivity coefficient for the component,  $b$  is the pathlength through the sample, and  $c$  is the concentration. The classical methods, therefore, relate the spectral absorbances and the concentrations.

There are two classical quantification methods that use multivariate analysis, classical least squares (CLS) and inverse least squares (ILS). These models can predict the concentration of components in mixtures when there is overlapping of bands.

CLS was not used for the studies described in this thesis because it requires knowledge of the complete composition of the calibration and independent standards. Although this method may be able to accurately quantify components in a synthetic mixture, it would not be capable of quantifying the components in a real sandstone rock. CLS is also very susceptible to baseline effects since the equations assume that the response at each wavelength is due entirely to the calibrated components. This makes the CLS model less robust.

In contrast to CLS, ILS can calibrate very complex mixtures since the concentrations of all the components in the mixtures are not required. Only the concentrations of the components of interest are required. ILS, however, was also not used for the studies described in this thesis since it requires a carefully selected number of specific wavelengths to obtain an accurate calibration model. If too few wavelengths are chosen then the model does not contain enough information. However, if too many are chosen then the model will include spectral noise which may not be present in the spectra of unknown samples. This leads to a reduction in prediction accuracy for "unknown" samples. Specific wavelengths must also be chosen using ILS and these must not be collinear, i.e. care must be taken to choose wavelengths that do not all increase and decrease by the same amount, as the concentrations of the components in the mixture change.

## 2.5.2 Eigenvector Quantification Methods

There are many different variations that make up a spectrum i.e. the components in the sample mixture, instrument variations, changing environmental conditions, and differences in sample handling. Eigenvector quantification methods such as PCR and PLS take account of all these variations by calculating the number of independent variations that occur in the spectral data. The largest variations in the training set would, hopefully, be due to different concentrations of the components. A training set is a collection of standards, i.e. mixtures of components, used for a calibration. PCR and PLS calculate a set of “variation spectra” that represent the changes in absorbances at all the wavelengths in the spectra of the training set. These “variation spectra” are then used instead of the raw spectral data for building the calibration model. Since, in most cases, there are fewer common variations than the number of calibration spectra, the number of calculations is reduced.

The “variation spectra” can be used to reconstruct the spectrum of a sample by multiplying each one by a different constant scaling factor and adding the results together until the new spectrum closely resembles the “unknown” spectrum. Each spectrum in the calibration set has a different set of scaling constants for each variation since the composition of each standard is different. The terms “variation spectra” and “scaling factor” are commonly substituted for “factors”, and “scores”, respectively [55]. The factors are related to the concentrations of the components in the standards and, therefore, can be used to predict the composition of “unknown” samples. The only difference between spectra of samples with different component concentrations is the fraction of each score.

The calculated scores are unique to each separate factor and training set spectrum, and can be used instead of absorbances in either of the classical model equations (CLS or ILS). Since the spectrum of the “unknown” is reduced from many wavelengths to a few scores, the ILS expression of Beer’s law is used to calculate concentrations due to the ability of ILS to calculate concentrations among interfering species. A large number of wavelengths from the spectra are used in CLS and this remains the case in eigenvector models since the factors are calculated from large portions of the spectrum, or the entire spectrum. Eigenvector models, therefore, combine features from both CLS and ILS

together in the same calculation. This is the reason why eigenvector models such as PCR and PLS are more accurate and robust than the classical models.

### **2.5.2.1 Principal Component Regression (PCR)**

In PCR, the factors and scores are used to calculate the calibration equations. A technique called principal components analysis (PCA) is used to calculate all possible variations in the spectra. PCA requires a training set that contains the components of interest that are present in the “unknown” samples and the components of the training set must span the concentration ranges expected in the “unknown” samples.

The training set data is often mean centred before applying PCA. This means that the average spectrum from all the calibration spectra is calculated and subtracted from every calibration spectrum. The result is that subtle differences between the spectra are enhanced.

PCA is effectively a process of elimination. Each independent variation is iteratively eliminated from the calibration spectra in series, creating a set of factors that represent changes in the absorbances that are common to all. One set of factors and scores is produced for the calibration after the training set has been fully processed by PCA. The factors calculated are, therefore, not optimised for each individual component which may cause a reduction in the accuracy of the quantification of some components.

The second step in PCR involves the regression of the scores against the component concentrations. A regression method similar to ILS is used. Since the regression is a separate second step, the factors and scores are actually calculated independently of any knowledge of the component concentrations. This means that they represent the largest common variations among the spectra in the training set rather than necessarily representing variations related to changes in the component concentrations. While some factors will be related to changes in the component concentrations, more factors than are necessary are often found in PCR models because some factors are not related to the components of interest.

### **2.5.2.2 Partial Least Squares (PLS) Regression**

PLS is another spectral decomposition technique related to PCR. In comparison to PCR, however, PLS uses the concentration of components in the training set as well as the spectral data to generate two sets of factors and two sets of scores for each component in the model. The factors calculated are, therefore, optimised for each individual component which should increase the accuracy of the calibration. PLS is a one step process with no separate regression step, unlike PCR. The use of concentration data in the decomposition step means that the spectra containing higher component concentrations are weighted more heavily than those containing low component concentrations. The main idea of PLS is to get as much concentration information as possible into the first few factors.

The two sets of scores (spectral and concentration) calculated are related to each other through a type of regression and a calibration model can be constructed. The factors are directly related to the constituents of interest in PLS, whereas in PCR it is assumed that the largest variations among spectra in the training set are due to changes in the component concentrations. PLS is therefore less likely than PCA to correlate the factors to irrelevant information [55] and is more robust [56]. PLS is used throughout this thesis since it does not require specific wavelength selection, in fact, the whole spectrum can be used. Also, in PLS only knowledge of the constituents of interest is required and PLS can sometimes be used to predict samples with constituents not present in the original calibration mixtures, i.e. contaminants. This is useful when studying real sandstone rocks since not all the constituents present in the rock will be known [55, 57].

#### **2.5.2.2.1 PLS-1 and PLS-2**

There are two subtly different versions of the PLS algorithm, PLS-1 and PLS-2. Like PCR, PLS-2 calibrates for all the components simultaneously. One set of factors and one set of scores are produced for the calibration. The factors calculated by PCR and PLS-2 are, therefore, not optimised for each individual component which may cause a reduction in the accuracy of the quantification of some components. PLS-1, on the other hand, calculates a separate set of factors and scores for each component. Using the optimum

number of factors for each component in a mixture can improve the accuracy of the quantification of components.

Despite the longer calculation time required by PLS-1 in comparison to PLS-2, the increase in accuracy of quantification of components by PLS-1 makes it a more attractive option. PLS-1 is particularly useful for analysing systems that have component concentrations that are widely varied [55]. Since the components in the training set described in this thesis have very different concentration ranges, it is thought that PLS-1 would most accurately quantify the components.

### **2.5.2.3 Comparison of PCR and PLS**

A diagram highlighting the main differences between PCR and PLS is shown in Figure 2.8. Some common uses for the two models are also shown.

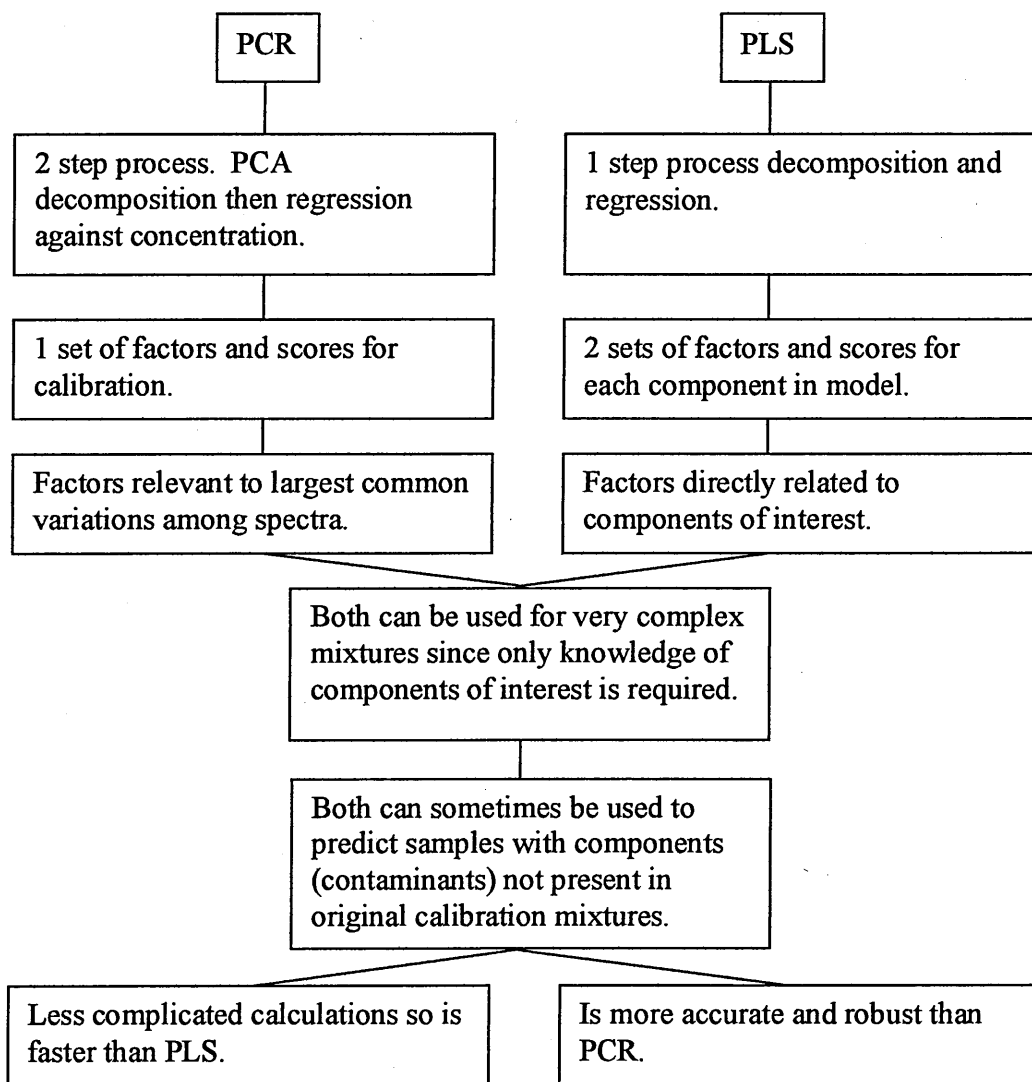


**Figure 2.8: Diagram showing the main differences between PCR and PLS and some common uses for both.**

### 2.5.2.4 Optimising PLS models

#### 2.5.2.4.1 Selecting the number of factors based on PRESS

Choosing the correct number of factors to use for each component in the model is important because changing the number of factors for a component alters the  $R^2$  value, i.e. the precision of the calibration. The earlier factors are most likely to be related to the constituents of interest while later factors have less information useful for predicting

concentration. It is also important to avoid overfitting, i.e. using too many factors or including noise factors, and underfitting, i.e. using too few factors resulting in a reduction in accuracy of predictions due to an insufficient number of terms being used to model all the spectral variations. To help in choosing the correct number of factors, the prediction residual error sum of squares (PRESS) can be calculated for every factor. This is calculated by predicting the training set itself against the model of the same training set using a certain number of factors. The sum of the squared difference between the predicted and actual concentrations gives the PRESS value for that model, then this is repeated for each factor [54]. A PRESS plot is a plot of these calculated PRESS values against the number of factors and generally the number of factors at the minimum of the PRESS plot is chosen as optimum.

#### 2.5.2.4.2 Cross Validation

Cross validation is a method of estimating the performance of a model by using the standards in the training set as unknowns. One training set standard is removed from the set and the decomposition and calibration is performed on the remaining standards using one factor. The concentration of the removed standard is then predicted. This process is then repeated for each factor, before the standard is placed back into the training set and another removed. The whole process is repeated for each of the training set standards, so that the model is validated with a large number of "unknown" samples, i.e. each standard in the training set. Cross validation therefore gives a very good indication of the error in accuracy of the model, when used to predict "real unknown" samples [55].

#### 2.5.2.4.3 Variance Scaling

Variance scaling is a pre-processing algorithm, often used with PLS, to give all information in the data equal weighting, so that the calibration errors are more consistent across all the components. Giving all values equal weighting emphasises small variations in the data. The response at each spectral data point is divided by the standard deviation of the responses of all training spectra at that point. The concentration data are scaled in the same way for each component. Variance scaling is most useful for analysing

components with low concentrations that have spectral bands that overlap those of components with higher concentrations [55].

#### 2.5.2.4.4 Pathlength Correction

The pathlength correction method, multiplicative signal correction (MSC) is often used with PLS and DRIFTS to compensate for differences in pathlength and sample thickness caused by particle size and scattering. It does this by correcting the spectra using the same “ideal” spectrum, which is calculated by taking the average spectrum from all the data. By using a regression of the original spectra and this ideal spectrum, a MSC corrected spectrum is calculated, where chemical information is preserved while differences between the spectra are minimised. MSC therefore removes the major source of random variance between sample spectra. It is only applicable to spectra that have fairly linear responses to concentration and to spectra of samples that have a similar composition. If the range of variability in the sample compositions is too great, then correcting to the mean spectrum will not be appropriate [55].

## 3. Literature Survey

### 3.1 Identifying Minerals

#### 3.1.1 Identifying Minerals using FTIR

##### 3.1.1.1 Clay Minerals

The infrared absorption bands due to structural OH and Si-O groups are used to differentiate between clay minerals. Kaolinite has four OH stretching bands which are well resolved compared with those of smectite, and are sensitive to subtle changes in the environment, so have been used to study the interlayer region [58]. The broad OH stretching band of smectite at around  $3430\text{ cm}^{-1}$  is due to H-O-H vibrations of absorbed water [20]. The position of this band for smectites depends on the ion type in the octahedral sheet coordinated to the hydroxyl group. The type of exchange cation will also affect the position of the OH stretching bands slightly since they have different hydration energies, valence charges and radii [20]. The amount of water absorbed in the interlayer space, shown by a peak intensity change, is also dependant on interlayer cation type although this intensity change is not linear. The polarising power of cations increases in the order  $\text{K}^+ < \text{Na}^+ < \text{Ca}^{2+} < \text{Mg}^{2+}$ . An increase in polarising power corresponds to a decrease in wavenumber position of the band, an increase in band intensity, and an increase in the amount of absorbed water. This is due to stronger hydrogen bonds between water molecules and the cations with higher polarising power [20].

Work by Ledoux and White [59] included the assignment of the OH stretching frequencies of kaolinite at  $3695$ ,  $3670$ ,  $3650$ , and  $3620\text{ cm}^{-1}$  to positions in the crystal lattice. They did this by studying the shift of these OH stretching frequencies upon formation of hydrogen bonds with intercalated species. They assigned bands at  $3695$ ,  $3670$ , and  $3650\text{ cm}^{-1}$  to inner-surface hydroxyls and the band at  $3620\text{ cm}^{-1}$  to inner hydroxyls. A definition of inner and inner-surface hydroxyls is found in section 1.4.2.1.1 of chapter 1. Changes in position, intensity and width of the bands related to inner-surface hydroxyls give information about the interlayer space. Information could be

found on structural disorder, interlayer bonding, and the identification and bonding of the guest species [58]. A reduction in intensity of the bands associated with inner-surface hydroxyls upon intercalation is due to the formation of hydrogen bonds between the hydroxyls of kaolinite and the intercalated molecule. Ledoux and White [59] reported no change in the  $3620\text{ cm}^{-1}$  peak on intercalation since it corresponds to inner hydroxyls, which are inaccessible to intercalated molecules. Johnston *et al.* [58] reported the appearance of a new band corresponding to inner hydroxyls at  $3628\text{ cm}^{-1}$  upon intercalation of hydrazine into kaolinite at reduced pressures, while at 1 atm of pressure, no change in the  $3620\text{ cm}^{-1}$  peak was observed. They suggested that the reason for the band shift at low pressures was due to the  $\text{NH}_2$  group keying into the kaolinite surface, causing repulsion between the OH and  $\text{NH}_2$  groups. This can only occur with molecules small enough to penetrate into or through the siloxane ditrigonal cavity. Both Ledoux and White [23] and Frost *et al.* [24] also reported changes in the spectra of kaolinite and the intercalating formamide when intercalation has occurred. Similarly to Johnston *et al.* [58], Frost *et al.* [24] also found an additional band at  $3628\text{ cm}^{-1}$  but assigned it to the OH stretching of inner-surface hydroxyls hydrogen bonded to the carbonyl group of formamide. Additional bands at  $3606\text{ cm}^{-1}$  and  $1595\text{ cm}^{-1}$ , in the hydroxyl stretching and water bending region respectively, are said to be due to non hydrogen bonded water involved in the intercalated structure, indicating that water functions as a space filling molecule. Kristóf *et al.* [60] suggested that the dehydroxylation mechanism of different kaolinites could be predicted from their IR spectra and that the split of the hydrogen bonded OH band at  $3605\text{ cm}^{-1}$  into  $3606\text{ cm}^{-1}$  and  $3602\text{ cm}^{-1}$ , indicated a multi-step dehydroxylation.

The shape and position of the OH bending and Si-O stretching bands in the  $1300\text{-}400\text{ cm}^{-1}$  region are also used to distinguish different clays. A shift of the OH deformation mode from  $915$  to  $905\text{ cm}^{-1}$  in a kaolinite spectrum, upon intercalation of formamide, is attributed to OH deformation of inner-surface hydroxyls hydrogen bonded to the formamide carbonyl group. The OH bending vibrations of dioctahedral smectites are seen in the  $950\text{-}800\text{ cm}^{-1}$  range. Peaks at  $916$  and  $844\text{ cm}^{-1}$  in SAz-1 montmorillonites correspond to  $\text{Al}_2\text{OH}$  and  $\text{AlMgOH}$  respectively and therefore indicate

partial substitution of octahedral Al by Mg. In kaolinite, the  $\text{Al}_2\text{OH}$  bending bands are observed at 914 and 936  $\text{cm}^{-1}$  corresponding to vibrations from inner and surface OH groups respectively. Smectites have only one broad Si-O stretching band, and in montmorillonite this is at 1030  $\text{cm}^{-1}$ . Kaolinite on the other hand gives several, strong, well resolved bands in the 1120-1000  $\text{cm}^{-1}$  region [20].

Since minerals have characteristic absorption bands in an FTIR spectrum, mineral identification is possible and FTIR is sensitive to both amorphous and crystalline phases [41]. Dispersive IR spectroscopy has also been used to characterise minerals but FTIR is found to be more sensitive since it enhances weak absorption bands [61].

### **3.1.1.2 Identifying Carbonate Minerals using FTIR**

Calcite has three infrared red active modes in the mid-infrared region. The asymmetric stretch near 1420  $\text{cm}^{-1}$  is the strongest broad band in the infrared spectrum of calcite. This band also had the greatest spread of position when different workers results were studied. The spread in position of this band was around 30  $\text{cm}^{-1}$ . The sharp bands around 875 and 712  $\text{cm}^{-1}$  were much more precise in their positions with spreads of 10 and 3  $\text{cm}^{-1}$ , respectively [62].

### **3.1.1.3 Identifying Feldspars using FTIR**

The composition of plagioclase feldspars in terms of the relative amounts of albite and anorthite was studied by Thompson *et al.* [63] using the pressed pellet technique and transmission infrared spectroscopy. Differences in the number and positions of absorption bands with different feldspar compositions were found. The band at 645  $\text{cm}^{-1}$  was found to shift towards longer wavelengths as the sample increased in anorthite content and this band was not influenced by the temperature history of the sample.

The proportion of end-member feldspars, K-, Na-, and Ca-feldspar, in a sample was also studied by Matteson *et al.* [64], again using the pressed pellet technique and transmission infrared spectroscopy. The composition of samples was determined by estimating pure

end-member spectra and then using a least-squares program to fit the spectra of samples to the spectra of these end-members. Matteson *et al.* found that bands in the spectra of the alkali feldspars were fairly insensitive to variations of Na and K. The shape of the bands did vary though with the degree of disorder, with band broadening occurring with a lower degree of structural order. A lower degree of structural order is thought to be due to a higher temperature of crystallisation. The shape of the bands in the spectra of the plagioclase feldspars also alter depending on the degree of disorder in the same way. However, similarly to Thompson *et al.* [63], Matteson *et al.* [64] found that bands in the spectra of the plagioclase feldspars shift as a function of composition.

### 3.1.2 Identifying Minerals using TGA

Bish and Duffy [53] stated that dioctahedral phyllosilicates dehydroxylate at lower temperatures than trioctahedral phyllosilicates, because trioctahedral minerals have a more uniform charge distribution around the OH groups, thus stabilising them.

Thermogravimetric analysis was used by Breen *et al.* [65] to differentiate between different exchange cations in montmorillonite, since the exchange cations change the properties of the clay. A probe molecule, dimethylformamide (DMF), desorbs from montmorillonite at different temperatures depending on the exchange cation present, 420 °C for Mg<sup>2+</sup>, 330 °C for Ca<sup>2+</sup> and 220 °C for Na<sup>+</sup>. The thermal stability therefore decreases in the order, Mg > Ca > Na. The polarising power of the cations also decreases in the same order, with Mg<sup>2+</sup> having the largest polarising power and therefore a greater ability to retain sorbed water [66]. This also implies that accumulation of the intercalating molecule is slower on Mg<sup>2+</sup> since it is more difficult to displace the coordinated water from Mg<sup>2+</sup> than from Ca<sup>2+</sup> or Na<sup>+</sup> [66]. Bish and Duffy [53] described an increase in physisorbed water lost when the exchange cation changed from Cs<sup>+</sup> to Li<sup>+</sup>. They considered that it was the difference in hydration energies that accounted for this change. The stability of the acrylonitrile-montmorillonite complex investigated by Sohn *et al.* [67] was also found to be directly related to the polarising power of the interlayer cation. Bloodworth *et al.* [68] suggested that the dehydroxylation temperature of kaolinite was related to its degree of ordering and crystal size, with fine-grained, poorly

ordered kaolinite giving a lower dehydroxylation temperature than coarse grained, well ordered kaolinite.

### 3.1.3 Identifying Minerals using XRD

Texts such as those by Brindley and Brown (1980) [69] and Moore and Reynolds (1997) [19] review the identification of minerals using XRD. Identification of clay minerals using XRD is based on recording a series of diffraction patterns before and after various treatments. The positions, intensities, and shapes of the peaks in a diffraction pattern, and the changes in these peaks after various treatments, form the basis for all identifications. Common states to record XRD traces of samples are; in an untreated air-dried state, after treatment with ethylene glycol, and after heating the sample to various temperatures [70]. With the use of a diffractometer using Co  $K\alpha$  radiation, illite can be characterised by the presence of peaks at about 10, 5, and 3.3 Å.

A strong peak is found at 17 Å in the XRD trace for smectite after glycolation and the 003 peak is present at 5.65 Å. Typical peaks for kaolinite are found at 7.15 Å and 3.58 Å, whilst the 003 peak is weak [70]. Different peaks are associated with chlorite depending on the exact structure of the mineral since chlorites are a very diverse group of minerals [70].

## 3.2 Clay Organic Interactions

The adsorption of organic molecules between clay layers has received much attention in various industries for different purposes. The preferential adsorption of organic molecules by some minerals and not others can be used as a basis for identification and quantification of minerals. Potassium acetate, hydrazine, formamide and urea [23, 71, 60] have been studied for their ability to enter the gallery space of montmorillonite and kaolinite. There are however only a limited number of small polar molecules that can intercalate into kaolinite [58]. One reason why these interactions are important is because intercalated molecules in clays can be used as chemical probes. A mineral mixture or rock is exposed to the chemical probe and the interactions of the molecules with different clay minerals are exploited to detect the clay mineral content. This is

possible since, when heated, the probe desorbs at a temperature characteristic of the minerals present [21]. This is particularly useful for mixtures where there is a low concentration of one component, where conventional methods would not be able to detect it. Clegg [21] found dimethylformamide (DMF) and *N*-methylformamide (NMF) to be effective chemicals to use as probes to determine swelling clays in the presence of nonexpanding minerals. Forsyth [57] evaluated several chemicals for their use as chemical probes to determine the surface mineralogy of rocks. Dimethylformamide was found by Forsyth [57] to be the most appropriate chemical probe to use due to its rapid intercalation between clay layers and its desorption temperatures being specific to clay mineral type. NMF and *N,N*-dimethylacetamide were found to intercalate directly into kaolinite, whereas DMF intercalated into kaolinite very slowly [65]. The adsorption of DMF by montmorillonite is faster than the adsorption of NMF since DMF does not form intermolecular hydrogen bonds and therefore has a higher vapour pressure [65].

### 3.2.1 Kaolinite-Organic Interactions

Formamide was used as a chemical probe by Churchman *et al.* [22] to differentiate between halloysite and kaolinite since the difference between the XRD patterns of the two kaolin minerals is subtle. They found that halloysite intercalates formamide much more rapidly than kaolinite does. If a mixture of the two was exposed to formamide for an hour, only the halloysite would be intercalated. The intensity of the XRD peak at 10.4 Å could then be measured to give the proportion of halloysite, while kaolinite would not expand beyond 7.2 Å. Churchman *et al.* [22] also found that interlayer complex formation was accelerated in the presence of water and that more expansion occurs in a more crystalline halloysite and in a less crystalline kaolinite.

Ledoux and White [23] and Frost [24] agreed on XRD results for the *d*(001) spacing of kaolinite before and after intercalation with formamide to be 7.1 Å and 10.1 Å, respectively.

Frost *et al.* [24] stated that the intercalation process depends on whether the kaolinite is ordered (low defect) or disordered (high defect). Using the width of the *d*(001) peak in an XRD trace, they found that the intercalation of a low defect kaolinite with formamide

did not change the defect structure whereas intercalation of a high defect kaolinite removed some of the defects. Similarly to Kristóf *et al.* [60], Frost *et al.* [24] found that a higher amount of formamide can interact with the clay if water is present.

### 3.2.2 Montmorillonite Organic Interactions

Montmorillonites have high surface areas and therefore high cation exchange capacities, and so can adsorb polar organic molecules relatively easily, although this is highly dependant on the type of exchangeable cation on the clay surface [67] and the surface charge density [72]. The exchangeable interlayer cations are hydrated, the extent of the hydration depending on the nature of the interlayer cation and composition of the layers [20]. The water that hydrates the interlayer cations can be replaced by polar organic molecules, or the hydration sphere can act as a water bridge between the cation and an organic molecule. Water surrounding the cations can also act as Bronsted acid sites since they can donate protons to organic molecules [25]. Bronsted acidity is highest when using small cations with a high charge [25]. Breen *et al.* [65] suggested that DMF is most likely to interact with montmorillonite through its carbonyl group either directly or through a water bridge, since oxygen is a strong electron pair donor and strongly coordinates to metal ions. Breen *et al.* [65] also stated that DMF-water clusters were likely to occur since the interaction between DMF and water molecules is stronger than the attractive forces between DMF molecules.

The intercalated organic molecule can adopt different arrangements depending on the size and shape of the organic cation as well as the charge density of the clay surface. If the charge density of the clay is low, then the organic molecule's preferred orientation is parallel to the clay layer. However, when the charge density increases, the preferred orientation becomes nearly perpendicular to the clay layer.

The use of DMF as a chemical probe with DRIFTS and PLS was investigated in this thesis in chapter 4. A three component mixture of kaolinite, smectite, and calcite, was exposed to DMF vapour for 2 days in the hope that the quantification of smectite would

be improved. The presence of a strong DMF absorbance band in the spectrum of both smectite and kaolinite, however, meant that quantification was not improved. Despite the presence of the DMF band in the kaolinite spectrum, the XRD trace of kaolinite exposed to DMF indicated no expansion of kaolinite, so it is thought that DMF had intercalated into only the edges of the kaolinite layers.

### 3.3 Quantitative Analysis of Minerals

#### 3.3.1 Quantitative Analysis using FTIR

The sensitivity of infrared techniques to detect low concentrations of components in a mixture was investigated by Madejová *et al.* [73]. Using infrared transmission and the KBr pellet technique, it was found that in a kaolinite-smectite mixture, detection as low as 0.5 wt% kaolinite was possible. However, smectite could not be detected below 40 wt%. Peak fitting was used and only a semi-quantitative estimation of kaolinite content in mixtures could be found due to overlapping peaks. XRD patterns of the mixtures indicated that XRD is a much more sensitive technique for the detection of low smectite concentrations, i.e. 1% kaolinite and 5% smectite concentrations could be detected. The strong 001 reflections in XRD patterns of mixtures were used for the identification of minerals. Madejová *et al.* [73] used both transmission and reflection geometries in XRD, but found more noise in transmission traces.

Peak fitting was also used by de la Fuente *et al.* [74] to quantify mixed-layer illite-smectite (I-S) in glass matrices using FTIR. XRD methods do not provide accurate results for the quantification of small amounts of minerals in the presence of glass, so the use of diffuse reflectance and transmission spectra for quantification, was investigated. A calibration was prepared by mixing known amounts of I-S with volcanic glass, and peak fitting, using the OH stretching band near  $3620\text{ cm}^{-1}$ , was applied. The detection limit for I-S using the transmission spectra was found to be around 2%. While de la Fuente *et al.* found both transmission and diffuse reflectance methods useful for quantitative determination, diffuse reflectance was thought to be better, provided samples were

dehydrated, since sample preparation is faster, simpler, and it is more reproducible than the transmission method.

Again, infrared spectroscopy and peak fitting was used by Graham *et al.* [75], to quantify the quartz content in clays. By calcinating the clay, the crystalline structure of the clay was destroyed, while the quartz structure remained intact. This enabled peak fitting of the quartz band near  $691\text{ cm}^{-1}$ , since the band was no longer overlapped by clay bands. The percentage of quartz present in the clay was quantified with a maximum error for predictions of less than  $\pm 4.8\text{ wt}\%$ .

Moudgil *et al.* [76] used DRIFTS to quantitatively analyse dolomite mixtures made up of three dolomites that differed only in surface chemical groups. Only one of the dolomites had a hydroxyl peak at  $3619\text{ cm}^{-1}$  and the intensity of this peak in relation to the carbonate peak at  $2900\text{ cm}^{-1}$  was used to obtain a linear calibration. The amount of this dolomite in a mixture of dolomites could then be determined from this calibration.

The composition of end-member, Na-, K-, and Ca-feldspars, were determined by Matteson *et al.* [64] using transmission FTIR spectroscopy, and a least-squares program. The end-member spectra were estimated by preparing a calibration using the FTIR spectra of synthetic mixtures, and using a least squares program. From the spectrum of an unknown sample, the composition of the unknown could then be obtained. The composition of a feldspar sample could be determined to within  $\pm 1.6\text{ wt}\%$  for each of the end-member components using this technique.

### 3.3.2 Quantitative Analysis using XRD

A detailed review of quantitative analysis of clay minerals using XRD is given by Brindley and Brown (1980) [69].

XRD has been used by many for mineral identification and the intensity, shape, breadth, and position of peaks in a diffraction pattern give information about the character of a sample. Quantitative information can be found from the breadth of a peak, since clay minerals can be distinguished from other minerals present and also all members of the 001

series for a specific clay mineral have the same breadth. XRD does, however, have limitations for quantitative analysis of mixtures since it cannot differentiate between components that have different surface chemical groups but the same crystal structure [76].

Limitations of XRD for quantitative analysis include changes in reflection intensities caused by ionic substitution, preferred orientation in the sample mount, grain size of different particles, differential absorption of X-rays by various minerals in the mixture [77], and homogeneity of the sample [78]. Variations in mineral crystallinity also reduce the accuracy of quantitative results using XRD since minerals must be crystalline for XRD analysis [41]. Hillier [70] stated that care must be taken to ensure homogeneity in clay mineral mixtures for XRD analysis, so methods which allow particle size segregation to develop as the sample is prepared should be avoided. This is because smectites tend to be finer than kaolinite causing them to be concentrated at the surface of a sample. If the clay mixtures were not homogeneous, the XRD peak intensities produced in a trace would not be proportional to the abundance of the mineral present throughout the mixture since the X-ray beam is diffracted mostly from the surface of the sample. The thickness of the sample must also be controlled so that it is thick enough to diffract the X-ray beam for the whole angular range. The type of minerals present and their concentrations affect the thickness required. Hillier [70, 79] also stated that the area rather than height of XRD peaks should be measured since clay minerals have natural variation in peak shapes and widths.

Ouhadi *et al.* [80] highlighted the problems associated with quantification of minerals based on the peak areas or heights alone. Differences in the mass absorption coefficients of different minerals means that using the peak areas or peak heights alone is not a reliable quantitative method. Ouhadi *et al.* suggested that a more reliable quantification method involves studying not only the major reflection lines but also other reflection lines of minerals, taking into account the impact of clay microstructure.

If orientation of the clay mineral on the sample mount is perfect, then only the  $d(001)$  spacings contribute to the diffraction pattern [19]. Achieving random orientation is

important for quantitative analysis, since it allows correct relative intensities to be obtained in the diffraction pattern [81]. This is difficult, however, since clays are platy in character [19]. An XRD pattern from a randomly orientated powder can give a rough estimate of the amount of clay and non clay mineral present [19].

Procedures to achieve random orientation are discussed by Bish and Post [82]. Methods include side or back packing sample mounts, using filler materials that surround the particles, or sprinkling the powder on a mount coated in a viscous material [82]. Środoń *et al.* [78] used side loading as it provided reproducible density, and rigid samples with a lack of preferred orientation. They produced reproducible XRD patterns with this technique, obtaining a linear relationship between wt% kaolinite and intensity of the kaolinite reflections 001, 020, 060, which is only possible with a random orientation. More complicated methods to achieve random orientation include ejecting the sample into a filter in the tubular aerosol suspension method, wetting the particles suspended in water with a liquid immiscible in water to form spherical bodies [82], and spray drying, where an aqueous suspension of the sample is sprayed into a heated chamber where it dries in spherical agglomerates [81].

Although spray drying minimises the problem of preferred orientation, the equipment is expensive and product recovery only 50%, since large droplets do not dry before reaching the base of the chamber. Hillier [81] designed a cheaper instrument and developed an airbrush technique where small and uniform droplets can be obtained. Compressed air and the water/sample slurry are mixed internally and then sprayed with an airbrush that acts as a miniature spray gun. Wet grinding of the sample was preferable to dry grinding to reduce the particle size, as it results in a narrow grain size distribution [78]. Środoń *et al.* [78] suggested grinding in methanol to reduce drying time and prevent swelling of minerals. In spray drying, however, the sample can be ground in water since a water/sample slurry is required. A small amount of polyvinyl alcohol (PVA) can be added to give strength to the dried product. However this is often not required with high clay content samples. Finer grained samples and those containing a high swelling mineral content require more PVA. Smectites are difficult samples to spray dry due to

their high water content, and the small irregular shape of the droplets they form. Despite this, Hillier [81] managed to achieve 70% product recovery using this technique. The effectiveness of spray drying as a technique to achieve random orientation was tested by comparing to freeze dried samples. Spray drying gave better quantitative results with no preferred orientation.

Non clay minerals present in a mixture will mask some of the 001 reflections and could destroy the preferred orientation so that identification of clay minerals would be difficult. By analysing only the small size fraction, much of the non clay minerals can be removed.

Kahle *et al.* [79] described four general methods for quantifying clay minerals using XRD. In the method of known additions, known amounts of a mineral present within the sample are added to the sample, and then the intensity of a suitable peak plotted and extrapolated to zero in order to calculate the original content of the mineral. In the absorption-diffraction method, the intensity of a diffraction peak associated with a particular mineral in the trace of a mixture, and the intensity of the same peak in a trace of the pure mineral, are ratioed and the weight fraction of the mineral calculated. The full-pattern method uses all the data in a given pattern and Rietveld method to quantify minerals. However, this method requires that the crystal structure of the mineral is known. The quantification method used by Kahle *et al.* involved the mineral intensity factors (MIF) in combination with the so-called 100% approach. The MIF describe the relationship between the intensity ratio of specific XRD peaks and the weight fraction ratio of two phases in a mixture. The 100% approach means that the sum of all phases quantified in a sample is 100%, so the method assumes that all the mineral phases in a mixture have been identified.

The Rietveld (1969) quantitative XRD method was used by Ward *et al.* [77] to quantitatively predict the mineral content in powdered samples. This method relies only on information about the crystal structure for the minerals analysed. Rietveld parameters cause variations in the intensity of the XRD data, and these are adjusted theoretically, to fit a calculated profile to the measured pattern. The calculated pattern is adjusted by least-squares fitting to obtain the best profile match with the experimental pattern. The

Rietveld scaling factors give the mineral weight fraction of the sample. SIROQUANT is a software system which can quantify up to 25 minerals in a mixture from a powder XRD pattern using the Rietveld method. It can also be used to develop reference patterns so that minerals with only partly known or poorly developed crystal structures can be used in the analysis and this is particularly useful for clay minerals [77]. Normative analysis can also be used to obtain quantitative results by determining normative mineral percentages from a rock's chemical composition. This technique has been more commonly used to characterise igneous rocks, than sedimentary rocks due to the uncertainties in allocating several elements to different minerals in sedimentary materials. The use of a multi-option computation method, called SEDNORM, allows more flexibility, with elemental allocations varied to suit the material under study. Ward *et al.* [77] compared the results of point counting, SIROQUANT and SEDNORM and found relatively poor correlations. However they suggested that SIROQUANT offers the most direct method for quantification.

Oriented aggregate techniques were developed because bulk sample powder XRD patterns were seen by some to be inadequate at identifying clay minerals and in particular expandable lattice minerals. However, only a selected size fraction of the bulk sample is studied with oriented aggregate techniques [83]. Ruan *et al.* [83] prepared orientated aggregate samples by saturating the clay with ethylene glycol and heating to collapse any expandable lattice structures. They compared the results of a quantitative analysis of clay minerals using the Rietveld-based SIROQUANT and oriented aggregate techniques and found them to be in agreement.

Środoń *et al.* [78] stated that different classes of XRD reflections have different sensitivities to chemical and structural variations. Środoń *et al.* chose reflections insensitive to structural and chemical variations, instead of whole-pattern fitting to obtain better quantitative results. In the quantitative XRD procedure used by Środoń *et al.*, the samples were finely crushed and thoroughly mixed to limit the variations in diffraction peaks from sample to sample. Due to the crushing and mixing required, it is a technique

used to determine the bulk mineralogy and cannot distinguish surface mineralogy from bulk.

### **3.3.3 Other Techniques**

Evolved water analysis (EWA) is based on the principle that clay minerals have different amounts of water bound in their structure, which are released when the mineral is heated during thermogravimetric analysis (TGA). Heating to about 200 °C releases absorbed water, while further heating to about 900 °C releases structural water [84], i.e. water vapour evolved from the dehydroxylation of a mineral. Bloodworth *et al.* [68] used evolved water analysis to determine kaolinite concentrations as low as 0.25% in artificial mixtures of kaolinite and quartz. Clay minerals have distinctive patterns of water evolution and the amount of water produced and the temperature at which it occurs can give the concentration of different minerals in a mixture.

Evolved gas analysis (EGA) is similar to EWA, and was used by Morgan [85] to quantify minerals in natural mineral mixtures. The decomposition of individual minerals could be studied and the quantification of minerals in mixtures could be found by measuring the evolution of water, carbon dioxide, and sulphur dioxide. The concentration of the three volatiles was measured as the temperature of the sample was increased. The evolution profiles were integrated to calculate the total weight of volatile.

A limitation of TGA highlighted by Clegg [21] is that desorption of DMF from Mg exchanged montmorillonite, in a mixture with quartz, could only be detected when 5 wt% or more Mg exchanged montmorillonite was present. Mass spectrometry i.e. analysis of the evolved gases, however, can detect Mg exchanged montmorillonite in mixtures with quartz, kaolinite, illite and chlorite at concentrations as low as 2 wt% [57].

## **3.4 Quantitative Analysis of Rocks**

Determining the properties and composition of rocks is important to many industries including the oil, water, construction and ceramics industries. Generally for sedimentary rocks, it is the quantification of clays that is of particular importance because their

presence provides information about past processes affecting the rock and because of the unique properties of clays, such as swelling, fine particle size, and high chemical reactivity. Due to the fine particle size, plate shape, and chemical and structural variability of the clays, their quantification in rocks remains challenging. Many different techniques have been used to quantify minerals in rocks, however where clays are involved, XRD remains the dominant technique [86]. Sedimentary rocks were traditionally analysed using point counting techniques with optical microscopy, however XRD is now more commonly used for mineral identification as it does not suffer from the same heterogeneity problems that point counting does [77]. Some examples of different techniques used by different investigators to quantify minerals in rocks are described in this section.

Thornley and Primmer [87] combined EWA and TGA with XRD for a more quantitative analysis of mineral content in artificial mixtures of minerals than each technique alone. Artificial mixtures were made up of kaolinite, illite, and chlorite mixed with quartz to give mineral concentrations typical of those found in reservoir sandstones. Whole-rock XRD is widely used but can only give semi quantitative results for the abundance of clay minerals, especially in sandstones where the mineral content is low [87]. Thermal methods have also been used for quantitative analysis of clay minerals although clay minerals in sandstone cannot be resolved with thermal methods alone [87]. Thornley and Primmer [87] studied clay mineral dehydroxylation using TGA in order to quantify the total hydroxyl content of clay minerals in a whole rock sample. Since most reservoir rocks contain carbonate minerals, evolved water was measured using an infrared water vapour analyser, otherwise carbon dioxide evolution would be detected, and weight loss data would be invalid. These data were then combined with those from separated clay sized fraction XRD traces to assign amounts of structural water to each clay mineral. Individual clay mineral abundances in the whole rock could then be calculated. Thornley and Primmer [87] applied the technique to quantify the illite and kaolinite content of a sandstone reservoir, and therefore its permeability characteristics. They found that the lower porosity of the water zone in comparison to the oil zone, in the sandstone reservoir studied, did not correspond to an increase in illite content but instead

to an increase in quartz content. The increase in quartz content narrowed the pore throats so that illite, the concentration of which remained constant, occupied less space and could bridge the narrow pores, reducing permeability.

Jianhong *et al.* [84] also combined EWA and XRD to quantify illite and examine illite distribution in the Morecambe Gas Field, East Irish Sea. Given that permeability decreases with an increase in illite concentration, the permeability of the sandstone was also found. These techniques were combined by measuring the amount of structural water using EWA, and the proportions of different clay minerals present using XRD, in order to determine the percentage of each clay mineral present in the rock sample. XRD was able to determine the ratio of feldspar to quartz in the reservoir sandstones.

In work by Özer *et al.* [88] the physical structure, together with the chemical and mineral composition of a phosphate rock, were determined using techniques including chemical analysis, TGA, XRD, and scanning electron microscopy (SEM). The TGA results showed weight loss due to water desorption, and separation of other volatile components such as organic matter, up to 617 °C. From 617-767 °C the negative first derivative of the weight loss curve from TGA showed a peak due to the evolution of CO<sub>2</sub> from the decomposition of calcium carbonate. XRD results identified the main minerals present in the rock while SEM results showed that the rock had two phases, one phosphorus rich and the other calcium rich.

Środoń *et al.* [78] used XRD to quantify the mineral content of both synthetic mineral mixtures and natural shale samples, describing the errors encountered and choosing the optimum procedure. The 060 reflections were selected rather than the basal reflections (001), since they are relatively strong, less sensitive to defects, and the reflections of different clays only have partial overlap. The basal reflections (001) on the other hand have variable intensities, even in kaolin minerals, which have a stable chemical composition and orientation, and do not have mixed layering. The mineral content of the samples was calculated using an equation that relates wt% of mineral to the intensity of a reflection corresponding to that mineral, in the XRD pattern of a mixture. All minerals

were therefore quantified individually. The deviation of the sum of the measured minerals from 100% was used as a test of the robustness of the analysis. Any deviation of the sum from 100% may be due to the presence of amorphous material. The results for real shale rock samples indicated a variation in quartz content. Środoń *et al.* found that rocks with low quartz content were rich in either kaolinite or 2:1 Fe clay, while rocks with high quartz content were rich in 2:1 Al clay.

Hillier [70] has described two approaches for quantitatively analysing minerals such as illite, smectite, kaolinite and chlorite using XRD. One approach involved using a clay fraction that had been removed from the rock, usually prepared into an orientated layer of clay on a substrate. For quantitative analysis of sandstones, Hillier [70] used a size fraction of <6 µm and suggested that minimal grinding of the sandstone should be carried out to release the clay minerals. The second approach used a bulk or whole rock sample, prepared into a random powder. The data obtained from the clay fraction approach was used to get detailed information on the clay minerals present, whereas from the bulk sample approach, the amounts of different clay minerals present could be determined. Hillier [70] discussed the use of reference intensity ratios (RIR) to make quantitative analyses without having pure mineral specimens. RIRs for 001 clay mineral peaks can be calculated using NEWMOD software [89, 90]. Using the internal standard method and the RIR method, each mineral was quantified independently.

Mandile *et al.* [91] used the Rietveld XRD method and the SIROQUANT program to determine the mineral and organic content of a rock quantitatively. They found that an organic “hump” was present in the XRD traces of organic rich rocks and, if ignored, then the higher the organic content, the more the determined percentages of mineral components were overestimated. SIROQUANT was used to determine the organic content, from which the mineral content could be deduced.

SEM was used by Morad *et al.* [92] to study feldspars. The kaolinisation and illitisation of feldspars in sandstone was studied. Kaolinite can replace feldspar to various extents and illite can fill dissolution voids and can also occur as coatings on feldspar grains.

Morad *et al.* found that when kaolinite and illite cements contain kaolinised and illitised feldspars, respectively, the alteration had occurred under one set of diagenetic conditions. The feldspars are decomposed into soluble ions and/or into Si-Al chains before kaolinite or illite are precipitated. It was found that when samples were cleaned in an ultrasonic water bath, the hair-like illite substantially disappeared. It is suggested that this illite in hydrocarbon reservoirs might migrate during the production of oil and gas and get trapped in pore-throats, building an impermeable filter cake [92].

The quantification of minerals in carbonate rocks was investigated by Matteson *et al.* [93] using transmission FTIR spectroscopy and the spectral fitting programs; Least-Squares (LS) and Bounded-Least-Squares (BLS). The standards contained ten minerals, including quartz, feldspars, clays and carbonates. Matteson *et al.* found that the carbonate minerals from different locations showed natural variability which could be observed as slight differences in their IR spectra. It is therefore reported that it is important to establish a large data base of not only a variety of mineral standards but also a large number of standards from different locations. By comparing the predictions found, with results derived from chemical analysis, Matteson *et al.* report that the maximum prediction error for the carbonate minerals was  $\pm 5$  wt%, and for all the other minerals,  $\pm 4$  wt%.

In this thesis DRIFTS was used with the chemometric technique, partial least squares (PLS) regression to quantify minerals in both synthetic mixtures and in sandstones.

### **3.5 Chemometrics**

#### **3.5.1 Partial Least Squares (PLS) Regression**

The chemometric techniques, PLS and PCR are described in section 2.5 of chapter 2. The pioneering work in PLS was done in the late sixties by H. Wold. Geladi *et al.* [56] have produced a tutorial describing the PLS method.

### 3.5.1.1 Quantification using PLS and FTIR Spectroscopy

Clegg [21] applied PLS modelling to DRIFTS spectra to quantify the mineral content of synthetic mixtures and rock samples. Clegg [21] developed a PLS model using a 21 standard training set and 7 mineral components. The components in synthetic mixtures were quantified using this model. The model was then used to quantify minerals in sandstone rocks. The model that gave the most successful predictions combined montmorillonite and illite to represent one component, since their DRIFTS spectra are very similar.

The method used by Clegg [21], whereby pure component mixtures are prepared and used as calibration standards, is a common approach to the calibration of a multivariate model. Hughes *et al.* [37], however, built a calibration model to determine cement composition, from direct measurements on a large set of cements. The method used by Clegg [21] could not be used for cements because of the difficulty in obtaining both pure components and also components with the same particle size distribution as the cements under study. A PLS model was developed with the spectral region sensitive to atmospheric carbon dioxide (2390-2290  $\text{cm}^{-1}$ ) removed, with resolution reduced to 8  $\text{cm}^{-1}$  and with baseline shifts removed by using MSC. All components were predicted to within  $\pm 5$  wt% of the value measured by bulk chemical analysis.

The use of PLS and the direct measurement of the DRIFTS spectra of a large set of soil samples was used by Janik *et al.* [54] to quantify the soil components. GRAMS software was used for PLS manipulation. The optimum spectral region was chosen and the spectra pre-processed with baseline correction and mean centring. The nonlinearity of the regression meant that a large number of factors was required, introducing problems associated with overfitting. Janik *et al.* proposed the use of a locally linear modification to the infrared PLS procedure, where the full concentration range was broken up into two or three subsets, with samples from each subset having relatively close mineralogy and spectral features. This eliminated the influence of samples with widely different compositions from the sample being analysed, and produced more accurate predictions.

Jiang *et al.* [94] proposed that the selection of specific wavelength intervals in a spectrum used to build a PLS model, could improve the performance of the model. In this method, uninformative spectral regions contained in the full spectrum were ignored. Useful spectral intervals could be located by using the moving window partial least-squares regression (MWPLSR) procedure. A less complex PLS model was produced, since the selection of specific wavelength intervals reduced the size of the calibration set. PLS models could be built for each interval separately and then combined, or one model could be built from the selected intervals.

### 3.5.1.2 Quantification using PLS and MS

Forsyth [57] applied PLS to mass spectrometry data to quantify the proportion of each mineral in a mixture. A training set with 6 mineral components was prepared and exposed to DMF vapour. The DMF acted as a probe molecule, intercalating the clay mineral layers. The use of the TIC (total ion current) profile, the  $m/z = 73$  DMF parent ion, and the  $m/z = 18$  ion were investigated for predicting clay minerals in rocks. Forsyth [57] found that the  $m/z = 18$  ion gave the greatest promise for prediction of smectite in rocks. However, the prediction of illite was not successful.

### 3.5.1.3 Quantification using Other Methods

Xu *et al.* [41] discussed the application of a non-negative least squares (NNLS) method to the FTIR spectra of minerals predominantly found in an oil well, to calculate the mineral composition of a core sample. Unlike traditional least squares models, NNLS does not allow negative concentrations to be calculated. Xu *et al.* [41] also investigated a "linear background subtraction procedure" (LBSP) to minimise the variation between spectra caused by differences in the background. The use of LBSP was found to improve the accuracy of quantitative results. Unlike Jiang *et al.* [94], Xu *et al.* [41] did not find that the use of specific spectral regions significantly improved the accuracy of calculated mineral percentages. Jiang *et al.* [94] however used MWPLSR which selected very narrow useful wavelength regions, while Xu *et al.* [41] used LBSP and selected a very broad useful wavelength region.

Artificial neural networks (ANN) can be used for the interpretation of spectroscopic data since they are capable of pattern recognition and can model non-linear variations. ANN are however complex and difficult to interpret [95].

Neural networks are a system of interconnected nodes, each one being a processing unit which combines information being inputted to give a single numerical output. The transfer function is a non-linear function and gives the strength of the output signal from the weighted sum of the input signals. A full network is capable of giving a fast response to input signals, filtering out noise in the input data and can make predictions for new situations. It does however require much data and long calibration times. In order to reduce the computation time, the number of variables in FTIR spectra must be reduced before being inputted to neural networks. This is achieved using PCA so that information is reduced to a set of principal components [96]. Fletcher *et al.* [96] used artificial neural networks to estimate cement quality, by detecting ageing and contamination of a cement and also testing batch to batch variation.

#### **3.5.1.4 Comparing Results from using Partial Least Squares (PLS) Regression and Artificial Neural Networks (ANN)**

PLS is easier to use than ANN, but is not as capable at modelling non-linear variations. Luinge *et al.* [95] compared ANN to PLS, and found that both show similar results when predicting functional groups from the spectra. However, the ease of use of PLS and its ability to detect spectral outliers, makes it more attractive as a routine tool.

The use of ANN and PLS were also compared by Yang *et al.* [97]. The predictive ability of the two calibration methods was compared when synthetic data sets showed non-linear behaviour, i.e. band shifts with increasing concentration, a non-linear relationship between peak height and concentration, or a combination of both types of nonlinearities. The results from both calibration methods indicated that when the combination of both types of nonlinearities was present in the data set, the predictions were the least accurate. Overall Yang *et al.* found that the ANN calibration method performed better than the

PLS calibration method for these nonlinear data sets. However, the computation time was much less for the PLS method and the PLS method was much easier to use.

Since the interpretation of IR spectra can be time consuming and is dependant on the knowledge of the operator, techniques such as ANN and PLS have been investigated for their use in recognising characteristic features in IR spectra. Visser *et al.* [98] found that the recognition of band shapes and patterns in IR spectra by spectroscopists was more accurate than using ANN and PLS. Results using ANN and PLS were, however, improved when specific spectral intervals were analysed.

## **4. Results - Quantification of small amounts of swelling mineral, smectite, in synthetic mixtures using Diffuse Reflectance Infrared Fourier Transform Spectroscopy (DRIFTS)**

### **4.1 Determining low amounts of smectite**

It is important to determine low quantities (0.1-30 wt%) of smectite in mixtures with kaolinite since, in industry, processing problems can arise if small amounts of swelling material are present with non-swelling material. Processing problems are caused by the difference in surface area between the non-swelling kaolinite (15-30 m<sup>2</sup> per gram) and swelling mineral, smectite (700-850 m<sup>2</sup> per gram). This surface area issue is a problem for the coatings industry, as well as for reservoir rock analysis, since the proportion of swelling minerals present in the rock will influence the composition of treatment fluid injected. DRIFTS was used in the current study since it requires only a small amount of sample, is fast, and is a relatively inexpensive technique compared to XRD. In this study, synthetic mixtures of smectite, kaolinite, and an additional mineral, calcite, were prepared and the powerful spectral decomposition technique, partial least squares (PLS) regression, used to quantify the minerals in “unknown” samples.

### **4.2 Experimental**

#### **4.2.1 Equipment**

A spectrum of each standard was collected using two different spectrometers and using a different sample preparation method on each. At Sheffield Hallam University (SHU) a Mattson Polaris FTIR Spectrometer (manufactured by Thermo Electron Corporation Ltd.) with a Mercury Cadmium Telluride (MCT) detector was used to collect spectra of standards, while at Schlumberger Cambridge Research (SCR) a Nicolet NEXUS FTIR Spectrometer (manufactured by Thermo Electron Corporation Ltd.) equipped with a

pyroelectric triglycine sulphate (DTGS) detector was used. Fitted to the Mattson Polaris FTIR Spectrometer was a Graseby-Specac Selector DRIFTS accessory (manufactured by Specac Ltd.) while fitted to the Nicolet NEXUS FTIR Spectrometer was a Spectra-Tech™ Collector™ DRIFTS accessory (manufactured by Thermo Electron Corporation Ltd.).

A ball mill was used to grind the diluent KBr powder for samples, the spectra of which were collected at SCR. The ball mill used was a Retsch MM2 grinder, with two tungsten carbide grinding pots (internal volume of 10 ml) and two tungsten carbide grinding balls (diameter of 12 mm) for each pot. Batches of 5 g of KBr were ground for 5 minutes at a frequency of 45 Hz.

#### 4.2.2 Spectral Collection

The instrumental parameters for the Mattson Polaris FTIR Spectrometer were as follows:

Number of scans = 276

Resolution =  $4 \text{ cm}^{-1}$

Gain = 1

Velocity =  $1.264 \text{ cm s}^{-1}$

Iris = 85%

The instrumental parameters for the Nicolet NEXUS FTIR Spectrometer were as follows:

Number of scans = 176

Resolution =  $4 \text{ cm}^{-1}$

Gain = 8

Velocity =  $0.6329 \text{ cm s}^{-1}$

Data spacing =  $1.928 \text{ cm}^{-1}$

The Graseby-Specac Selector DRIFTS accessory fitted to the Mattson Polaris FTIR Spectrometer was adjusted manually to maximise the throughput radiation to reach the detector, prior to spectral data collection. Difficulty in aligning the beam in the Nicolet

NEXUS FTIR spectrometer at SCR meant that a higher gain was required to obtain spectra. The number of scans and velocity used for each spectrometer were chosen in order to obtain a spectrum within a few minutes with a high signal-to-noise ratio. Slightly lower quality spectra were obtained using the Mattson Polaris FTIR Spectrometer compared with using the Nicolet NEXUS FTIR spectrometer so more scans were collected on the Mattson Polaris FTIR Spectrometer in order to improve the signal-to-noise ratio in the spectra. Before spectral collection in both instruments, the chamber, containing the sample cup, was purged with dry, CO<sub>2</sub> free air for 1 minute, and then the chamber was purged continuously during data collection. FIRST software was used to collect spectra on the Mattson Polaris FTIR Spectrometer, while OMNIC software was used to collect spectra on the Nicolet NEXUS FTIR Spectrometer. OMNIC software was used to ratio each sample spectrum against a pre-recorded KBr spectrum background.

#### **4.2.3 OMNIC and GRAMS Software**

OMNIC software was used to view, reprocess and subtract spectra. Turboquant software is part of the OMNIC package and can be used to pre-process OMNIC spectra. It can also be used to quantify components present in the mixtures using PLS analysis. GRAMS (Grams32-PLS-PLUS IQ, Galactic Industries Corporation, NH, USA) is a different software program that can also pre-process the same spectra and be used for PLS analysis.

### **4.3 Reproducibility Studies**

#### **4.3.1 Introduction**

Prior to deciding upon a procedure for sample preparation for use on the Mattson Polaris FTIR Spectrometer, studies were carried out on kaolinite and SAz-1, each diluted in KBr, to measure the reproducibility of the DRIFTS spectra collected.

### 4.3.2 Turning Sample Cup

A spectrum of 5 wt% kaolinite in KBr was collected. The sample cup was then turned 90°, and another spectrum collected. A further two spectra were then collected at 180° and 270° from the original position. Figure 4.1 shows the different band intensities found in the OH stretching region of the collected spectra when the cup was in different positions. The differences observed in the band intensities could be due to a rough sample surface, uneven cup packing, an inhomogeneous sample/KBr mixture and/or inhomogeneous particle sizes.

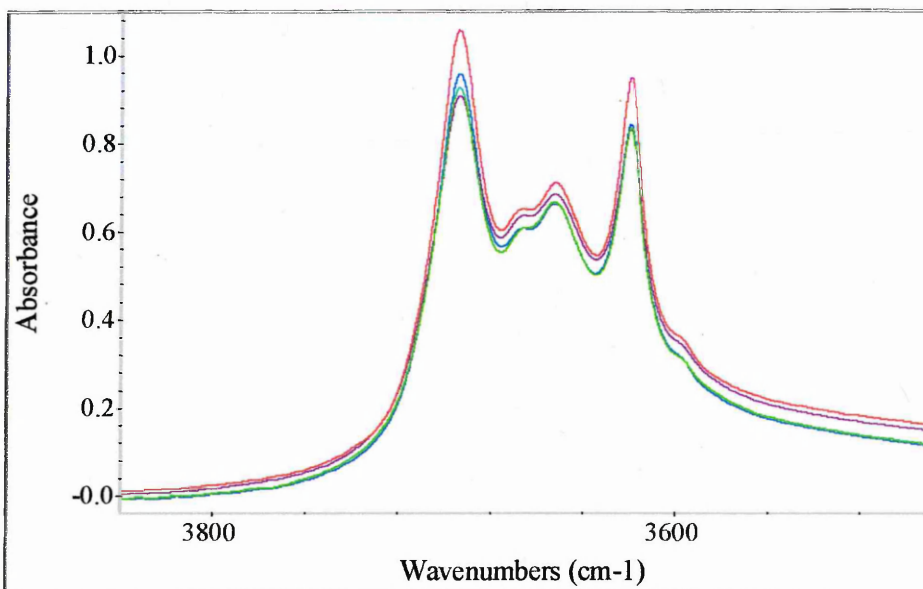


**Figure 4.1: DRIFTS spectra of 5 wt% kaolinite in KBr. The four individual spectra were collected after the sample cup had been rotated 90° from the position at which the previous spectrum had been collected.**

### 4.3.3 Compaction in Sample Cup

In the first compaction method, all 0.32 g of a 5 wt% kaolinite in KBr mixture was placed in the cup and pressure was applied on a glass slide to compact the sample. Using this method, however, some sample was lost from the cup during compaction resulting in different quantities of mixture being present in each cup. Four samples were prepared in this way and spectra collected, shown as black spectra in Figure 4.2. A wide range of

peak intensities were observed in the spectra. It was discovered that a double packing method gave more reproducible spectra, again when four samples were prepared, and these are shown as pink spectra in Figure 4.2. In the double packing method around 75% of the 0.32 g sample/KBr mixture was placed in the cup and a glass slide used to compact this before the remaining mixture was added and compacted.

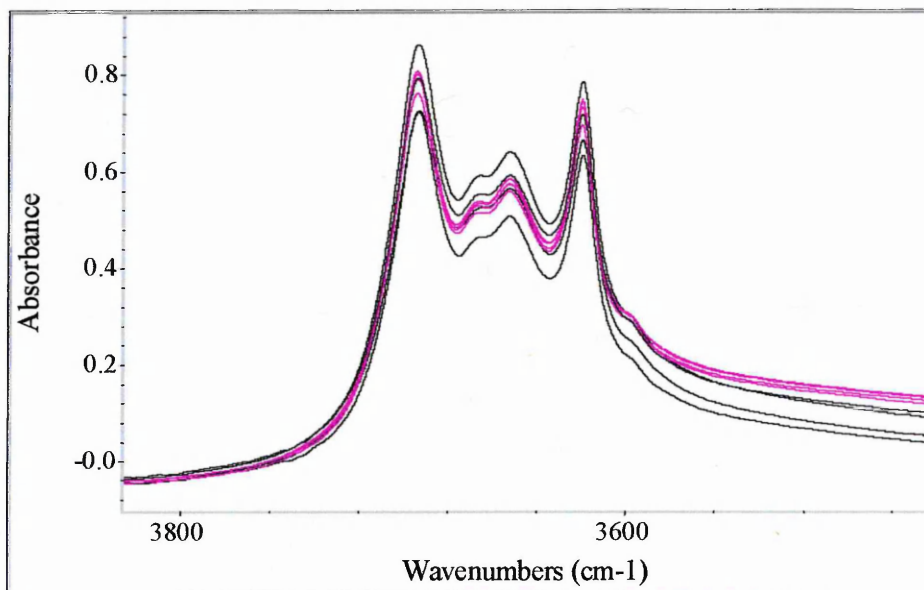


**Figure 4.2: DRIFTS spectra of 5 wt% kaolinite in KBr. Four spectra were collected after the sample had been single packed (black) and four spectra were collected after the sample had been double packed (pink).**

#### 4.3.4 Differentiating Sample Concentration by Peak Intensity

Spectra of 4, 5, and 6 wt% kaolinite in KBr were collected to investigate how easily different percentages could be distinguished and to determine whether small weighing errors would significantly alter the peak intensities. Four spectra were collected of each percentage, with the sample cup emptied and repacked between measurements. The repeated spectra are shown in Figure 4.3. Although the peak intensities were greater with higher sample concentrations, the increase was not linear, which is to be expected since the spectra were in diffuse absorbance units and not Kubelka-Munk (K-M) units. Unlike diffuse absorbance, the K-M function gives a linear relationship between sample

concentration and peak intensity provided certain criteria, discussed in section 2.1.5.6.1, are met. The spectra of 5 and 6 wt% samples, in diffuse absorbance units, overlapped at some peaks and spectra of the 4 wt% sample were more reproducible than that of 5 and 6 wt%. It was therefore decided that the sampling method was optimised at 4 wt% sample in KBr and that this concentration should be used for subsequent experiments.

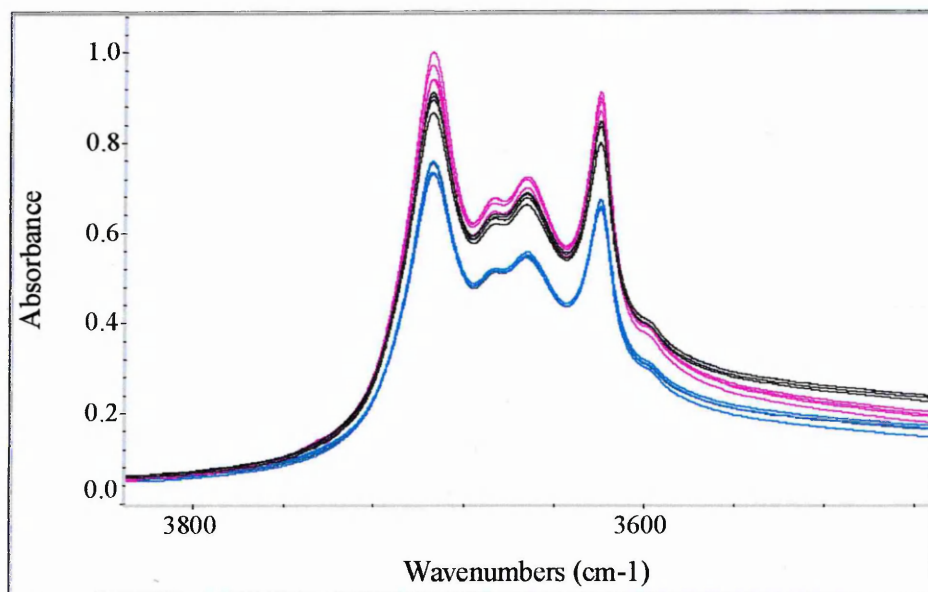


**Figure 4.3: DRIFTS spectra of repeated samples of 4, 5, and 6 wt% kaolinite in KBr, in blue, black, and pink, respectively.**

#### **4.3.5 Altering Grinding Time of Sample and KBr**

The initial sample preparation method involved grinding the KBr and sample together in a mortar and pestle manually for 1 minute prior to placing the mixture in the cup. Figure 4.4 shows, in black, spectra of three repeats of 4 wt% SAz-1 prepared in this way. Since decreasing the particle size decreases the amount of specular reflectance, and therefore increases the amount of spectral information that can be collected from the sample, it was thought that increasing the grinding time would improve the spectra. Also with smaller particle sizes, it was easier to pack and level the cup, and therefore improve reproducibility of the spectra collected. However, it has been found that grinding clay minerals for a few minutes damages their structure, so the KBr was ground alone for 5

minutes, again in a mortar and pestle by hand, before being mixed with the sample in the mortar and pestle. Spectra of three repeats of 4 wt% SAz-1 in KBr, that had been ground for 5 minutes, are shown in Figure 4.4 in pink. The spectra where the samples had been ground with KBr were of higher intensity than those where the sample was only mixed with KBr since it has been reported that a smaller particle size gives higher intensity, sharper peaks [21].

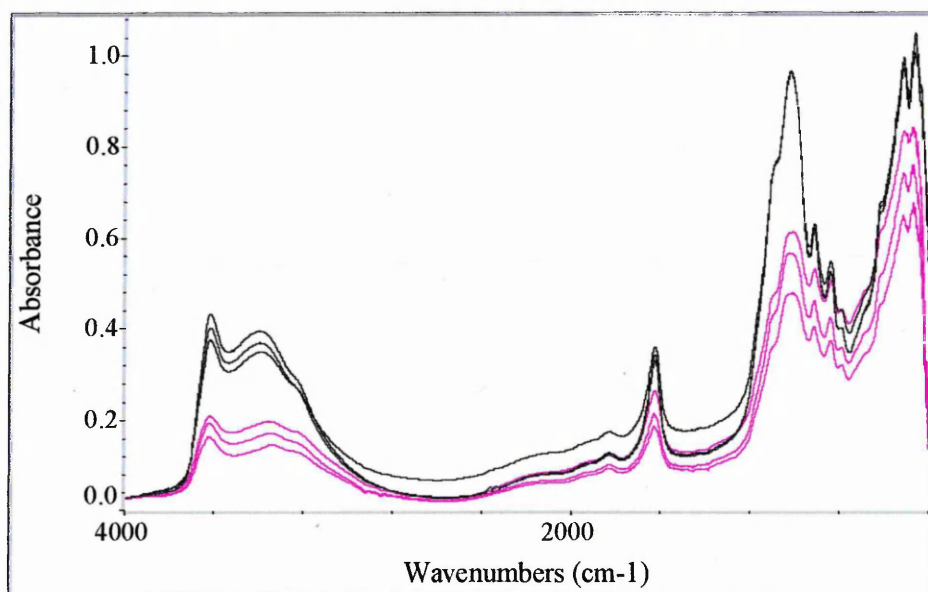


**Figure 4.4: Three DRIFTS spectra of 4 wt% SAz-1 in KBr samples ground for 1 minute (black) and three spectra where KBr has been ground separately for 5 minutes then mixed with SAz-1, i.e. 4 wt% SAz-1 (pink).**

Figure 4.4 indicates that there appeared to be no improvement in spectra reproducibility found when KBr was ground for a longer time and in fact a longer grinding time for KBr seemed to worsen the reproducibility of spectra at lower wavenumbers. It was thought that this lack of reproducibility was caused by insufficient grinding of the sample with KBr, leading a more heterogeneous mixture. It was therefore decided that subsequent samples, such as the standards used to create the SHU PLS models, described in section 4.8.3, be ground with KBr for 1 minute rather than be mixed with pre-ground KBr.

#### 4.4 Use of PLS

In this study, the decomposition technique, PLS, was used to construct a calibration model and predict the composition of artificial mineral mixtures. PLS requires a system with more than two components, since it cannot cope with collinearity. Collinearity is an effect that occurs when there are only two components, because their concentration values can only alter by the same amount when preparing standards for the training set. For example, if in one standard the concentrations of the components were 30 wt% and 70 wt%, and in another standard the concentrations of components were 35 wt% and 65 wt%, then each component had changed concentration by 5 wt%. Since PLS correlates the change in concentration to changes in the spectra, it cannot differentiate collinear components and therefore produces unstable calibrations.

A third component was added to the system used in this project so that the collinearity could be reduced. As more components are added to a system, the less collinear it becomes. However, in this study the aim was to create a simple robust model so only three components were used.

Calcite was chosen as the third component since it is an easily available chemical purchased from a supplier. Another advantage of choosing calcite was that its infrared spectrum displayed distinct peaks such as those around  $1436\text{ cm}^{-1}$ ,  $2510\text{ cm}^{-1}$ , and  $2873\text{ cm}^{-1}$ , that were not masked by peaks associated with kaolinite and SAz-1, as seen in Figure 4.5.

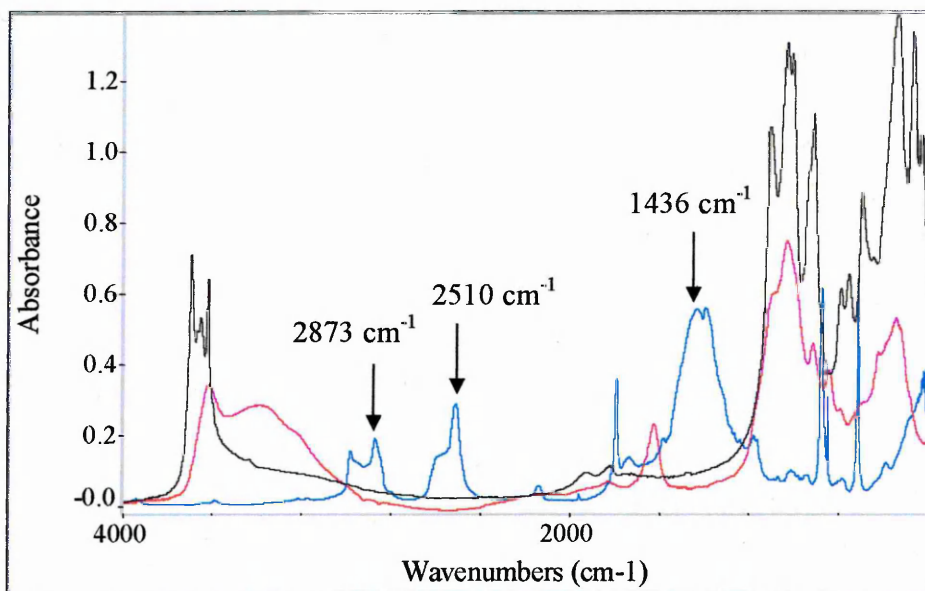


**Figure 4.5: DRIFTS spectra of 4 wt% kaolinite (black), 4 wt% SAz-1 (red), and 4 wt% calcite (blue) in KBr.**

#### 4.5 Standard Preparation

A batch of each standard was prepared to minimise weighing errors. The amount of standard diluted in KBr to prepare a 4 wt% sample of 0.32 g is 0.0128 g, so a 1.28 g batch of each standard was prepared, i.e. one hundred times the amount of standard required for one sample. The training set consisted of thirty two standards each with varying concentrations of the components, kaolinite, SAz-1, and calcite as shown in Table 4.1. Despite the concentration range of interest for SAz-1 being 0.1-30 wt%, a range of 0-95 wt% was used for each component because the smaller the concentration range of one component the more collinear the system.

Twenty one of the standards were calibration standards, that is, their spectra were used to prepare the calibration model. Initially five mixtures (standards 22 to 26) with various concentrations of kaolinite, SAz-1, and calcite were prepared but not included in the model, and quantitative predictions of the components within these samples were obtained. Those mixtures that were not included in the training set were called independent standards. In order to obtain predictions for a wider range of concentrations

of each component in the mixtures, a further six independent standards (standards 27 to 32) were prepared, and predictions found. The models developed with spectra collected at SCR, using ball milled KBr and a compaction device, were calculated using only the initial five independent standards.

Standard Number	Kaolinite (wt%)	SAz-1 (wt%)	Calcite (wt%)
1	35	30	35
2	75	15	10
3	40	60	0
4	45	0	55
5	60	20	20
6	0	75	25
7	40	20	40
8	10	15	75
9	35	35	30
10	25	30	45
11	30	35	35
12	35	50	15
13	15	30	55
14	50	0.1	49.9
15	15	5	80
16	80	1	19
17	95	1	4
18	3	95	2
19	2	3	95
20	8	80	12
21	36	7	57
22	45	20	35
23	55	25	20
24	39.5	0.5	60
25	44.8	0.2	55
26	42	27	31
27	50	5	45
28	35	9	56
29	21	13	66
30	43	17	40
31	28	30	42
32	13	37	50

**Table 4.1: Mineralogical composition of the standards used in the training set.**

**Standards 22-32 are the independent standards.**

## 4.6 Sample Preparation

The sample cups used on the Mattson Polaris FTIR Spectrometer held 0.32 g of powder. The spectra of the standards were collected from samples containing 4 wt% of each sample mixed with KBr (>99%) which had not been dried in an oven. The sample/KBr mixtures were ground in a mortar and pestle for 1 minute before being transferred to the sample cup, and compressed, using the double packing method, into the cup by applying pressure to a glass slide on the cup. Previous reproducibility studies (sections 4.3.3 and 4.3.5) indicated that this procedure gave the most reproducible spectra.

At SCR the KBr used for the background and diluent had been ball milled in 5 g batches at 45 Hz for 5 minutes. The sample cup used on the Nicolet FTIR Spectrometer held 0.45 g and, when collecting spectra of the sample, 4 wt% of this was sample. The ball milled KBr was ground with the sample by hand in a mortar and pestle for 1 minute. After being transferred to a cup situated inside a specially built compaction cell, the sample was compacted under a 20 kg load for 1 minute. A razor blade was used to scrape off excess sample so that the top was level with the sides.

## 4.7 Standard Exposure to Dimethylformamide (DMF)

For this procedure 0.0128 g of each prepared standard was placed in small sample vials. Each open vial was then placed in an incubation chamber, as shown in Figure 4.6, containing a separate open vial with 5 ml of DMF.

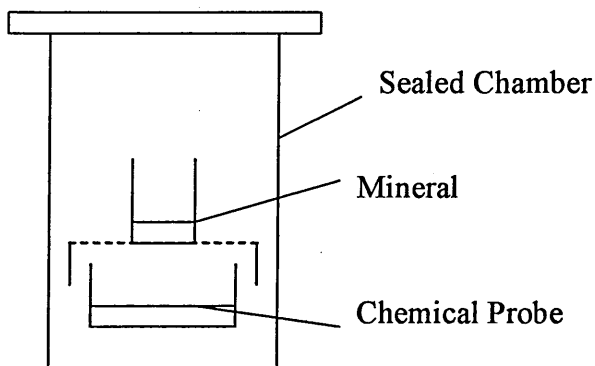


**Figure 4.6: Procedure for exposure of minerals to the chemical probe.**

The standards were incubated for 2 days at room temperature to ensure complete intercalation of the clay by DMF from the vapour phase [21]. The molecular structure of DMF is shown in Figure 4.7.

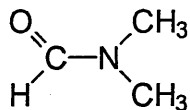


**Figure 4.7: Molecular structure of dimethylformamide (DMF).**

## **4.8 Results and Discussion**

### **4.8.1 Visual Examination of Spectra from Standards**

Spectra of the standards were collected using two different types of spectrometer (section 4.2.1), each with different sample preparation methods, one method (at SCR), included ball milling KBr and using a compaction device. Therefore, both the spectrometers and the preparation methods could be compared. Two types of software, OMNIC and GRAMS, were used to obtain quantitative predictions of components in the mixed clay/calcite samples, so the two types of software could also be compared. Furthermore, a sample of each standard was exposed to DMF for 2 days, the spectra of these standards collected, and the two software types used to obtain quantitative predictions. Predictions for standards with and without DMF treatment could therefore be compared.

Figure 4.8 shows the spectra of a selection of standards and the spectra of pure kaolinite, SAz-1 and calcite that had not been treated with DMF and not been prepared with ball milled KBr. Standard 2, standard 20, and standard 8 had high concentrations of kaolinite, SAz-1, and calcite, respectively in the presence of the other two components.

The bands characteristic of each component became more pronounced at high concentrations of that component. The four bands in the OH stretching region, 3695-3620  $\text{cm}^{-1}$  were strong in the spectrum of standard 2 since this standard had a high concentration of kaolinite. The spectrum of SAz-1 was less rich in information in this OH stretching region as can be seen from the spectrum of standard 18. The Si-O

stretching region,  $1200-1000\text{ cm}^{-1}$ , could also be used to distinguish kaolinite from SAz-1. The table in Figure 4.8 indicates the composition of the standards under discussion, where K, S, and C correspond to kaolinite, SAz-1, and calcite, respectively.

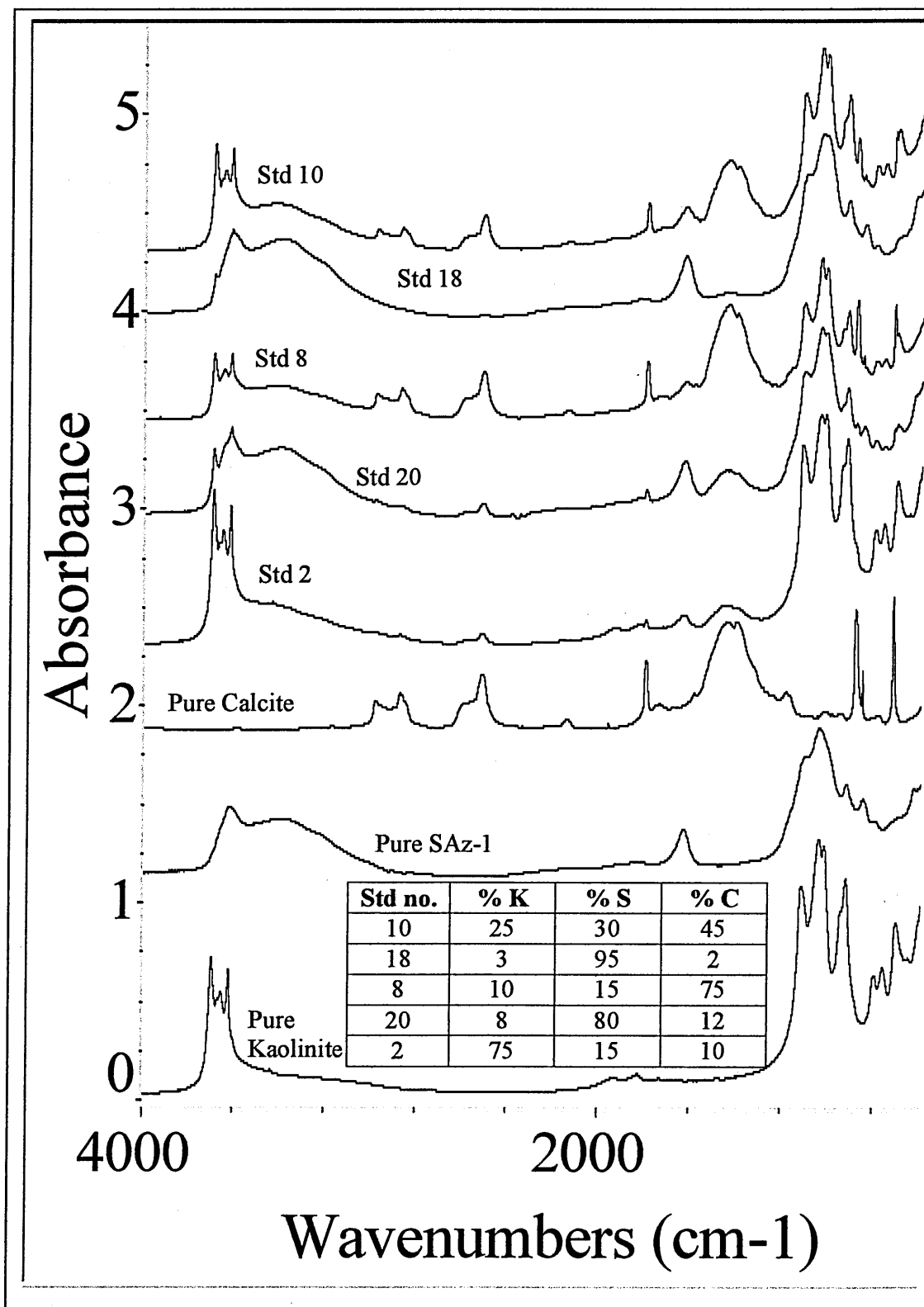
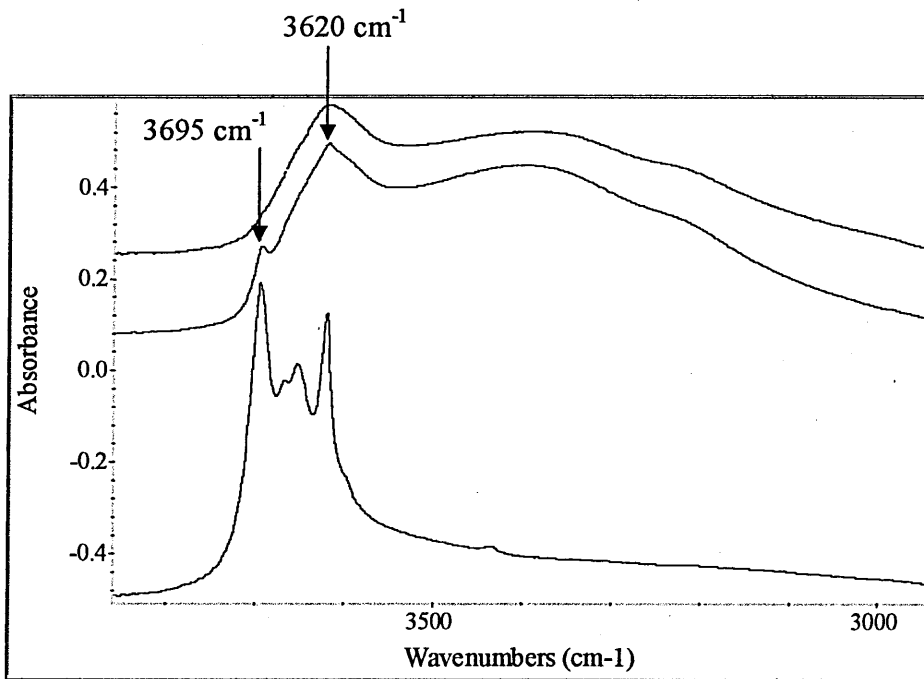


Figure 4.8: Spectra of standards 10, 18, 8, 20, and 2, and of calcite, SAz-1, and kaolinite. Compositions of the standards are given in the inserted table, where K, S, and C represent kaolinite, SAz-1, and calcite, respectively.

#### 4.8.2 Visual Detection of Components

In the spectrum of standard 18 (Figure 4.8), the OH stretching bands at 3695 and 3620  $\text{cm}^{-1}$ , diagnostic of kaolinite, could still be detected in the spectrum even though the standard contained only 3 wt% kaolinite in the presence of 95 wt% SAz-1. The OH stretching region of the spectra for pure SAz-1 standard 18, and pure kaolinite is shown in more detail in Figure 4.9.



**Figure 4.9: OH stretching region of DRIFTS spectra of pure SAz-1 (upper spectrum), standard 18 (middle spectrum), and pure kaolinite (lower spectrum) all at 4 wt%. The composition of standard 18 is 3 wt% kaolinite, 95 wt% SAz-1, and 2 wt% calcite.**

The broad band at 845  $\text{cm}^{-1}$ , in the OH bending region, was assigned to AlMgOH deformation and was used to detect the presence of SAz-1 while the sharper band at 848  $\text{cm}^{-1}$  was assigned to calcite. The spectrum of the standard which contained no SAz-1 did not exhibit a band at 845  $\text{cm}^{-1}$  and the band could not be detected in the spectra of standards which contained 5 wt% SAz-1. The band was just visible when 20 wt% SAz-1 was present, as shown in Figure 4.10. Standard 10 contained 30 wt% SAz-1 and

this was the lowest concentration at which SAz-1 could clearly be detected visually in the recorded spectra.

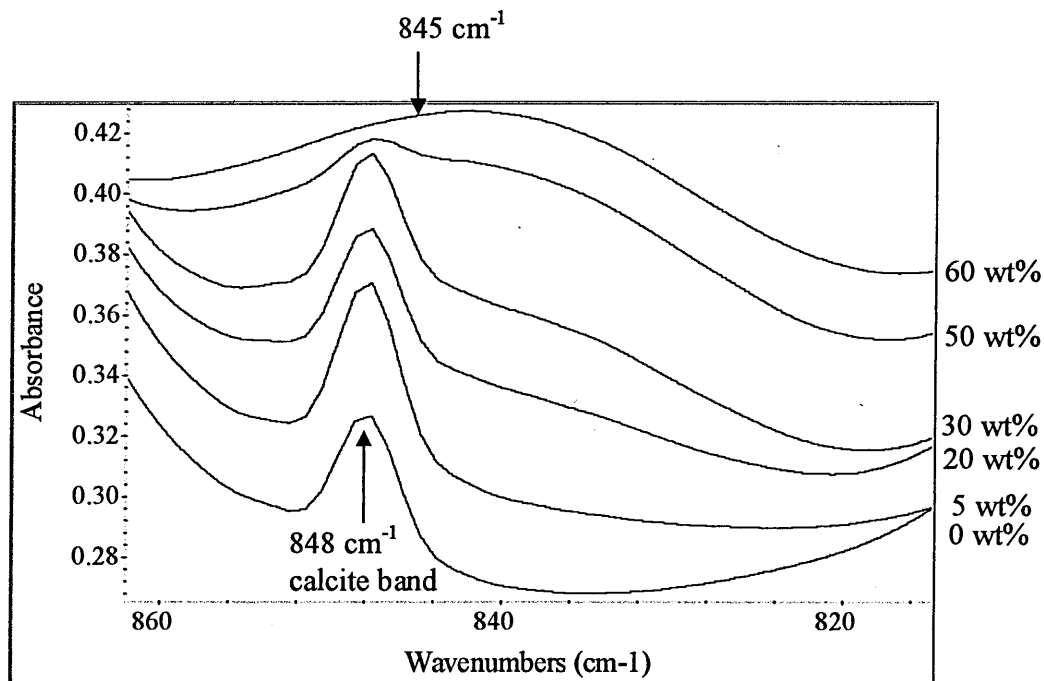


**Figure 4.10: DRIFTS spectra displaying peak at  $845\text{ cm}^{-1}$  for 6 standards containing different concentrations of SAz-1. From uppermost to the lowest spectrum, 60 wt%, 50 wt%, 30 wt%, 20 wt%, 5 wt%, 0 wt% SAz-1.**

#### 4.8.3 Results obtained using OMNIC and GRAMS Software

Six PLS models were developed, three using OMNIC software and three using GRAMS software. Models 1 and 2 were developed using spectra of standards collected at SHU, where the KBr was not ball milled and no compaction device was used. Models 3 and 4 were also developed using standards collected at SHU. However, the standards had also been exposed to DMF. Models 5 and 6 were developed using spectra of standards collected at SCR, where the KBr had been ball milled and a compaction device used. Models 1, 3, and 5 were developed using OMNIC software, while Models 2, 4, and 6 were developed using GRAMS software. In Models 1a, 2a, 3, and 4, the components in eleven independent standards were quantified to determine the predictive ability of the

models, while in Models 1b, 2b, 5, and 6, the components in five independent standards were quantified.

The pre-processing and wavenumber regions chosen for each model were those that gave the most accurate and precise predictions. For the models developed using OMNIC software (which uses PLS-1), cross validation was used and pre-processing included variance scaling, the pathlength correction, multiplicative signal correction (MSC), and no base line correction. These pre-processing techniques were described in section 2.5.2.1. The region 2150-500  $\text{cm}^{-1}$  of the spectra was used in Model 1 (OMNIC, SHU) and Model 3 (OMNIC, SHU, DMF treated), while the region 2150-680  $\text{cm}^{-1}$  was used in Model 5 (OMNIC, SCR).

For the models developed using GRAMS software, PLS-1 and cross validation were used. Pre-processing included variance scaling, no pathlength correction, but automatic baseline correction. Again, the region 2150-500  $\text{cm}^{-1}$  of the spectra was used in Models 2 (GRAMS, SHU) and 4 (GRAMS, SHU, DMF treated), while region 2150-680  $\text{cm}^{-1}$  was used in Model 6 (GRAMS, SCR). Models 5 and 6 used a slightly different low wavenumber region than Models 1-4 due to limitations of the spectrometer used.

In all the models, a low wavenumber region was used since this gave more precise and accurate predictions than using the full wavenumber region. The results obtained when Model 2a (a model developed using GRAMS software, at SHU, and predicting components in 11 independent standards), using the low wavenumber region 2150-500  $\text{cm}^{-1}$ , was compared with Model 2a, using the full spectral region, 4000-500  $\text{cm}^{-1}$ , are shown in Table 4.2. The  $R^2$  values for the calibrations and predictions of the components give an indication of the precision of the models, while the sum of the squares of the differences (SSD) between predicted and actual percentages of components gives an indication of the accuracy of the models.

	Model 2a- 2150-500 cm <sup>-1</sup>			Model 2a- 4000-500 cm <sup>-1</sup>		
	Kaolinite	SAz-1	Calcite	Kaolinite	SAz-1	Calcite
<b>No. of Factors</b>	3	3	2	4	4	4
<b>R<sup>2</sup> of Calibration</b>	0.9453	0.9711	0.9889	0.9388	0.9726	0.9847
<b>R<sup>2</sup> of Prediction</b>	0.9659	0.9893	0.986	0.908	0.9398	0.9905
<b>SSD (wt%<sup>2</sup>)</b>	61	52	39	151	226	65

**Table 4.2: Precision and accuracy of predictions for components using Model 2a. Comparison between results using the wavenumber regions 2150-500 cm<sup>-1</sup> and 4000-500 cm<sup>-1</sup>.**

The R<sup>2</sup> values for the calibration using the two models were very similar. The R<sup>2</sup> values for the predictions of kaolinite and SAz-1, however, were slightly lower in the model using the full wavenumber region, suggesting that this model gave slightly less precise predictions than the model using the low wavenumber region. The number of factors required for the components, and the values of the sums of the squares of the differences, were greater for the model using the full wavenumber region, indicating that this model was not as accurate as the model using the low wavenumber region. All the models discussed in this chapter therefore used the wavenumber region, 2150-500 cm<sup>-1</sup>.

The spectra were studied in a diffuse absorbance format rather than K-M format since PLS is, to some extent, capable of modelling non-linear response-concentration relations. A comparison of the results obtained when Model 2a (GRAMS, SHU) was prepared with spectra in diffuse absorbance format, and with spectra in K-M format is shown in Table 4.3.

	Model 2a- Diffuse absorbance			Model 2a- K-M		
	Kaolinite	SAz-1	Calcite	Kaolinite	SAz-1	Calcite
<b>No. of Factors</b>	3	3	2	4	4	4
<b>R<sup>2</sup> of Calibration</b>	0.9453	0.9711	0.9889	0.9378	0.9871	0.9664
<b>R<sup>2</sup> of Prediction</b>	0.9659	0.9893	0.986	0.9492	0.9933	0.9848
<b>SSD (wt%<sup>2</sup>)</b>	61	52	39	113	51	95

**Table 4.3: Precision and accuracy of predictions for components using Model 2a. Comparison between results using the spectra in diffuse absorbance format and in K-M format.**

The R<sup>2</sup> values for the calibration and prediction of the components using the two models were very similar, suggesting that the models were equally precise. However, the number of factors required for the components, and the values of the sums of the squares of the differences, were greater for the model with spectra in K-M format, indicating that this model was not as accurate as the model with spectra in diffuse absorbance format. All the models discussed in this study were therefore prepared with spectra in diffuse absorbance format.

Initial calibration results for the 21 standard training set using Model 1a (OMNIC, SHU, 11 independent standards) and Model 2a (GRAMS, SHU, 11 independent standards), using the spectral range 2150-500 cm<sup>-1</sup>, are shown in Table 4.4.

	OMNIC Model 1a		GRAMS Model 2a	
	Correlation Coefficient	Number of Factors	Correlation Coefficient	Number of Factors
Kaolinite	0.94913	7	0.9453	3
SAz-1	0.96679	3	0.9711	3
Calcite	0.94391	6	0.9889	2

**Table 4.4: Comparison of calibration correlation coefficients and numbers of factors for each named component using Models 1a and 2a.**

The correlation coefficients were higher and the number of factors required lower for the GRAMS model, indicating that predictions should be better for this model than for the OMNIC model.

A plot of predicted percentages, calculated by Model 1a (OMNIC, SHU, 11 independent standards) and Model 2a (GRAMS, SHU, 11 independent standards), against actual percentages are shown in Figures 4.11, 4.12, and 4.13 for each component. Calibration plots for the components are not shown. The spectra of standards included in these models were collected using a Mattson Polaris FTIR Spectrometer. The standards had not been exposed to DMF, nor had the KBr been ball milled, and no compaction device was used. The least accurate predictions for both models were found for SAz-1. That is, the predicted percentages fell furthest from the  $45^\circ y = x$  line and the four standards containing 30 wt%, 27 wt%, 0.5 wt% and 0.2 wt% SAz-1 were clearly under predicted. The predictions for SAz-1, however, were more precise, than the other components, since they had the highest  $R^2$  value. Overall the predictions found using the GRAMS software were more accurate and precise than those found using OMNIC.

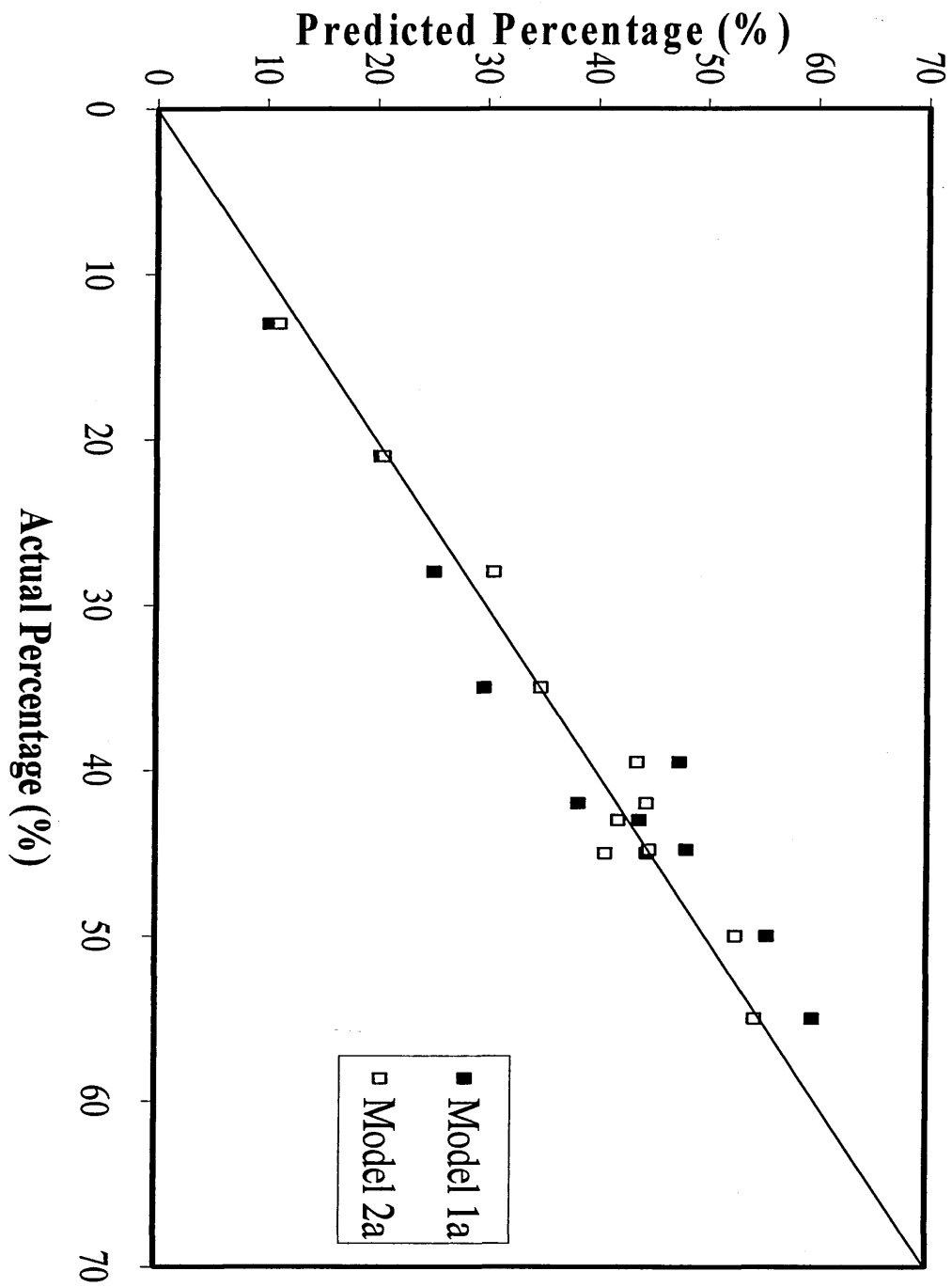


**Figure 4.11: Predicted against actual percentage of kaolinite for Model 1a and Model 2a. The full line represents the  $45^\circ y = x$  line.**

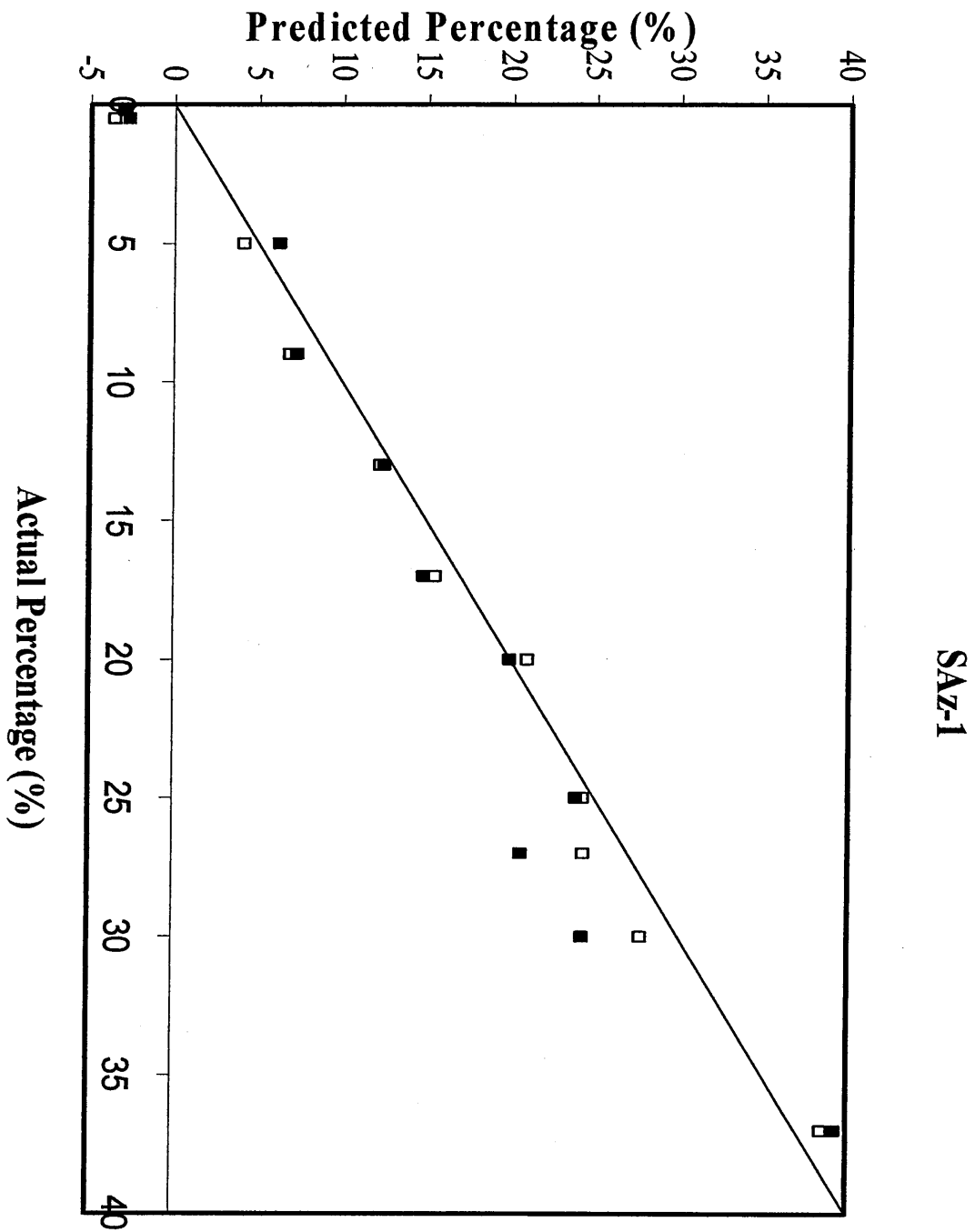


**Figure 4.12: Predicted against actual percentage of SAz-1 for Model 1a and Model 2a, legend as for kaolinite. The full line represents the 45° y = x line.**

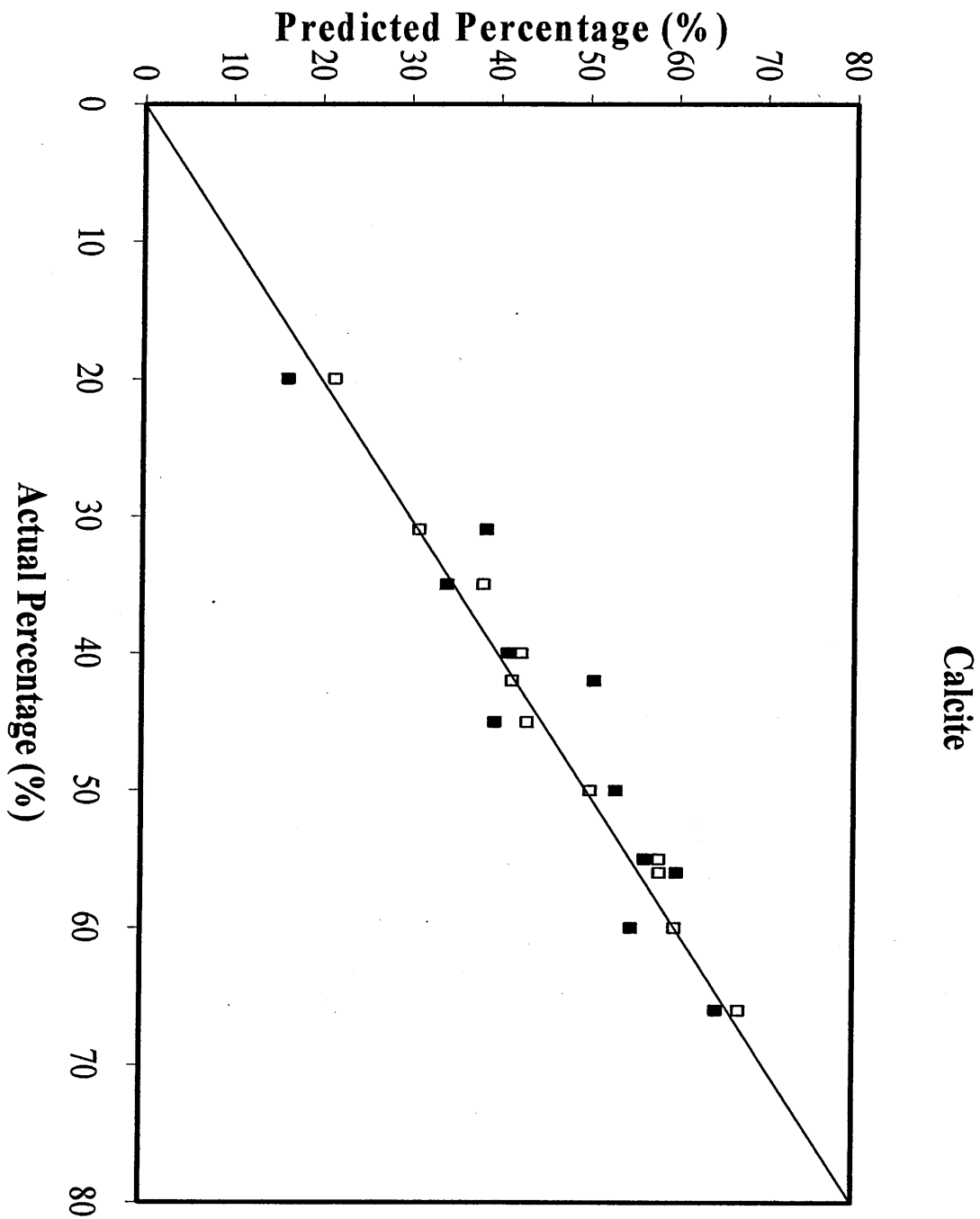
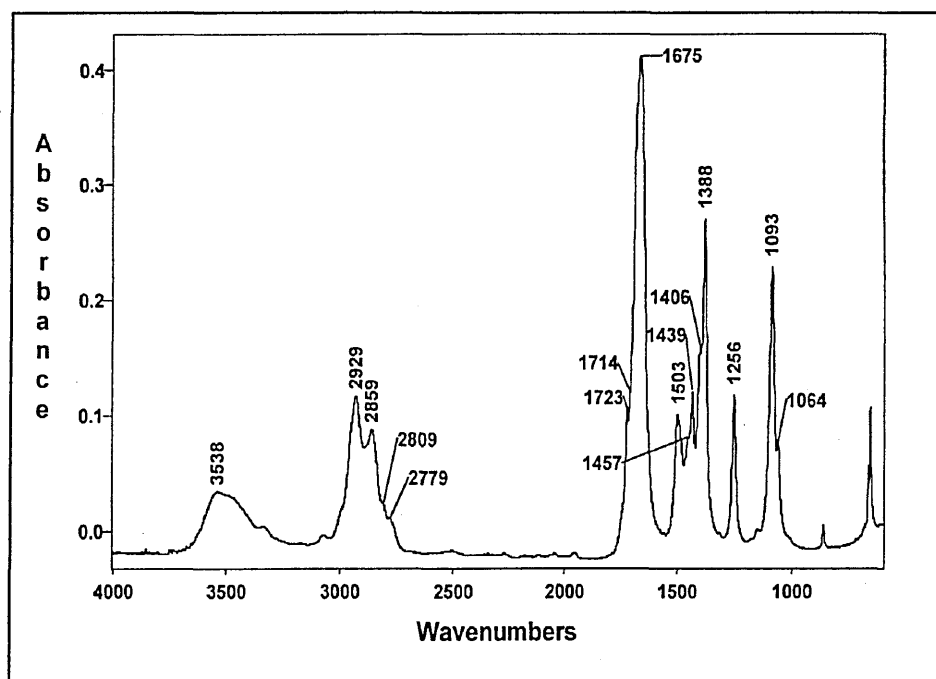


Figure 4.13: Predicted against actual percentage of calcite for Model 1a and Model 2a, legend as for kaolinite. The full line represents the 45° y = x line.

#### 4.8.4 Results from Chemical Probe Treated Standards

DMF was chosen as the probe molecule due to its rapid intercalation between the layers of readily expanding clays, such as SAz-1, and because the temperature at which the most strongly bound DMF was desorbed could be used to distinguish different ions occupying the exchange sites in the gallery. DMF also had a large distinctive band at  $1675\text{ cm}^{-1}$  associated with the C=O bond, as seen in Figure 4.14, which shifted to  $1658\text{ cm}^{-1}$  when DMF was complexed to exchangeable cations in the clay. This indicated that DMF molecules adsorb onto the clay via their carbonyl group. This carbonyl band was not masked by those of kaolinite or SAz-1.



**Figure 4.14: Infrared spectrum (transmission) of DMF ( $4000\text{-}600\text{ cm}^{-1}$ ).**

Since the carbonyl peak was so distinctive, it was thought that its presence might improve the quantitative results of standards that had been exposed to DMF, particularly the SAz-1 component, because the intensity of the peak at  $1658\text{ cm}^{-1}$  should increase with increasing SAz-1 content.

Spectra for standard 24 (which contained 39.5 wt% kaolinite, 0.5 wt% SAz-1, and 60 wt% CaCO<sub>3</sub>) and standard 24 exposed to DMF are shown in Figure 4.15. A band near 1670 cm<sup>-1</sup>, associated with the carbonyl bond of DMF, was present in the spectrum of standard 24 exposed to DMF even though this standard had only 0.5 wt% SAz-1. It was initially thought that this gave a good visual indication of the presence of SAz-1 in a mixture from the spectra alone, prior to the use of PLS.

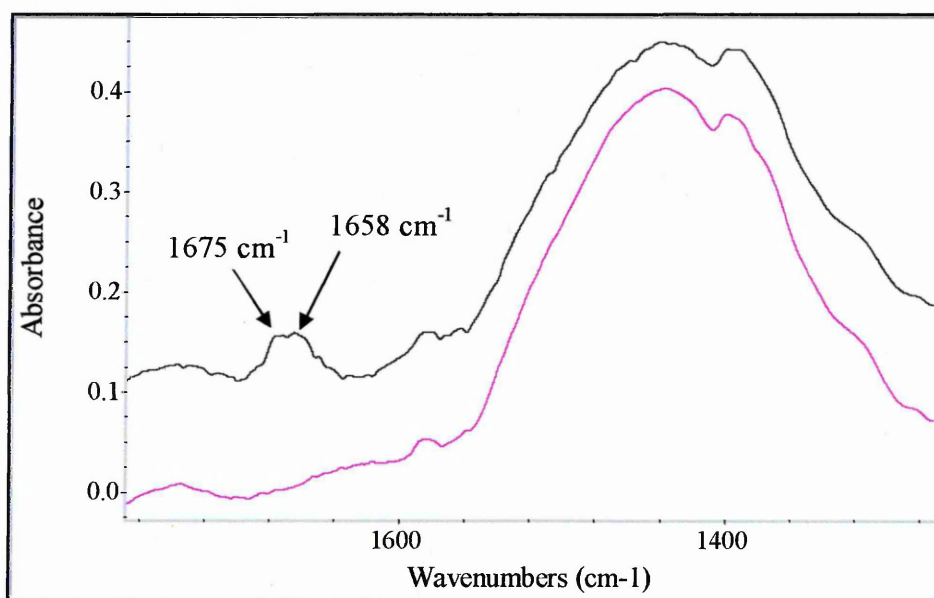


**Figure 4.15: Spectra of standard 24 (pink) and standard 24 exposed to DMF for 2 days (black) both at 4 wt% in KBr.**

A plot of the peak area in the 1680-1650 cm<sup>-1</sup> region against wt% SAz-1 is shown in Figure 4.16 and the peak area in the 1680-1650 cm<sup>-1</sup> region in the spectra for two selected standards are indicated. Standard 17 contained 1 wt% SAz-1, while standard 19 contained 3 wt% SAz-1.

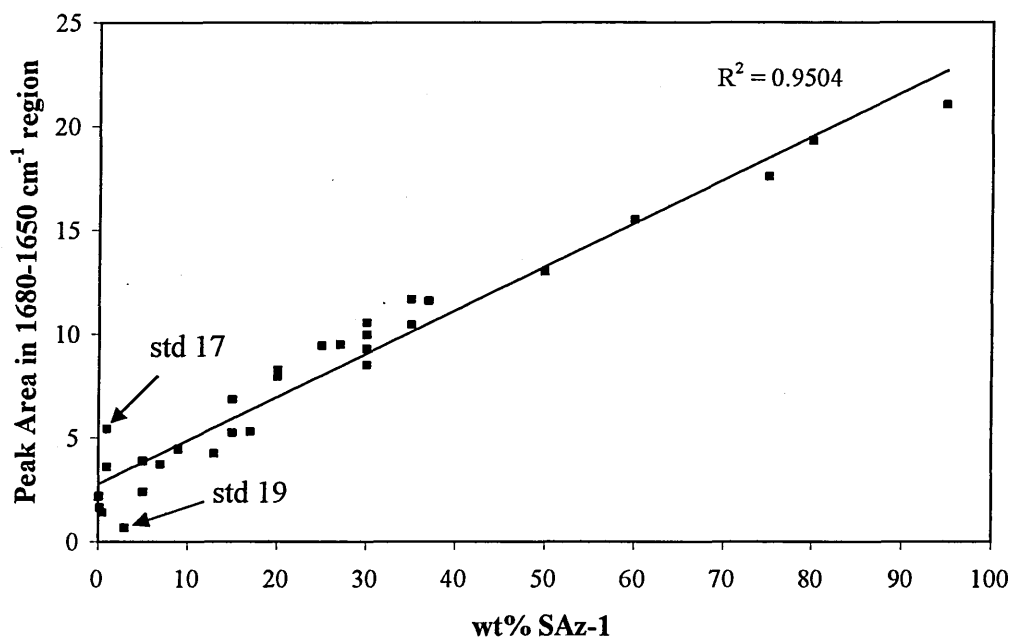


**Figure 4.16: Relationship between peak area 1680-1650 cm<sup>-1</sup>, associated with the C=O bond of DMF in DRIFTS spectra, and the wt% of SAz-1 in the standards described in Table 4.1.**

Although the  $R^2$  value was low at 0.9504, there did appear to be a correlation between the area of the band in the 1680-1650 cm<sup>-1</sup> region and the wt% of SAz-1. This was another indication that introducing a probe molecule to the standards would result in more accurate quantitative predictions of the concentrations of components. The best fit line did not go through zero and it was suspected that this was due to the influence of kaolinite on the intensity of the C=O peak. Standard 17 contained 1 wt% SAz-1 and 95 wt% kaolinite and had a C=O peak intensity greater than expected had the peak been due solely to the presence of SAz-1. This suggested that the presence of a high concentration of kaolinite greatly increased the intensity of the C=O band and this could be due to partial intercalation of DMF between layers of kaolinite. Standard 19 contained 3 wt% SAz-1 and 2 wt% kaolinite and the peak intensity was markedly less than that of standard 17, despite standard 17 containing less SAz-1. The area of the band in the 1680-1650 cm<sup>-1</sup> region of the spectrum for standard 19 had a stronger correlation with the concentration of SAz-1, i.e. it lay closer to the  $x = y$  line and this could be because the

concentration of kaolinite was not large enough to significantly increase the peak intensity.

After studying the intensity and position of the carbonyl band in standards with different SAz-1 and kaolinite concentrations, shown in Figure 4.17, it became clear that this peak could not be assigned exclusively to SAz-1. At concentrations of SAz-1 as low as 5 wt%, the C=O peak was at the expected position of  $1658\text{ cm}^{-1}$ , while at lower concentrations of SAz-1, and therefore higher kaolinite concentrations, the peak was centred at a higher wavenumber. This again implied that kaolinite, as well as SAz-1, may intercalate a proportion of DMF between the aluminosilicate layers.

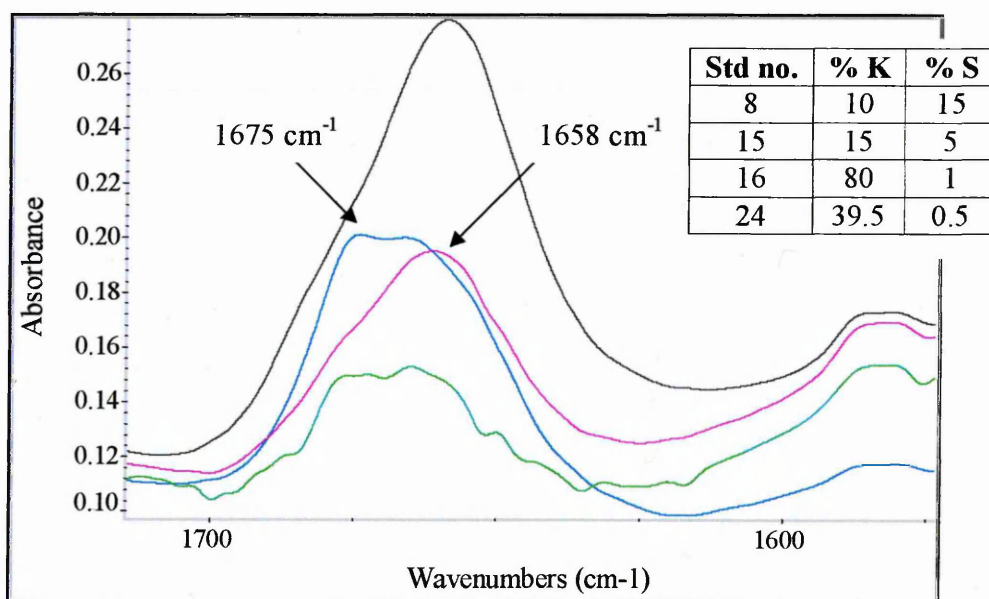


**Figure 4.17: The carbonyl band region in DRIFTS spectra of standards 8 (black), 15 (pink), 16 (blue) and 24 (green) all at 4 wt% in KBr. Compositions of the standards are given in the inserted table, where K, S, and C represent kaolinite, SAz-1, and calcite, respectively.**

Figure 4.18 shows the spectra of 4 wt% kaolinite and 4 wt% kaolinite after exposure to DMF. The carbonyl band appeared as two peaks at  $1675\text{ cm}^{-1}$  and  $1665\text{ cm}^{-1}$  as indicated. If the appearance of this carbonyl band in the spectra of kaolinite were to confirm that kaolinite intercalates DMF, then since kaolinite layers are held together tightly by hydrogen bonding, it is suggested that DMF would intercalate into the edges of

the kaolinite layers. It should be noted that no peak associated with DMF was observed in the XRD trace for kaolinite which had been exposed to DMF vapour, again suggesting that DMF may only intercalate into the edges of the kaolinite layers.

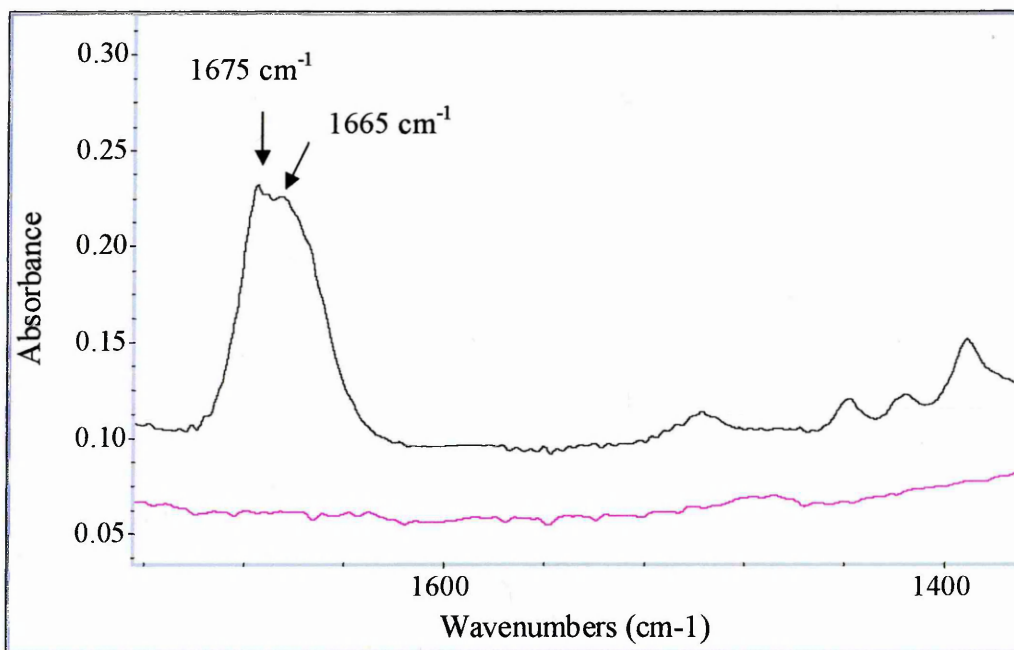


**Figure 4.18: DRIFTS spectra of kaolinite (pink) and kaolinite after exposure to DMF (black) both at 4 wt% in KBr.**

Calibration results for the DMF treated training set using Model 3 (OMNIC, SHU, DMF treated) and Model 4 (GRAMS, SHU, DMF treated), are shown in Table 4.5.

	OMNIC Model 3		GRAMS Model 4	
	Correlation Coefficient	Number of Factors	Correlation Coefficient	Number of Factors
Kaolinite	0.92552	5	0.9329	3
SAz-1	0.95288	3	0.9780	4
Calcite	0.98164	6	0.9771	3

**Table 4.5: Comparison of calibration correlation coefficients and numbers of factors for each named component using Models 3 and 4.**

Again the predictions calculated by GRAMS should be better than those calculated by OMNIC since overall the correlation coefficients were higher and the number of factors used lower. The correlation coefficients were slightly lower and number of factors slightly greater for the GRAMS model for standards exposed to DMF, than for the GRAMS model where standards were untreated indicating that untreated standards should therefore give better predictions.

Figures 4.19, 4.20, and 4.21 compare predictions, for each component, in the standard samples that had been exposed to DMF (filled and open triangles) with those predictions reported previously (filled and open squares), that had not been exposed. Again the calibration plots are not shown. The spectra of samples that had been exposed to DMF were all collected using the Mattson Polaris FTIR Spectrometer, and prepared in the same way as those samples that had not been exposed. Contrary to expectation, the predicted concentrations for all components were markedly less accurate and less precise for the samples that had been exposed to DMF. Models 3 and 4 seriously under predicted the concentration of kaolinite, and Model 4 had a clear tendency to over predict the SAz-1 concentration. The concentration predictions for calcite were seriously under predicted by Model 3 and over predicted by Model 4.

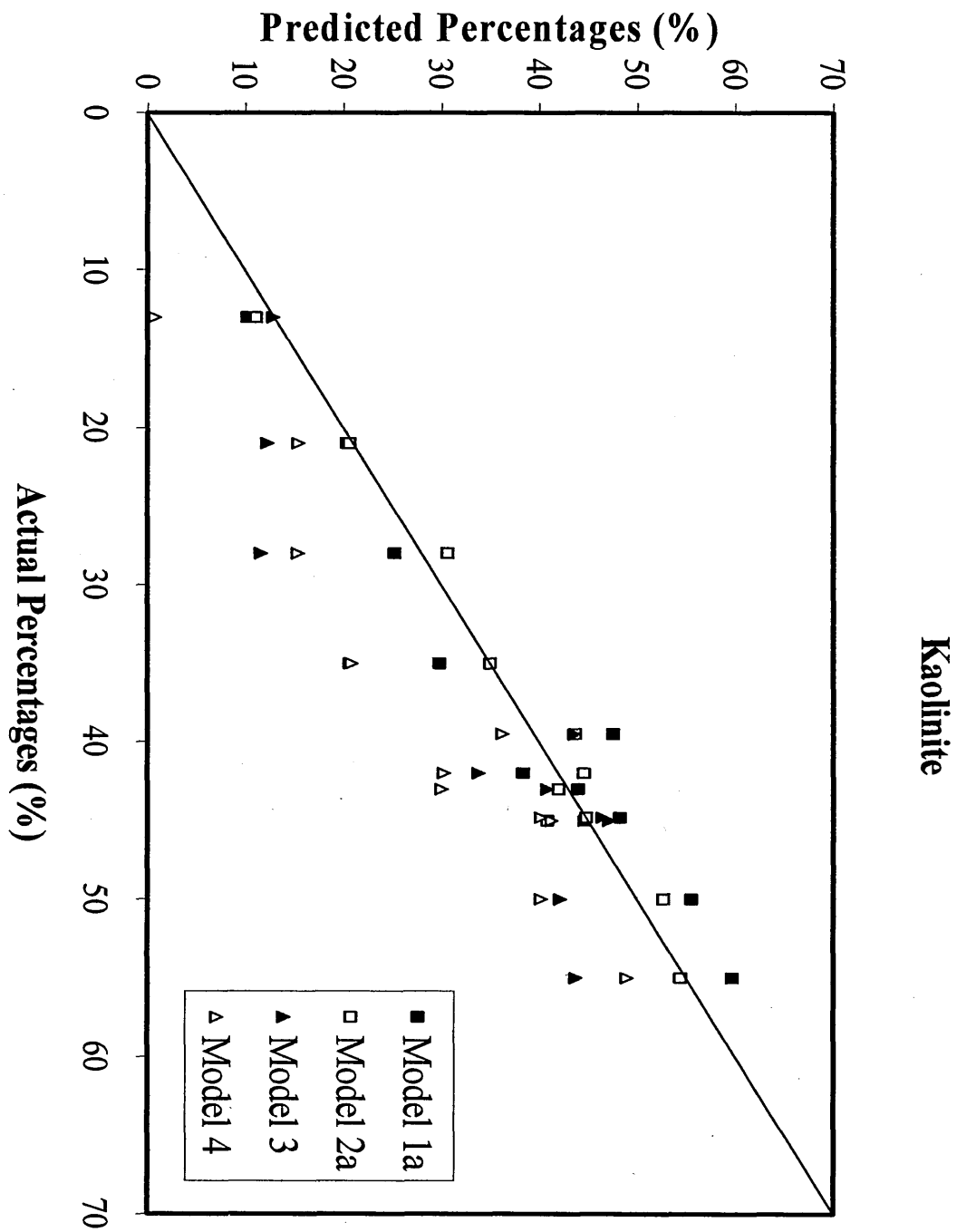


**Figure 4.19: Predicted against actual percentage of kaolinite for Models 1a, 2a, 3 and 4. The full line represents the 45°  $y = x$  line.**

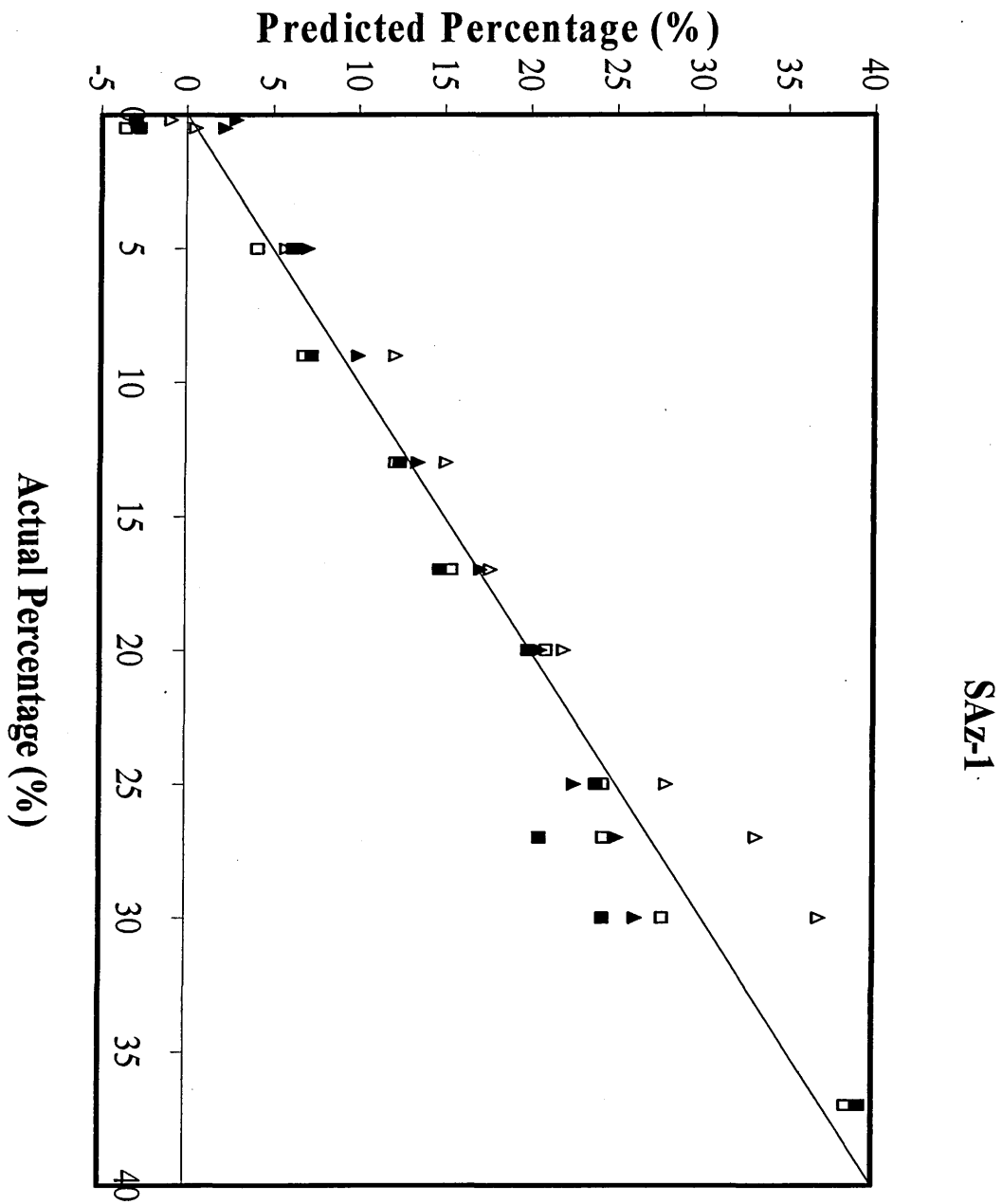


**Figure 4.20: Predicted against actual percentage of SAz-1 for Models 1a, 2a, 3 and 4, legend as for kaolinite. The full line represents the 45° y = x line.**

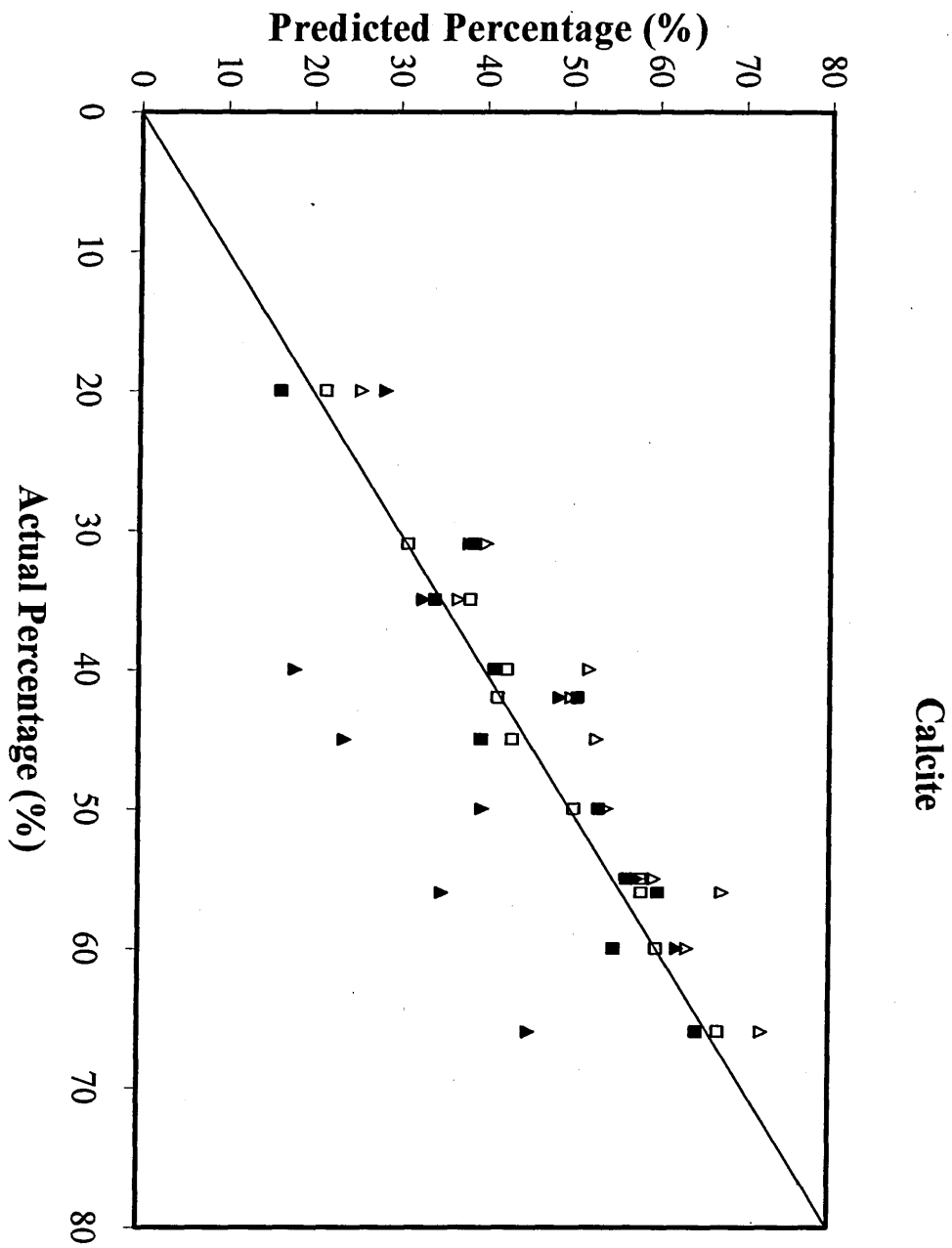


**Figure 4.21: Predicted against actual percentage of calcite for Models 1a, 2a, 3 and 4, legend as for kaolinite. The full line represents the 45° y = x line.**

#### 4.8.5 Results from Ball Milled and Compacted Standards

The KBr used for the background and diluent was ball milled at SCR. It was thought that this would give more reproducible spectra because the resulting particle size distribution would be more reproducible. Using the compaction device should also improve spectral reproducibility since each standard would be packed evenly at exactly the same pressure. A comparison of spectra collected at SCR with those collected at SHU included a comparison of the different instrument models and different preparation methods and is shown in Figure 4.22. The spectra of standard 26, which contained 42 wt% kaolinite, 27 wt% SAz-1, and 31 wt% calcite, were compared.

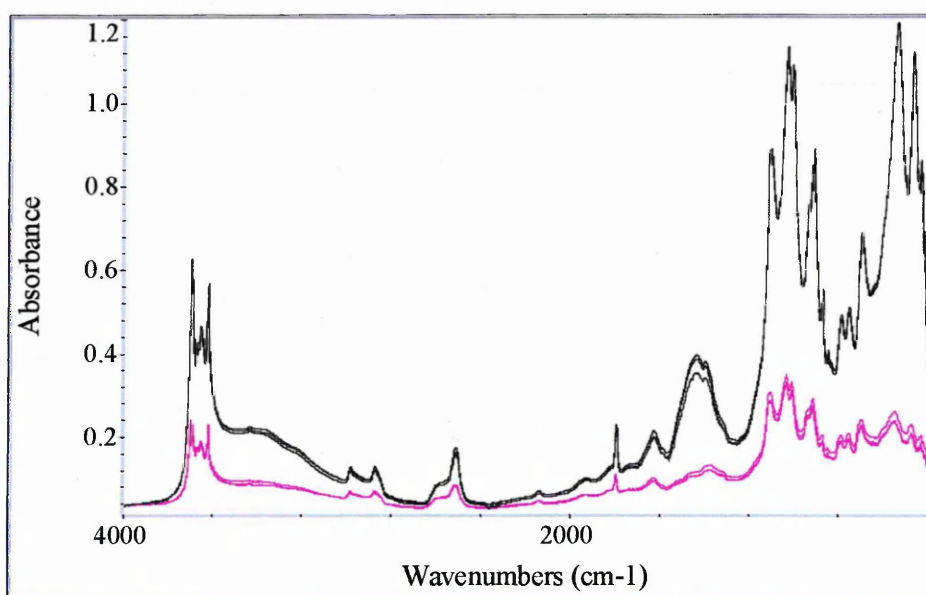


**Figure 4.22: DRIFTS spectra of repeated samples of 4 wt% standard 26 collected at SHU (black) and at SCR (pink).**

The spectra collected at SCR using the Nicolet NEXUS FTIR Spectrometer were lower in intensity than the spectra collected at SHU using the Mattson Polaris FTIR Spectrometer, and also the calcite band near  $1400\text{ cm}^{-1}$  was a different shape in the spectra from the different instruments. With the Mattson Polaris FTIR Spectrometer, a doublet was seen at  $1436$  and  $1400\text{ cm}^{-1}$ , while the Nicolet NEXUS FTIR Spectrometer showed a single peak at  $1380\text{ cm}^{-1}$  with a large shoulder near  $1440\text{ cm}^{-1}$ . Figure 4.23 shows the spectra of standard 26 in the region near  $1400\text{ cm}^{-1}$  in more detail.

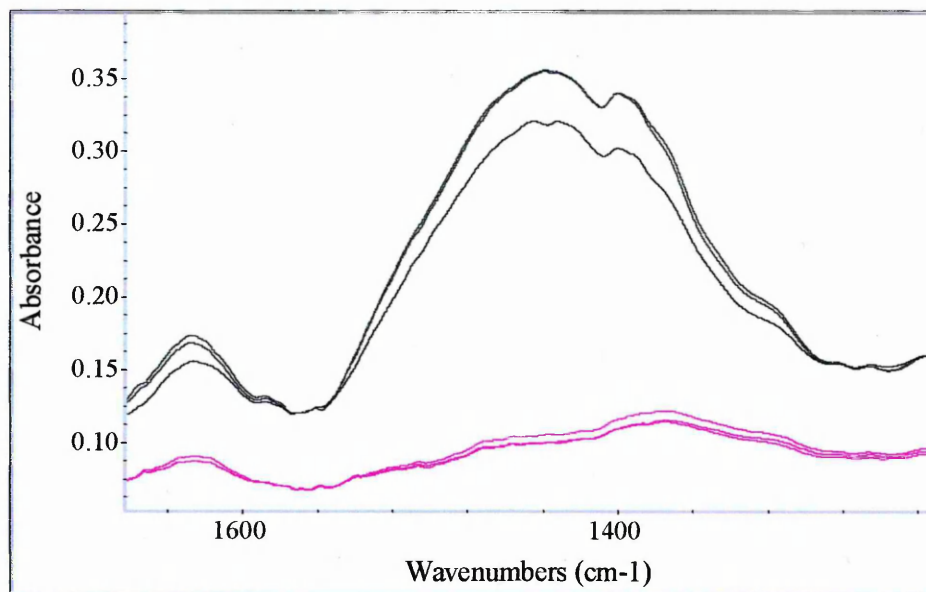


**Figure 4.23: DRIFTS spectra of repeated samples of 4 wt% standard 26 collected at SHU (black) and at SCR (pink) in the region near 1400  $\text{cm}^{-1}$ .**

The low intensity of the spectra collected using the Nicolet FTIR spectrometer was most likely to be due to the low throughput, possibly occurring due to a slight misalignment of the beam.

Calibration results for Model 5 (OMNIC, SCR) and Model 6 (GRAMS, SCR) for training set samples in which the KBr had been ball milled and a compaction device used, are shown in Table 4.6.

	OMNIC Model 5		GRAMS Model 6	
	Correlation Coefficient	Number of Factors	Correlation Coefficient	Number of Factors
Kaolinite	0.98183	5	0.9865	7
SAz-1	0.99288	7	0.9948	4
Calcite	0.96451	6	0.9891	3

**Table 4.6: Comparison of calibration correlation coefficients and numbers of factors for each named component using Models 5 and 6.**

Again the GRAMS model gave higher correlation coefficients and generally used fewer factors than the OMNIC model. The correlation coefficients for Models 5 and 6 were higher than for Models 1 and 2, indicating that ball milling KBr and using a compaction device should give better predictions.

Only the initial 5 independent standards were used to compare predictions calculated from spectra collected at SCR and those calculated from spectra collected at SHU, since these were the only spectra of independent standards collected at SCR. Figures 4.24, 4.25, and 4.26 compare prediction results for each component using Models 1b, 2b, 5 and 6. Overall, the predictions calculated by Model 6 (GRAMS, SCR, 5 independent standards) were the most accurate and the precision of the calibrations from Model 6 higher than from other models. The precision of predictions was also high using Model 6, with  $R^2$  values for all components above 0.95. The highest error in kaolinite predictions was  $\pm 2.2\%$ , in SAz-1 was  $\pm 3.8\%$ , and in calcite was  $\pm 4.9\%$  using Model 6.

It should also be noted that the precision of kaolinite predictions for spectra collected at SHU were poor, with  $R^2$  values of only 0.7053 and 0.6617 calculated by Model 2b (GRAMS, SHU, 5 independent standards) and Model 1b (OMNIC, SHU, 5 independent standards) respectively. However, Model 5 (OMNIC, SCR, 5 independent standards) had the worst precision for prediction of kaolinite, with an  $R^2$  value of only 0.2887, despite having an  $R^2$  value above 0.98 for the precision of the calibration of kaolinite.

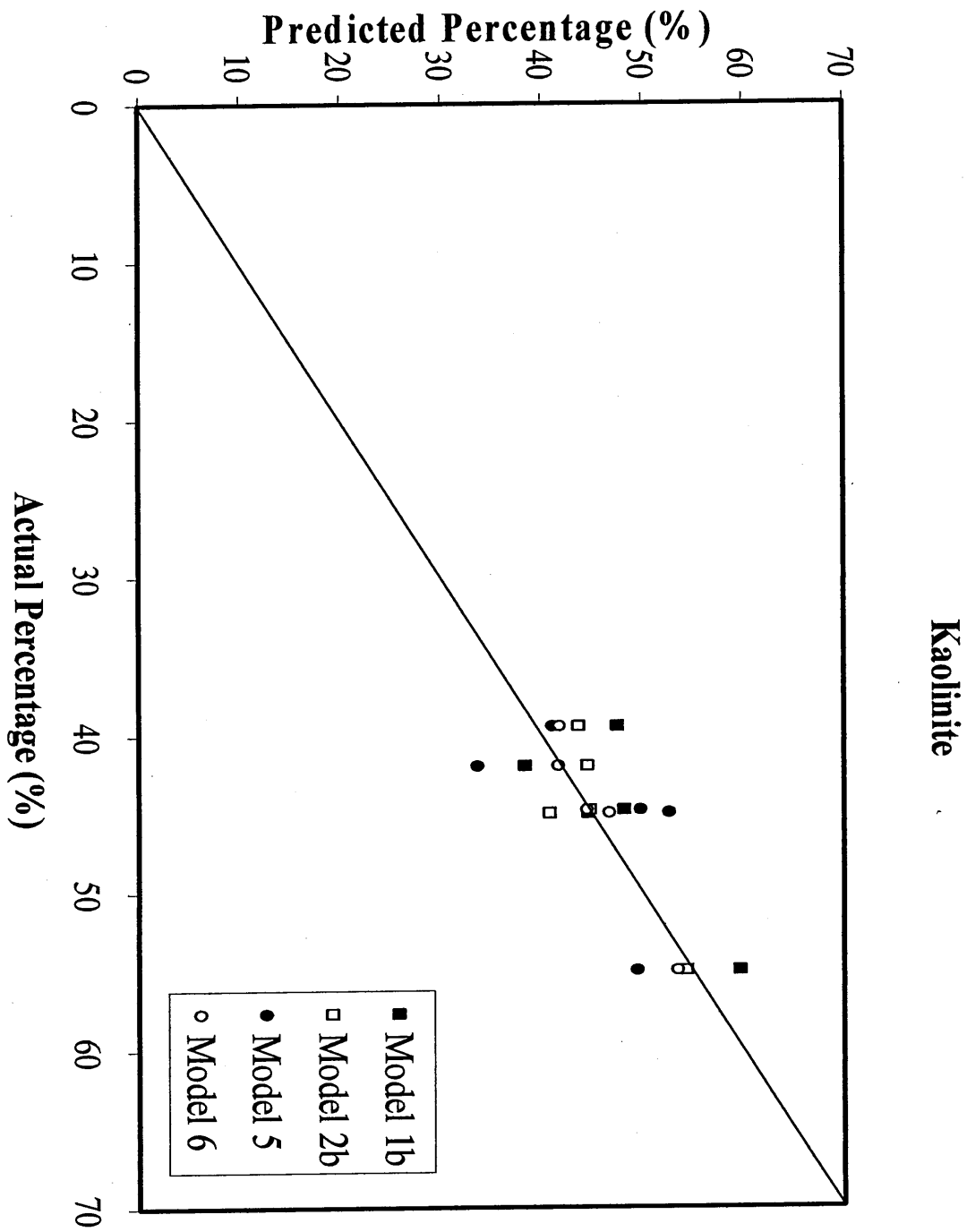


**Figure 4.24: Predicted against actual percentage of kaolinite for Models 1b, 2b, 5 and 6. The full line represents the 45°  $y = x$  line.**



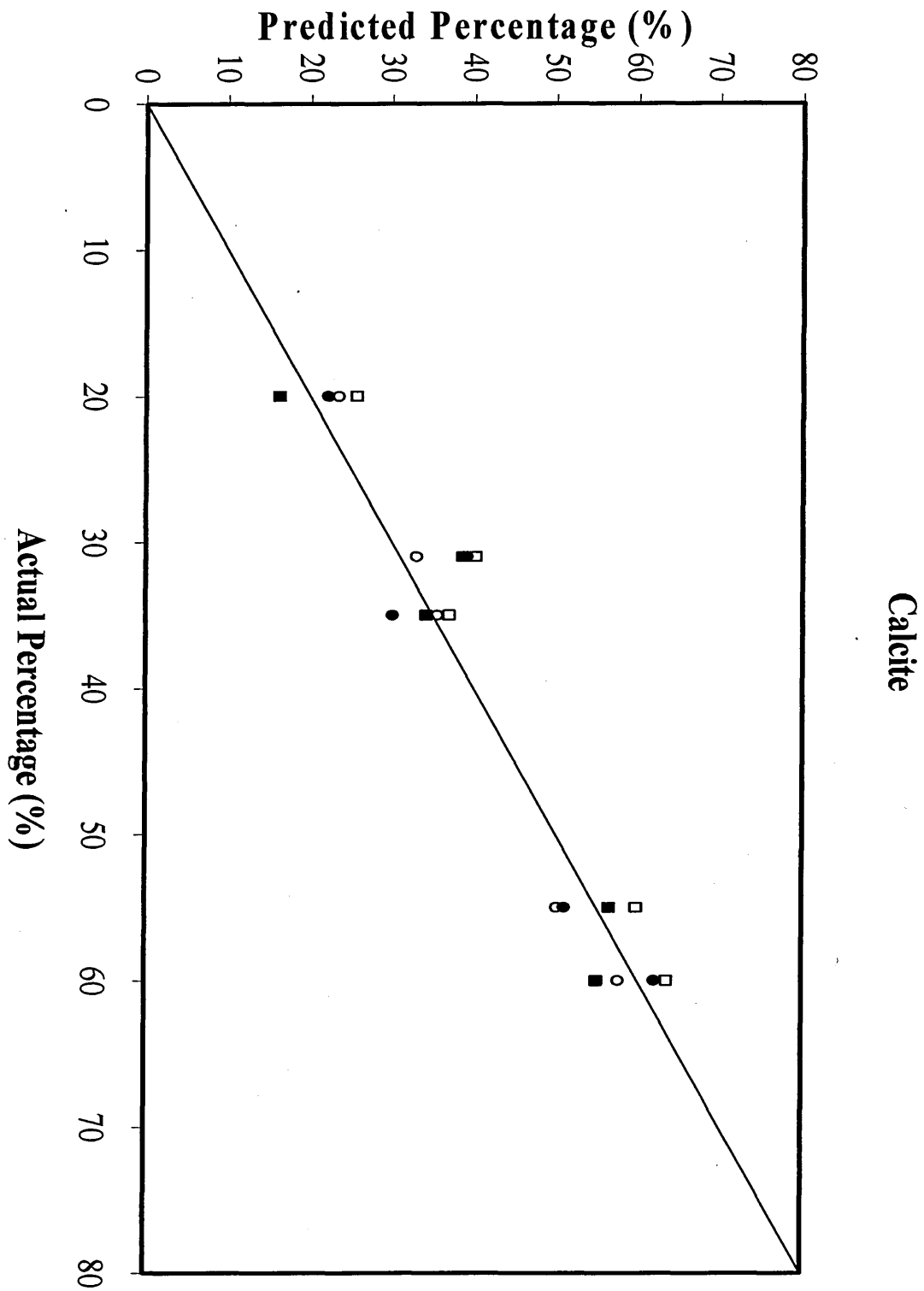


**Figure 4.26: Predicted against actual percentage of calcite for Models 1b, 2b, 5 and 6, legend as for kaolinite. The full line represents the 45° y = x line.**

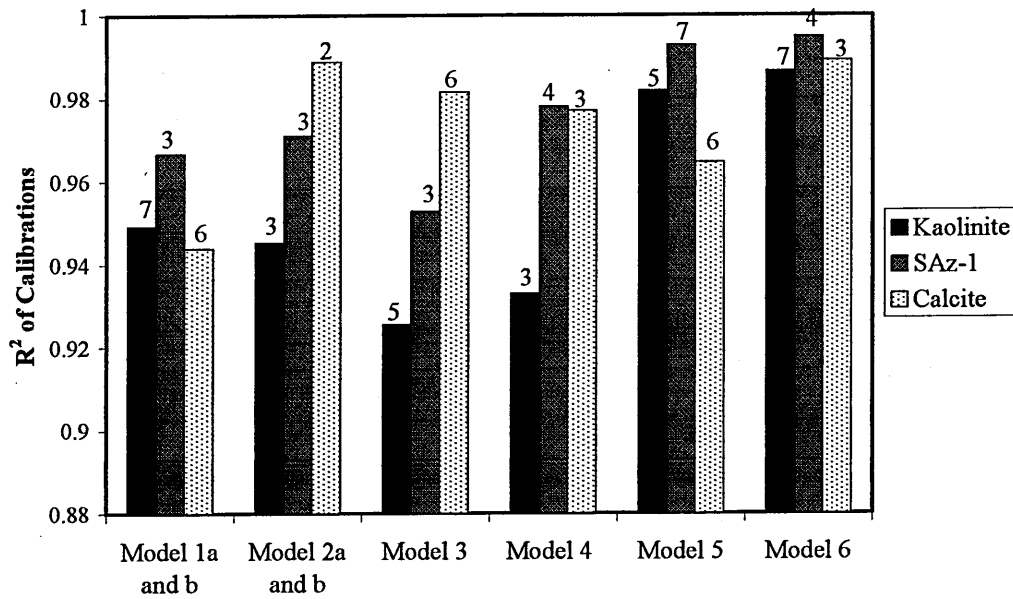
#### 4.8.6 Comparing the Precision of Calibrations

Chart 4.1 shows bars indicating the  $R^2$  values for the calibrations of each component in each model. The number above each bar indicates the number of factors used for that component in that particular model. The number of factors for each component and model was chosen based on the minimum of each PRESS plot. For each of the three ways in which the standards were treated, the GRAMS models, i.e. Models 2, 4, and 6, had higher  $R^2$  values, and were therefore more precise than the OMNIC Models 1, 3, and 5, respectively. Overall the  $R^2$  values in Model 6 were the highest, over 0.98 for each component, and therefore was the model that had the most precise calibration. There is, however, a chance that using more than 4 factors could make the model overfit despite choosing the number of factors from the minimum of the PRESS plot. This is because some noise may be present in the spectra of more than one standard and so the addition of more factors improves the calibration. However, unless these noise factors are present in an unknown sample, the predictive ability of the model will worsen.

Pearson [97] stated that if the number of factors chosen was greater than the number of calibration standards divided by three, then overfitting should be strongly suspected. It was also stated by Pearson that if the number of factors chosen was less than the number of calibration standards divided by six, then overfitting was unlikely. By following these rules in the current study containing 21 standards, using more than 7 factors could cause overfitting and using less than 3 or 4 factors suggests overfitting is unlikely.

Generally, fewer factors were used in GRAMS Models 2, 4 and 6 than in the corresponding OMNIC models and if focussing solely on the GRAMS models it was only kaolinite in Model 6 that used more than 4 factors and could therefore be overfit. It was therefore more likely that GRAMS models contained the optimum number of factors and were not overfit.

Models 1a and 1b could be grouped together in Chart 4.1 since the calibration for both was the same, and it was only the number of independent standards, and therefore the  $R^2$  value of predictions and sum of the squares of the differences in the predictions, that were different. The same was true for grouping Models 2a and 2b together.



**Chart 4.1: R<sup>2</sup> values for each of the named components in each of the named models, indicating the precision of calibrations. The number above each bar indicates the number of factors used for that component and model.**

#### 4.8.7 Comparing the Accuracy of Predictions

The sums of the squares of the differences between predicted and actual percentages were calculated and are shown as bars in Chart 4.2. The models and components with the highest bars had the least accurate predictions.

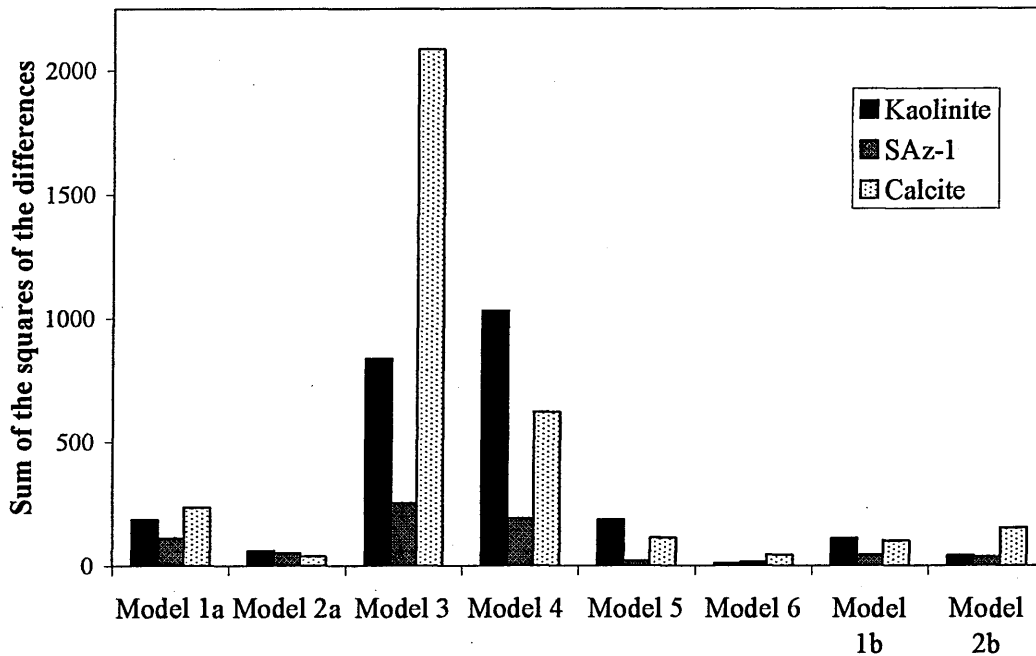


**Chart 4.2: The height of bars indicates the sum of the squares of the differences (in wt%<sup>2</sup>) between the actual and predicted percentages of each named component using each of the named models.**

It was immediately clear that the predictions found using Model 3 (OMNIC, SHU, DMF treated) and 4 (GRAMS, SHU, DMF treated) were the least accurate and that the predictions for Model 6 (GRAMS, SCR, 5 independent standards) were the most accurate. There also appeared to be a tendency for the models that were calculated using GRAMS to be more accurate than those calculated using OMNIC.

It should also be noted that the predictions for kaolinite by Models 3 and 4 were seriously under predicted, predictions for SAz-1 by Model 4 were under predicted, predictions for calcite by Model 3 were seriously under predicted and predictions for calcite by Model 4 were seriously over predicted.

#### 4.8.8 Comparing the Precision of Predictions

From the plots of predicted percentages against actual percentages, the  $R^2$  values of individual models gave a numerical indication of the precision of the predictions which can be seen in Chart 4.3.

The highest  $R^2$  values were found for Model 6 (GRAMS, SCR, 5 independent standards), indicating that this model gave the most precise predictions whilst the least precise predictions were found with Model 3 (OMNIC, SHU, DMF treated). The highest  $R^2$  values were found for SAz-1, indicating that predictions for this component were more precise than for kaolinite and calcite.

It should be noted that despite the low  $R^2$  value for predicting kaolinite in Model 5, the sum of the squares of the differences indicated that the accuracy of these predictions was quite good. The precision of the kaolinite predictions by Model 5 may improve if more independent standards, containing a wider range of kaolinite concentrations, were quantified.

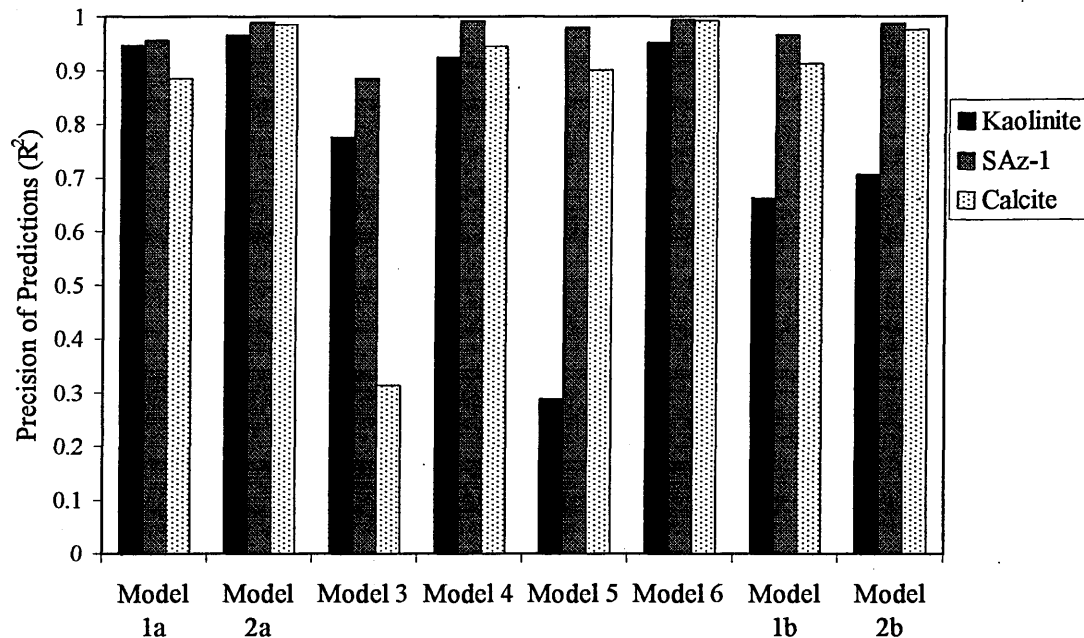


**Chart 4.3:  $R^2$  values for each of the named components in each of the named models, indicating the precision of predictions.**

#### 4.8.9 Comparing Results with Literature

Other groups have worked on determining low amounts of smectite and kaolinite in mixtures using various techniques. Madejová *et al.* [73] used XRD to determine 1 wt% kaolinite and 5 wt% smectite, and as low as 0.25 wt% kaolinite and 30 wt% smectite using the peak fitting technique with FTIR spectra obtained in transmission mode. Smectite was determined at 5 wt% in quartz using thermogravimetric analysis by Clegg [21]. Evolved water analysis was used by Bloodworth *et al.* [68] to determine kaolinite in mixtures with quartz, at concentrations as low as 0.25 wt%, while 2 wt% smectite in quartz was determined by Forsyth [57] using mass spectrometric determination of evolved DMF and water.

Madejová *et al.* [73] reported that smectite could be detected visually from a spectrum of a mixture with as low as 40 wt% using the peak at  $845\text{ cm}^{-1}$  as an indicator and the study discussed in this chapter also suggested that smectite could be detected visually at around 30 wt%, using this peak. Madejová *et al.* [73] found that kaolinite could be detected visually from a spectrum at levels as low as 0.5 wt% using the OH stretching band at  $3695\text{ cm}^{-1}$ . It was not the aim of the study discussed in this chapter to try and improve this detection limit so the lowest concentration of kaolinite used in the training set was 2 wt%, which could be detected visually. In the study discussed in this chapter, which used PLS instead of peak fitting, concentrations of SAz-1, as low as 0.2 wt% were quantified, with a maximum (absolute) error of  $\pm 3.8\text{ wt}\%$ .

Clegg [21] reported quantitative results from DRIFTS spectra using PLS. Samples were prepared in the same way as for Models 5 and 6, i.e. the KBr was ball milled and a compaction device used. Clegg used OMNIC software to calculate predictions, as was done in Model 5. However, he used the spectral range  $3900\text{--}450\text{ cm}^{-1}$ , while Model 5 (OMNIC, SCR) used the range  $2150\text{--}680\text{ cm}^{-1}$ . Clegg used a 7 component mixture, containing high concentrations of quartz, and found the best model when montmorillonite and illite were combined. While he found a correlation coefficient of 0.92 with 5 factors for this component combination, Model 5 had a correlation coefficient of 0.99 with 7 factors for montmorillonite (SAz-1) alone. Correlation coefficients for kaolinite in the

two models were very similar (both at 0.98), but while Clegg's PLS model required 8 factors for kaolinite, Model 5 required only 5 factors.

Joussein *et al.* [100] also used IR spectroscopy to determine the ratio of kaolinite and smectite in binary mixtures. They found that by visual detection of the bands at 3692 and 3620  $\text{cm}^{-1}$  kaolinite could not be detected below 5 wt%. Both the spectra of smectite and kaolinite showed an OH stretching band at 3620  $\text{cm}^{-1}$ , so this band could not directly be used to calculate the concentration of either. The smectite was saturated with  $\text{NH}_4^+$ , and the band at 1400  $\text{cm}^{-1}$  (associated with  $\text{NH}_4^+$ ) measured and related to the concentration of smectite. Using the relationship between the absorbance of the band at 1400  $\text{cm}^{-1}$  and the concentration of smectite, the absorbance of the OH stretching band at 3620  $\text{cm}^{-1}$  attributed to smectite, could be calculated. The relative absorbance of the 3620  $\text{cm}^{-1}$  band which was due to smectite and kaolinite would then be known and the relative concentration of each could be determined. It should be noted that while in this study the smectite was saturated with  $\text{NH}_4^+$  in isolation, Joussein *et al.* claimed that the smectite/kaolinite mixture could be saturated with the same results, provided the variable charges of kaolinite were negligible with regards to that of smectite. The work in this chapter suggested that a kaolinite/smectite mixture should not be saturated with a probe molecule since the strongest probe molecule infrared band was found to be present in the spectra of both SAz-1 and kaolinite after exposure to the probe molecule and its presence did not improve the accuracy or precision of predictions.

A three component PLS model was developed with GRAMS software by Berzas *et al.* [101] in a similar way to the models described in this chapter. Berzas *et al.* used cross validation and a 32 standard training set to develop the PLS model. In contrast to the study described in this chapter, however, Berzas *et al.* studied the spectrophotometric absorption spectra of synthetic mixtures of three different food dyes. Berzas *et al.* found that only 2 or 3 factors were required to accurately quantify the three components. Two separate spectral regions were used for the PLS analysis and were chosen because they contained the main spectral information for the three components.

## 4.9 Conclusion

The overall aim of this study was to determine whether using PLS could improve the detection limit, set by Madejová *et al.* [73] using peak fitting, for SAz-1 in a mixture with kaolinite. It is important to be able to determine low amounts of smectite because of their high surface area and swelling ability.

The most accurate models for the 21 standard training set in this study did not include the OH stretching region, but instead used only the wavenumber region below  $2150\text{ cm}^{-1}$ .

Initial spectra of the standards were collected on a Mattson Polaris FTIR Spectrometer.

The GRAMS program was found to give more precise calibrations and more precise and accurate predictions than the OMNIC program.

The training set was then exposed to a chemical probe, DMF, for 2 days to allow complete intercalation into the swelling clay. It was thought that the presence of the peak at  $1658\text{ cm}^{-1}$ , assigned to intercalated DMF, would improve the models predictive ability, particularly for SAz-1. However, the peak was found to be present in the spectra of both SAz-1 and kaolinite after exposure to DMF and its presence did not improve the accuracy or precision of predictions.

Spectra of the training set, without DMF exposure, were then collected at SCR on a Nicolet NEXUS FTIR Spectrometer after the KBr diluent had been ball milled for 5 minutes and the sample compacted into the cup with a compaction device. It was thought that the smaller particle size distribution and homogeneous compaction would improve model predictions. It was found that Model 6 (GRAMS, SCR) gave the most accurate predictions of all models and the most precise calibrations and predictions. Results from Model 6 indicated that the highest error in kaolinite prediction was  $\pm 2.2\text{ wt}\%$ , in SAz-1 was  $\pm 3.8\text{ wt}\%$ , and in calcite was  $\pm 4.9\text{ wt}\%$ . In conclusion, it has been found that SAz-1 could be detected at lower concentrations ( $0.2\text{ wt}\%$ ) using PLS than could be detected visually ( $30\text{ wt}\%$ ) from a peak on a spectrum, with an error of  $\pm 3.8\text{ wt}\%$ .

## 5. Results - Heterogeneity of Sandstone Rock Cores

### 5.1 Introduction

It is important to study the heterogeneity of sandstones to improve knowledge on the length scale over which the mineralogy varies, and also to help determine what a representative sample size is. Predicting mineral concentrations at one position of a heterogeneous core could potentially give quite different results to a prediction from another position in the core. If there is no knowledge of the heterogeneity, errors in predicted mineral concentrations may go unnoticed and comparisons with similar work by others would be more difficult.

The heterogeneity of sandstone rock cores was initially studied by visual detection of XRD patterns of slices of cores. Seven quarried sandstone cores were studied; Hollington Red, Birchover, Yorkstone, Stancliffe, Berea, Clashach, and Castlegate. XRD patterns were collected on rock and powder samples at different positions along the cores to study whether differences in the core could be detected visually.

### 5.2 Experimental Strategy

The seven quarried sandstone cores studied were obtained from Schlumberger Cambridge Research. Each core was marked along its length prior to cutting so that once sliced, sliced disks could be lined up in the correct orientation, as shown in Figure 5.1. Each core was then dry cut using a circular saw into 5 mm thick disks.



**Figure 5.1: Photograph of rock core sliced into disks with orientation markings shown.**

The powder produced from cutting each of the slices was collected for analysis since it was unknown whether certain minerals would preferentially remain in the rock slice, or be lost to the powder collected, due to the vibration of the saw during cutting, or due to differences in the friability of the sample. It was clear by looking at the rock surfaces and also during the cutting process that some of the sandstone cores were more dense and harder than others. Birchover, Yorkstone, and Stancliffe were harder rocks, while Berea was slightly softer. Hollington Red, Clashach, and Castlegate were the softest sandstones studied and were easiest to cut. It was found that more powder was collected during the cutting process of the harder rocks than during cutting of the softer rocks. It was assumed that more powder was produced due to the longer cutting times (and therefore more vibration) of the harder, less friable rocks. Methven and Hughes [102] investigated the chemical and physical properties of sandstones. They found that Hollington Red and Clashach contained a larger number of large pores (10-100  $\mu\text{m}$ ) and had a higher porosity (22-25%) than Birchover, Yorkstone, and Stancliffe, which had smaller pores (<1-10  $\mu\text{m}$ ) and lower porosity (11-16%). This accounted for why Birchover, Yorkstone, and Stancliffe appeared denser and were harder to cut than the other sandstones.

The uncrushed rock slices and the powder collected from cutting were studied using XRD.

Additionally, Dr. Stephen Hillier from the Macaulay Land Use Research Institute was approached to carry out detailed XRD analysis on samples of crushed cores. Although the same sandstones were studied by Hillier as were studied in this chapter, different areas of the same cores, or entirely different cores, were investigated.

## **5.3 Coarse Survey of Rock Cores**

### **5.3.1 Introduction**

In the first instance a rapid survey designed to provide an initial indication of gross changes in mineralogy was undertaken with XRD. Low resolution XRD traces were collected initially for speed, to minimise the resource investment.

### 5.3.2 Experimental

The handbook, "The Building Sandstones of the British Isles" [103], was used to select the quarried sandstones studied, except for Berea and Castlegate, which came from the USA. The quarried rocks studied, their source and colour, are listed in Table 5.1. The constituent minerals of the sandstones, as determined by Hillier, are also listed.

Quarry Rocks	Source	Colour	Constituent Minerals
Hollington Red	Hollington, Staffordshire	Dull red, with darker banding.	Quartz, K-Feldspar, Kaolinite, Illite/Montmorillonite, Hematite.
Birchover	Matlock, Derbyshire	Pink to buff.	Quartz, K-Feldspar, Na- Feldspar, Kaolinite, Illite/Montmorillonite.
Yorkstone	West Yorkshire	Light buff.	Quartz, K-Feldspar, Na- Feldspar, Calcite, Kaolinite, Illite/Montmorillonite, Chlorite.
Stancliffe	Chesterfield, Derbyshire	Buff.	Quartz, K-Feldspar, Na- Feldspar, Kaolinite, Illite/Montmorillonite.
Berea	Amherst, Ohio	Buff.	Quartz, K-Feldspar, Na- Feldspar, Kaolinite, Illite/Montmorillonite, Chlorite.
Clashach	Hopeman, Moray Firth Coast	Buff to fawn.	Quartz, K-Feldspar, Kaolinite, Illite/Montmorillonite.
Castlegate	Southern Wasatch plateau, Utah	Dull orange.	Quartz, Na-Feldspar, Kaolinite, Illite/Montmorillonite.

**Table 5.1: Source, colour [103], and constituent minerals of named sandstone quarry rocks.**

The X-ray diffractometer used was a Philips PW3710 with a Cu  $K\alpha$  radiation source, operating at 40 kV and 40 mA. A goniometer was used to rotate the detector during experiments, to reach the required angle. Parameters used to collect XRD traces are listed below;

Angle range =  $2-65^\circ 2\theta$

Step size =  $0.05^\circ 2\theta$

Time per step = 5 seconds

For the coarse survey, the samples were studied under static conditions, i.e. no spinning.

### 5.3.3 Reproducibility of XRD traces

To determine the variation within one slice of a core, XRD traces of the front and back faces of the same slice of Stancliffe were collected, and are shown in Figure 5.2a and b.

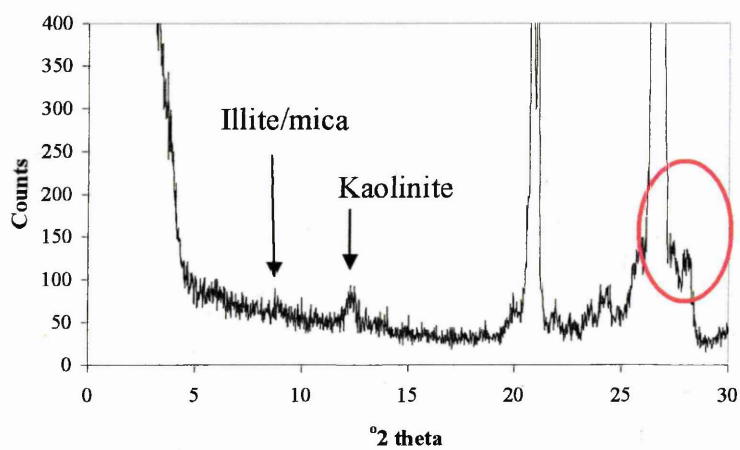


**Figure 5.2a: Low resolution XRD trace for the front of a Stancliffe rock slice. The red circle indicates the position of peaks associated with feldspar.**

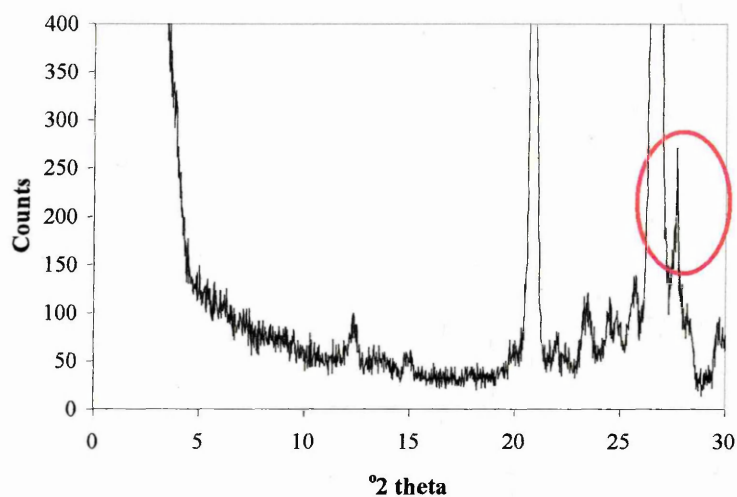


**Figure 5.2b: Low resolution XRD trace for the back of a Stancliffe rock slice. The red circle indicates the position of peaks associated with feldspar.**

Surprisingly, the traces were quite different in terms of peak intensity. The most obvious dissimilarity between XRD traces of different sides of the same rock slice were the feldspar peaks near  $28^{\circ} 2\theta$  (highlighted by the red circle), even in these low quality traces. One possible reason for differences in the traces is that the surface roughness of the rock sample may not be the same on each side of the slice. The differences could also be due to slight mineralogical differences between areas as small as within the irradiated area of one core slice.

To determine how reproducible powder sample packing was, the XRD trace of powder obtained when cutting slice 15 of Stancliffe was collected. The holder was then emptied, and the procedure repeated twice more with the same powder. The traces are shown in Figure 5.3a, b, and c.

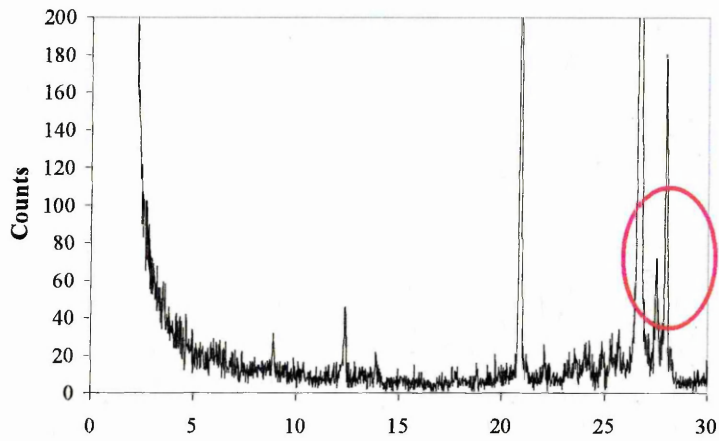


**Figure 5.3a**  $^{\circ}2\theta$

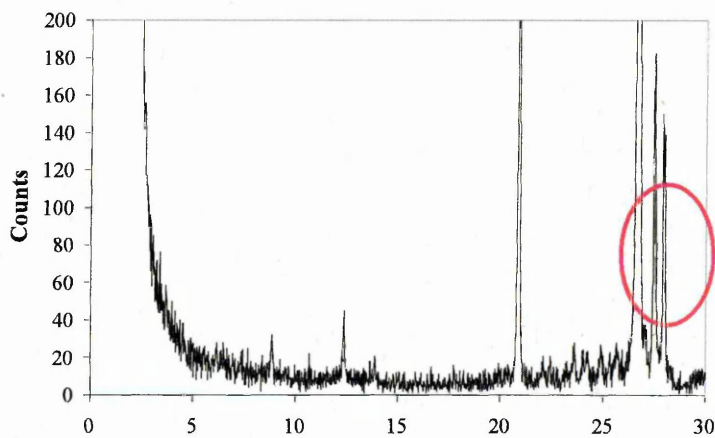


**Figure 5.3b**  $^{\circ}2\theta$

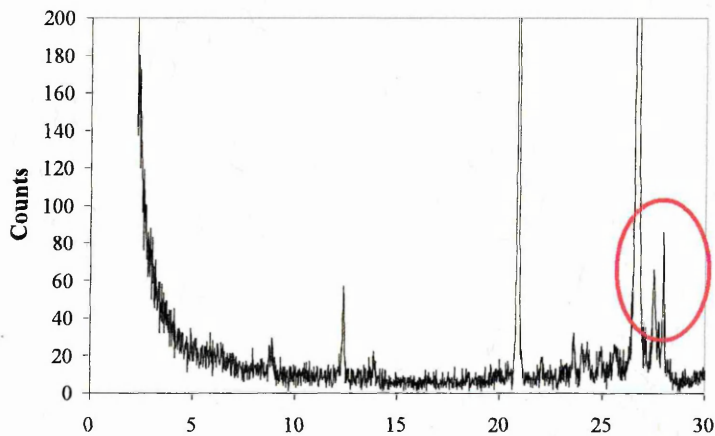


**Figure 5.3c**  $^{\circ}2\theta$

**Figure 5.3a-c: Low resolution XRD traces for the powder from cutting slice 15 of Stancliffe. The red circles indicate the position of peaks associated with feldspar.**

Again, the differences in peak intensities between traces of the same powder were surprising, and in the case of these powdered samples, differences in surface roughness should not be significant. The most obvious dissimilarity between the powder XRD traces was again associated with the feldspar peaks near  $28^{\circ} 2\theta$ . The XRD peaks of feldspars are notoriously difficult to study since the low symmetry of feldspars means that they have complex diffraction patterns. Feldspars can be ordered and disordered and their peak positions can even shift with composition. It is generally thought that, when looking at orientated aggregates, the most identifiable peaks are near  $27.5^{\circ} 2\theta$  and near  $28^{\circ} 2\theta$ , indicating that some variety of K-feldspar and some variety of Na-feldspar are present respectively [19]. There were also intensity variations between the peaks for the clay minerals in the  $4-20 (^{\circ} 2\theta)$  range.

Generally, the clay peaks were better defined against the background in powdered samples than in rock slices. This was probably due to the different ways in which the samples were presented to the diffractometer. The powder sample was packed, giving it a smooth level surface, while the rock would naturally have a more uneven surface. Clay in the powder sample would be better aligned than clay present in the rock sample and this preferred orientation of the clay in the pressed powder was the likely cause of the intense 001 diffraction pattern [19]. However, there was also a possibility that clay may have been released from the rock during the cutting process and there may be a correlation between the friability of the rock and the amount of clay in the powder obtained from cutting.

## **5.4 Mineralogical Variation along Core Length**

### **5.4.1 Introduction**

Having found important variations within slices, it was decided to evaluate the gross differences in mineralogy along the length of the different cores. Three slices from each core were analysed; one from the front of the core, one from the middle and one from the end. XRD traces of the front faces of the three rock slices were collected for each core. In addition, XRD traces of the powders from cutting the three selected slices were collected for each core.

## 5.4.2 Experimental

XRD traces of the rock and powder samples were collected on a Philips X'Pert PRO X-ray Diffractometer with Cu K $\alpha$  radiation, equipped with a PW3015/20 X'Celerator detector. The powdered samples were back packed. Each was collected with sample spinning and the parameters used to collect the XRD traces are listed below;

Angle range = 2-75° 2 $\theta$

Step size = 0.02° 2 $\theta$

Time per step = 10 seconds

Spinning rate = 8 seconds per revolution

The slits and mask size chosen for samples are listed below:

For powdered samples;

Divergence slit = 0.125°

Antiscatter slit = 0.25°

Mask size = 10°

For rock slices samples;

Divergence slit = 0.25°

Antiscatter slit = 0.5°

Mask size = 15°

The divergence slit helped to limit and direct the incident beam before it struck the sample. After striking the sample, the beam passed through the antiscatter slit before it reached the detector. While the size of the divergence slit determined the length of the sample that was irradiated by the incident beam, the size of the mask defined the width of the sample that was irradiated by the incident beam. Finer slit sizes can improve the resolution and sharpness of the peaks in an XRD trace. However, they also diminish the intensity of the peaks [19].

Smaller slit sizes were used for powder than for rock samples to avoid the irradiated area exceeding the sample area, since the surface area of the powder exposed was less than that of the rock sample. It has been reported that any spread of the incident radiation beyond the sample surface may cause background scattering and possible reflections from the sample holder [69]. The lengths of the different cores, and the number of slices cut from each is listed in Table 5.2.

	Length of core studied (cm)	Number of slices
Hollington Red	10	20
Stancliffe	8.5	17
Yorkstone	4	8
Berea	2	4
Clashach	2	4
Castlegate	3	6
Birchover	1.5	3

**Table 5.2: The length and number of slices cut, from each named sandstone.**

### 5.4.3 Results and Discussion

#### 5.4.3.1 XRD traces of Powder from cutting and Rock slices.

As an example of the peaks identified in the XRD traces studied, a more detailed analysis of the XRD trace (in the 0-30° 2θ range) from the powder from cutting slice 1 of Yorkstone is shown in Figure 5.4, with peaks identified. The components relating to the identified peaks are shown in Table 5.3.

	Component	Peak position (° 2θ)
Chl	Chlorite	6.2
I/M(1)	Illite/Muscovite	8.9
K(1)	Kaolinite	12.4
K-F(1)	K-Feldspar	13.6
Na-F(1)	Na-Feldspar	13.9
I/M(2)	Illite/Muscovite	17.8
Q(1)	Quartz	20.9
Na-F(2)	Na-Feldspar	22.0
Na-F(3)	Na-Feldspar	23.1
Na-F(4)	Na-Feldspar	23.6
Na-F(5)	Na-Feldspar	24.3
K(2)	Kaolinite	24.9
Q(2)	Quartz	26.6
K-F(2)	K-Feldspar	27.1
K-F(3)	K-Feldspar	27.5
Na-F(6)	Na-Feldspar	27.9
Na-F(7)	Na-Feldspar	28.2

**Table 5.3: Peaks identified from the XRD trace of powder from cutting slice 1 of Yorkstone (Figure 5.4), the peak positions, and minerals associated with the peaks.**

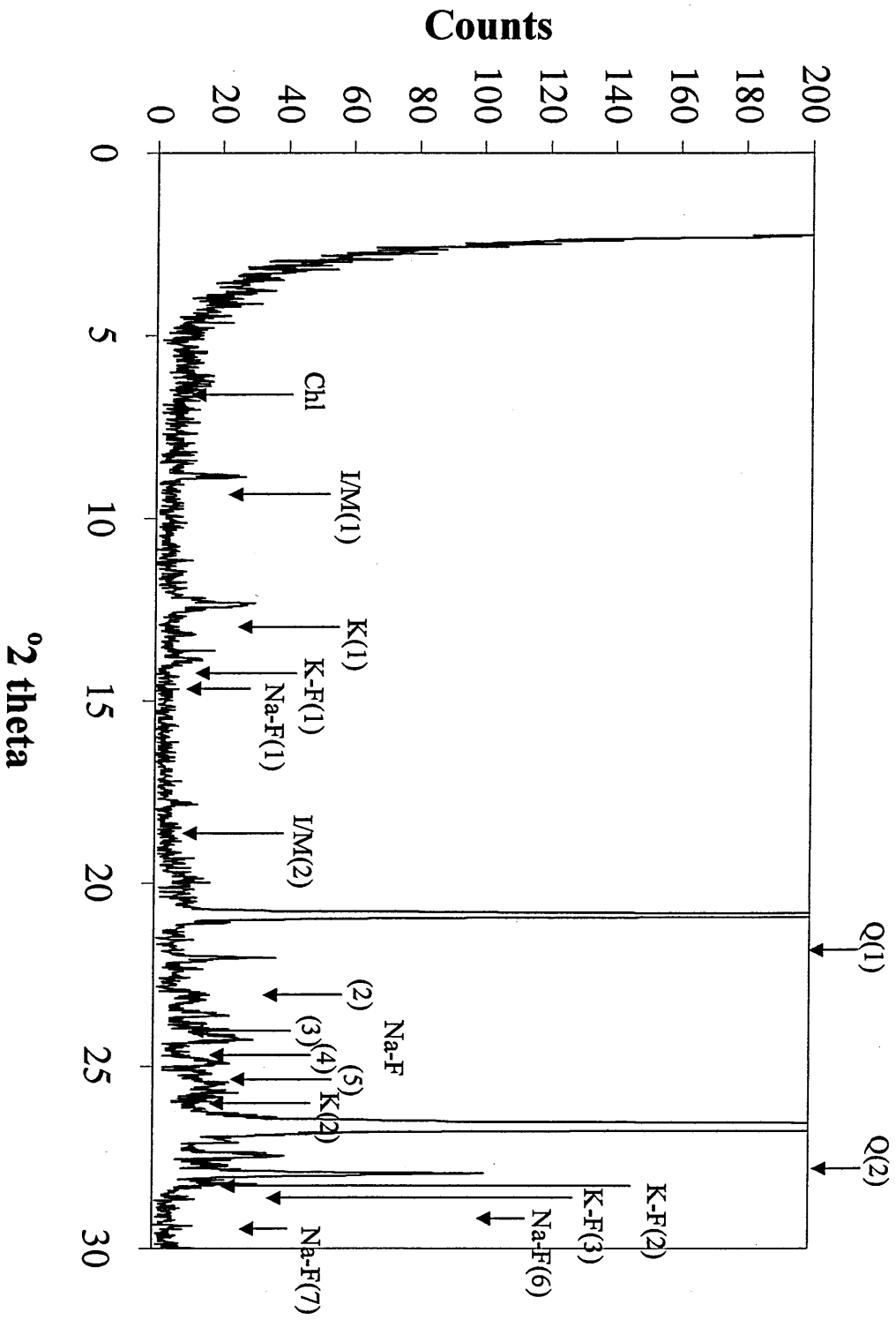


Figure 5.4: XRD trace of the powder from cutting slice 1 from Yorkstone. The peaks identified and the minerals associated with these peaks are listed in Table 5.3.

The mineral components identified from visual inspection of the XRD trace of Yorkstone (Figure 5.4), were also identified by Hillier's XRD analysis (Table 5.1).

The XRD traces of the powder from cutting the three slices and of the rock slices themselves are presented in Figures 5.5-5.18a, b, and c, for each sandstone. The peaks on the traces are identified with labels corresponding to the components listed in Table 5.3.

Of all the sandstones studied, the most significant differences in the XRD traces at different positions along the cores were observed for the Hollington Red core. This was expected since Hollington Red is a banded sandstone, i.e. it contains regions of clay rich strata with finer particles between regions more rich in silica [102]. The Hollington Red core studied had been cored through a band so that each slice contained both clay rich and silica rich parts. However, each slice may have had a slightly different proportion of each part.

The XRD traces for the powder from cutting the three slices of Hollington Red are shown in Figure 5.5a, b, and c, while the XRD traces for the Hollington Red rock slices themselves are shown in Figure 5.6a, b, and c.

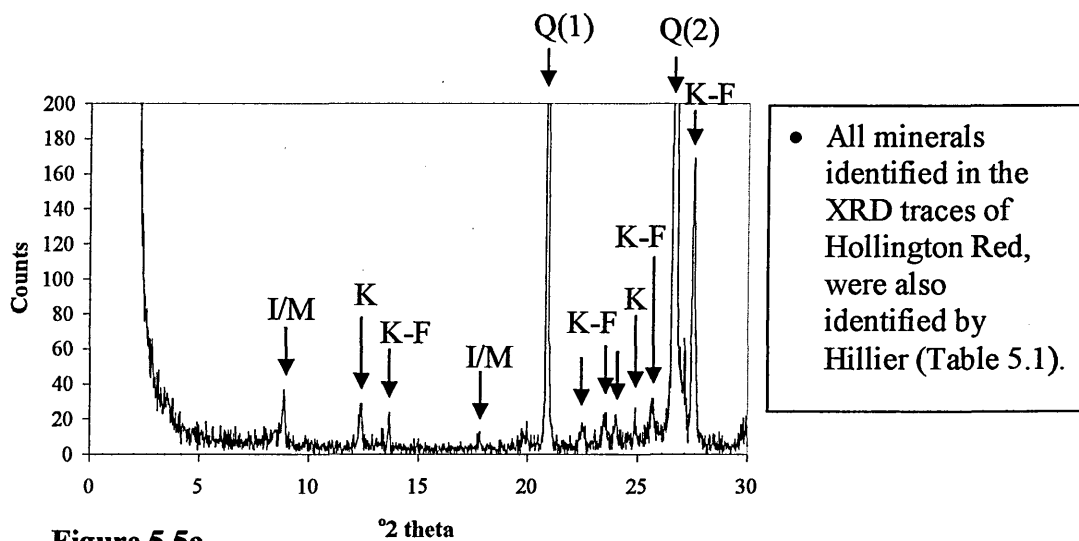


Figure 5.5a

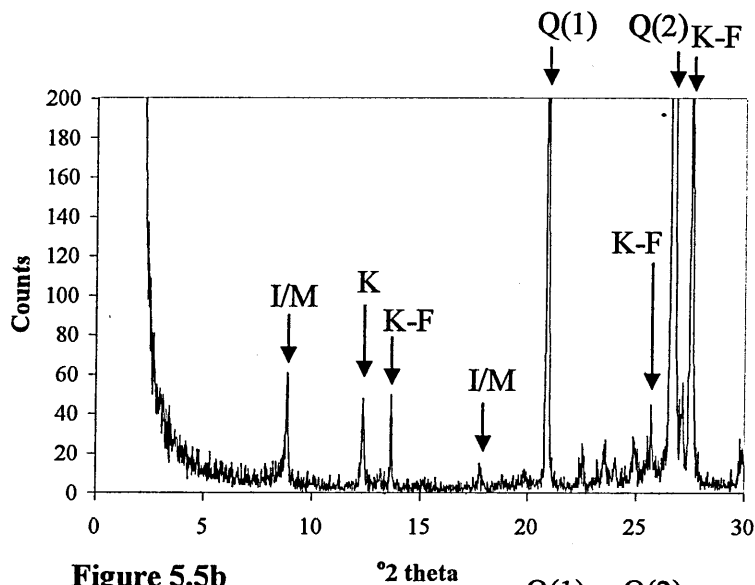


Figure 5.5b

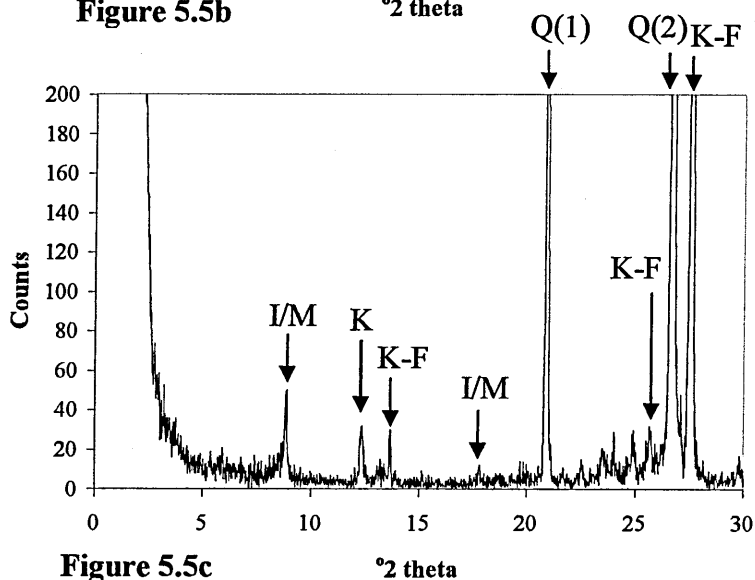


Figure 5.5c

Figures 5.5a-c: XRD traces of the powders from cutting slices 1, 10, and 20 from Hollington Red. The minerals associated with the peaks identified are shown in Table 5.3.

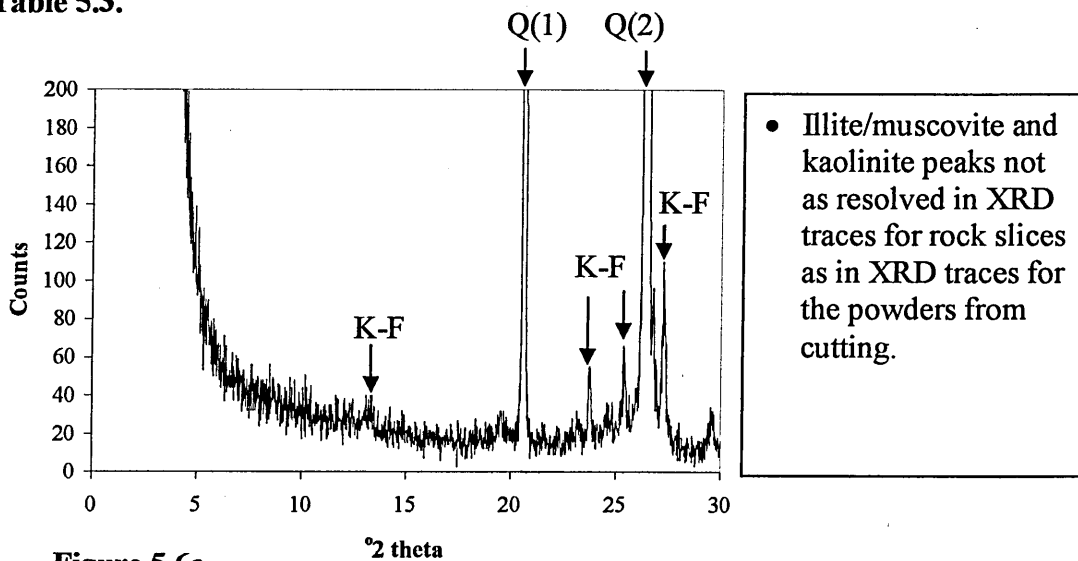


Figure 5.6a

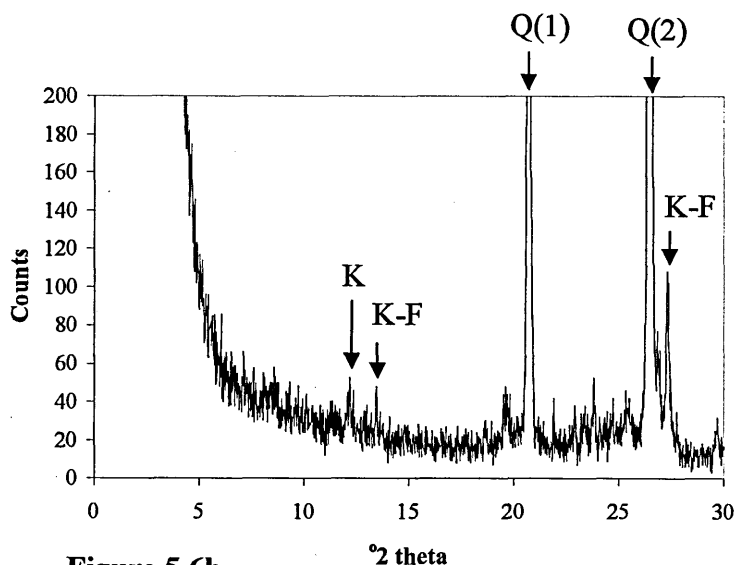


Figure 5.6b

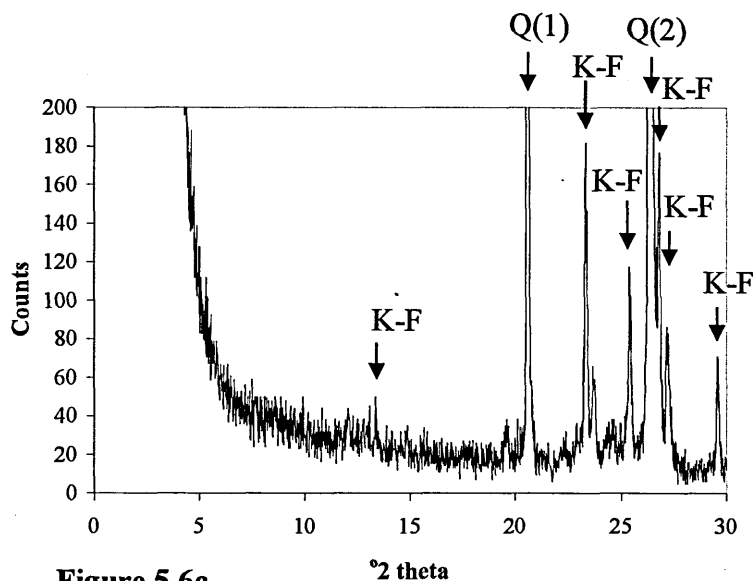


Figure 5.6c

- Large variation in the intensity of the K-feldspar peaks in the XRD traces for the rock slices.

**Figures 5.6a-c: XRD traces of the front faces of rock slices 1, 10, and 20 from Hollington Red. The minerals associated with the peaks identified are shown in Table 5.3.**

It should be noted that all the peaks in the XRD traces for the rock slices occurred at an angle of  $0.3^\circ 2\theta$  less than the angle at which they occurred on the XRD traces for the powder samples. This was thought to be due to a difference in the height of the rock slice in the XRD sample holder, compared with the height of the powder sample in the sample holder.

It should also be noted that the peaks tended to be less well resolved and of higher intensity in the XRD traces for the rock samples compared to those in the traces of the powder samples. This was also mentioned in section 5.3.3 and was thought to be due to the effect of preferred orientation of the clays in the powder sample and due to the larger particle size and roughness of the rock surface. The different slit and mask

sizes used for the powder and for the rock samples, however, would also have an effect, as mentioned in section 5.4.2. Smaller slit and mask sizes were used for collecting XRD traces of the powder samples than were used for collecting XRD traces for the rock samples. This would cause an increase in peak resolution and decrease in peak intensity in the XRD traces of the powder samples.

The XRD traces for the powder from cutting, and for the rock slices at different positions along a core of Hollington Red showed large differences, especially in the peaks associated with K-feldspar. The XRD traces for the powder from cutting, and for the rock slices of Castlegate, at different positions along a core, were very similar, however. XRD traces for the powder collected from cutting three slices of Castlegate are shown in Figures 5.7a-c, while the XRD traces for the corresponding three rock slices of Castlegate are shown in Figures 5.8a-c.

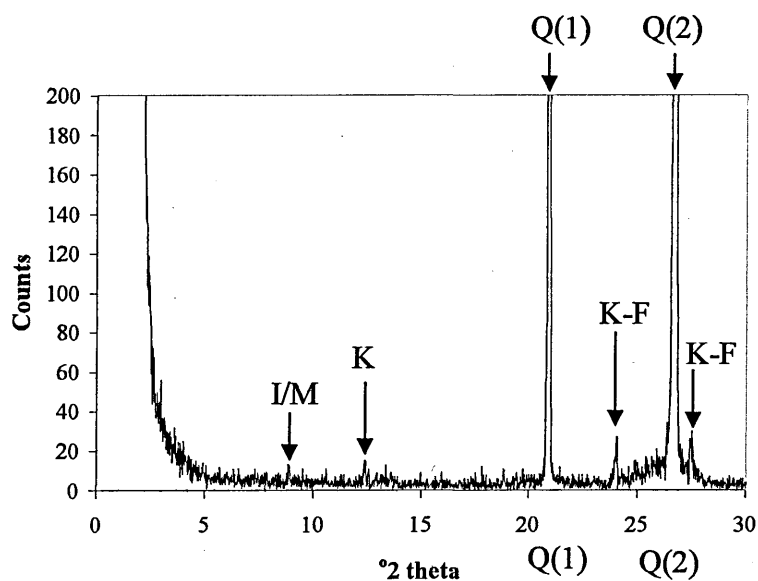


Figure 5.7a

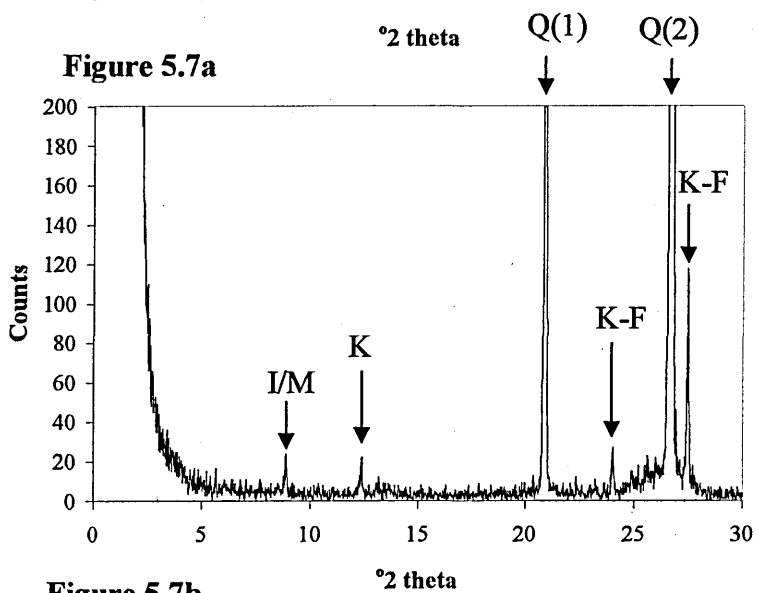


Figure 5.7b

- Low intensity clay and feldspar peaks were observed compared with the XRD traces for powders from cutting Hollington Red.
- Castlegate was a “clean” sandstone.
- K-feldspar peaks observed rather than Na-feldspar peaks even though Hillier predicted that only Na-feldspar was present.

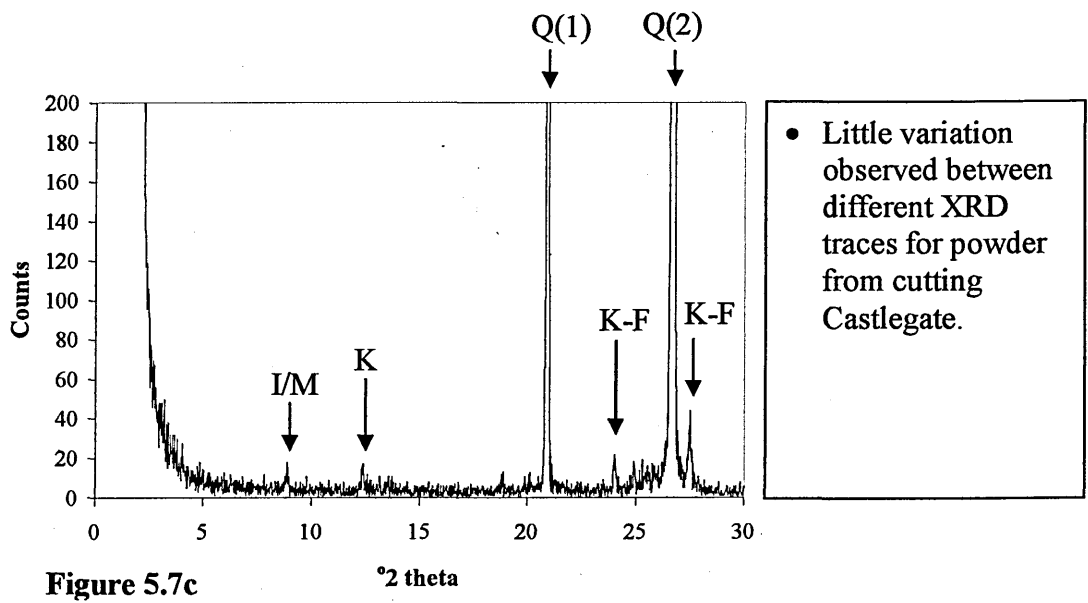


Figure 5.7c

Figure 5.7a-c: XRD traces of the powders from cutting slices 1, 3, and 6 from Castlegate. The minerals associated with the peaks identified are shown in Table 5.3.

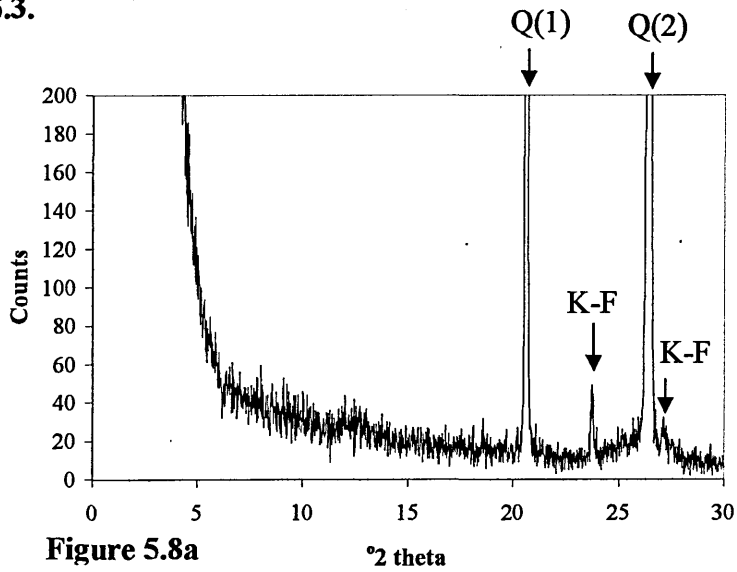


Figure 5.8a

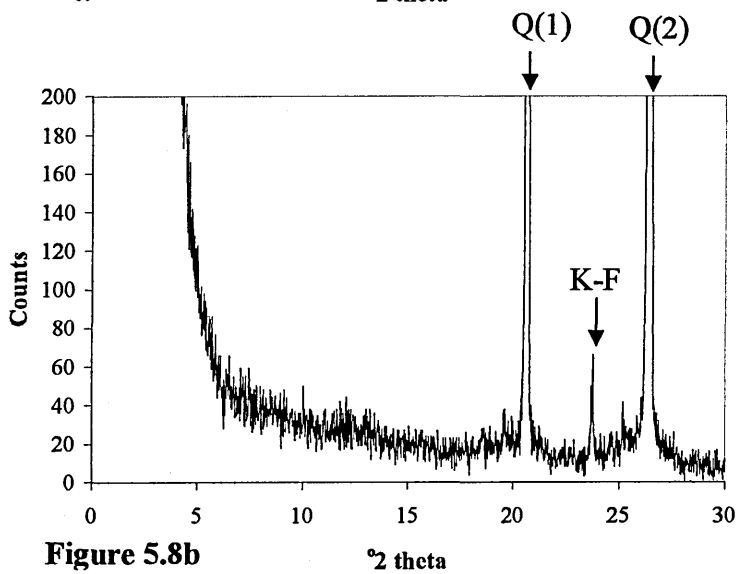


Figure 5.8b

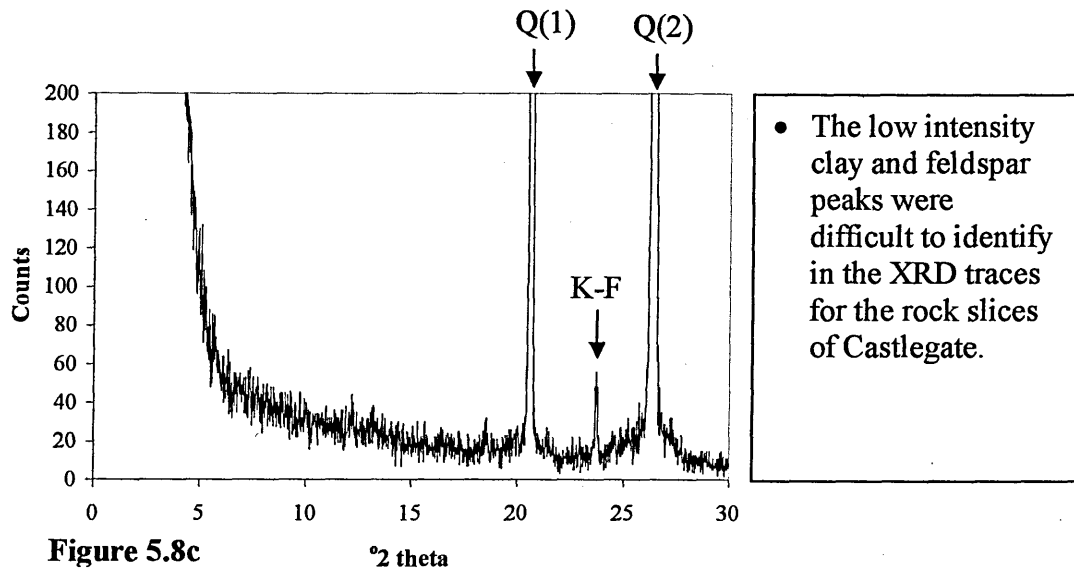
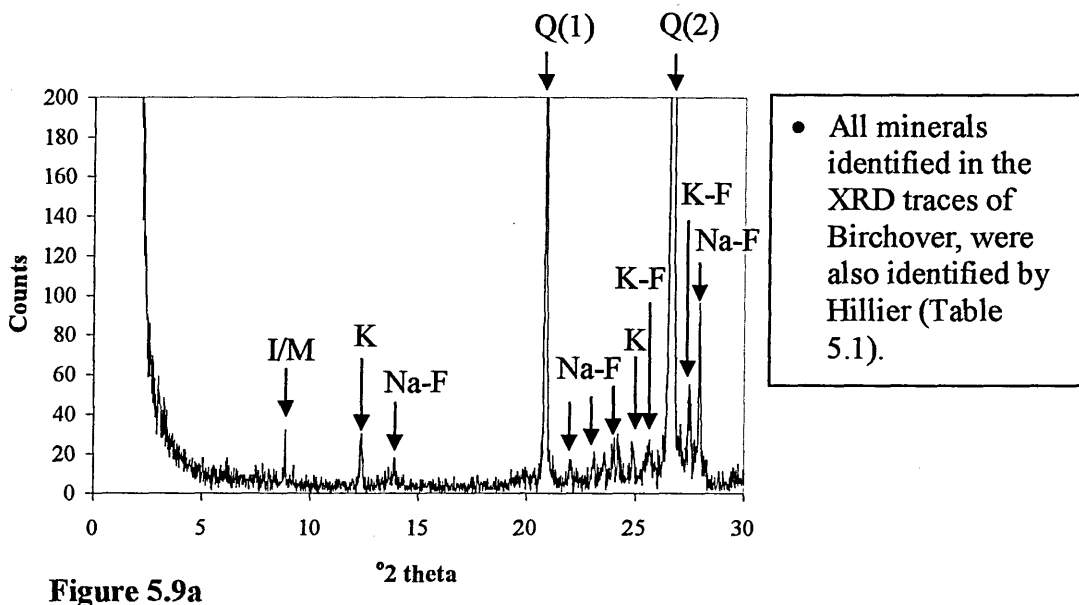


Figure 5.8a-c: XRD traces of the front faces of rock slices 1, 3, and 6 from Castlegate. The minerals associated with the peaks identified are shown in Table 5.3.

The XRD traces for the powder from cutting and for the rock slices themselves for the remaining sandstones are shown in Figures 5.9-5.18a, b, and c.



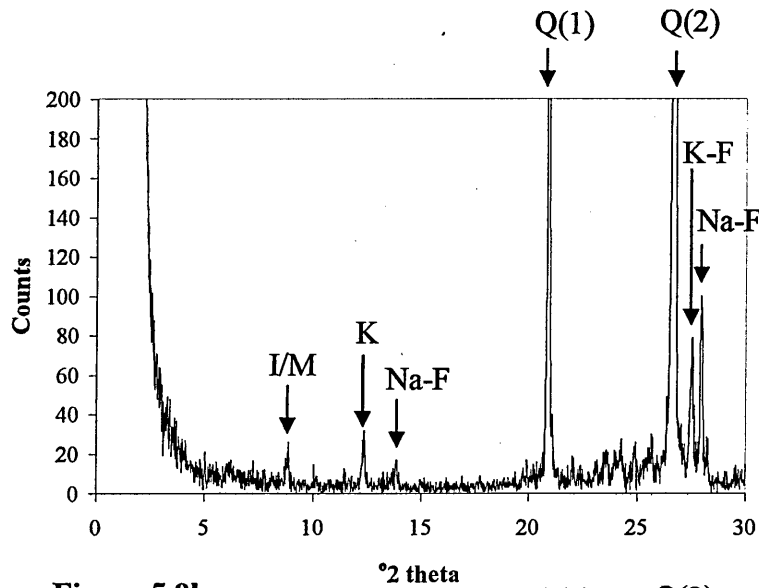


Figure 5.9b

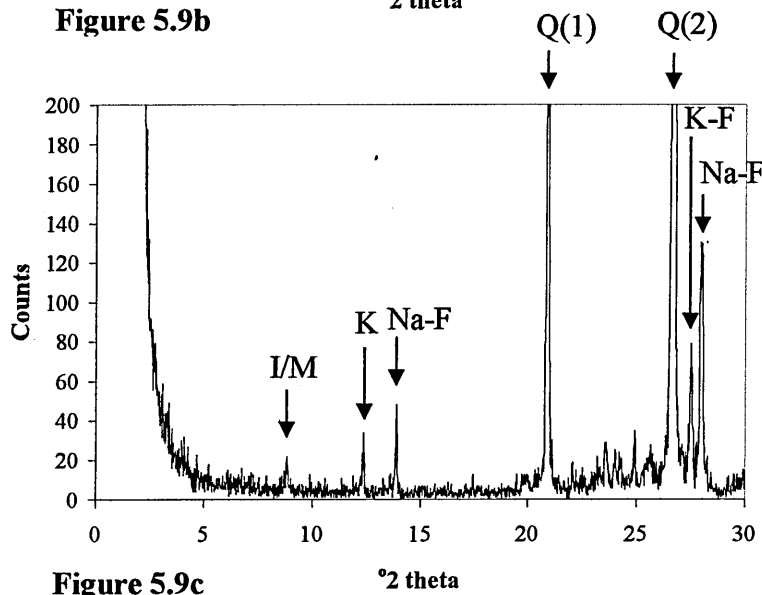


Figure 5.9c

- Generally more variation in peak intensities observed in the XRD traces of Birchover than in those of Castlegate but less variation than those of Hollington Red.

Figure 5.9a-c: XRD traces of the powder from cutting slices 1, 2, and 3 from Birchover. The minerals associated with the peaks identified are shown in Table 5.3.

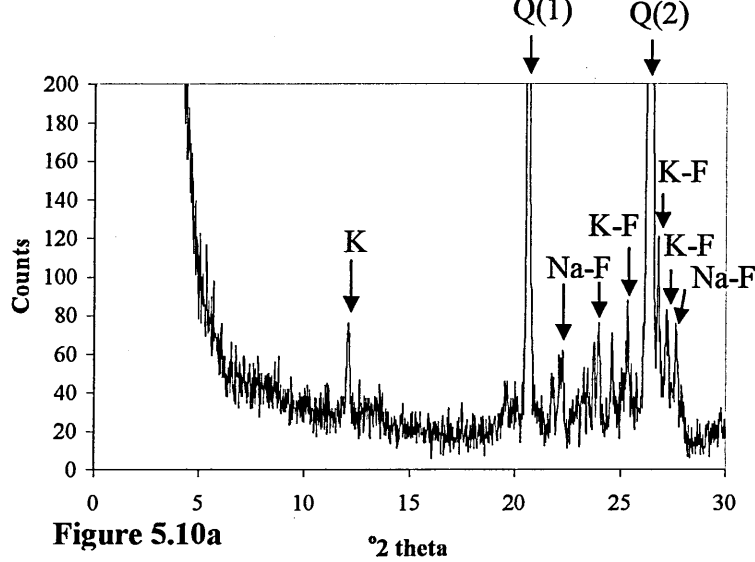


Figure 5.10a

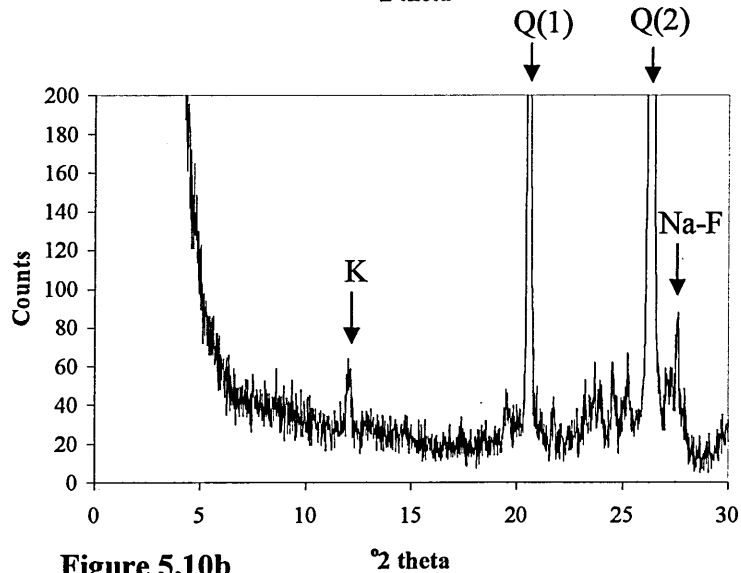


Figure 5.10b

Figure 5.10 a-b: XRD traces of the front faces of rock slices 2 and 3 from Birchover. The minerals associated with the peaks identified are shown in Table 5.3.

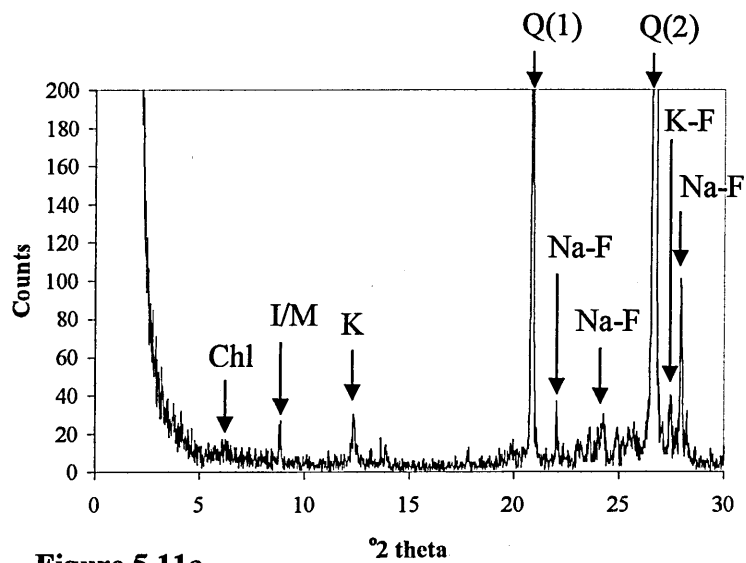


Figure 5.11a

- All minerals identified in the XRD traces of Yorkstone, were also identified by Hillier (Table 5.1).

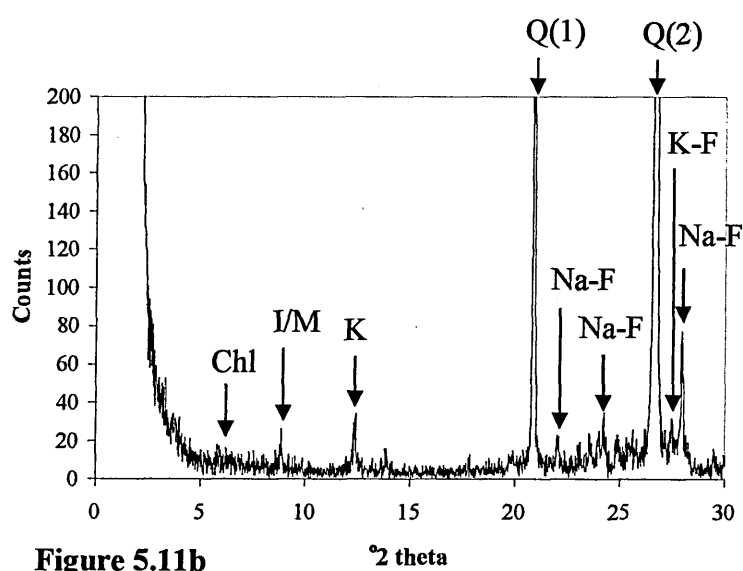


Figure 5.11b

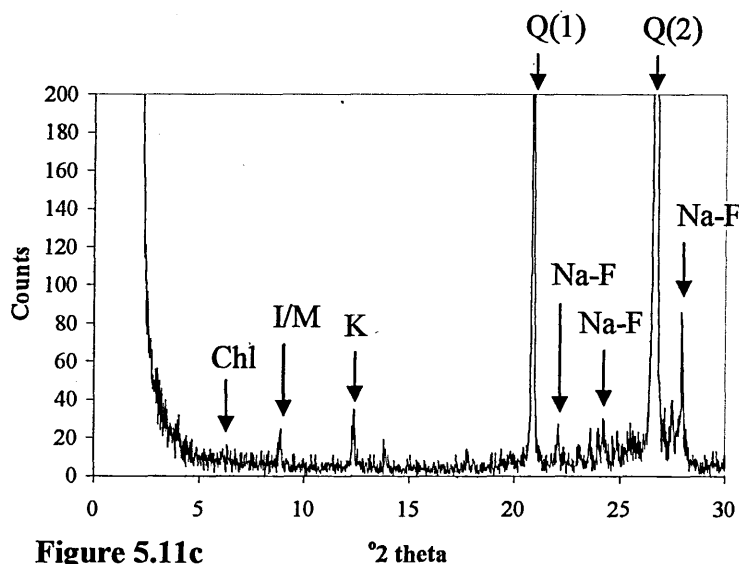


Figure 5.11c

- There was little variation in the XRD traces for powders from cutting Yorkstone.

Figure 5.11a-c: XRD traces of the powder from cutting slices 1, 4, and 8 from Yorkstone. The minerals associated with the peaks identified are shown in Table 5.3.

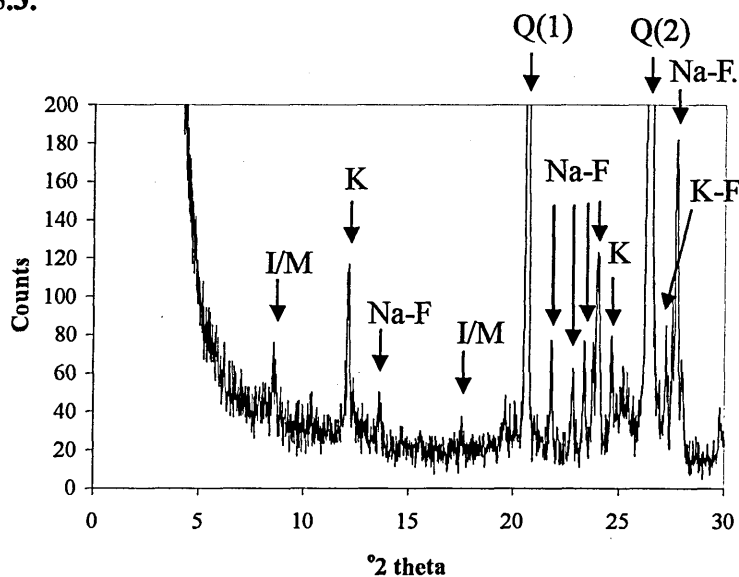


Figure 5.12a

- Unlike the XRD traces for the rock slices of Hollington Red and Birchover, in XRD traces for the rock slices of Yorkstone the illite/muscovite peak could still be observed.

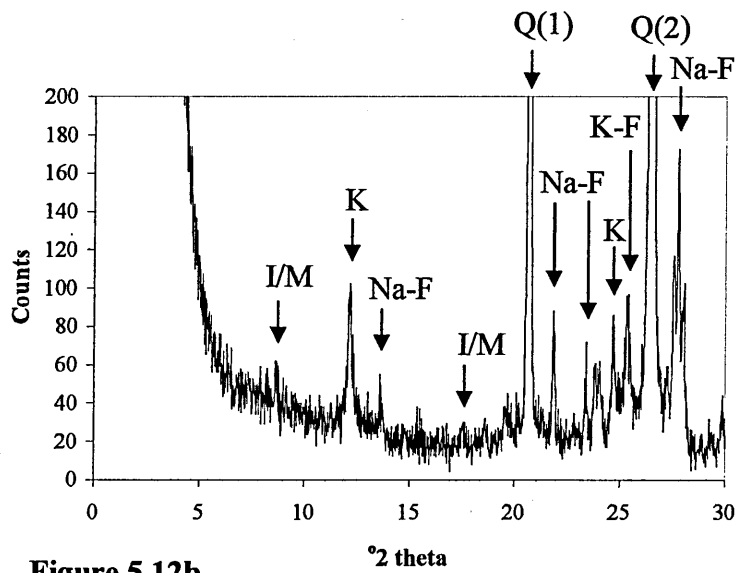


Figure 5.12b

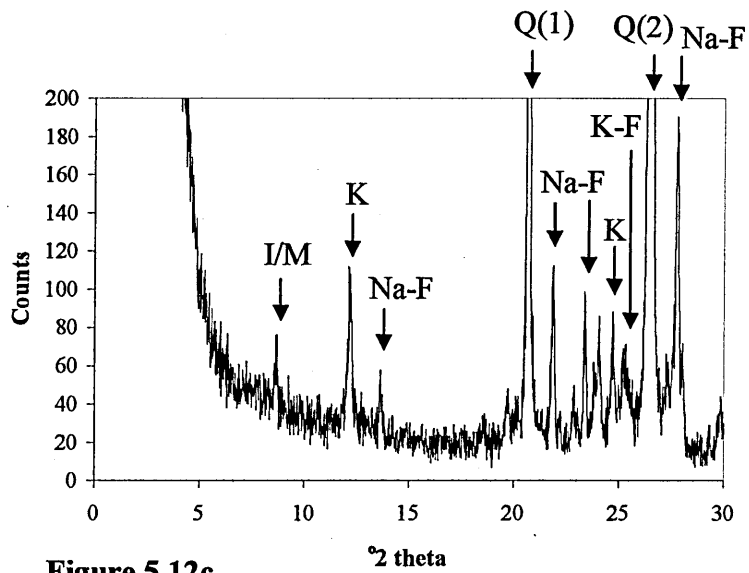
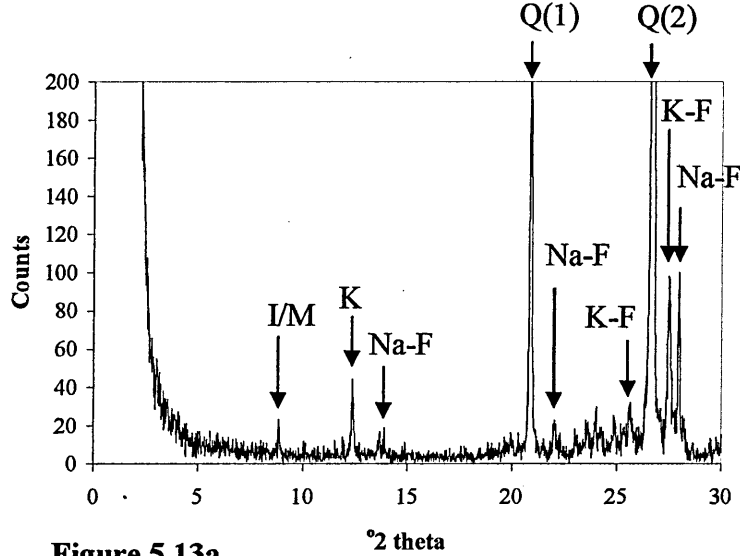


Figure 5.12c

Figure 5.12a-c: XRD traces of the front faces of rock slices 1, 4, and 8 from Yorkstone. The minerals associated with the peaks identified are shown in Table 5.3.



• All minerals identified in the XRD traces of Stancliffe, were also identified by Hillier (Table 5.1).

Figure 5.13a

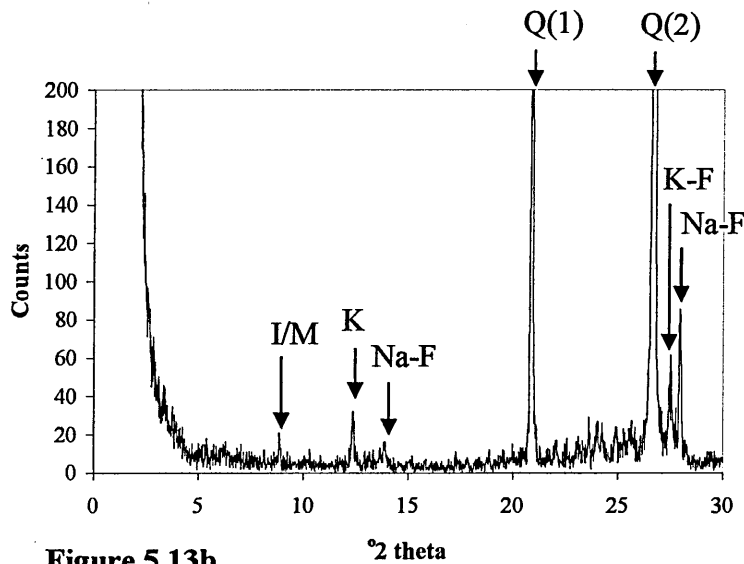
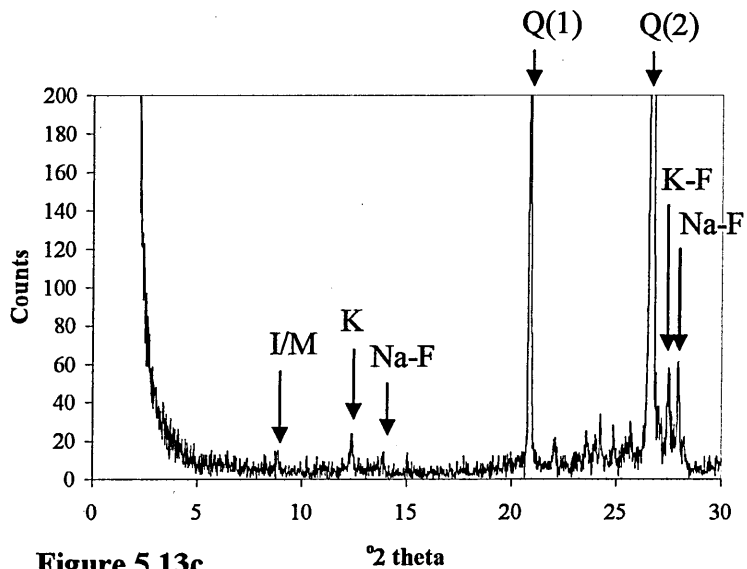


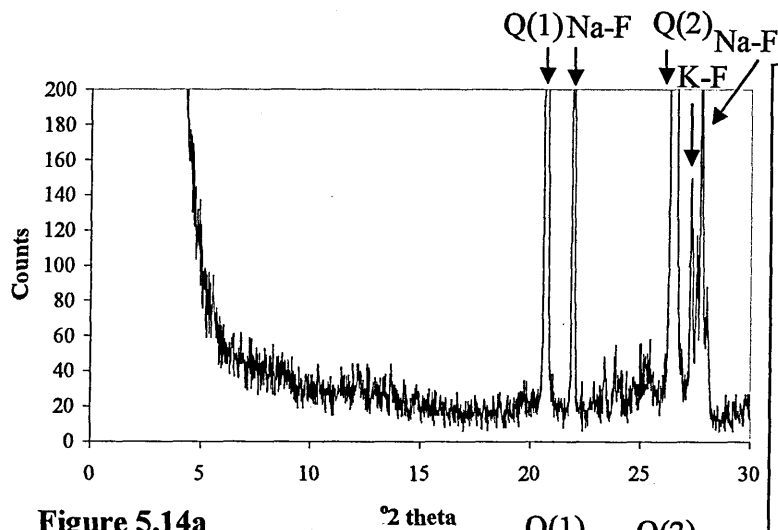
Figure 5.13b



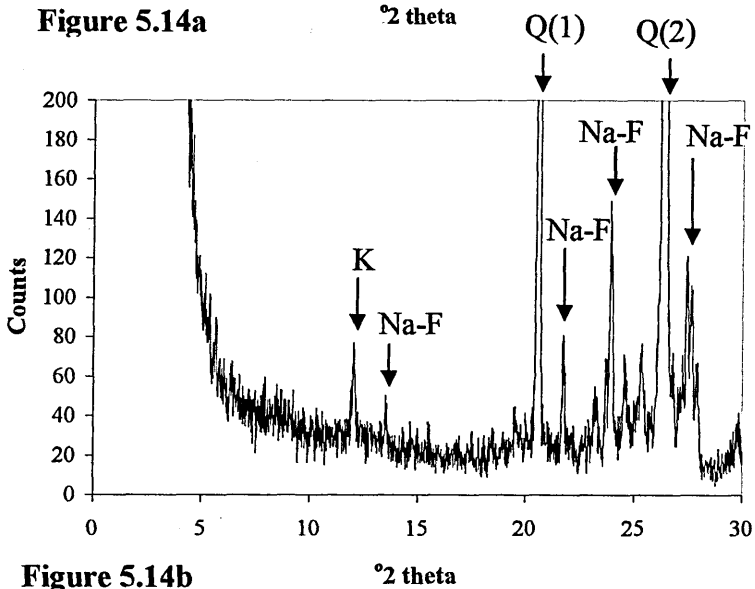
• A slight variation in intensities of the feldspar peaks was observed in the XRD traces for the powders from cutting Stancliffe.

Figure 5.13c

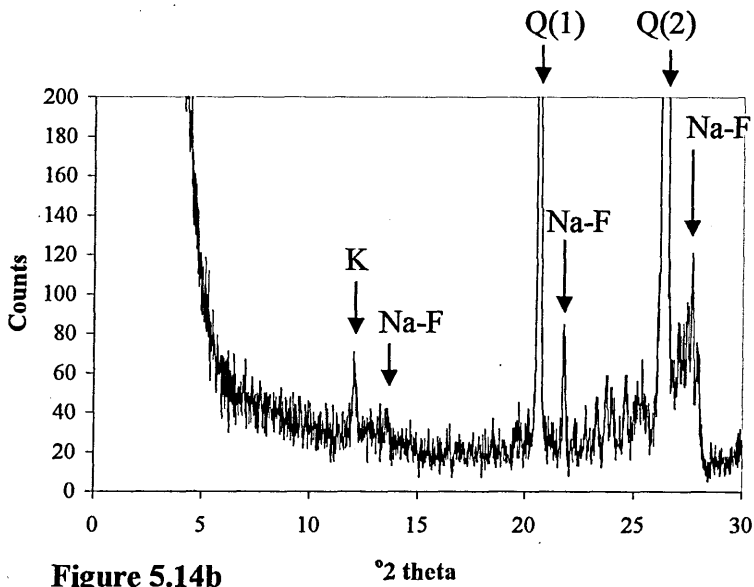
Figure 5.13a-c: XRD traces of the powders from cutting slices 1, 9, and 17 from Stancliffe. The minerals associated with the peaks identified are shown in Table 5.3.



- Very strong Na-feldspar peaks were observed in the XRD trace for rock slice 1 of Stancliffe.
- No illite/muscovite peak and no kaolinite peak observed in the XRD trace of rock slice 1.



- Na-feldspar peaks were weaker in intensity in the XRD trace of slice 9, than observed in the XRD trace of slice 1.
- No illite/muscovite peak was observed in the XRD trace of rock slice 9, however the kaolinite peak was observed.



- Na-feldspar peaks were weaker than those observed in the XRD traces of rock slices 1 and 9.
- As for slice 9, in the XRD trace for slice 17 the kaolinite peak was observed.

Figure 5.14a-c: XRD traces of the front faces of rock slices 1, 9, and 17 from Stancliffe. The minerals associated with the peaks identified are shown in Table 5.3.

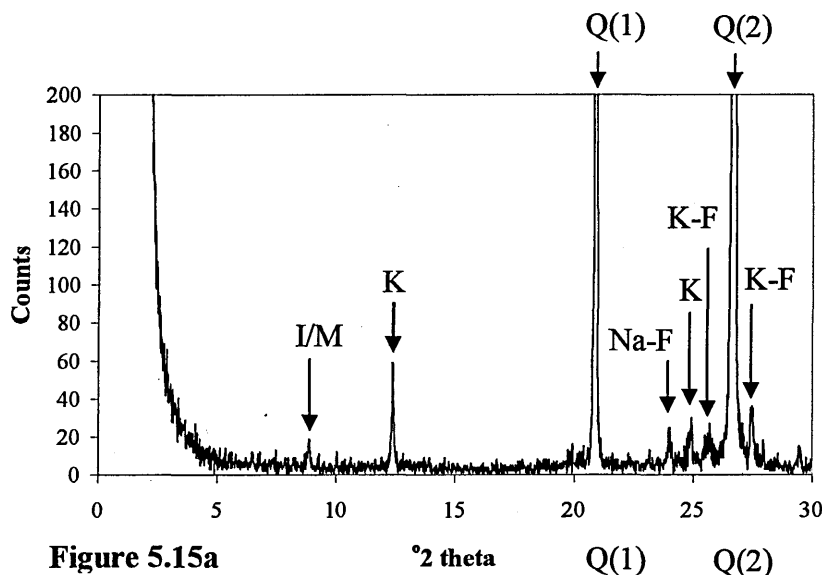


Figure 5.15a

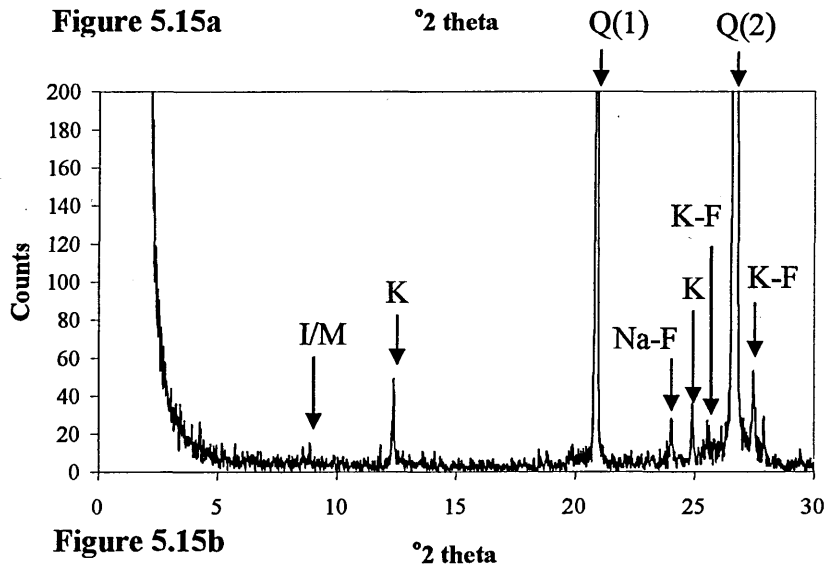


Figure 5.15b

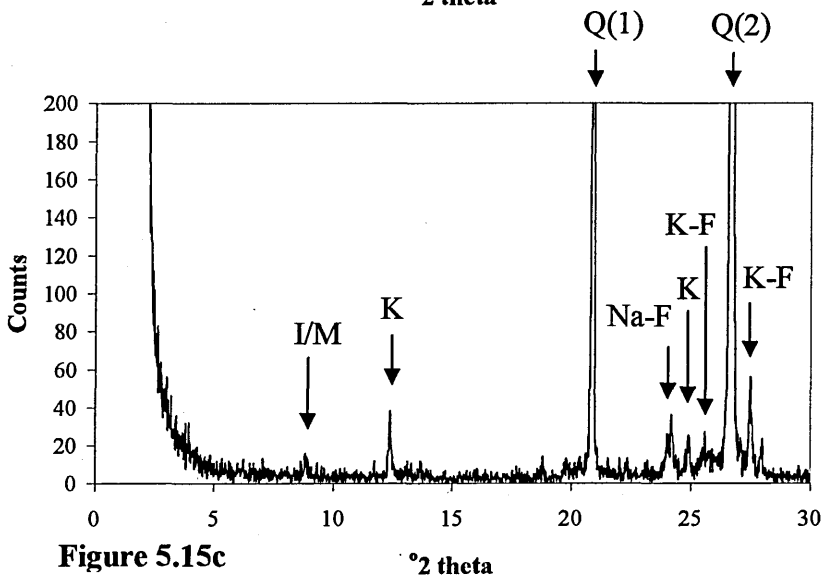
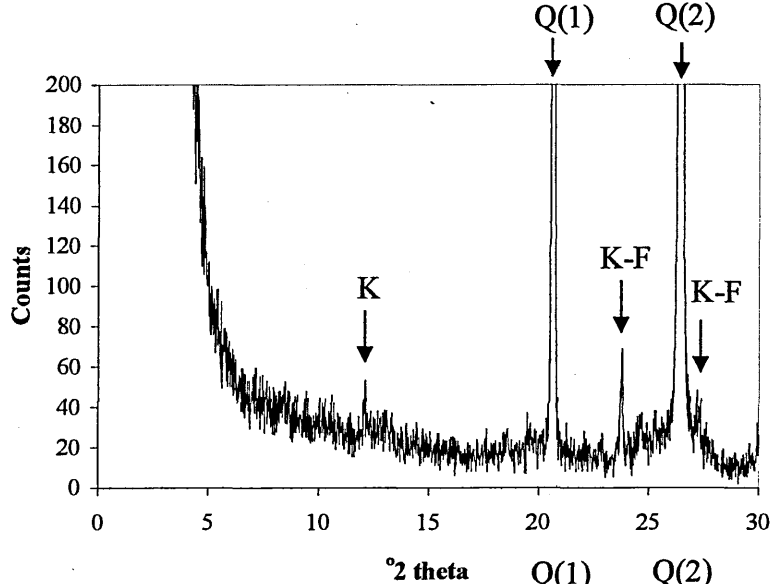


Figure 5.15c

- All minerals identified in the XRD traces of Berea, were also identified by Hillier (Table 5.1).
- Chlorite was not identified in the XRD traces, however Hillier identified presence of chlorite in Berea.

- Like Castlegate, only slight differences in the XRD traces for the powders from cutting Berea were observed.

Figure 5.15a-c: XRD traces of the powders from cutting slices 1, 2, and 4 from Berea. The minerals associated with the peaks identified are shown in Table 5.3.



- The weak illite/muscovite peak at  $8.9^\circ 2\theta$  in the XRD traces for the powders from cutting Berea were not visible in the XRD traces for the rock slices of Berea.

Figure 5.16a

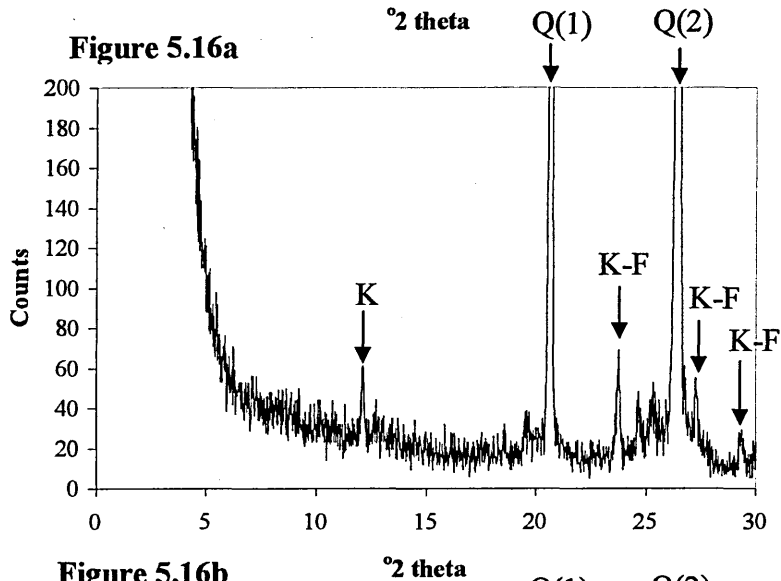


Figure 5.16b

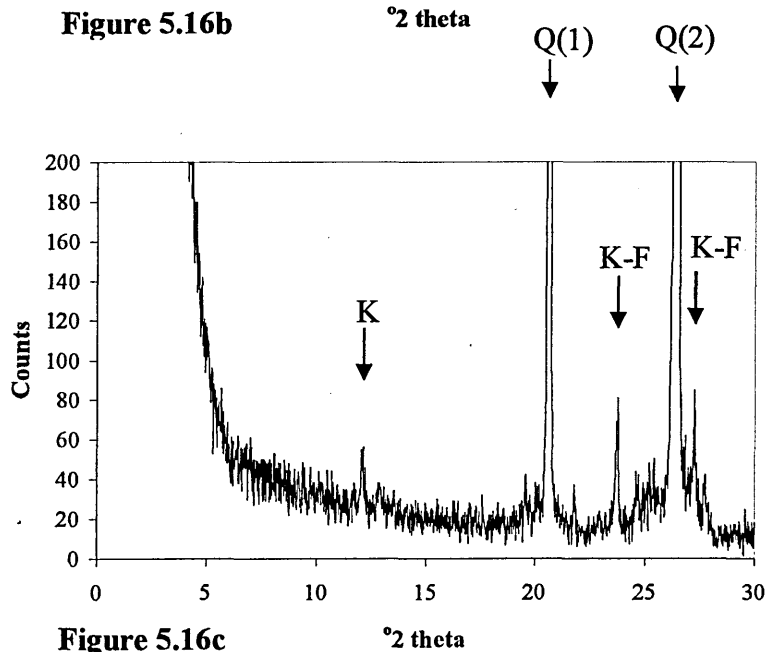
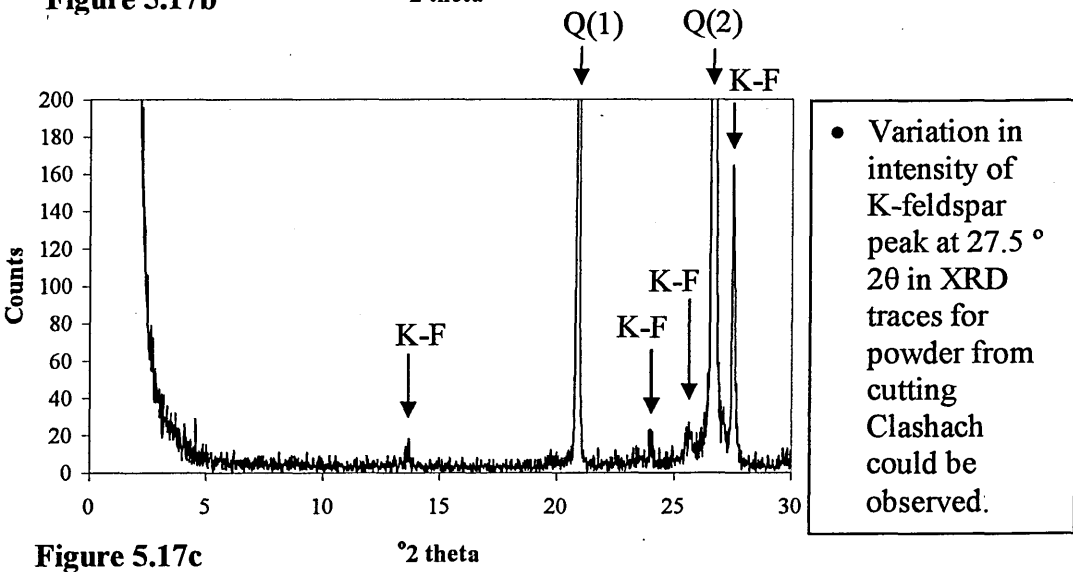
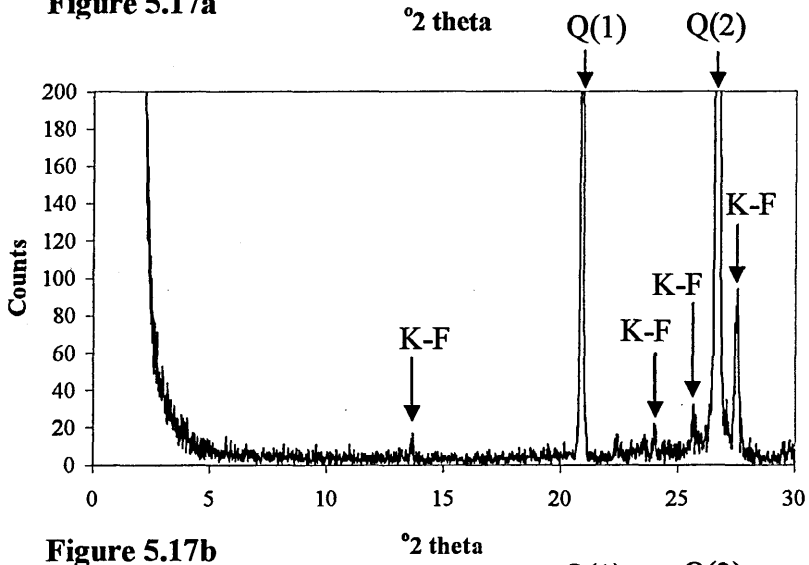
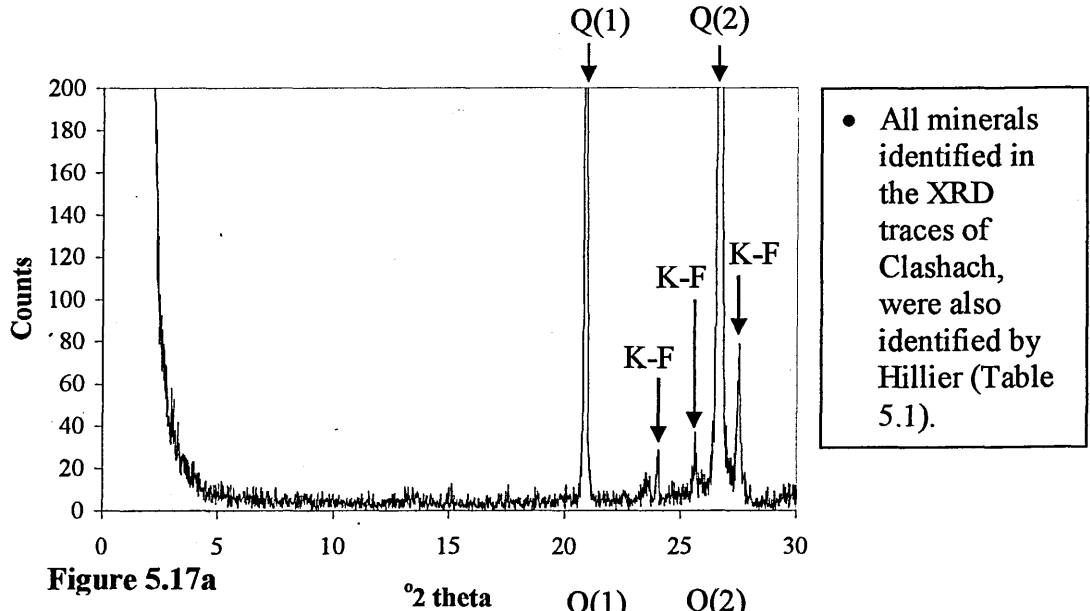


Figure 5.16c

- Only very slight differences in peak intensities observed in the XRD traces of the different rock slices of Berea.

Figure 5.16a-c: XRD traces of the front faces of rock slices 1, 2, and 4 from Berea. The minerals associated with the peaks identified are shown in Table 5.3.



**Figure 5.17a-c: XRD traces of the powders from cutting slices 1, 2, and 4 from Clashach. The minerals associated with the peaks identified are shown in Table 5.3.**

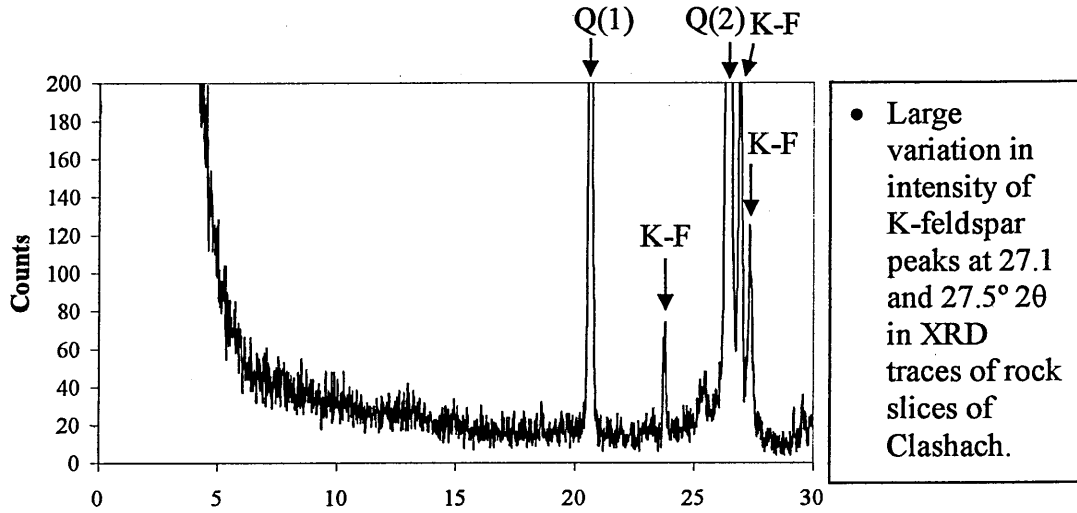


Figure 5.18a

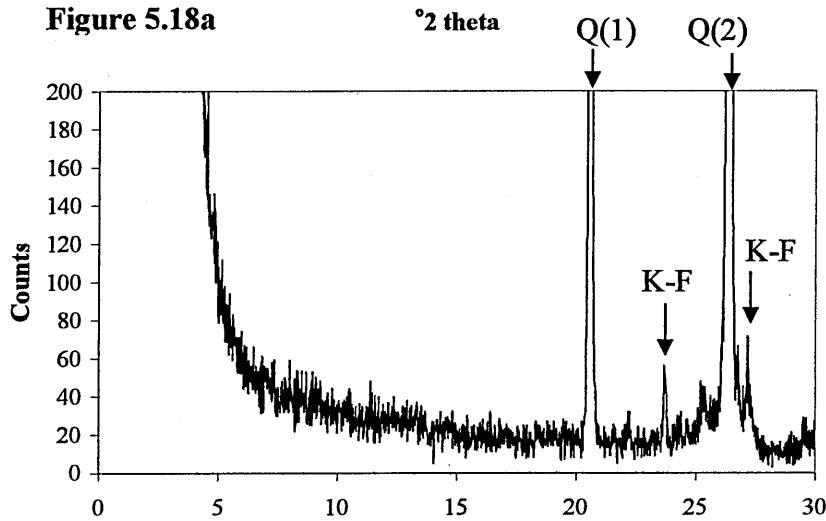


Figure 5.18b

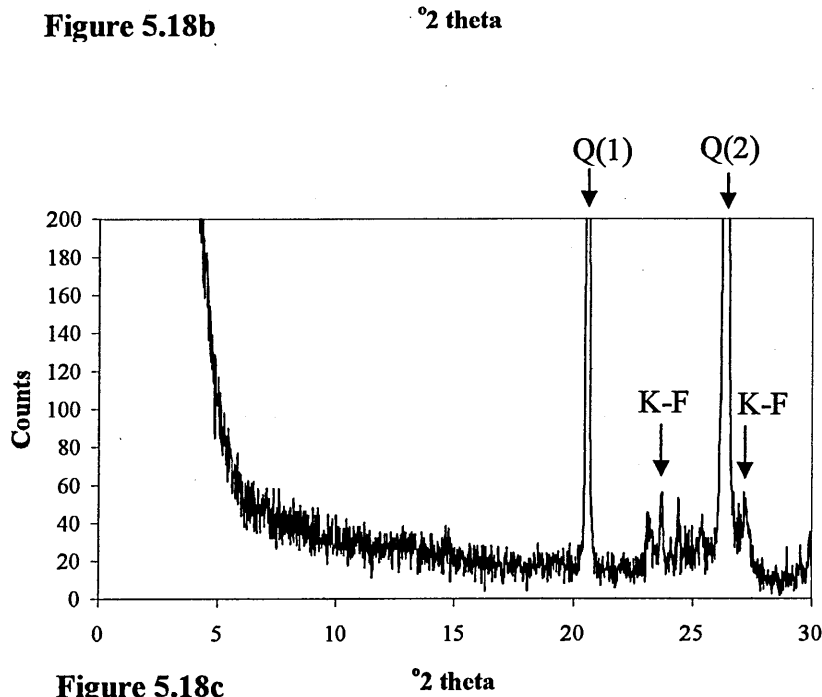
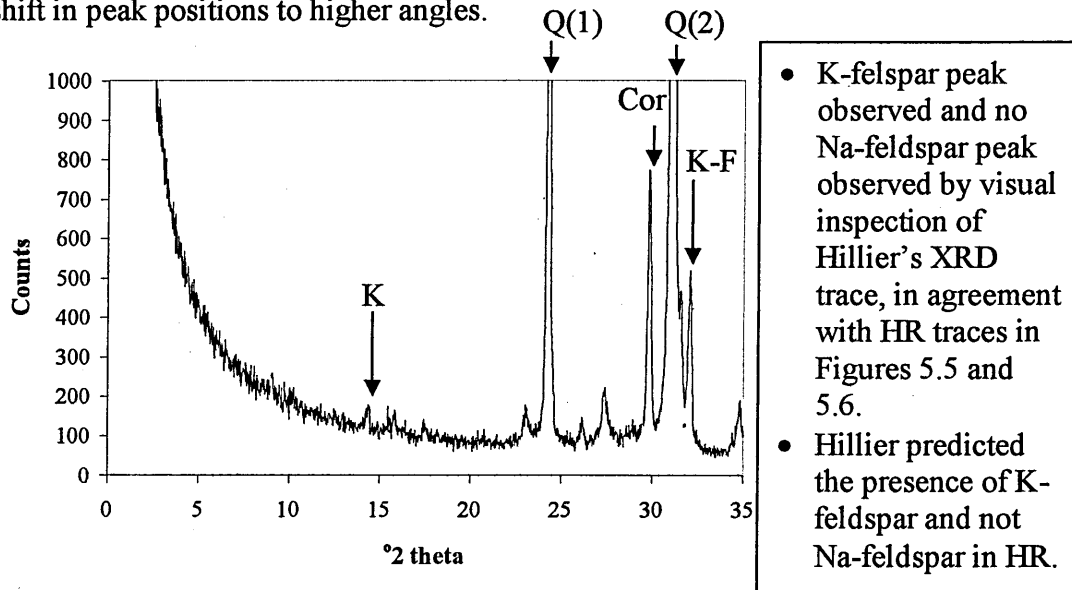


Figure 5.18c

Figure 5.18a-c: XRD traces of the front faces of rock slices 1, 2, and 4 from Clashach. The minerals associated with the peaks identified are shown in Table 5.3.

### 5.4.3.2 XRD traces collected by Hillier

For comparison, the XRD traces of the longest cores, bulk powdered Hollington Red (HR), Stancliffe (S) and Yorkstone (Y), collected by Hillier, are shown in Figures 5.19-5.21. An internal standard of 20% corundum ( $\text{Al}_2\text{O}_3$ ) was added to each sample for quantification purposes, and the peak associated with corundum, at  $29.8^\circ 2\theta$ , is indicated on the traces with "Cor". It should be noted that the traces were collected on an X-ray Diffractometer using Co radiation, rather than Cu, which accounts for the shift in peak positions to higher angles.



**Figure 5.19: XRD trace of bulk Hollington Red (HR) with 20% added corundum. The minerals associated with the peaks identified are shown in Table 5.3, and the peak associated with corundum indicated with "Cor".**

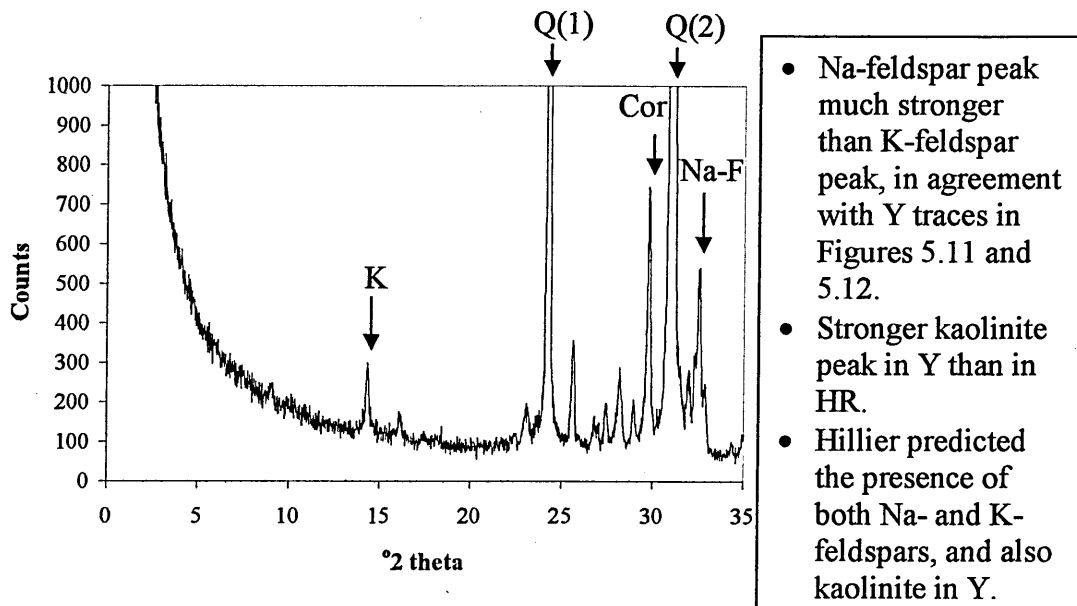
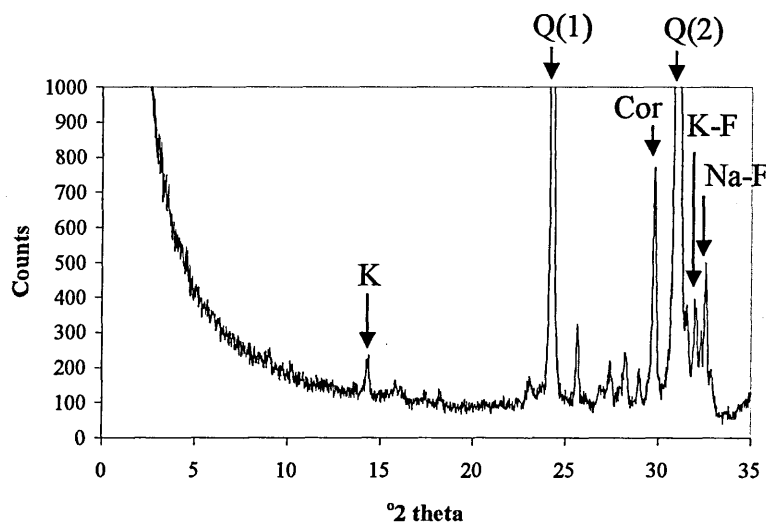


**Figure 5.20: XRD trace of bulk Yorkstone (Y) with 20% added corundum. The minerals associated with the peaks identified are shown in Table 5.3, and the peak associated with corundum indicated with "Cor".**



- Both Na- and K-feldspar peaks observed, in agreement with S traces in Figures 5.13 and 5.14.
- Stronger kaolinite traces in Figures 5.13 and 5.14.
- Hillier predicted the presence of both Na- and K-feldspars, and also kaolinite in S.

**Figure 5.21: XRD trace of bulk Stancliffe (S) with 20% added corundum. The minerals associated with the peaks identified are shown in Table 5.3, and the peak associated with corundum indicated with “Cor”.**

The relative Na- and K-feldspar peak intensities in the sandstone XRD traces collected by Hillier (Figures 5.19, 5.20, and 5.21) were in agreement with those in the XRD traces of the powders from cutting (Figures 5.7, 5.11, and 5.13).

The peak at  $14.4^\circ 2\theta$ , associated with kaolinite, could be detected by visual inspection of the XRD traces of Hollington Red (Figure 5.19), Yorkstone (Figure 5.20), and Stancliffe (Figure 5.21) collected by Hillier. However, the peak was not as well resolved as it was in the XRD traces of the powders from cutting (Figures 5.7, 5.11, and 5.13). Other clay peaks, such as for illite/muscovite, which could be detected by visual inspection of the XRD traces of the powders from cutting Hollington Red (Figure 5.7), Yorkstone (Figure 5.11), and Stancliffe (Figure 5.13), could not be clearly detected in the XRD traces collected by Hillier (Figures 5.19, 5.20, and 5.21). This was thought to be due to the preferred orientation of the clays in the powders from cutting, compared to those in Hillier’s samples. The alignment of the clays in the powders from cutting, induced by packing the sample into the holder, caused diffraction from the clays to be enhanced, and diffraction from other minerals to be diminished, as discussed in sections 5.3.3 and 5.4.3.1. Preferred orientation would lead to variation in peak intensities, which was observed in the reproducibility study in section 5.3.3, since some minerals in a mixture would be more susceptible than

others to orientation and not all minerals would orientate in the same way [70].

Hillier used a spray drying method to eliminate preferred orientation, and produced reproducible XRD traces [81]. The spray drying method is described in section 3.3.2 of chapter 3.

The quantification of minerals in the sandstones by Hillier using XRD is reported and discussed in chapter 7. Hillier used the internal standard RIR (reference intensity ratios) method to quantify the powdered samples. The percentages of components in the sandstones, predicted by Hillier, were obtained by dividing the measured peak intensities in the XRD trace of a sample, by the intensity of the peak for the standard, and multiplying by an RIR scale dependent on the amount of added standard. The peak intensities measured were integrated intensities, i.e. peak areas [70].

#### **5.4.3.3 Clay Peaks**

The intensity of the clay mineral peaks in the 4-20 ( $^{\circ} 2\theta$ ) range of the XRD traces for the powders from cutting, and for the rock slices themselves, showed variations and were studied further by investigating the intensity ratios of a kaolinite peak and an illite/muscovite peak compared with the most intense quartz peak. By studying the peak intensity ratios, differences between the slices, differences between the powder and rock samples, and between the sandstones, could be compared without the added concern of the differences in intensity values. Charts 5.1 and 5.2 show the ratio of the intensity of the kaolinite peak at  $12.4^{\circ} 2\theta$  to the quartz peak at  $26.6^{\circ} 2\theta$  and the illite/muscovite peak at  $8.9^{\circ} 2\theta$  to the quartz peak at  $26.6^{\circ} 2\theta$ , respectively.

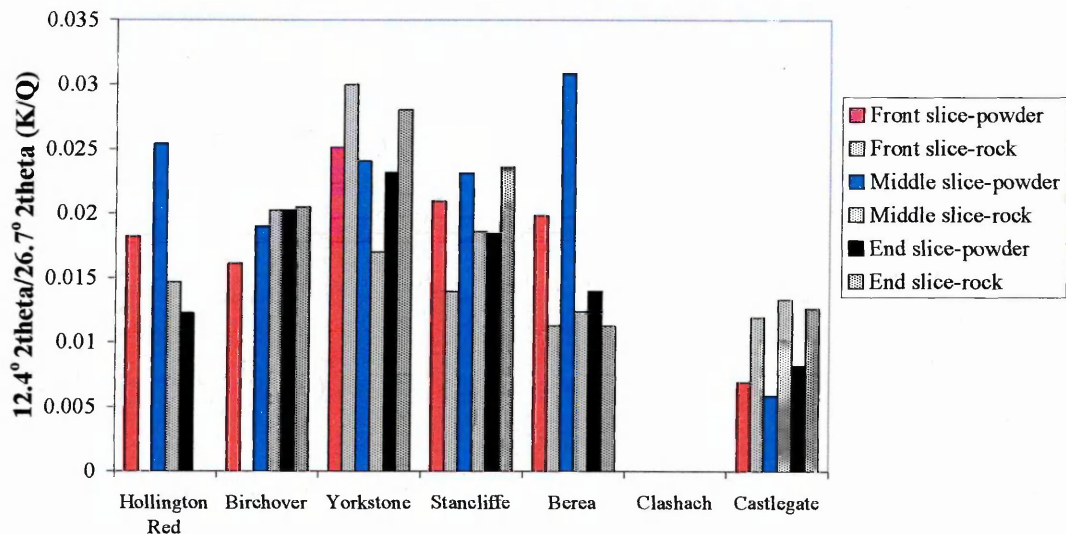


**Chart 5.1: Ratio of intensities of the kaolinite peak (at 12.4° 2θ) to quartz peak (at 26.7° 2θ) in the XRD traces of powder from cutting and rock slices at positions named for each of the named sandstones.**

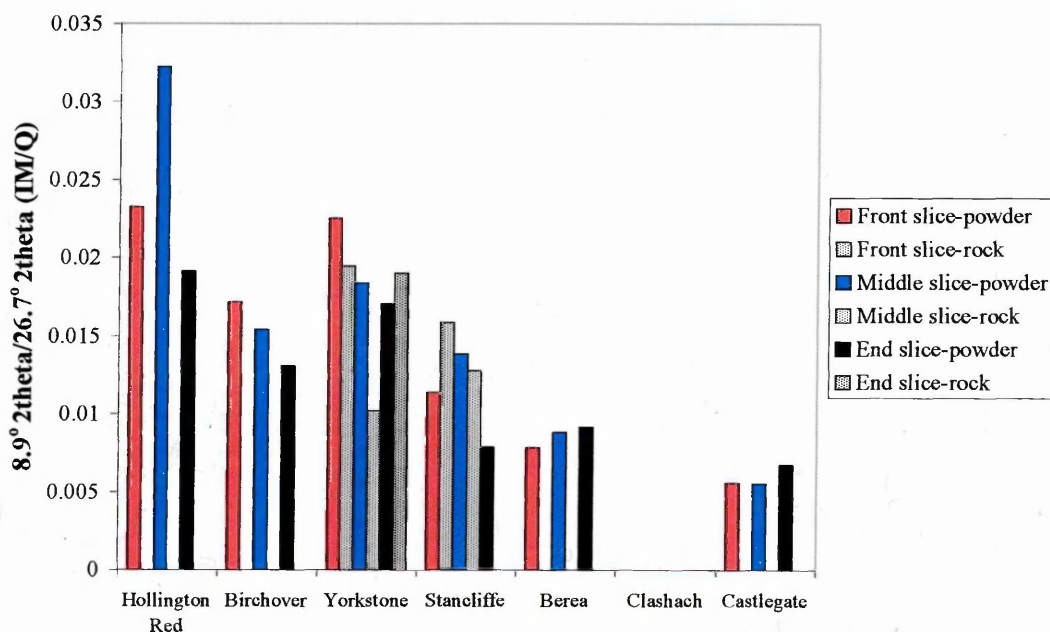


**Chart 5.2: Ratio of intensities of the illite/muscovite peak (at 8.9° 2θ) to quartz peak (at 26.7° 2θ) in the XRD traces of powder from cutting and rock slices at positions named for each of the named sandstones..**

Where no bars were shown in Charts 5.1 and 5.2, no peaks were observed, by visual detection, in the XRD traces of these powders or rock slices.

The ratios suggested differences in the clay content of each slice of sandstone. The highest amount of illite/muscovite was found in Hollington Red (particularly the middle slice), followed by Yorkstone, and then Birchover and Stancliffe containing around the same amount. The decreasing amount of clay content continued with Berea, followed by Castlegate, with no illite/muscovite peak observed in the XRD traces for Clashach.

With the exception of Hollington Red, which is a special case as already discussed in section 5.4.3.1, the intensities of the kaolinite and illite/muscovite peaks did vary with the hardness of the sandstones. The harder sandstones; Birchover, Yorkstone, and Stancliffe, generally had more intense clay peaks in their XRD traces, than the softer sandstones; Berea, Clashach, and Castlegate. Charts 5.1 and 5.2 suggested that the softer rocks (Clashach and Castlegate) were “cleaner”, i.e. contained less clay than the harder rocks.

A less intense illite/muscovite peak was generally observed in the XRD traces for the rock slices than in the XRD traces for the powders from cutting, implying that illite/muscovite may be released from the rock in the cutting process. In fact, the only sandstones whose XRD traces for the rock slices displayed the illite/muscovite peak were Yorkstone and Stancliffe. The more intense illite/muscovite peak observed in the XRD traces for the powders from cutting, however, could also be due to the preferred orientation of the clays in the powder samples enhancing the diffraction from the clays.

It should be noted that the location of clays within different rocks can vary. Clays can be present as discrete particles, or can line or bridge pores, affecting the rock porosity. Crocker *et al.* [104] investigated the clays within Berea using SEM, and found that most of the clay minerals present were located between the grains, acting as weak cement. The pores within Berea therefore had clean silica surfaces and were larger than if the clays were pore-lining.

To determine whether the cores varied in mineralogy to the same extent per unit length, XRD traces for the powders from cutting slices 1, 2, 3, and 4 of Stancliffe were collected for comparison with XRD traces of the short cores Berea, Birchover,

Castlegate and Clashach. The ratio of the intensity of the kaolinite peak at  $12.4^\circ 2\theta$  to the quartz peak at  $26.6^\circ 2\theta$  (K/Q), and the illite/muscovite peak at  $8.9^\circ 2\theta$  to the quartz peak at  $26.6^\circ 2\theta$  (IM/Q), for the powders from cutting slices 1, 2, 3, 4, 9, and 17 of Stancliffe are shown in Figure 5.22.

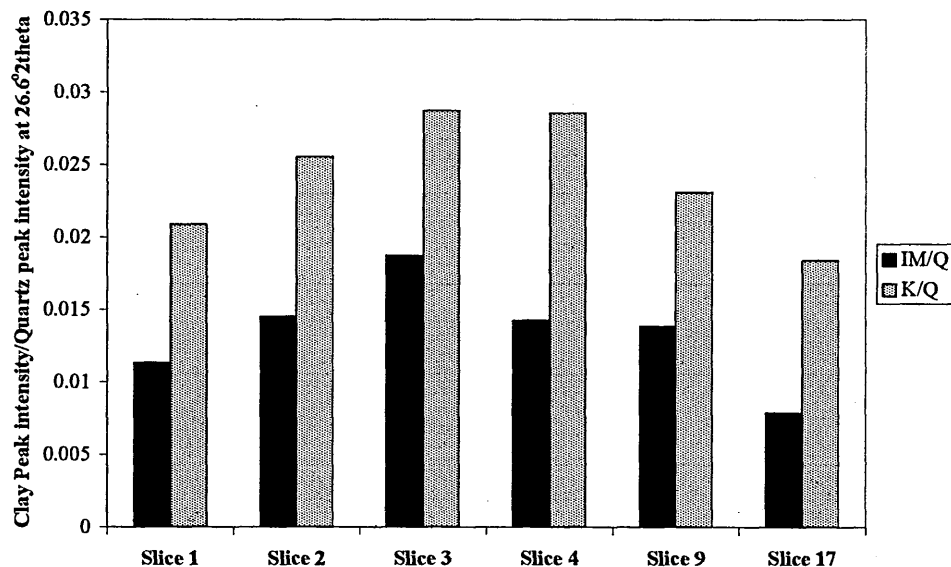


**Figure 5.23: Ratio of intensities of the illite/muscovite peak (at  $8.9^\circ 2\theta$ ) to quartz peak (at  $26.7^\circ 2\theta$ ) (IM/Q) and the kaolinite peak (at  $12.4^\circ 2\theta$ ) to quartz peak (at  $26.7^\circ 2\theta$ ) (K/Q) in the XRD traces of powders from cutting each of the named slices of Stancliffe.**

Generally, variation in the illite/muscovite peak and the kaolinite peak (with respect to the quartz peak at  $26.6^\circ 2\theta$ ) between consecutive slices was greater for Stancliffe than for the shorter cores. One exception was Berea which has a greater variation in kaolinite than Stancliffe.

## 5.5 Conclusion

The heterogeneity of sandstone rock cores was studied by visual inspection of XRD traces of sandstone slices. It was important to study the gross heterogeneity of the sandstones to improve knowledge on the length scale over which the mineralogy varies, and also to help determine a representative sample size for further studies.

The coarse survey of reproducibility revealed the feldspar peaks near  $28^\circ 2\theta$  to be the least reproducible. The mineralogical variation along each sandstone core was then

studied by visual inspection of the XRD traces of the powder produced from cutting slices and of the rock slices at three positions along each core. The most significant differences in XRD traces for the powders from cutting and for the rock slices along the different sandstone cores was observed for Hollington Red, indicating that this core contained the greatest mineralogical variation. The XRD traces for the Castlegate core, on the other hand, indicated the least amount of mineralogical variation along the length of the core.

The peak intensity ratios between clay and quartz peaks were studied and suggested varying amount of clay in each slice of sandstone. The highest amount of illite/muscovite was found in Hollington Red, followed by Yorkstone, Birchover and Stancliffe, Berea, Castlegate, and Clashach, which, with the exception of Hollington Red, follows the order of decreasing rock hardness. Less intense illite/muscovite peaks were generally observed in XRD traces for the rock slices than in XRD traces for powders collected from cutting, implying that clay may be released from the emerging rock surface in the cutting process, though this could only be confirmed by further quantitative studies.

Ideally, to study the mineralogy of a sandstone core, a large proportion of the core should be ground and mixed to ensure homogeneity. A small sample could then be taken from the bulk, for analysis. This would reduce the errors in identifying minerals present in the sandstones, caused by localised heterogeneity of the sandstone cores.

## 6. Results - Sandstone Absolute PLS Model

### 6.1 Introduction

While the XRD traces and DRIFTS spectra of sandstone rocks could be investigated visually to provide qualitative information with regards their mineral content, the ability of PLS to provide quantitative predictions of mineral concentrations within a sample has been proven in a previous study with the three component system (kaolinite, smectite, and calcite), discussed in chapter 4. The three component PLS model was useful for determining low concentrations of smectite in synthetic mixtures. However, an extended model was required to quantify minerals in real rock samples.

Previous work by Clegg [21] resulted in the development of a seven mineral component PLS model to quantify minerals in sandstone rocks. The seven components included in this model were quartz, montmorillonite, kaolinite, illite, dolomite, Na-feldspar, and chlorite. The PLS model created in this study extended the previous seven component model in order to incorporate two different carbonates, two different feldspars and also the addition of hematite and muscovite. This has generated a more complete model, with mineral content more similar to that of a real sandstone rock. The eleven mineral components used to create the PLS model were quartz, montmorillonite, kaolinite, illite, calcite, dolomite, Na-feldspar, K-feldspar, hematite, chlorite, and muscovite. Synthetic mixtures of these minerals were prepared to form a training set comprising of calibration standards (used to prepare the model) and independent standards (used to test the model). The absolute PLS model generated was optimised for each component after considering the wavenumber region, the pre-processing and the number of factors to be used. The precision and accuracy of the model for prediction of compositions of synthetically prepared independent standards was discussed in this chapter before use of the model to predict the mineral content of real rock samples is investigated in chapter 7.

## 6.2 Experimental

### 6.2.1 Equipment

Each standard contained varying, known concentrations of each mineral component, and 3 g of each were weighed out prior to ball milling. To ball mill the standards and the KBr diluent, a Retsch MM2 grinder was used, with two tungsten carbide grinding pots and two tungsten carbide grinding balls. For each standard and for KBr, batches of 3 g were ground for 5 minutes at 45 Hz. A Nicolet NEXUS FTIR Spectrometer (manufactured by Thermo Electron Corporation Ltd.), equipped with a mercury cadmium telluride (MCT) detector, and fitted with a Graseby-Specac Selector DRIFTS accessory (manufactured by Specac Ltd.), was used to collect spectra of all the standards.

### 6.2.2 Spectral Collection

The instrumental parameters for the Nicolet NEXUS FTIR Spectrometer were as follows:

Number of scans = 64

Resolution =  $4 \text{ cm}^{-1}$

Gain = 1

Velocity =  $1.8988 \text{ cm s}^{-1}$

Data spacing =  $1.928 \text{ cm}^{-1}$

The accessory was adjusted, as before, to maximise the throughput radiation to reach the detector, prior to spectral data collection. The number of scans and velocity used were chosen in order to obtain spectra within a few minutes with a high signal-to-noise ratio. The high quality and highly reproducible spectra obtained by the Nicolet NEXUS FTIR Spectrometer used, meant that collecting 64 scans was sufficient. In the same way as described in chapter 4, the chamber, containing the sample cup, was purged with dry,  $\text{CO}_2$  free air for 1 minute before spectral collection, and then the chamber was purged continuously during data collection. OMNIC software was used to collect spectra and each sample spectrum was ratioed against a pre-recorded KBr background automatically using the OMNIC software. Grams32-PLS-PLUS IQ

software was used to pre-process the spectra during creation of the PLS model. The PLS model was then used to quantify the components in the standards.

### 6.3 Training Set Components

#### 6.3.1 Components Structural Formula and Source

Standards in the training set were composed of eleven mineral components, in varying concentrations, that represent the mineral composition of a real sandstone rock. The eleven components, their structural formula, and source are listed in Table 6.1.

Component	Typical Structural Formula	Source
Quartz (Chelford sand)	$\text{SiO}_2$	Macclesfield, Cheshire (operated by Hepworth Minerals and Chemicals Ltd.).
Montmorillonite (SWy-2)	$[(\text{Al}, \text{Mg}, \text{Fe})_2(\text{OH})_2\text{Si}_4\text{O}_{10}(\text{Ca}, \text{Mg}, \text{Na}, \text{K})]_n\text{H}_2\text{O}$	Clay Minerals Repository
Kaolinite (KGa-2)	$\text{Al}_4\text{Si}_4\text{O}_{10}(\text{OH})_8$	Clay Minerals Repository
Illite (Silver Hills illite, 1 Mt illite)	$\text{Al}_4\text{Si}_4\text{O}_{10}(\text{OH})_2.\text{K}, \text{Al}$	Clay Minerals Repository
Calcite	$\text{CaCO}_3$	Aldrich (99.95-100%)
Dolomite	$\text{CaMg}(\text{CO}_3)_2$	British Chemical Standard No. 368
Na-Feldspar	$\text{NaAlSi}_3\text{O}_8$	British Chemical Standard No. 375
K-Feldspar	$\text{KAlSi}_3\text{O}_8$	British Chemical Standard No. 376
Hematite	$\text{Fe}_2\text{O}_3$	Aldrich (99.999%)
Chlorite (CCa-1 Ripidolite)	$(\text{Mg}, \text{Fe}, \text{Al})_6(\text{Al}, \text{Si})_4\text{O}_{10}(\text{OH})_8$	Clay Minerals Repository
Mica (Muscovite)	$\text{KAl}_2(\text{AlSi}_3\text{O}_{10})(\text{F}, \text{OH})_2$	Mandoval (UK) Ltd.

**Table 6.1: The components used in the training set, their structural formula and source.**

Although synthetic quartz is available and would be of high purity, it was thought that Chelford sand should be used since it more closely resembles the quartz found in sandstone rocks. Other samples representative of quartz, obtained from Hepworth Minerals and Chemicals Ltd., were analysed by Clegg [21]. Clegg [21] found Chelford sand to be the most pure quartz sample.

It should be noted that all the minerals included in the training set were used as obtained, without any purification. The purity of some of the clay components of the training set is discussed in section 7.7.2.3 in chapter 7.

### 6.3.2 DRIFTS Spectra of the Pure Components used in the Training Set

The main characteristic bands in the DRIFTS spectra of the pure components used in the training set are shown in Table 6.2.

Mineral	Main Characteristic Bands
Quartz	Bands in the overtone/combination region (2000-1400 $\text{cm}^{-1}$ ). Bands at 1107, and 1057 $\text{cm}^{-1}$ (antisymmetric Si-O-Si stretching). Bands at 800, and 781 $\text{cm}^{-1}$ (symmetric Si-O-Si stretching). Band at 695 $\text{cm}^{-1}$ (O-Si-O bending).
Montmorillonite (SWy-2)	Bands at 3620 and 1628 $\text{cm}^{-1}$ (OH stretching and bending respectively). Bands at 921, 885, and 856 $\text{cm}^{-1}$ (AlAlOH, AlFeOH, and AlMgOH deformation, respectively). Bands at 1045, 800, and 781 $\text{cm}^{-1}$ (Si-O-Si stretching).
Kaolinite	Bands at 3695, 3669, 3650, and 3620 $\text{cm}^{-1}$ (OH stretching). Bands at 934, and 915 $\text{cm}^{-1}$ (AlAlOH deformation of surface and inner OH, respectively). Bands at 1112, 1029, 1013, 793, and 754 $\text{cm}^{-1}$ (Si-O-Si stretching). Band at 696 $\text{cm}^{-1}$ (O-Si-O bending).
Illite	Band at 3620 $\text{cm}^{-1}$ (OH stretching). Band at 915 $\text{cm}^{-1}$ (AlAlOH deformation). Bands at 1022, 800, 781, and 754 $\text{cm}^{-1}$ (Si-O-Si stretching).

Calcite	Doublet at 1436 and 1398 $\text{cm}^{-1}$ (asymmetric stretch of carbonate ion). Sharp bands at 875 and 712 $\text{cm}^{-1}$ (out-of-plane bend and in-plane bend of carbonate ion, respectively).
Dolomite	Band at 1469 $\text{cm}^{-1}$ (asymmetric stretch of carbonate ion). Sharp bands at 884 and 730 $\text{cm}^{-1}$ (out-of-plane bend and in-plane bend of carbonate ion, respectively).
Na-Feldspar	Bands at 1148, 1100, 1039, 1021, 788, 762, 746 and 725 $\text{cm}^{-1}$ (Si-O-Si stretching).
K-Feldspar	Bands at 1052, 1137, 1021, 774 and 730 $\text{cm}^{-1}$ (Si-O-Si stretching).
Hematite	Difficult to identify. Bands at 1540, 1384, and 1206 $\text{cm}^{-1}$ .
Chlorite	Bands at 3556 and 3415 $\text{cm}^{-1}$ (OH stretching). Bands at 970, and 754 $\text{cm}^{-1}$ (Si-O-Si stretching).
Muscovite	Band at 3620 $\text{cm}^{-1}$ (OH stretching). Bands at 925, and 885 $\text{cm}^{-1}$ (AlAlOH, and AlFeOH deformation, respectively). Band at 749 $\text{cm}^{-1}$ (Al-O-Si stretching). Bands at 1060 and 1006 $\text{cm}^{-1}$ (Si-O-Si stretching).

**Table 6.2: Characteristic infrared bands for the pure mineral components to be used in the PLS training set.**

DRIFTS spectra of Chelford sand (quartz) ground by hand in a mortar and pestle, and ball milled are shown in Figure 6.1.

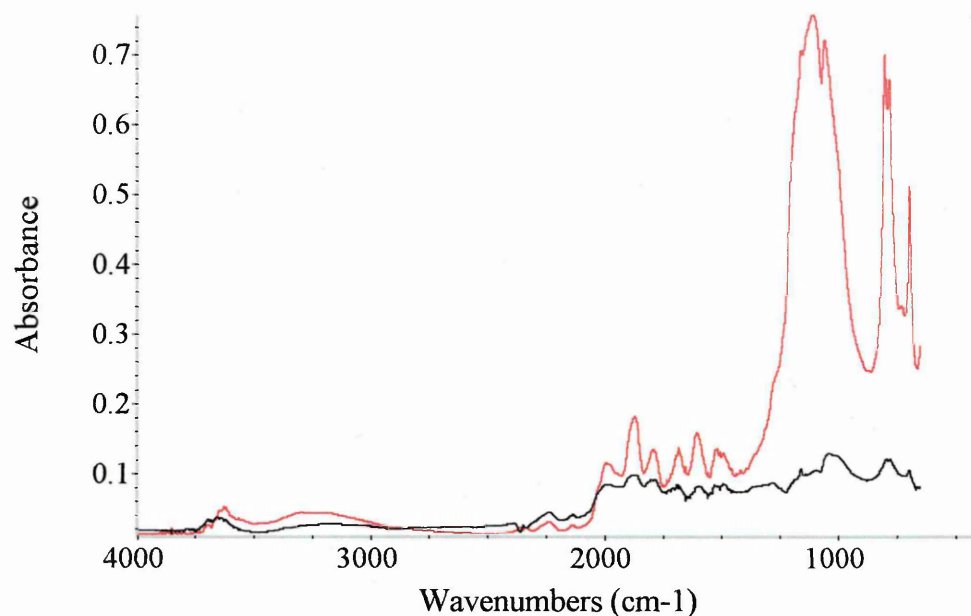


**Figure 6.1: DRIFTS spectra of Chelford sand ground (black) and ball milled (red).**

The band intensities and shape were greatly affected by the particle size of the sample. The spectrum of ground Chelford sand had less well defined bands of much lower intensity than the spectrum of ball milled Chelford sand in the region below  $2000\text{ cm}^{-1}$ . There also appeared to be a shift in the band in the  $3700\text{-}3600\text{ cm}^{-1}$  OH stretching region of the spectrum of ground Chelford sand. The training set standards were ball milled for 5 minutes prior to spectral collection, ensuring spectra with well defined intense bands. The effect of different ball milling times was not investigated in this study since 5 minutes of ball milling was found to be adequate. A ball milling time of 5 minutes was sufficient to produce powders with particle sizes small enough to obtain DRIFTS spectra with strong well defined bands, and yet leave the structure of the clay minerals undamaged.

The DRIFTS spectra of the clay components of the training set are shown in Figure 6.2.

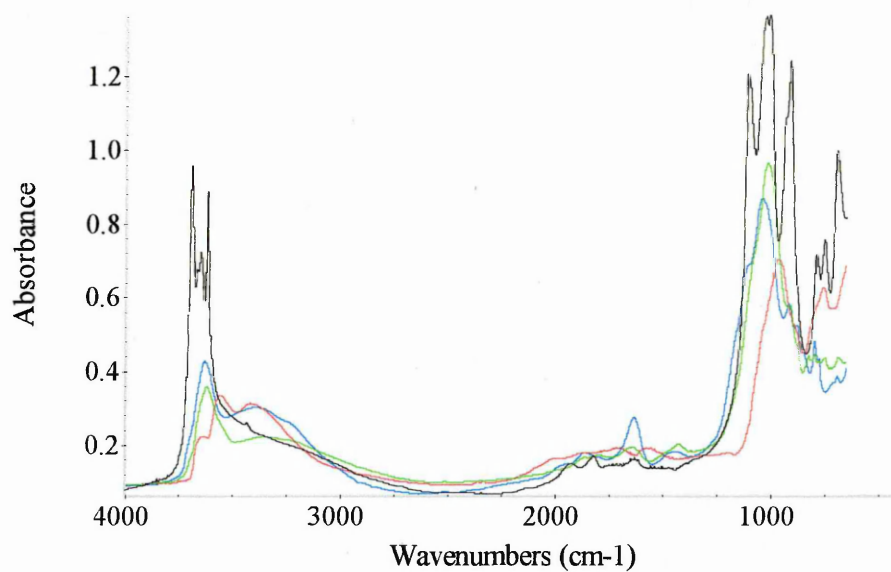


**Figure 6.2: DRIFTS spectra of SWy-2 (blue), KGa-2 (black), illite (green), and chlorite (red).**

The spectra of clays showed strong, well resolved bands and differences between the spectra of the clays in the 3700-3400  $\text{cm}^{-1}$  OH stretching region and in the 1200-700  $\text{cm}^{-1}$  Si-O stretching and OH deformation region meant they were easily distinguishable. PLS should, therefore, be quite capable of predicting concentrations of each clay, in a mixture.

The DRIFTS spectra of the carbonate components, calcite and dolomite are shown in Figure 6.3.

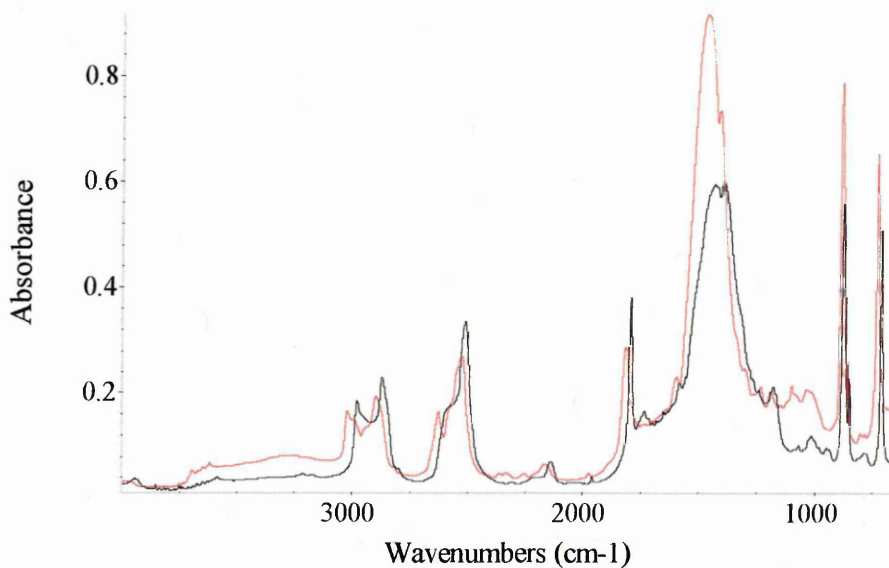


**Figure 6.3: DRIFTS spectra of calcite (black) and dolomite (red).**

The spectra of calcite and dolomite, though similar, were easily distinguishable due to an offset in band positions, so again PLS should be able to differentiate between the two and predict the concentration of each in a mixture.

The DRIFTS spectra of Na-feldspar and K-feldspar are shown in Figure 6.4.

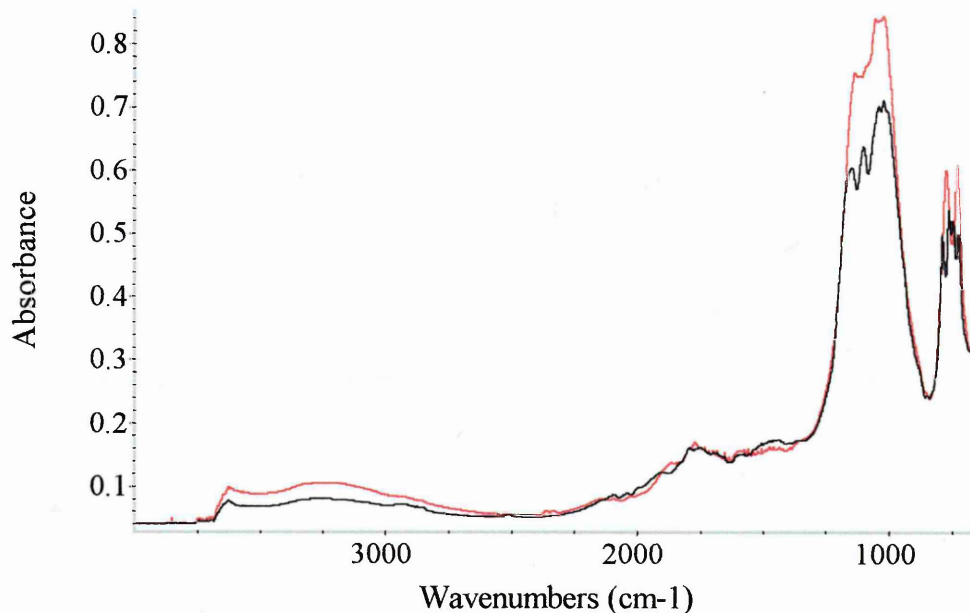


**Figure 6.4: DRIFTS spectra of Na-feldspar (black) and K-feldspar (red).**

Although in the high wavenumber region ( $>2500\text{ cm}^{-1}$ ) Na- and K-feldspar could not be distinguished, the Si-O stretching region of each was quite different. Bands in the  $800\text{-}700\text{ cm}^{-1}$ , Si-O stretching, region were particularly different, with the spectrum of K-feldspar displaying only two bands at  $774$  and  $730\text{ cm}^{-1}$  while the spectrum of Na-feldspar displayed four bands at  $788$ ,  $762$ ,  $746$  and  $725\text{ cm}^{-1}$ . Difficulty in distinguishing visually between the two feldspars in a mixture may occur if one is present at a much greater concentration than the other as the bands would overlap. PLS, however, was designed to deal with mixtures of components and spectra with overlapping bands, so it should be possible to predict the concentration of each feldspar separately.

The DRIFTS spectra of the remaining components, mica (muscovite) and hematite (iron(III) oxide) are shown in Figure 6.5.

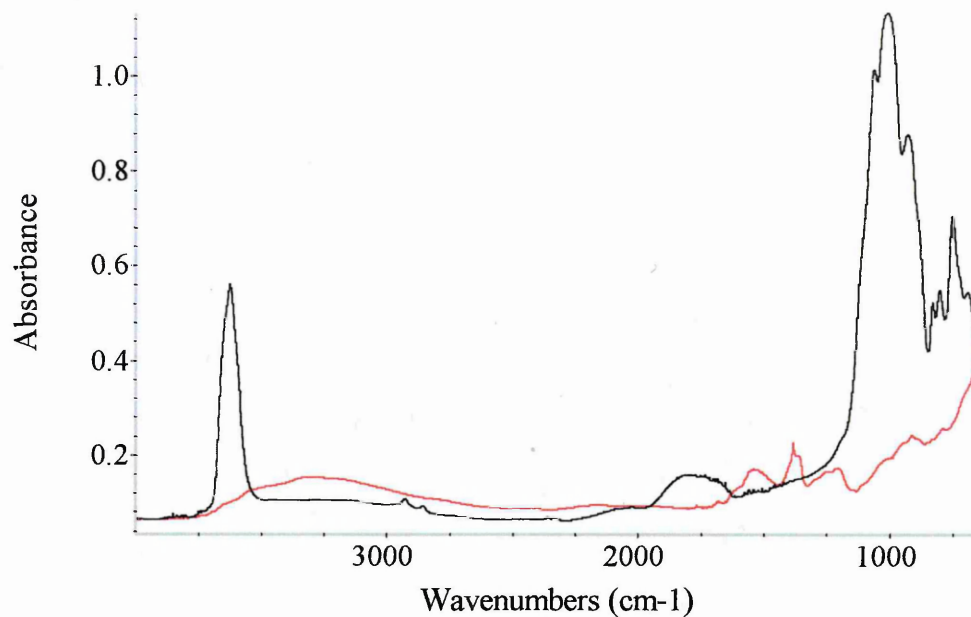


**Figure 6.5: DRIFTS spectra of muscovite (black) and hematite (red).**

The spectrum of muscovite was similar to that of illite with a strong OH stretching band at  $3620\text{ cm}^{-1}$  and similarly positioned Si-O stretching bands in the  $1200\text{--}700\text{ cm}^{-1}$  region. Notably, however, muscovite did not display the broad OH stretching band at around  $3430\text{ cm}^{-1}$  that was present in the spectrum of illite and montmorillonite. This was because the  $3430\text{ cm}^{-1}$  band was due to H-O-H vibrations of absorbed water, and while illite and montmorillonite can absorb water by hydration of the interlayer cations, muscovite contains unhydrated interlayer cations. Again, the problem of peak overlap in the spectra of muscovite and illite may occur. However, PLS should be able to distinguish between the two. The spectrum of hematite, on the other hand, was difficult to distinguish from that of other minerals since it had no strong distinct bands. It is unclear how PLS would cope with the inclusion of the spectrum of such a mineral.

#### 6.4 Standard Preparation

A 3 g batch of each standard was prepared to minimise weighing errors. The training set was comprised of fifty standards each with varying concentrations of the 11 components. Each 3 g batch of the standards was ball milled for 5 minutes at 45 Hz.

The range of concentrations for each component in the standards was different to reflect the concentrations that would be observed in a real sandstone rock sample. The concentration ranges chosen are shown in Table 6.3.

<b>Training set component</b>	<b>Concentration range (%)</b>
Quartz	50-90
Montmorillonite	0-10
Kaolinite	0-10
Illite	0-20
Calcite	0-30
Dolomite	0-30
Na-Feldspar	0-20
K-Feldspar	0-20
Hematite	0-10
Chlorite	0-10
Muscovite	0-10

**Table 6.3: The concentration ranges of components used in the training set.**

Table 6.4 shows the forty calibration standards, used to prepare the calibration model, and the ten independent standards left out of the model for later quantification using the model. The independent standards were numbered 5, 13, 14, 21, 23, 24, 27, 37, 39, and 48 and are indicated in Table 6.4 with an asterisk (\*).

Standard No.	Quartz	Montmorillonite	Kaolinite	Illite	Calcite	Dolomite	Na-Feldspar	K-Feldspar	Hematite	Chlorite	Muscovite
1	58	3	2	5	8	9	5	4	2	3	1
2	90	0	0	10	0	0	0	0	0	0	0
3	50	7	10	3	4	0	2	15	1	1	7
4	67	10	6	0	0	1	11	0	0	5	0
5*	76	2	0	0	0	12	0	2	4	0	4
6	61	0	0	7	17	2	0	7	1	3	2
7	53	0	1	20	2	0	7	0	6	8	3
8	52	1	8	0	0	25	2	5	5	2	0
9	50	8	0	1	6	0	14	10	10	0	1
10	72	5	0	3	0	14	3	3	0	0	0
11	50	0	4	0	10	8	20	0	2	0	6
12	56	3	0	9	22	4	1	1	0	4	0
13*	62	2	1	6	3	6	6	7	3	1	3
14*	84	0	1	3	5	0	0	0	7	0	0
15	50	4	3	13	0	0	0	20	0	0	10
16	66	5	5	0	0	0	10	6	0	7	1
17	74	1	0	0	1	13	0	0	6	0	5
18	70	0	0	0	11	2	0	14	0	1	2
19	53	0	0	10	0	0	17	0	1	10	9
20	51	0	1	1	0	30	1	2	9	5	0
21*	50	7	9	0	5	1	12	9	5	2	0
22	69	0	0	8	0	11	8	4	0	0	0
23*	54	0	3	0	13	20	6	1	0	0	3
24*	60	3	0	3	21	4	2	0	0	7	0
25	56	1	1	4	7	8	4	11	2	1	5
26	71	0	4	7	17	0	0	0	1	0	0
27*	50	6	7	11	1	0	0	17	0	0	8
28	72	2	3	0	0	3	15	0	0	5	0
29	86	1	0	2	3	6	0	0	1	0	1
30	78	0	0	0	12	0	1	3	0	4	2
31	57	0	2	16	0	1	10	0	8	2	4
32	55	0	8	0	0	17	0	10	4	6	0
33	50	3	0	3	30	0	6	6	2	0	0
34	73	0	0	10	2	10	4	1	0	0	0
35	50	0	1	0	25	14	9	0	0	0	1
36	50	4	0	2	14	22	0	0	0	8	0
37*	59	1	7	5	5	4	12	1	3	3	0
38	66	0	5	12	8	0	1	0	5	0	3
39*	54	8	3	17	0	2	0	9	0	0	7
40	80	7	2	0	0	0	10	0	0	1	0
41	67	2	4	8	1	1	6	3	2	2	4
42	84	5	0	1	0	3	3	0	0	4	0
43	75	0	1	0	10	7	0	6	0	0	1
44	56	1	0	4	5	18	0	13	1	0	2
45	62	0	6	0	20	0	5	0	7	0	0
46	51	3	3	6	0	4	16	1	4	6	6
47	78	0	0	14	3	0	0	4	0	1	0
48*	50	6	0	3	0	12	11	11	2	0	5
49	57	10	10	0	12	6	2	0	0	3	0
50	65	0	1	9	4	0	4	16	0	0	1

**Table 6.4: Mineralogical composition of the standards used in the training set.**

**The standards marked with an asterisk are the ten independent standards.**

## 6.5 Sample Preparation

As mentioned previously, each of the standards, and also the KBr (>99%) diluent, were ball milled in 3 g batches at 45 Hz for 5 minutes. The KBr was oven dried overnight prior to spectral collection. Samples were prepared by mixing 4 wt% ball

milled standard with ball milled KBr in a mortar and pestle for 1 minute. The sample (0.32 g) was then transferred to the DRIFTS sample cup and packed using the double packing method described in section 4.3.3.

## 6.6 Results and Discussion

### 6.6.1 Visual Examination of Spectra from Standards

The spectra of a selection of standards are shown in Figure 6.6, in order to discuss the assignment of peaks to individual components and the overlapping of peaks.

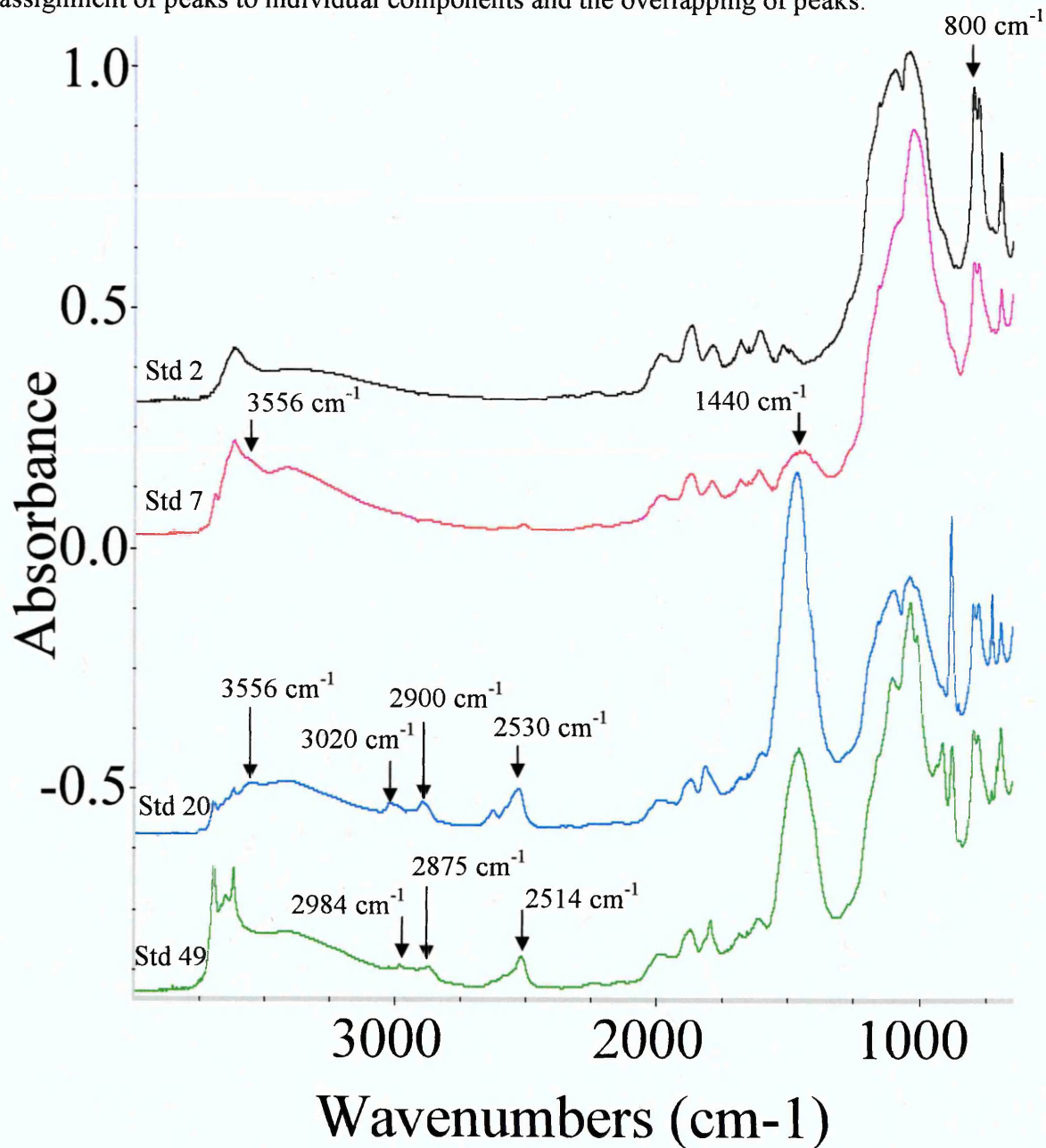


Figure 6.6: Spectra of standards 2 (black), 7 (red), 20 (blue), and 49 (green).

The spectrum of standard 2 showed distinct quartz overtone bands in the region 2000-1400  $\text{cm}^{-1}$ , and strong Si-O stretching bands at 800, 781, and 685  $\text{cm}^{-1}$ , indicating high quartz content. The absence of bands in the 3695-3620  $\text{cm}^{-1}$  region indicated that no kaolinite was present and, since no bands were observed in the 1470-1430  $\text{cm}^{-1}$  region, this indicated the absence of carbonate in the standard. Standard 2 in fact contained only 2 components, 90% quartz and 10% illite.

The spectrum of standard 7 indicated the ease at which low concentrations of kaolinite could be observed using FTIR spectroscopy. Standard 7 contained only 1 wt% kaolinite and yet the distinct peaks at 3695 and 3620  $\text{cm}^{-1}$  could be clearly observed despite the high concentration (20 wt%) of illite which also showed a strong peak at 3620  $\text{cm}^{-1}$ . A high concentration of chlorite, at 8 wt%, was also present in standard 7 and this could be seen as a shoulder at 3556  $\text{cm}^{-1}$ . This chlorite peak was overlapped by the peaks of kaolinite and illite at 3695  $\text{cm}^{-1}$ . A broad carbonate peak could also be observed in the spectrum near 1440  $\text{cm}^{-1}$  due to the presence of 2 wt% calcite in the standard, again indicating the sensitivity of FTIR spectroscopy for detecting these components. The Si-O stretching region, 1200-950  $\text{cm}^{-1}$ , was different in the spectrum of standard 7 than in that of standard 2. This was because, unlike the spectrum of standard 2, which was dominated by quartz (90 wt%), this region in the spectrum of standard 7 was dominated by illite (20 wt%), muscovite (3 wt%), and Na-feldspar (7 wt%).

It was immediately obvious from the spectrum of standard 20 that it contained a high concentration (30 wt%) of dolomite, due to bands at 3020, 2900, 2530, and the strong band at 1469  $\text{cm}^{-1}$ . The spectrum also showed the 3695 and 3620  $\text{cm}^{-1}$  hydroxyl stretching bands of kaolinite despite the presence of only 1 wt% kaolinite. The 5 wt% of chlorite present in the standard could be observed by the clear band at 3556  $\text{cm}^{-1}$ .

The spectrum of standard 49 showed a spectrum dominated by the high concentration (10 wt%) of kaolinite. The four strong hydroxyl stretching bands between 3695-3620  $\text{cm}^{-1}$  were clear as were the distinct Si-O stretching bands in the 1200-950  $\text{cm}^{-1}$  region, indicative of kaolinite. The presence of both calcite (at 12 wt%) and dolomite (at 6 wt%) in the standard could be observed from the spectrum. Bands at 2984, 2875, and 2514  $\text{cm}^{-1}$  in the spectrum were indicative of calcite, while the strong band at 1460

$\text{cm}^{-1}$ , indicated the presence of both carbonates, since pure calcite had a doublet at 1436 and 1398  $\text{cm}^{-1}$  while pure dolomite had a band at 1469  $\text{cm}^{-1}$ .

## **6.6.2 Pre-processing Studies**

### **6.6.2.1 Introduction**

To create the eleven component PLS model, PLS-1, variance scaling, and cross validation were used. Various models were prepared using different spectral wavenumber regions and different pre-processing, to investigate how these affected the precision and accuracy of predictions of the independent standards and to find the optimum model. In the first two models, different spectral wavenumber regions were selected to test both how robust the model could be using only a small wavenumber region and also to find which region gave the most precise and accurate predictions. The next set of models were created to investigate the pre-processing techniques MSC (multiplicative signal correction, a pathlength correction) and automatic baseline correction. Pre-processing terms are described in section 2.5.2.1. The precision and accuracy of predictions were studied with no corrections, and with either MSC or baseline correction. The numbers of factors chosen for each component in each model were based upon the positions of the minima in the PRESS plots and on the  $R^2$  values of the calibrations. Once the optimum wavenumber region and pre-processing were chosen, this model was then further optimised by choosing factors based upon the precision of the model ( $R^2$  value of the calibrations and  $R^2$  value of the predictions), and also on the accuracy of the model (sum of the squares of the differences). A low value for the sum of the squares of the differences (SSD) indicated a more accurate prediction. The best model would be one where  $R^2$  values of the calibration and predictions were high, and the SSD were low.

### **6.6.2.2 Wavenumber Region**

#### **6.6.2.2.1 Introduction**

The wavenumber region of the calibration standard spectra chosen for a PLS model affected the precision and accuracy with which the model could predict the independent standards. In the three component PLS model described in chapter 4, the

wavenumber region 2150-680  $\text{cm}^{-1}$  was chosen to be optimum, and this same region was studied for the eleven component model. A model was also created using the full spectral region (4000-655  $\text{cm}^{-1}$ ).

#### 6.6.2.2.2 Results

For comparison of effects due to the wavenumber region alone, the same pre-processing was used for each model. PLS-1, variance scaling, cross validation, automatic baseline correction, and no pathlength correction were used for each model. Model 1 studied the wavenumber region, 2150-680  $\text{cm}^{-1}$ , and Model 2 studied the region 4000-655  $\text{cm}^{-1}$ . The numbers of factors chosen for the two models were based upon the  $R^2$  values of the calibrations and the minima of the PRESS plots, and they are listed in Table 6.5 for each component.

Component	Number of Factors Chosen	
	Model 1	Model 2
Quartz	4	6
Montmorillonite	11	12
Kaolinite	4	6
Illite	10	10
Calcite	3	3
Dolomite	3	4
Na-feldspar	7	12
K-feldspar	6	12
Hematite	15	15
Chlorite	13	6
Muscovite	11	12

**Table 6.5: Number of factors chosen for each of the named components in Models 1, and 2.**

Plots comparing the  $R^2$  of calibration and  $R^2$  of prediction for Models 1, and 2 are shown in Figures 6.7 and 6.8, respectively. These plots give an indication of the precision of predictions of each component by the models.

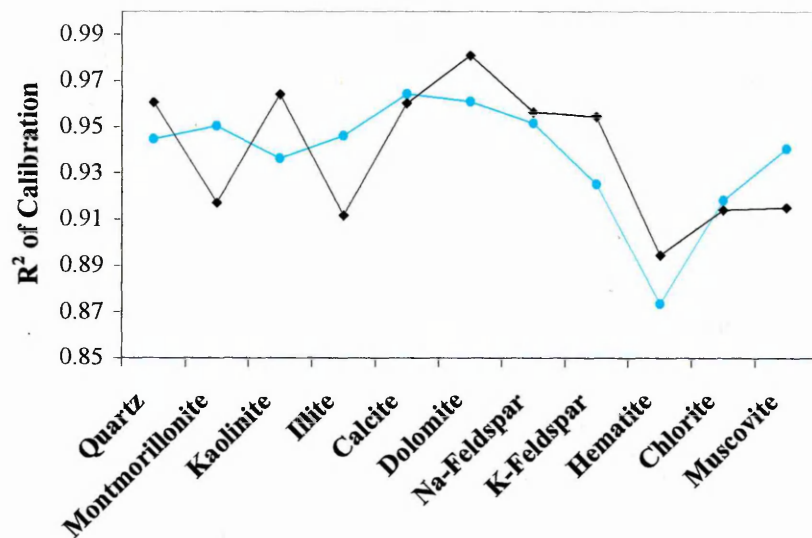


**Figure 6.7: R<sup>2</sup> values of calibrations for each of the named components in Models 1 (light blue), and 2 (black).**

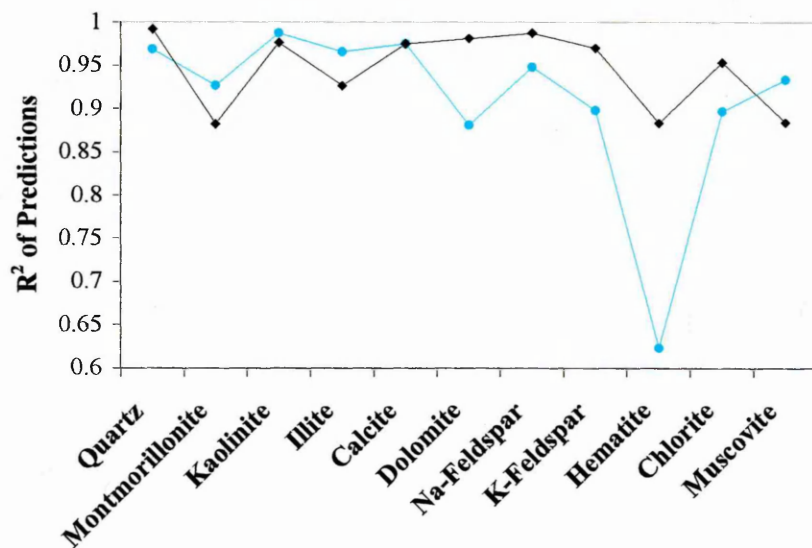


**Figure 6.8: R<sup>2</sup> values of predictions for each of the named components in Models 1 (light blue), and 2 (black).**

From the plots of the R<sup>2</sup> of the calibration and the prediction it was clear that the predictions of hematite gave the lowest R<sup>2</sup> values for both models and therefore it was the least precisely predicted component. The highest R<sup>2</sup> values were generally found using Model 2, suggesting that it gave the most precise predictions of components, although the factors required for some components were quite high.

The accuracy of predictions were compared for the different models and different components in Figures 6.9 and 6.10, which show the SSD, and the maximum error,

respectively. The maximum error was the value of the largest deviation from the actual prediction from a set of predictions, for each component. Therefore, the larger the maximum errors for each component, the less accurate the model was.

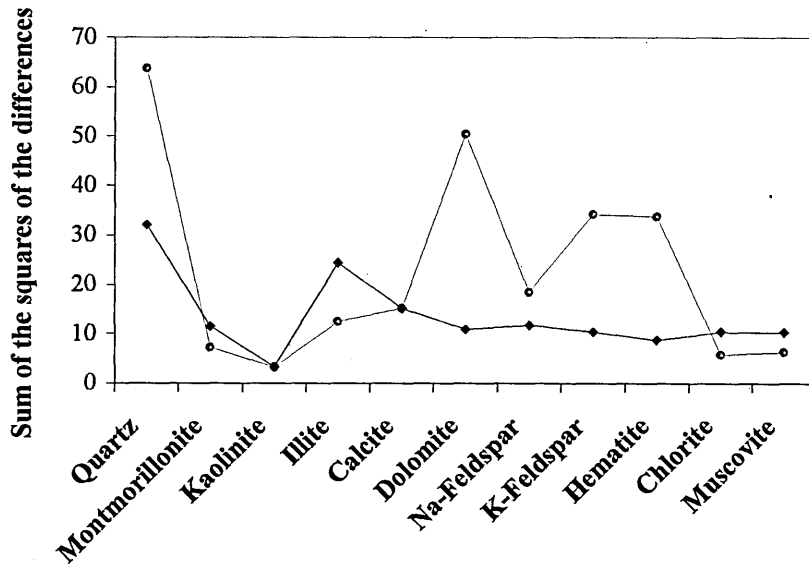


**Figure 6.9:** The sum of the squares of the differences (SSD), in wt%<sup>2</sup>, for each of the named components in Models 1 (light blue), and 2 (black).

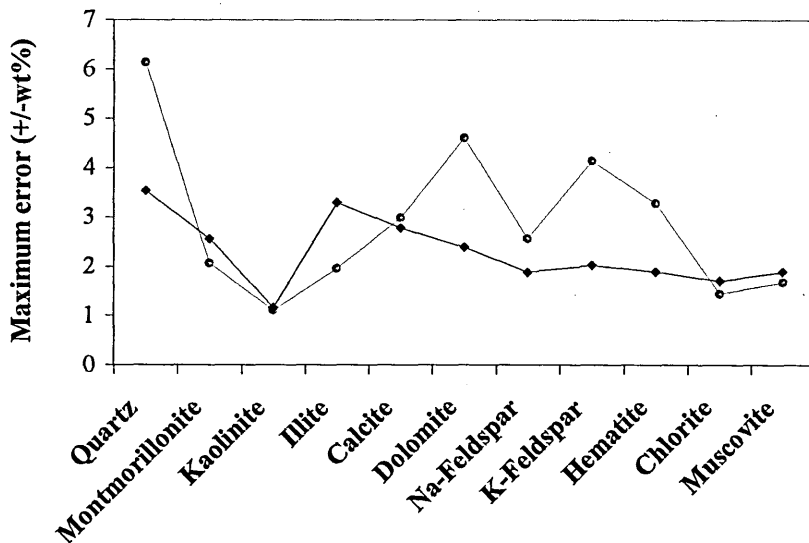


**Figure 6.10:** The maximum error for each of the named components in Models 1 (light blue), and 2 (black).

Figures 6.9 and 6.10 indicate that quartz was least accurately predicted component, producing the highest SSD values and the highest maximum error, while kaolinite was the most accurately predicted. Model 2 generally showed lower SSD values and

lower maximum errors (all below  $\pm 3.5$  wt%) than Model 1, especially for quartz, suggesting that Model 2 gave the most accurate predictions, although again it should be noted that for some components, more factors were chosen in Model 2 than in Model 1.

Overall, Model 2, which used the full (4000-655  $\text{cm}^{-1}$ ) region, gave more precise and accurate predictions than the model which used a smaller and lower wavenumber region. Although Model 1, which used the smaller wavenumber region, was not quite as precise and accurate with predictions of components such as quartz and hematite, the power of PLS at predicting other components when only a small wavenumber region was studied must be appreciated.

### **6.6.2.3 Pathlength and Baseline Corrections**

#### **6.6.2.3.1 Introduction**

The pre-processing techniques, MSC pathlength correction, and automatic baseline correction, affect the calibration spectra and therefore the results of the PLS model created using the spectra. The pre-processing chosen for the three component model using GRAMS software, described in chapter 4, included no pathlength correction but automatic baseline correction. The three models described in this study compared the use of none, or either one of these corrections and all models used the full, 4000-655  $\text{cm}^{-1}$ , wavenumber region.

#### **6.6.2.3.2 Results**

The three models created for this study included Model 2, which has been described previously in section 6.6.2.2, and used no pathlength correction but did use automatic baseline correction. Model 3 used no pathlength correction and no automatic baseline correction, and Model 4, used MSC and no automatic baseline correction. As in section 6.6.2.2.2, the numbers of factors chosen for the three models was done so based upon the  $R^2$  values of the calibrations and the minima of the PRESS plots. The number of factors chosen for each component for each model are listed in Table 6.6.

Component	Number of Factors Chosen		
	Model 2	Model 3	Model 4
Quartz	6	6	5
Montmorillonite	12	13	11
Kaolinite	6	5	5
Illite	10	12	9
Calcite	3	4	3
Dolomite	4	4	3
Na-feldspar	12	13	12
K-feldspar	12	13	11
Hematite	15	16	15
Chlorite	6	6	7
Muscovite	12	14	11

**Table 6.6: Number of factors chosen for each of the named components in Models 2, 3, and 4.**

Plots comparing the  $R^2$  of calibration and  $R^2$  of prediction for Models 2, 3 and 4 are shown in Figures 6.11 and 6.12 respectively.

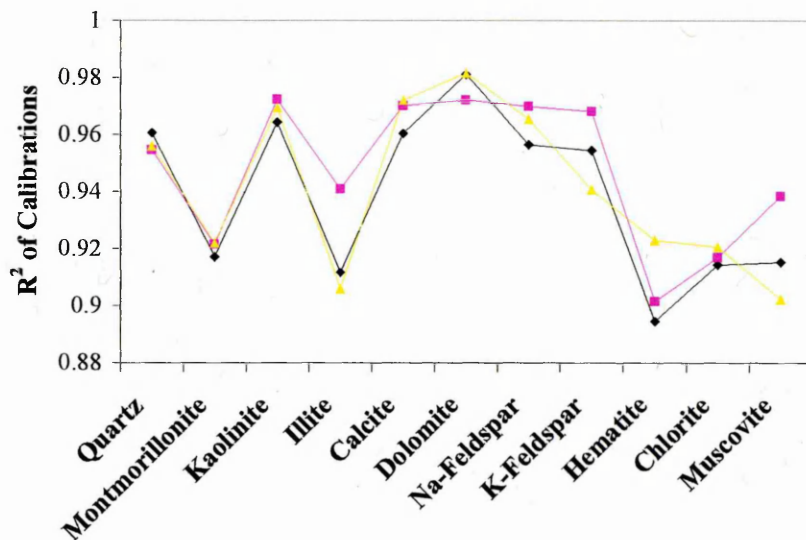


**Figure 6.11:  $R^2$  values of calibrations for each of the named components in Models 2 (black), 3 (pink), and 4 (yellow).**

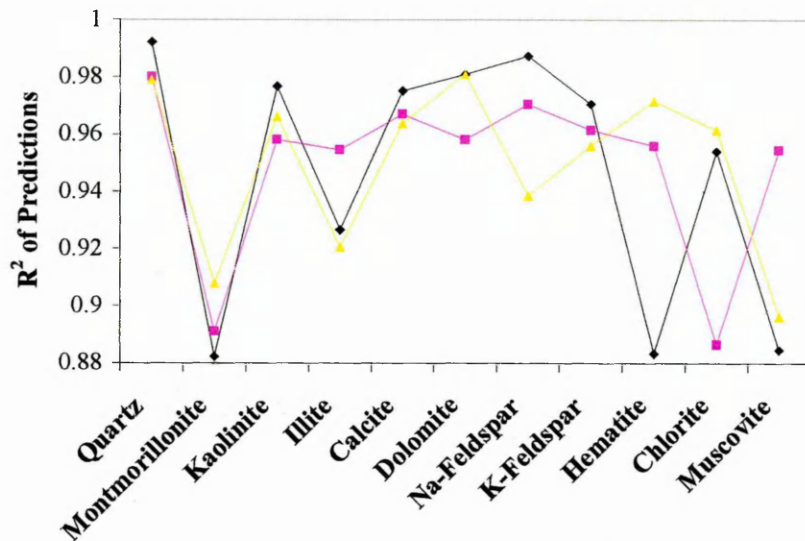


**Figure 6.12: R<sup>2</sup> values of predictions for each of the named components in Models 2 (black), 3 (pink), and 4 (yellow).**

The R<sup>2</sup> values of the calibrations and predictions for all the components, and for each model, were above 0.88, indicating that all the models were relatively precise. The plots indicated that there was little difference between the precision of Models 2, 3, and 4. The accuracy of predictions are compared in Figures 6.13 and 6.14, which show the SSD, and the maximum error respectively.

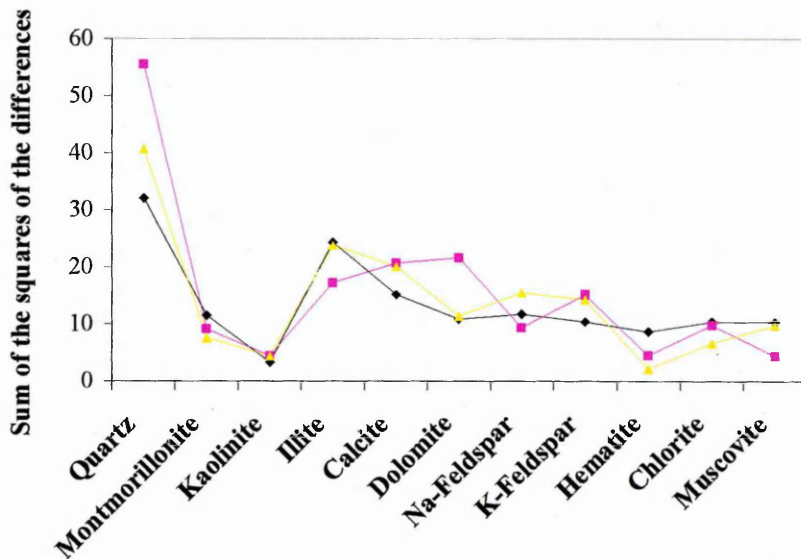


**Figure 6.13: The sum of the squares of the differences (SSD), in wt%<sup>2</sup>, for each of the named components in Models 2 (black), 3 (pink), and 4 (yellow).**

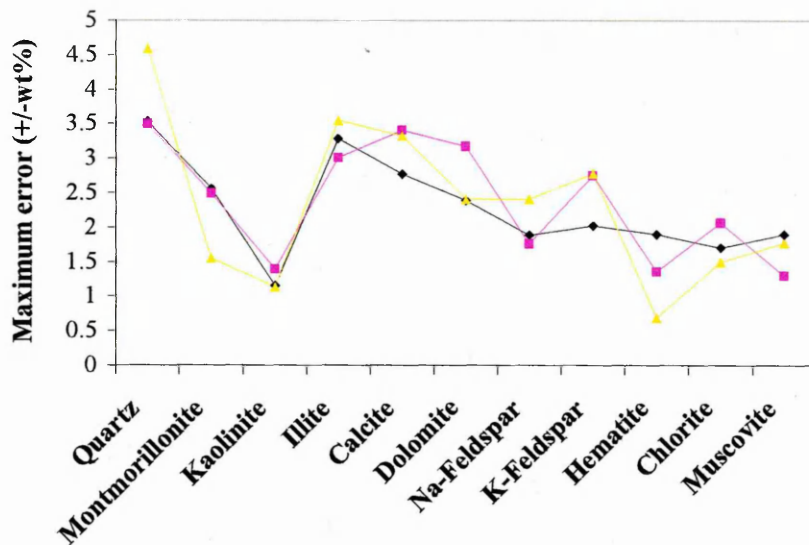


**Figure 6.14: The maximum error for each of the named components in Models 2 (black), 3 (pink), and 4 (yellow).**

As with Models 1, and 2, Models 3 and 4 also predicted quartz the least accurately. The reason for this will be discussed later in chapter 7. It was thought that the reason for the accurate kaolinite predictions could be due to the distinct kaolinite DRIFTS spectra containing particularly strong and well resolved bands. Overall the precision and accuracy of Models 2, 3, and 4 were similar, although the prediction of quartz was more accurate with Model 2. Model 2, which used the spectral region 4000-655  $\text{cm}^{-1}$  and the pre-processing, no pathlength correction, but automatic baseline correction, was therefore chosen as the model which gave the most precise and accurate predictions. Model 2 could be further optimised to create the absolute PLS model by investigating the effects of the number of factors chosen for each component.

### 6.6.3 Absolute PLS Model

#### 6.6.3.1 Introduction

In the absolute PLS model, PLS-1 and cross validation were used. The study of pre-processing in section 6.6.2.3 indicated that the most accurate and precise predictions were found when using variance scaling, no pathlength correction, but automatic baseline correction, and this pre-processing was used for the absolute PLS model.

The pre-processing chosen for this absolute PLS model was actually the same as that which was found to give the most accurate predictions in the three component model described in chapter 4. The study of wavenumber region used in section 6.6.2.2 indicated that the full mid-IR region (4000-655  $\text{cm}^{-1}$ ) should be used for the absolute PLS model to give the most precise and accurate predictions. The three component model described in section 4, however, used only the low wavenumber region, 2150-680  $\text{cm}^{-1}$ , to give the best results. The reason for this may be that, in comparison to the three component model, some components in the eleven component model, such as hematite, had little spectral information and more of the spectrum was required to give accurate predictions.

### 6.6.3.2 Optimising the Number of Factors

During the studies of different models, it became clear that altering the number of factors chosen for each component, greatly affected the predictions calculated. To ensure that the absolute PLS model gave the most precise and accurate predictions, while making certain the model was not over or under fit, the number of factors for each component was studied. Determining the correct number of factors to choose for each component can often be difficult because care must be taken not to underfit or overfit the model, as described in sections 2.5.2.1.1 and 4.8.6. Generally, as the number of factors increases, more information from the spectra is included and the precision and accuracy of predictions increases. However, if too many factors are used, noise in the spectra begins to be modelled. This results in a decrease in the precision and accuracy of predictions.

In this study, the number of factors for each component was chosen based on the precision ( $R^2$  value of the calibrations and predictions) and accuracy (SSD) of predicted concentrations in the independent standards. The plots shown in Figures 6.15 to 6.25 show how the  $R^2$  value of the calibration,  $R^2$  value of the predictions and the SSD vary for each component as the number of factors is increased. The number of factors chosen for each component is indicated on the plots with a vertical black arrow.

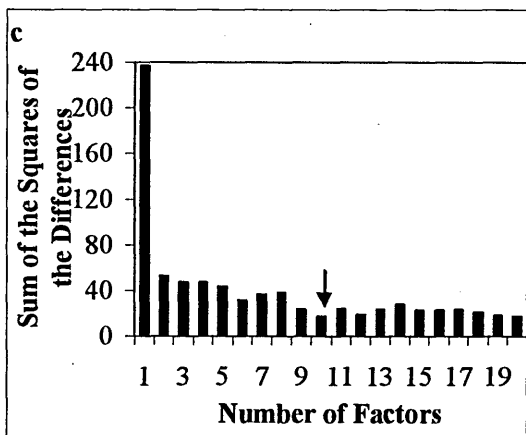
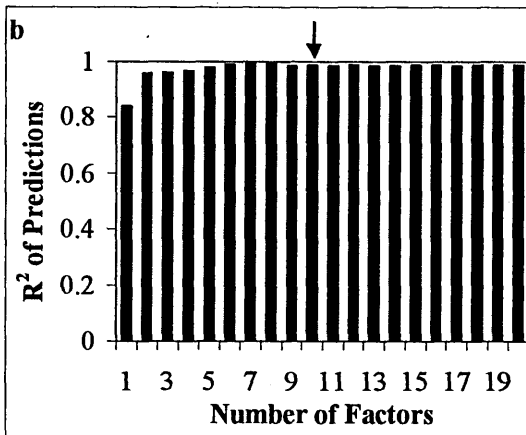
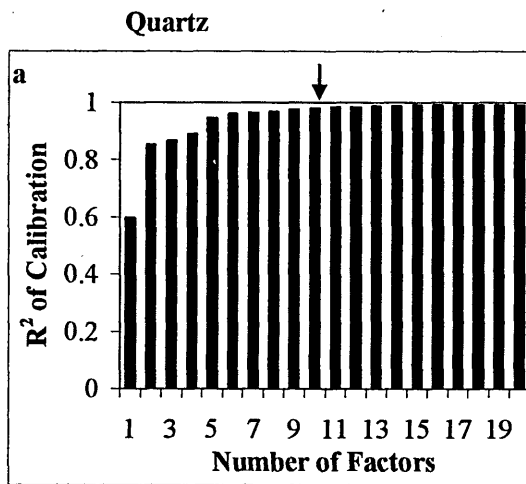


**Figure 6.15: The precision of (a) the calibration, (b) the predictions and (c) the accuracy of the predictions obtained from the absolute PLS model for quartz.**

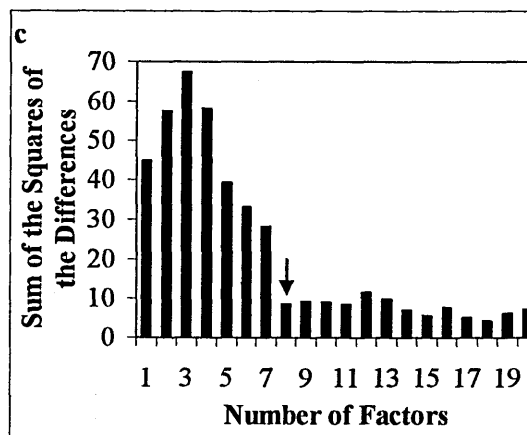
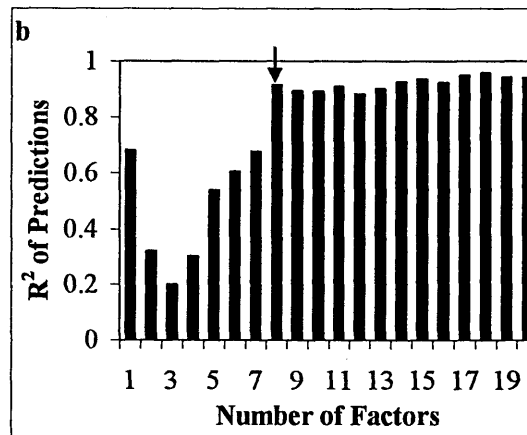
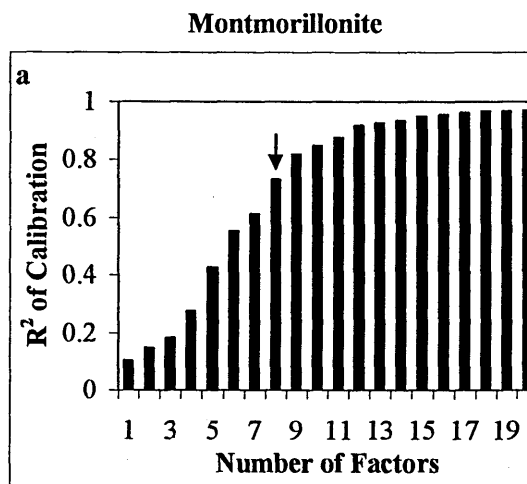


**Figure 6.16: The precision of (a) the calibration, (b) the predictions and (c) the accuracy of the predictions obtained from the absolute PLS model for montmorillonite.**

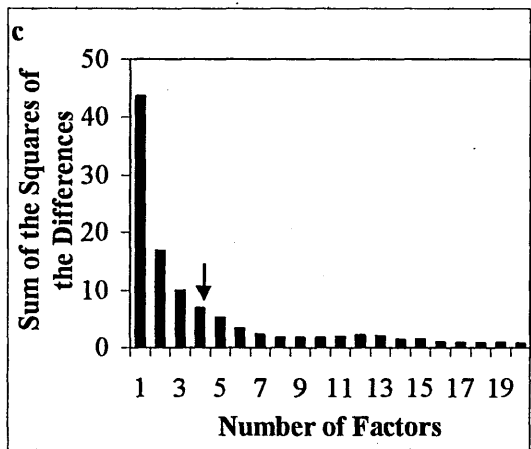
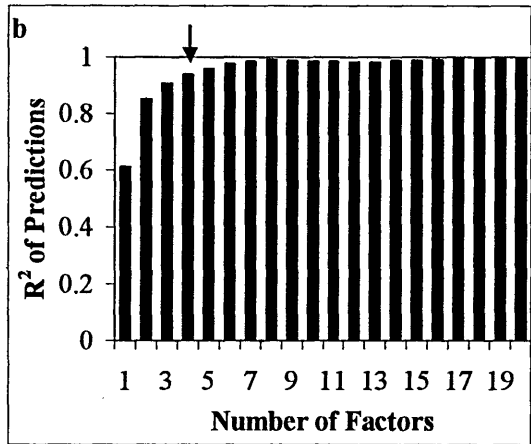
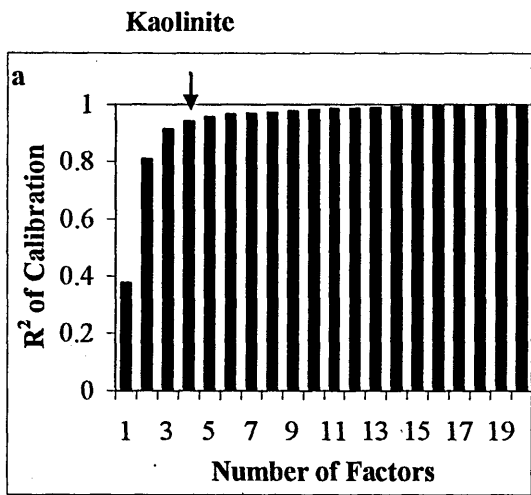


**Figure 6.17:** The precision of (a) the calibration, (b) the predictions and (c) the accuracy of the predictions obtained from the absolute PLS model for kaolinite.

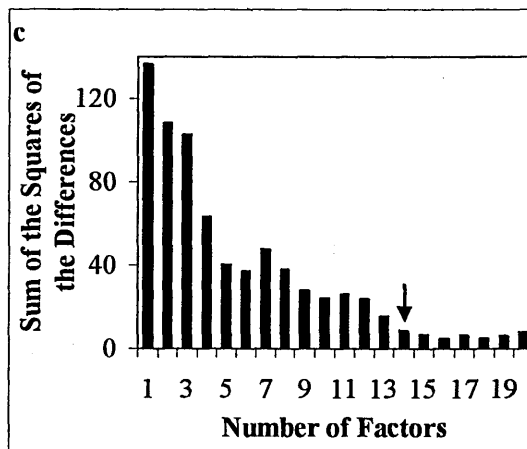
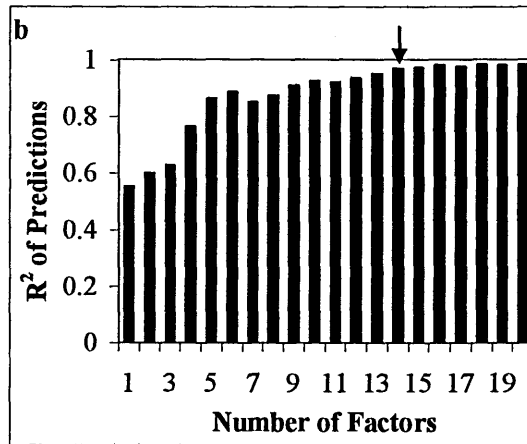
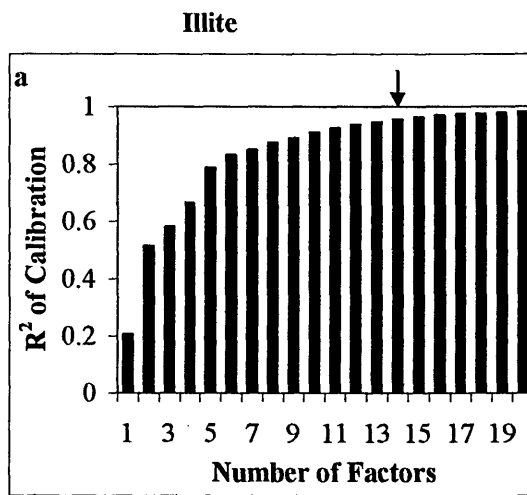


**Figure 6.18:** The precision of (a) the calibration, (b) the predictions and (c) the accuracy of the predictions obtained from the absolute PLS model for illite.

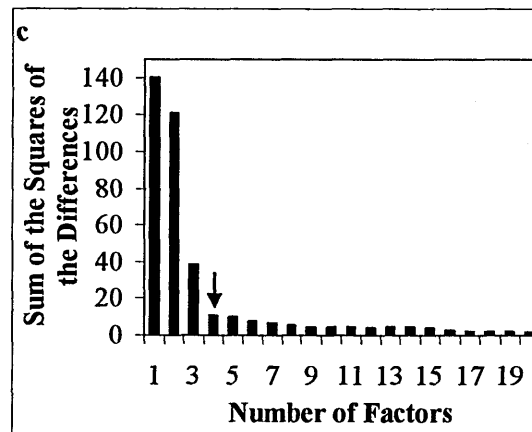
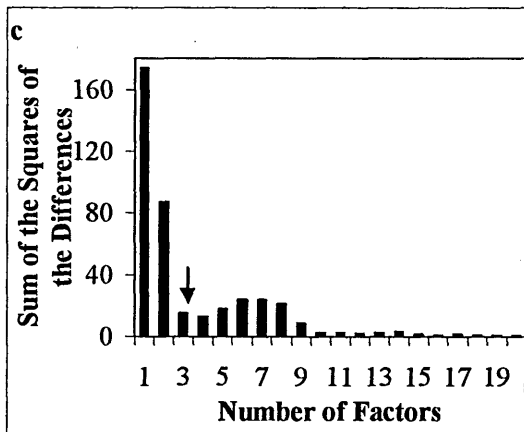
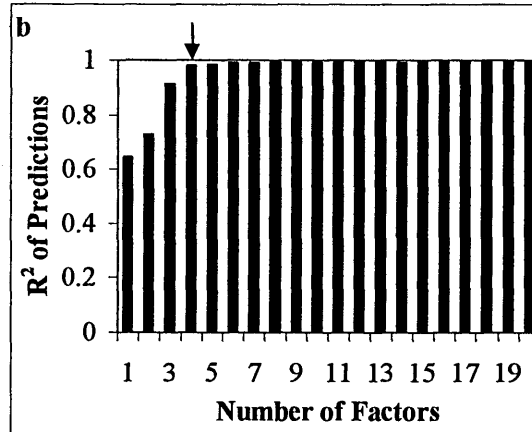
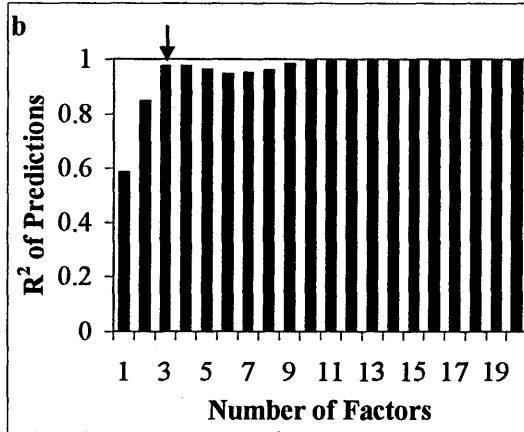
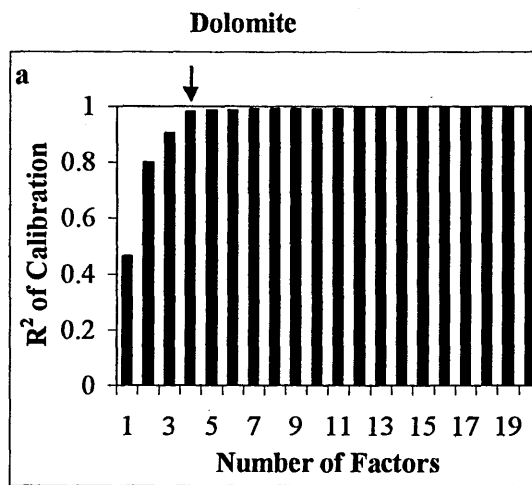
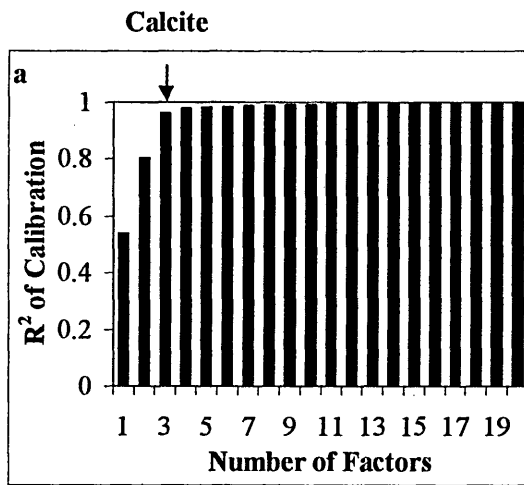


**Figure 6.19: The precision of (a) the calibration, (b) the predictions and (c) the accuracy of the predictions obtained from the absolute PLS model for calcite.**

**Figure 6.20: The precision of (a) the calibration, (b) the predictions and (c) the accuracy of the predictions obtained from the absolute PLS model for dolomite.**

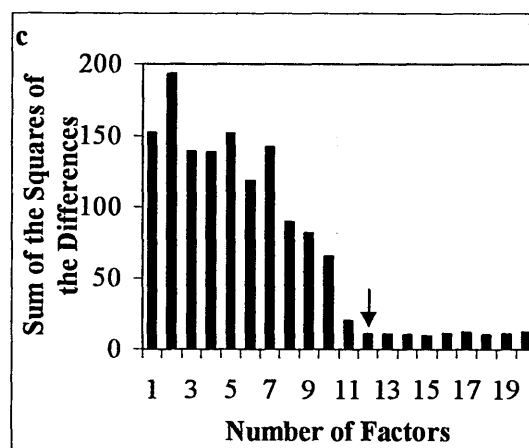
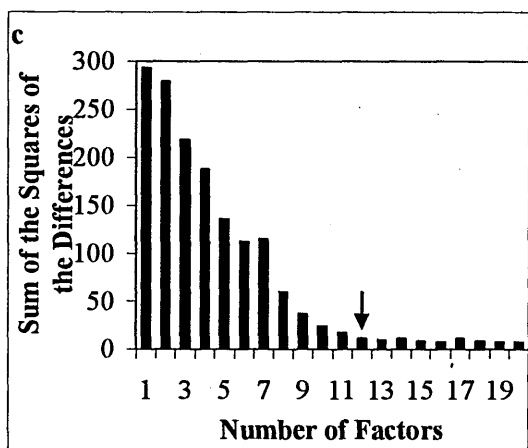
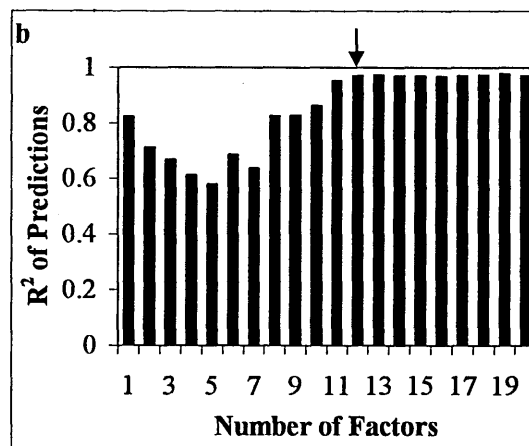
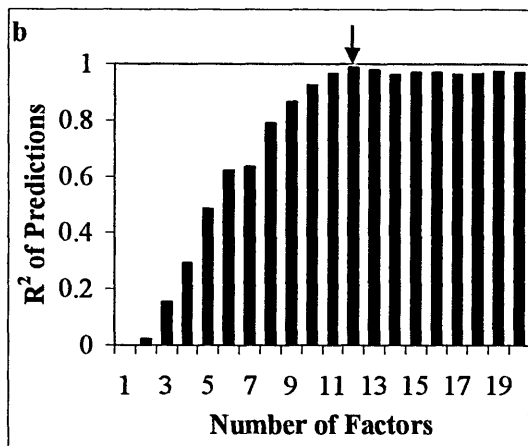
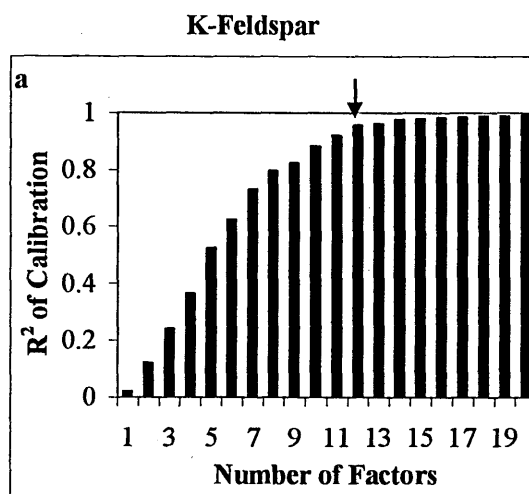
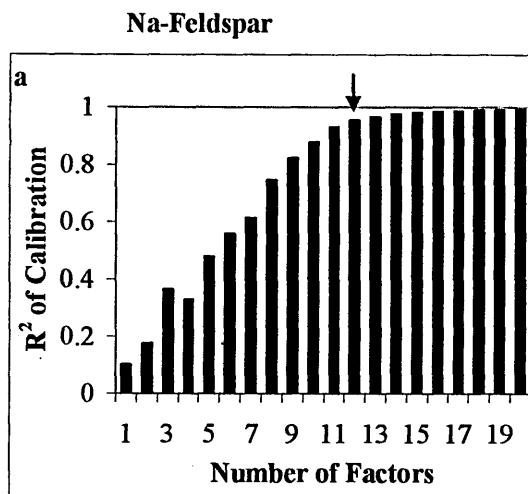


**Figure 6.21:** The precision of (a) the calibration, (b) the predictions and (c) the accuracy of the predictions obtained from the absolute PLS model for Na-feldspar.

**Figure 6.22:** The precision of (a) the calibration, (b) the predictions and (c) the accuracy of the predictions obtained from the absolute PLS model for K-feldspar.

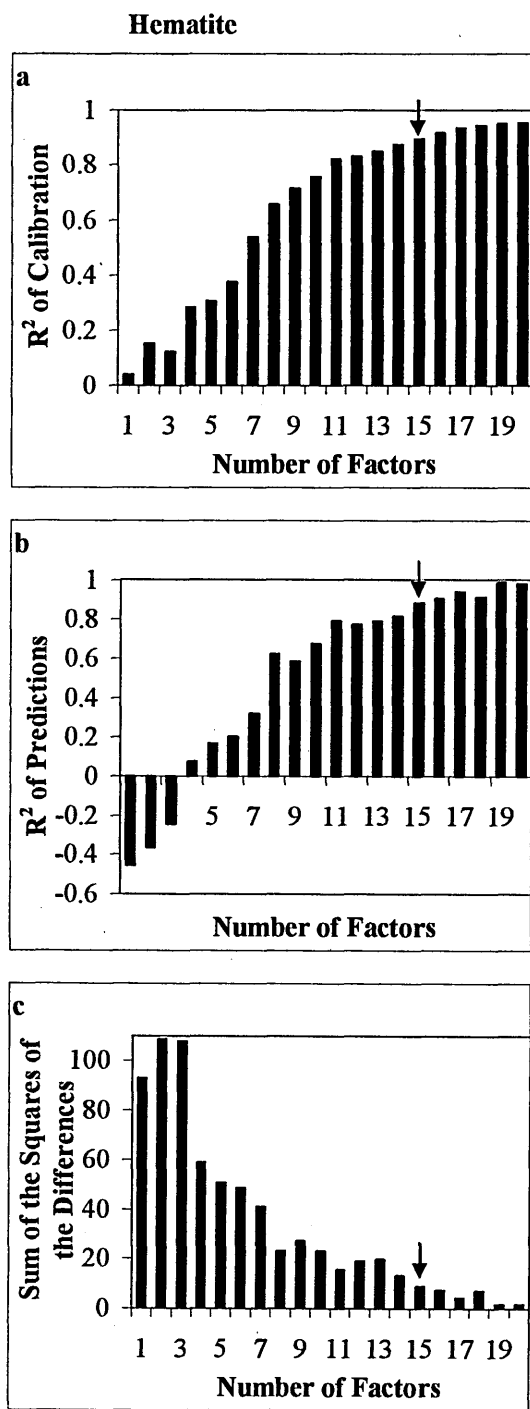


**Figure 6.23:** The precision of (a) the calibration, (b) the predictions and (c) the accuracy of the predictions obtained from the absolute PLS model for hematite.

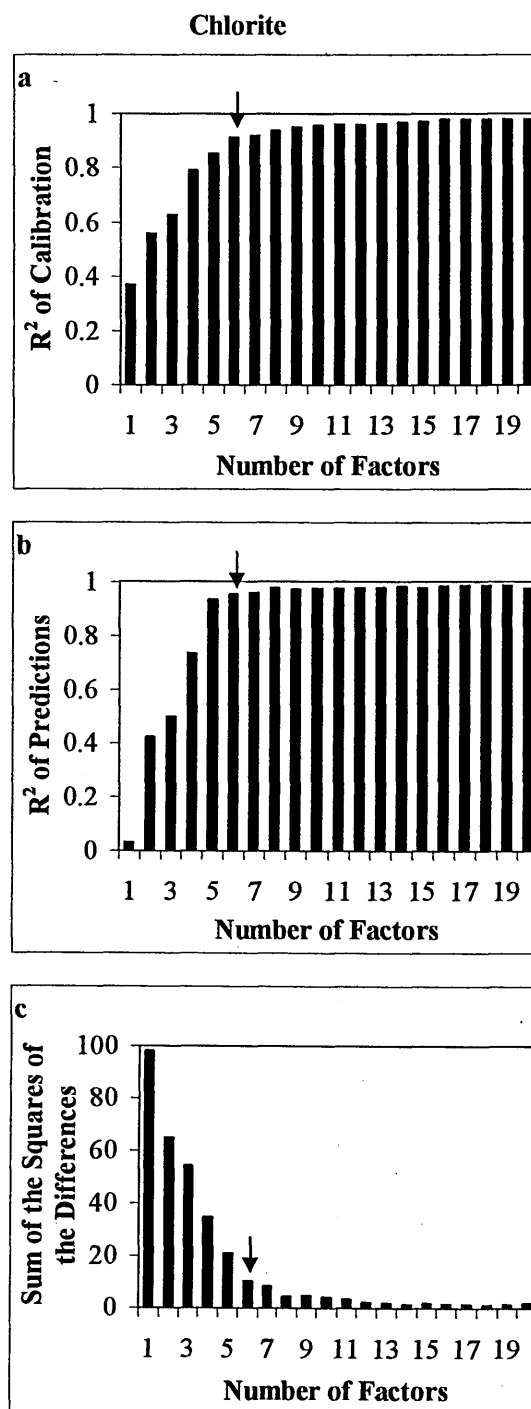


**Figure 6.24:** The precision of (a) the calibration, (b) the predictions and (c) the accuracy of the predictions obtained from the absolute PLS model for chlorite.

Muscovite

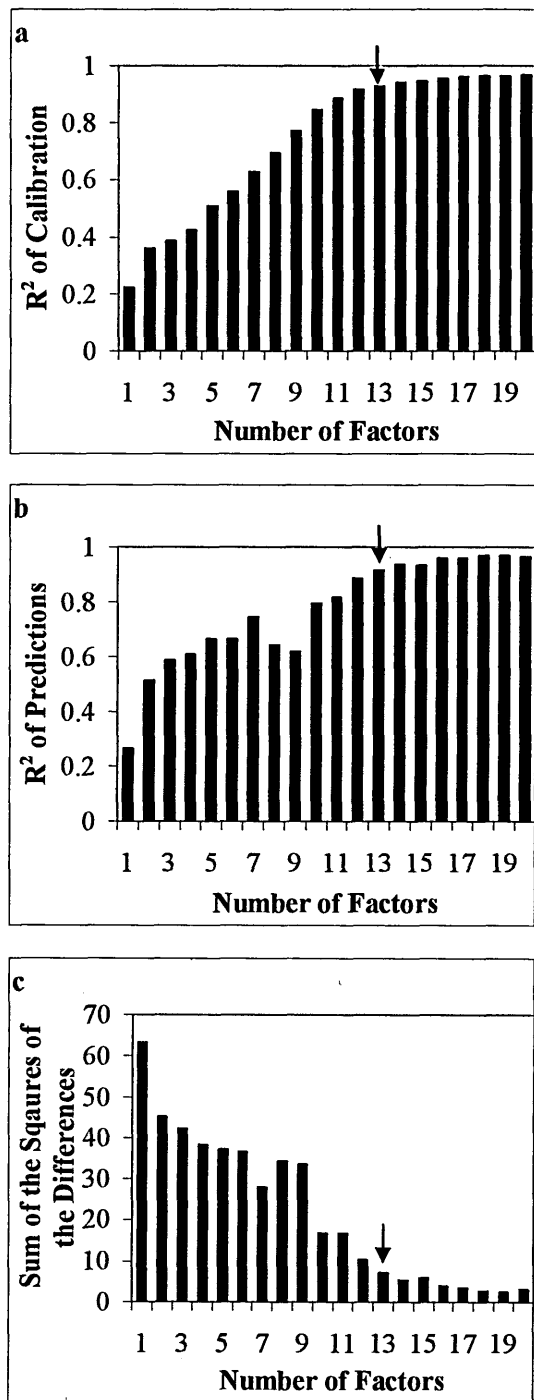


**Figure 6.25: The precision of (a) the calibration, (b) the predictions and (c) the accuracy of the predictions obtained from the absolute PLS model for muscovite.**

The optimum number of factors was chosen for each component based on a decrease in the rate of improvement in  $R^2$  values and sum of the squares of the differences. The resulting factors chosen for the optimum absolute PLS model are shown in Table 6.7, which also lists the  $R^2$  values for the calibration and predictions for each component.

Component	Number of Factors	$R^2$ of Calibration	$R^2$ of Prediction
Quartz	10	0.980	0.987
Montmorillonite	8	0.732	0.915
Kaolinite	4	0.942	0.938
Illite	14	0.956	0.971
Calcite	3	0.960	0.975
Dolomite	4	0.981	0.981
Na-Feldspar	12	0.956	0.987
K-Feldspar	12	0.954	0.971
Hematite	15	0.895	0.883
Chlorite	6	0.914	0.954
Muscovite	13	0.928	0.917

**Table 6.7: The resulting number of factors chosen, the  $R^2$  values for calibrations and predictions, for the optimum absolute PLS model.**

The low number of factors and high  $R^2$  values for both calcite and dolomite suggested they were precisely predicted components. This was expected since their DRIFTS spectra were very distinctive with strong bands in regions where no other components had bands. The lowest  $R^2$  values were seen for hematite, which also required the highest number of factors. The low precision of hematite predictions was expected since its DRIFTS spectrum had few distinct features and no strong bands. It is interesting to note that montmorillonite had the lowest  $R^2$  value for the calibration, at 0.732, and yet the  $R^2$  of prediction for this component was 0.915, suggesting the predictions were relatively precise.

### 6.6.3.3 Absolute PLS Model Predictions

For each component in the training set, the predicted concentrations of the ten independent standards were plotted against the actual concentrations. The component concentrations were expressed as percentages. Figures 6.26 to 6.36 show these predicted vs. actual percentages for each component.

The thick black line at 45° represents the ideal model and any deviation of the points from this line indicates errors in the model. The two full lines on each side of the 45° line indicate the maximum and minimum worst case error for that component, i.e. the value of largest difference between the actual and the predicted percentage. The two dashed lines indicate the maximum and minimum average error for that component, i.e. the average of the differences between the actual and the predicted percentages for all the independent standards.

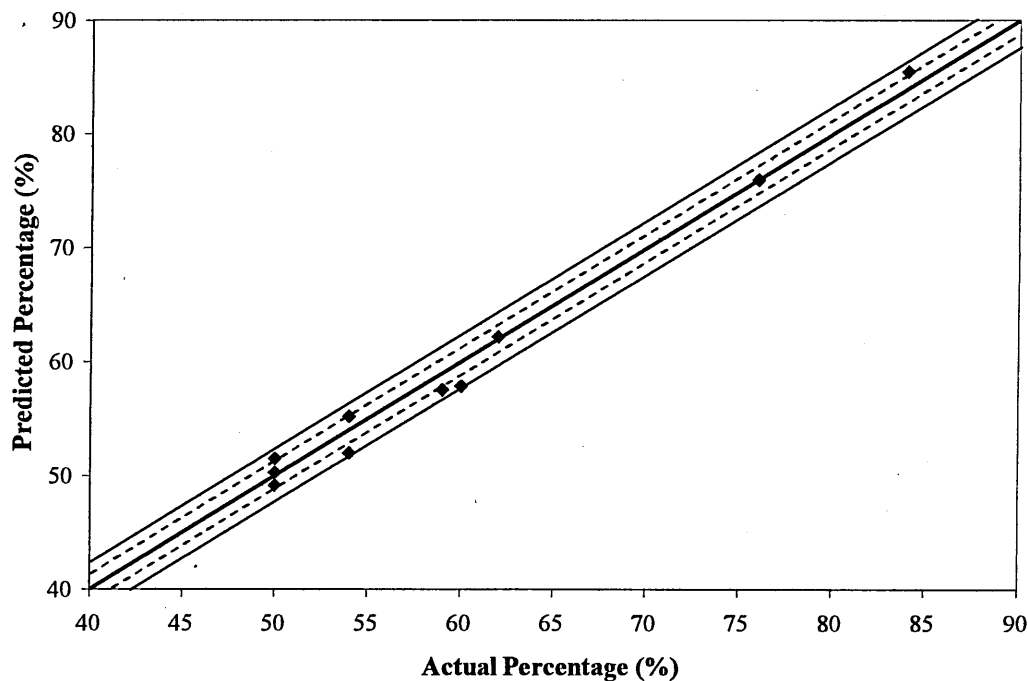


**Figure 6.26: Predicted against actual percentage of quartz for absolute PLS model. The full and dotted lines represent the maximum and average errors, respectively, of the predictions.**

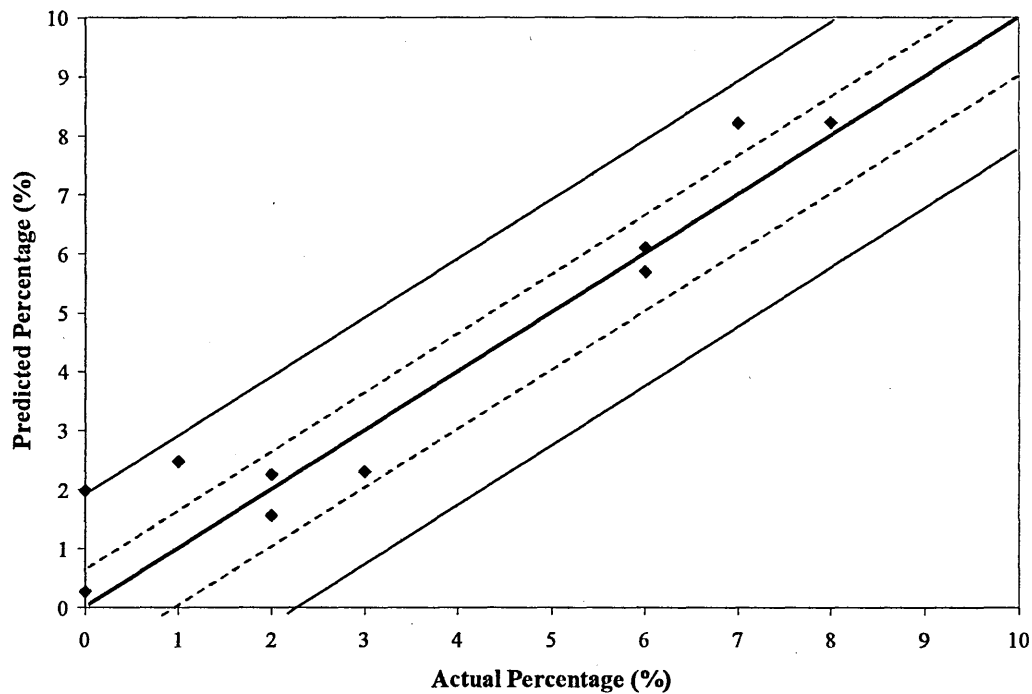


**Figure 6.27: Predicted against actual percentage of montmorillonite for absolute PLS model. The full and dotted lines represent the maximum and average errors, respectively, of the predictions.**

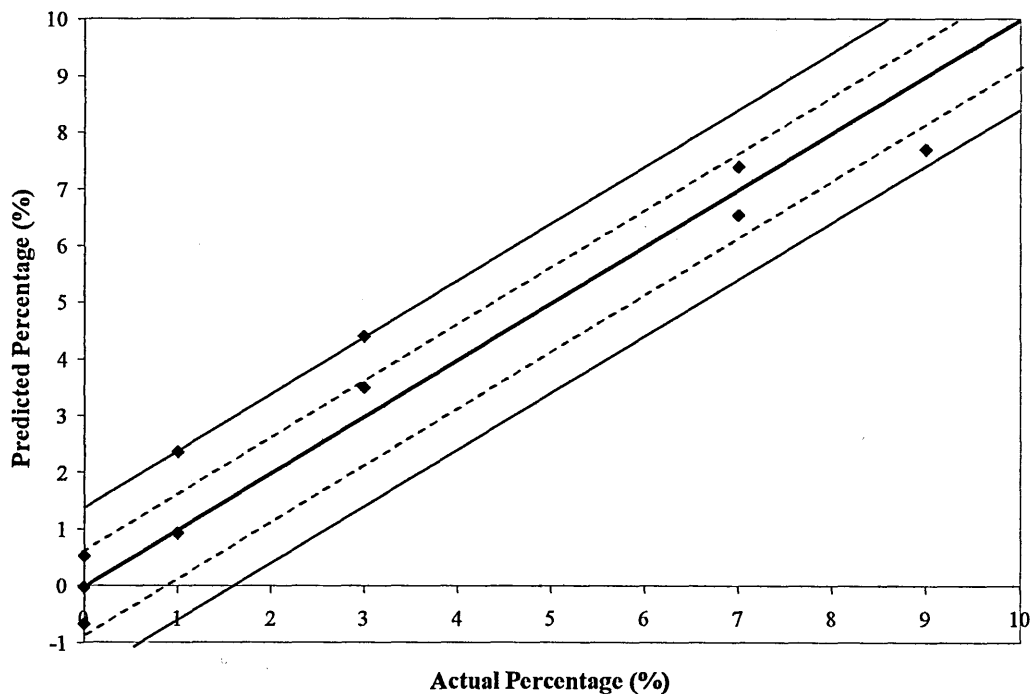


**Figure 6.28: Predicted against actual percentage of kaolinite for absolute PLS model. The full and dotted lines represent the maximum and average errors, respectively, of the predictions.**

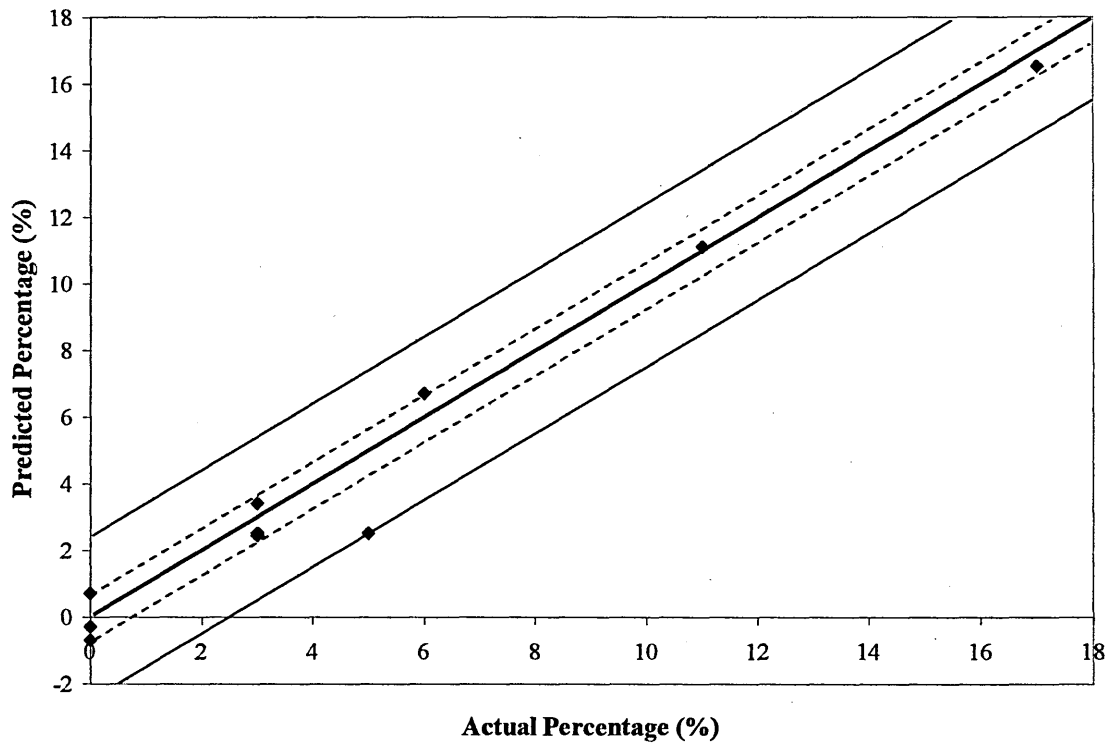


**Figure 6.29: Predicted against actual percentage of illite for absolute PLS model. The full and dotted lines represent the maximum and average errors, respectively, of the predictions.**

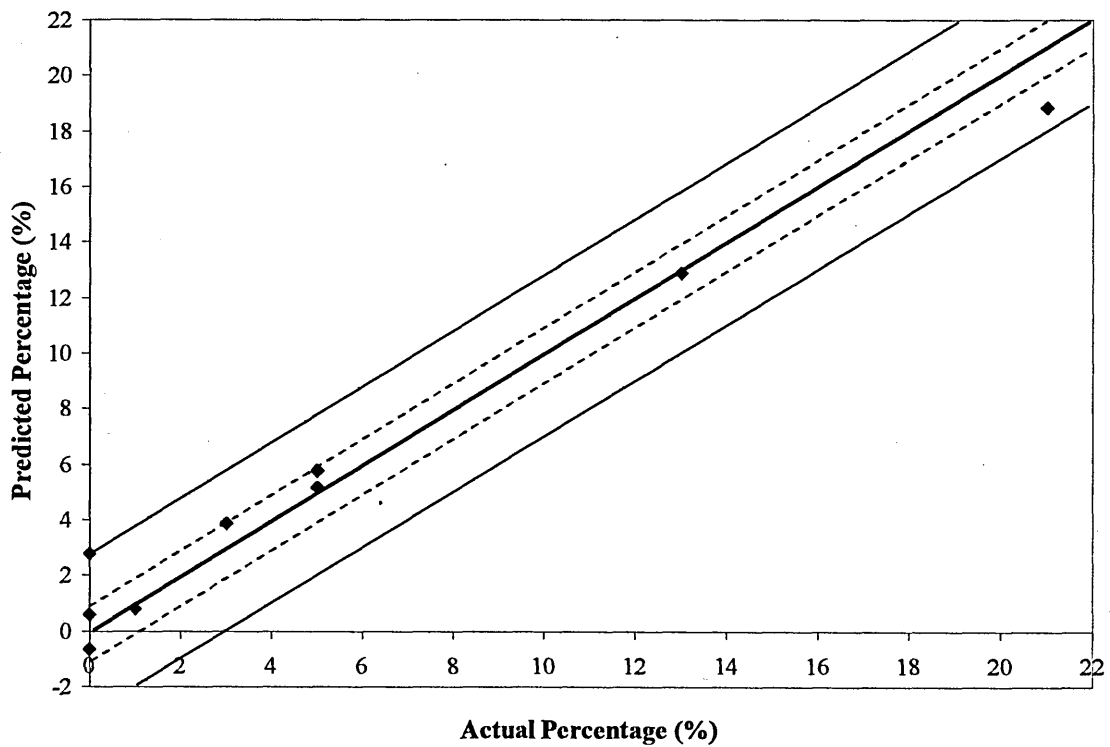


**Figure 6.30: Predicted against actual percentage of calcite for absolute PLS model. The full and dotted lines represent the maximum and average errors, respectively, of the predictions.**

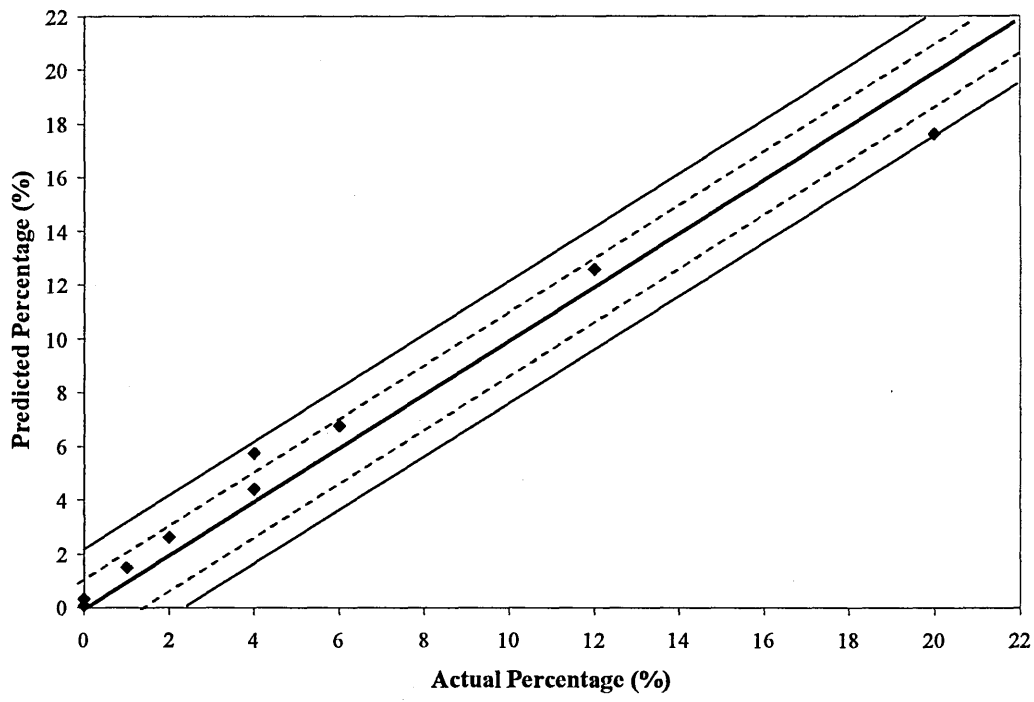


**Figure 6.31: Predicted against actual percentage of dolomite for absolute PLS model. The full and dotted lines represent the maximum and average errors, respectively, of the predictions.**

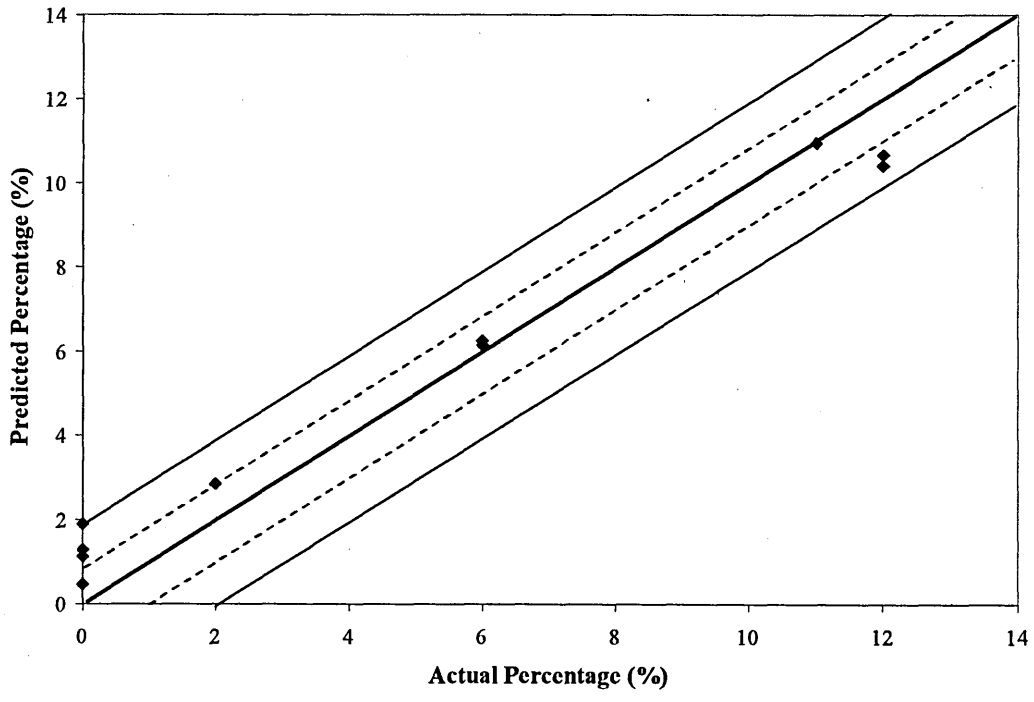


**Figure 6.32: Predicted against actual percentage of Na-feldspar for absolute PLS model. The full and dotted lines represent the maximum and average errors, respectively, of the predictions.**

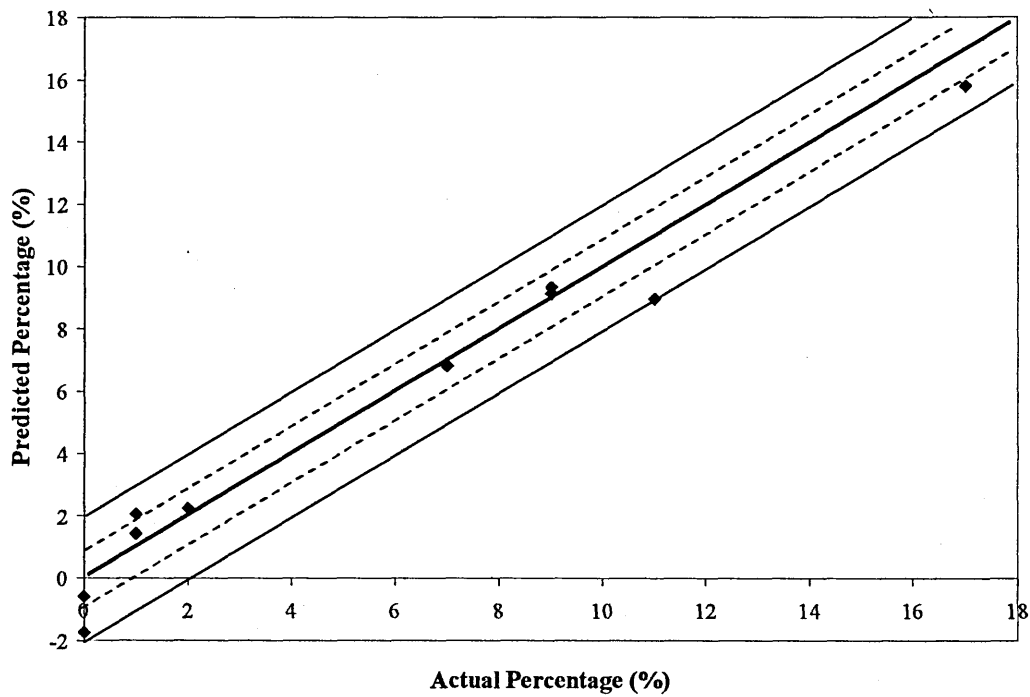


**Figure 6.33: Predicted against actual percentage of K-feldspar for absolute PLS model. The full and dotted lines represent the maximum and average errors, respectively, of the predictions.**

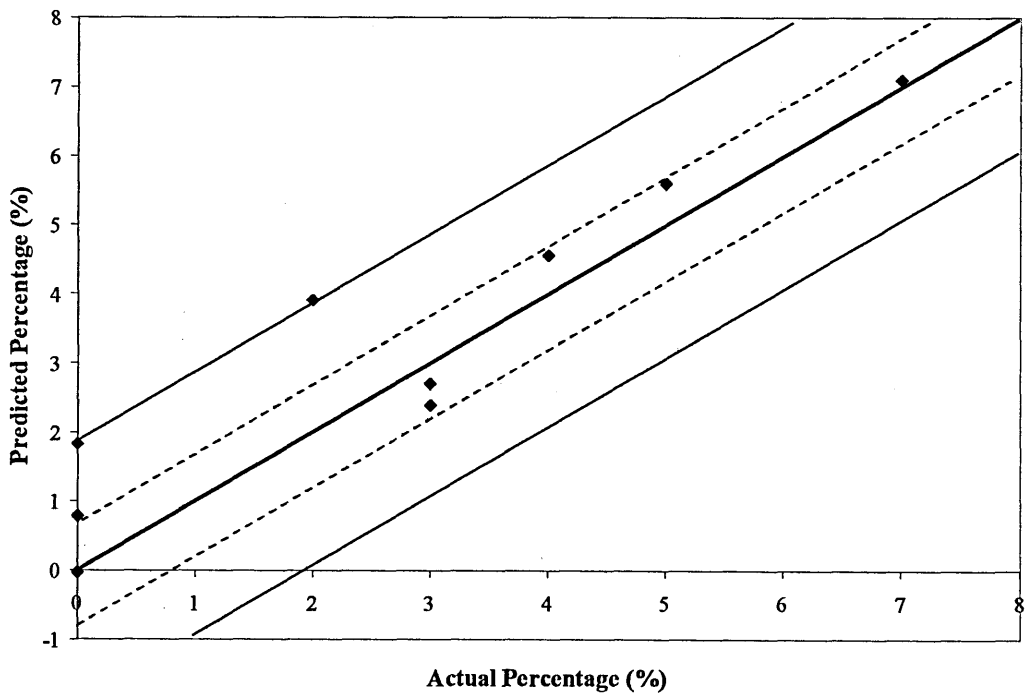


**Figure 6.34: Predicted against actual percentage of hematite for absolute PLS model. The full and dotted lines represent the maximum and average errors, respectively, of the predictions.**

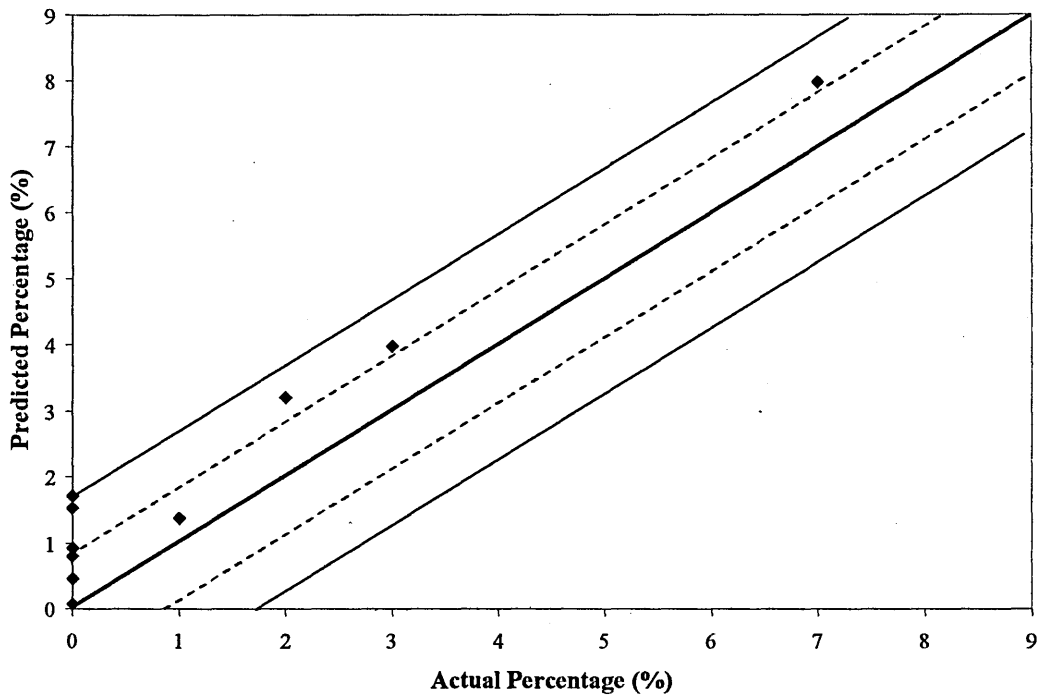


**Figure 6.35: Predicted against actual percentage of chlorite for absolute PLS model. The full and dotted lines represent the maximum and average errors, respectively, of the predictions.**

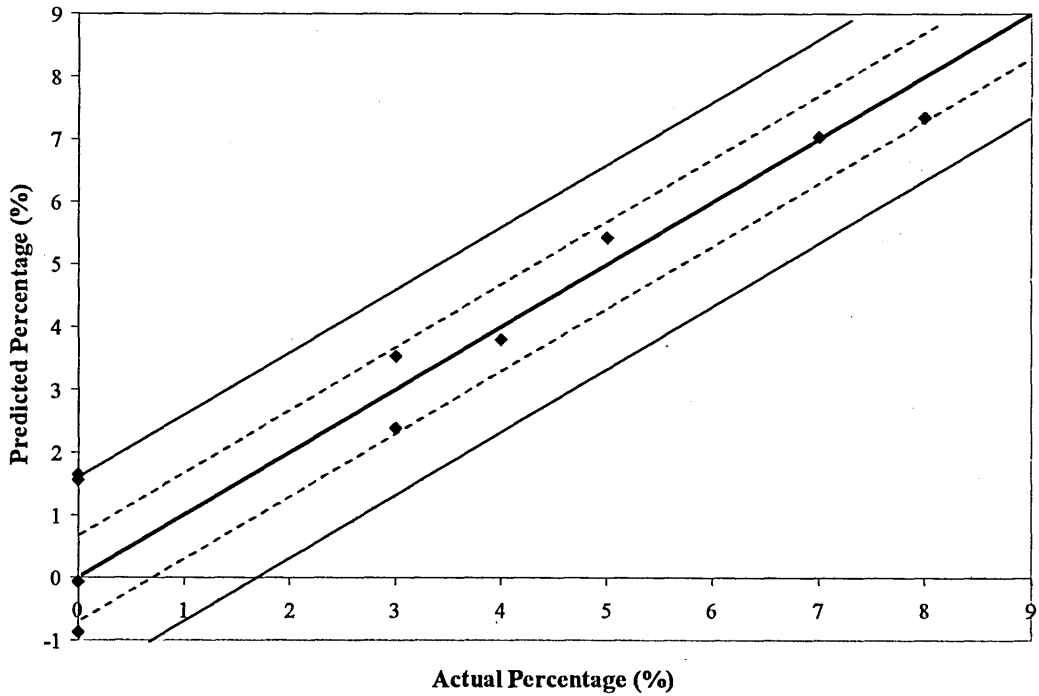


**Figure 6.36: Predicted against actual percentage of muscovite for absolute PLS model. The full and dotted lines represent the maximum and average errors, respectively, of the predictions.**

The spread of the points within the worst case error line (outer full lines) or average error lines (inner dashed lines) gave an indication of the accuracy of the model. The errors in the model were presented in these two ways since, for some components, including illite (Figure 6.29), calcite (Figure 6.30), and dolomite (Figure 6.31), there were only one or two outlying independent standards that had large errors while the other independent standard points lay close to the 45° line.

The plot of predicted against actual percentages for quartz showed that five out of the ten points lay within the average error lines. There were not any outlying points and points were equally distributed above and below the ideal 45° line. The maximum error for quartz was  $\pm 2.2$  wt%.

Montmorillonite was predicted with more precision. The predicted against actual percentages plot showed that seven out of the ten points lay within the average error lines. The remaining three points lay above the ideal 45° line indicating a slight over-prediction of montmorillonite, with the maximum error being  $\pm 2.0$  wt%.

The predicted against actual percentages plot for kaolinite also showed that seven out of the ten points lay within the average error lines. The remaining three points lay both above and below the ideal 45° line, and the maximum error was  $\pm 1.4$  wt%.

Illite was one of the most precisely predicted components with the predicted against actual percentages plot showing that nine out of the ten points lay within the average error lines. There was only one outlying point situated below the 45° line. Despite being so precisely predicted, the maximum error was relatively high compared with the other components, at  $\pm 2.5$  wt%.

The same was true for the carbonate components because, although the plots of predicted against actual percentages showed that eight out of the ten points lay within the average error lines for both calcite and dolomite, the maximum errors for calcite and dolomite were relatively high at  $\pm 2.8$  wt% and  $\pm 2.4$  wt%, respectively.

For Na-feldspar and K-feldspar, the predicted against actual percentages plots showed that five and six points, respectively, lay within the average error lines. The

remaining points lay above and below the 45° line. The maximum errors for Na-feldspar and K-feldspar were therefore,  $\pm 1.9$  wt% and  $\pm 2.0$  wt%, respectively.

The predicted against actual percentages plot for hematite showed that seven out of the ten points lay within the average error lines with remaining points lying above the ideal 45° line indicating a slight over-prediction of hematite and a maximum error of  $\pm 1.9$  wt%.

For chlorite, the predicted against actual percentages plot showed that only four out of the ten points lay within the average error lines, suggesting that chlorite was a less precisely predicted component. It should also be noted that all points on the plot lay above the ideal 45° line indicating that the model had a tendency to over-predict chlorite. The poor precision of the predictions was not reflected by the maximum error, which was only  $\pm 1.7$  wt%.

The predicted against actual percentages plot for muscovite showed it was predicted more accurately than chlorite, with seven out of the ten points lying within the average error lines. The maximum error for muscovite was  $\pm 1.6$  wt%.

## **6.7 Comparing Results with Literature**

Previous work by Clegg [21] included the use of DRIFTS and PLS to quantify mineral components in synthetic mixtures. A PLS model consisting of seven mineral components was developed with a view to quantifying minerals in sandstone rocks. The seven components included in this model were quartz, montmorillonite, kaolinite, illite, dolomite, Na-feldspar, and chlorite. The absolute PLS model discussed in this chapter extended this seven component model in order to incorporate two different carbonates, two different feldspars and also the addition of hematite and muscovite. It was thought that a larger model, with mineral content more similar to that of a real sandstone, would be able to more thoroughly quantify the minerals in a sandstone rock.

Clegg found that the minerals, montmorillonite and illite, were poorly calibrated individually in the model, with correlation coefficients of 0.76 and 0.72, respectively.

Combining the poorly calibrated components, montmorillonite and illite, increased the correlation coefficient to 0.92 in Clegg's model. However, this combination still produced the least accurate predictions of all the components. In the absolute PLS model, the  $R^2$  value of the calibration for illite was 0.96, indicating that it was possible to accurately quantify illite separately from montmorillonite. The  $R^2$  value of the calibration of montmorillonite, in the absolute PLS model, was on the other hand the lowest of all the components, at 0.73. The two components were, however, predicted separately in the absolute PLS model, and the  $R^2$  value of the predictions of montmorillonite was found to be 0.91, and the maximum error,  $\pm 2$  wt%, indicating that predictions for montmorillonite were still precise and accurate, despite the low  $R^2$  value of calibration.

The correlation coefficients of all the components in Clegg's PLS model were over 0.92, and the number of factors chosen range from 5 to 10. In the absolute PLS model, all the components had  $R^2$  values of calibrations over 0.89, except for montmorillonite, at 0.73, and the number of factors chosen ranged from 3 to 15.

Although initially this implied that the model developed by Clegg was more accurate, it tends to be the components not included in Clegg's model that required the high number of factors in the absolute PLS model, e.g. hematite and muscovite.

The maximum errors found for components in the absolute PLS model and in the PLS model developed by Clegg were of the same order. Clegg reported that the maximum error of quartz prediction in the independent synthetic mixtures was  $\pm 3$  wt%, and the other minerals  $\pm 1$  wt%, while the absolute PLS model quantified all minerals with a maximum error of  $\pm 2.8$  wt%.

As mentioned in section 5.4.3.2 in chapter 5, Hillier [70] used X-ray powder diffraction with the internal standard RIR (reference intensity ratios) method and the Rietveld method to quantify samples containing a wide range of clay and non-clay minerals. Corundum was used as the internal standard. Hillier obtained predictions for components by dividing the measured peak intensities in the trace of the sample by the intensity for the standard phase and multiplying by a RIR scale dependent on the amount of added standard. The peak intensities measured were integrated intensities, i.e. peak areas [70]. The maximum errors were reported to be typically within  $\pm 3$  wt% for each component although it was found that the error tends to be correlated with the concentration of the components. Hillier found that generally

errors were greatest when predicting low concentrations. The maximum error reported by Hillier for predicting components was very similar to that found by the absolute PLS model derived in this chapter ( $\pm 2.8$  wt%). Unlike the predictions for components by Hillier, no correlation between the error and the concentration of components was found in the development of the absolute PLS model.

Krivácsy *et al.* [105] used four different calibration methods to quantify quartz and calcite in atmospheric aerosols using DRIFTS and the Kubelka-Munk (K-M) function. The four methods included calibration with one measurement of each standard, calibration with an internal standard, calibration with multiple measurements of each standard, and multiple calibration followed by reference reflectance correction, where the reflectance of the reference material was included in the K-M function. The maximum error for determining quartz and calcite in the samples was within  $\pm 3.1\%$  and  $\pm 4.0\%$ , respectively, for the calibration with one measurement of each standard, and improved to within  $\pm 2\%$  and  $\pm 2.1\%$ , respectively, for the calibration with multiple measurements of each standard. Krivácsy *et al.* found the most accurate method for quartz and calcite quantification to be the multiple calibration followed by reference reflectance correction, where quartz was accurate within  $\pm 1.0\%$  and calcite, within  $\pm 0.7\%$ .

As was found by Krivácsy *et al.*, including two spectra of each standard in the absolute PLS model gave more accurate predictions than single measurements. The errors found for predicting components using the absolute PLS model were in the same order (within  $\pm 2.8$  wt%) as those found by Krivácsy *et al.* using the calibration with multiple measurements.

Reig *et al.* [106] used FTIR spectroscopy to quantify calcite and silica, in mixtures, using absorbance ratios. In this method, it was assumed that the bands due to the same compound maintained a constant relationship when the concentration of that compound varied. If one of the components had an absorbance band exclusively due to that component, then its contribution to the absorbance in the overlapped band could be predicted. Reig *et al.* found that they could predict calcite and silica in mixtures with a relative error of  $\pm 5\%$  and a standard deviation, for three replicas, of  $\pm 4.4\%$ . Although the relative error was reported by Reig *et al.*, the maximum error could be calculated from the data given. The maximum error was calculated as  $\pm 1\%$ .

This method was applied to the quantification of silica and calcite in a sandstone sample, a limestone sample, and a sample of sediments. The silica quantified by this method, in the sandstone, was within  $\pm 2.8\%$  of that calculated by chemical analysis. This error was the same as that found for the quantification of quartz using the absolute PLS model. However, while PLS could cope with overlapping of bands, the method by Reig *et al.* may struggle when more components are involved as it would be more difficult to find a single absorbance band associated with just one component.

Vagenas *et al.* [107] also used the selection of a specific absorbance band, associated with each component of a mixture, to quantify different calcium carbonate phases (calcite, aragonite, and vaterite) in ternary mixtures. To avoid complications arising from overlapping bands, the bands were deconvoluted. Beer's Law was then used to calculate the concentration of each component from the absorbance of each selected band. The relative errors found by Vagenas *et al.* for quantifying calcite, aragonite, and vaterite, were  $\pm 1$ ,  $\pm 8$ , and  $\pm 2.7\%$ , respectively. There was not enough information reported to be able to calculate the maximum errors of the components. The errors found for quantifying calcite and dolomite using the absolute PLS model were reported as maximum errors and were  $\pm 2.8$  and  $\pm 2.4$  wt%, respectively.

Vogt *et al.* [108] used QUAX software (Quantitative Phase-Analysis with X-ray Powder Diffraction) to quantify minerals in rocks. QUAX is a full-pattern method and uses a reference materials database. XRD patterns of minerals of different origin and chemistry are added to the database to improve its predictive ability. Reference materials in the QUAX software must be monomineralic and any impurities must be quantified. Vogt *et al.* investigated the presence of impurities in some Clay Mineral Society clays, by measuring both the bulk material and the  $< 2 \mu\text{m}$  fraction by XRD and by using XRF. Vogt *et al.* quantified the components in synthetic mixtures of quartz, plagioclase, K-feldspar, illite, kaolinite, and montmorillonite but did not report the maximum errors and instead reported the standard deviation of 8 mixtures. The standard deviation was found to be less than  $\pm 4.8\%$  for all the components.

Table 6.8 summarises the different types of errors reported by the different workers discussed in this section. Different errors were reported by Krivácsy *et al.* [105] for the different models they investigated. The maximum error reported in Table 6.8 for

Krivácsy *et al.* is for the most accurate model reported. Where the workers have reported individual errors for each component studied, the greatest error is reported in Table 6.8.

Error	Thesis author	Clegg [21]	Hillier [70]	Krivácsy <i>et al.</i> [105]	Reig <i>et al.</i> [106]	Vagenas <i>et al.</i> [107]	Vogt <i>et al.</i> [108]
Maximum ( $\pm$ wt%)	2.8	3.0	3.0	1.0	-	-	-
Relative ( $\pm$ wt%)	-	-	-	-	5.0	8	-
Standard Deviation ( $\pm$ wt%)	-	-	-	-	4.4	-	4.8

**Table 6.8:** A summary of the different types of errors reported by different workers for quantitative analysis of minerals. Where no value is given, the relevant worker did not report this error.

## 6.8 Conclusion

The sandstone absolute PLS model was constructed with a synthetic mineral training set comprising of eleven mineral components, to resemble the composition of a real sandstone rock. The fifty standards of the training set were composed of quartz, montmorillonite, kaolinite, illite, calcite, dolomite, Na-feldspar, K-feldspar, hematite, chlorite, and muscovite. The DRIFTS spectra of the eleven components in the training set all, except hematite, displayed strong, well resolved bands and could be distinguished from each other visually.

The model was optimised by studying the precision and accuracy of predicted component concentrations in a set of synthetically prepared independent standards. The prediction of components in real sandstone rocks, using the absolute PLS model is studied in chapter 7. Studies using different wavenumber regions and pre-processing in models, indicated that the most precise and accurate predictions were found when using the full (4000-655  $\text{cm}^{-1}$ ) region and when using no pathlength correction, but automatic baseline correction for the pre-processing. The model was

further optimised by altering the number of factors based on a more detailed study of the effects of the factors.

For the absolute PLS model, the  $R^2$  values of the calibrations and predictions for each component were mostly above 0.9. Hematite was the least precisely predicted component, with  $R^2$  of calibration and predictions at 0.89 and 0.88, respectively and the most number of factors required. This was expected since the DRIFTS spectrum of hematite had few distinctive features and no strong bands. However, the maximum error for hematite was only  $\pm 1.9$  wt%, so it was still predicted relatively accurately. Montmorillonite had the lowest  $R^2$  of calibration value, at 0.73. However, the  $R^2$  value of the predictions of montmorillonite was 0.91, and the maximum error  $\pm 2$  wt%, indicating that predictions were still precise and accurate. In the seven mineral component PLS model reported by Clegg [21], montmorillonite was also poorly calibrated, with a correlation coefficient of 0.76. Combining the poorly calibrated components, montmorillonite and illite, increased the correlation coefficient to 0.92 in Clegg's model. However, this combination still produced the least accurate predictions of all the components. The absolute PLS model described in this study attempted to predict each of the eleven components separately and overall the accuracy of the model was good, with the maximum error for all components being less than  $\pm 2.8$  wt%. This error was similar to that found by Hillier [70] for predictions of samples containing clay and non-clay minerals using X-ray powder diffraction. The absolute errors reported by Hillier were typically  $\pm 3$  wt% for each component.

## **7. Results – Quantification of Sandstone Rocks**

### **7.1 Introduction**

In this study, the absolute PLS model, developed in chapter 6, was used to predict the concentrations of minerals in real sandstone rocks from the DRIFTS spectra of powdered samples. The seven quarried sandstones studied were the same as those studied in chapter 5, and included; Hollington Red, Birchover, Yorkstone, Stancliffe, Berea, Clashach, and Castlegate.

It was suggested in chapter 5 that variations in mineralogy along the sandstone cores could be detected visually from XRD traces. In this chapter the mineralogy along the length of the sandstones was investigated by quantifying components using the DRIFTS spectra of the sandstones and the absolute PLS model.

Three different sets of sandstone powder samples were quantified using the PLS model. One set of powders analysed was the powder released during the cutting of the core into slices, as described in section 5.2 of chapter 5. The other two sets of powders originated from the rock slices themselves. Each slice was cut in half, and one half was ground by hand in a mortar and pestle to create the second set of powders, while the other half was ball milled to create the third set of powders. The effect of the different particle sizes of the powders on their DRIFTS spectra was investigated. Since the training set standards used in the PLS model were ball milled, it was thought that the ball milled core samples would give the most accurate predictions.

The predictions of components in the different sandstones, calculated by the absolute PLS model, were compared. The predictions were also compared with those calculated by models developed by others. These models included an XRD model by Dr. Stephen Hillier from the Macaulay Land Use Research Institute, a least square fitting technique with FTIR transmission spectroscopy by Schlumberger-Doll Research, and a PLS with DRIFTS model developed by Clegg [21].

The prediction of sandstone components by Hillier's XRD model was considered to be the most accurate since it was a well established technique. In order to improve the absolute PLS model so that predictions were more similar to those of Hillier, the number of factors chosen for the components were altered, and the pragmatic PLS

model was created. The errors in the models, and the influence of likely impurities in the training set components were also discussed.

## **7.2 Experimental**

### **7.2.1 Preparation of Powders**

Three slices from each sandstone rock were studied; one from the front, one from the middle, and one from the end of the core. Three sets of powders were collected for each slice. The first set of powder was the fine powder released during the cutting process due to the vibration of the rock by the saw. This powder was collected since it was unknown whether certain minerals would preferentially remain in the rock disk, or be lost to the powder collected, during cutting. As stated in section 5.2 of chapter 5, the sandstones differ in density and hardness and the amount of powder collected during cutting was related to this. The harder rocks, Birchover, Yorkstone, and Stancliffe produced more powder during cutting, than Berea, Hollington Red, Clashach, and Castlegate, presumably because of the longer cutting times and therefore longer vibration times of the less friable rocks. This first set of powders is referred to as the “powder from cutting” in discussions throughout this chapter. The second and third sets of powders were prepared from the core slices themselves. Each slice was cut in half, and the second set of powders was prepared by grinding one half of each of the three slices for each core. Grinding was carried out manually in a mortar and pestle until the powder was homogeneous by visual inspection. However, the particle size was still notably larger than the powders produced from cutting. The second set of powders is referred to as “ground slices” throughout this chapter. The third set of powders was produced from the remaining halves of the three slices from each core. The half slices were first crushed to approximately sand sized particles in a mortar and pestle before ball milling to produce a fine powder. Ball milling was carried out in 3 g batches for 5 minutes at 45 Hz. The third set of powders is referred to as “ball milled slices” throughout this chapter. The particle size of the different powders and the training set standards was not found. However, by ball milling the third set of powders for the same length of time as the standards in the training set, it was assumed that the particle size was similar and that the predicted concentrations of components in the ball milled sandstones were the most accurate.

### **7.2.2 Equipment**

As with the training set standards, a Nicolet NEXUS FTIR Spectrometer (manufactured by Thermo Electron Corporation Ltd.), equipped with a mercury cadmium telluride (MCT) detector, and fitted with a Graseby-Specac Selector DRIFTS accessory (manufactured by Specac Ltd.), was used to collect spectra of all the sandstone powders. To ball mill the core slices in order to prepare the third set of powders, a Retsch MM2 grinder was used, with two tungsten carbide grinding pots and two tungsten carbide grinding balls. Batches of 3 g were ground for 5 minutes at 45 Hz.

### **7.2.3 Sample Preparation**

The KBr (>99%) used as the diluent for the sandstone powders was also ball milled in 3 g batches at 45 Hz for 5 minutes and was oven dried overnight prior to spectral collection. Samples were prepared by mixing 4 wt% sandstone powder with ball milled KBr in a mortar and pestle for 1 minute. The sample (0.32 g) was then transferred to the sample cup and packed using the double packing method described in section 4.3.3 of chapter 4.

### **7.2.4 Spectral Collection**

The instrumental parameters used for the Nicolet NEXUS FTIR Spectrometer when collecting spectra of the sandstone powders were the same as those used when the spectra of training set standards were collected, and were described in section 6.2.2 of chapter 6. The procedure for spectral collection of the powders was also the same as that described in section 6.2.2. The Grams32-PLS-PLUS IQ software was used to create both the absolute and the pragmatic PLS models. By introducing the DRIFTS spectra of the sandstone powders to the PLS models in the Grams32-PLS-PLUS IQ software, the components in the sandstones could be quantified.

### 7.3 Qualitative DRIFTS study of Sandstones

The DRIFTS spectra of the sandstones were initially investigated visually to gain a qualitative understanding of the minerals present in each. The DRIFTS spectra of ball milled Hollington Red, Birchover, Yorkstone, and Stancliffe sandstones are shown in Figures 7.1 and 7.2. Figure 7.1 shows the high wavenumber region of DRIFTS spectra, displaying the OH stretching region, while Figure 7.2 shows the low wavenumber Si-O-Si stretching, and O-Si-O bending region.

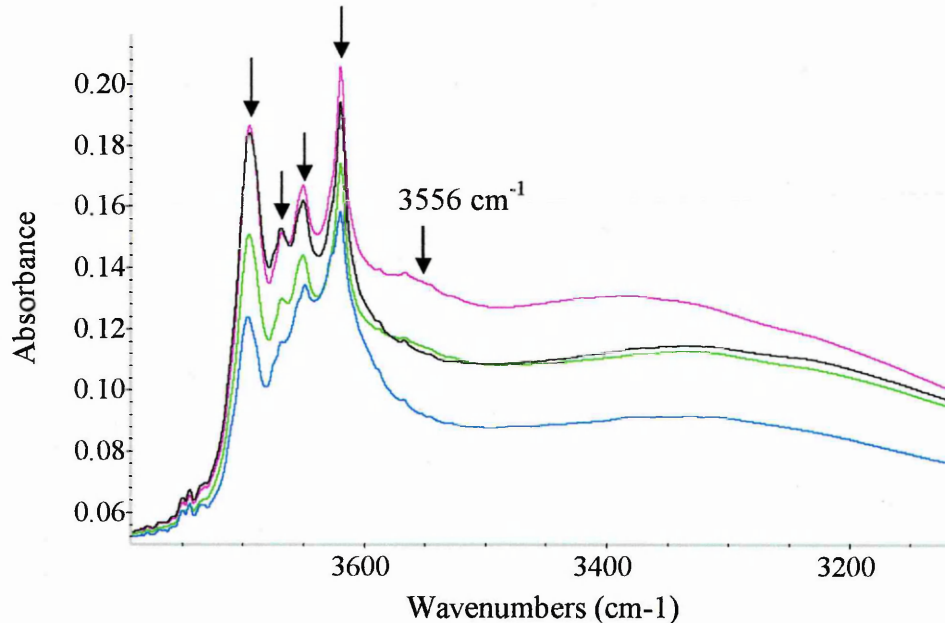


**Figure 7.1: The high wavenumber region of the DRIFTS spectra for ball milled Hollington Red (blue), Birchover (black), Yorkstone (pink), and Stancliffe (green) sandstones.**

All clays display a band near  $3620\text{ cm}^{-1}$ , but it was the four distinct OH stretching bands of kaolinite at  $3695$ ,  $3669$ ,  $3650$ , and  $3620\text{ cm}^{-1}$ , indicated by the arrows, that dominated this region. In the spectrum of pure kaolinite, the band at  $3695\text{ cm}^{-1}$  was equal in intensity or was more intense than the band at  $3620\text{ cm}^{-1}$ , as shown in Figure 6.2, in chapter 6. In the spectra of the sandstones, shown in Figure 7.1, the band at  $3620\text{ cm}^{-1}$  was more intense than that at  $3695\text{ cm}^{-1}$  and this indicated that some 2:1 layer minerals (montmorillonite, muscovite, chlorite and /or illite) were present. It was clear that all four of the sandstones contained kaolinite and the peak intensities and

resolution implied that Birchover and Yorkstone contained a similar amount of kaolinite, while Stancliffe contained slightly less and Hollington Red slightly less again. The broad band at  $3556\text{ cm}^{-1}$  in the spectrum of Yorkstone indicated that it contained chlorite.

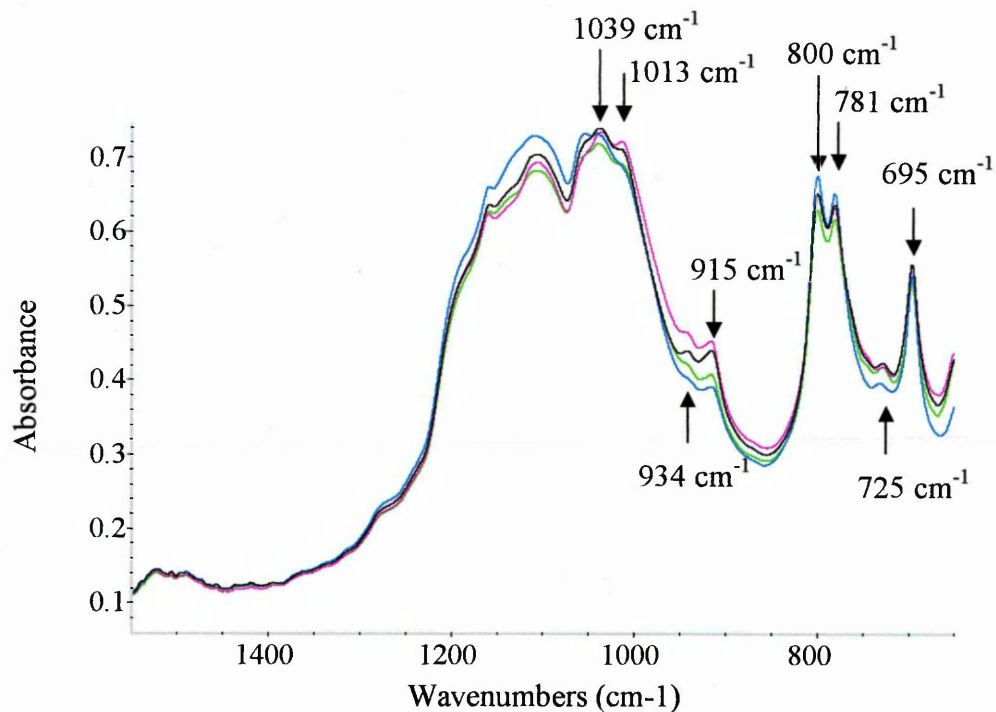


**Figure 7.2: The low wavenumber region of the DRIFTS spectra for ball milled Hollington Red (blue), Birchover (black), Yorkstone (pink), and Stancliffe (green) sandstones.**

Although the spectra of these sandstones were similar, slight differences in peak position, resolution and intensity could be observed. The band at  $1013\text{ cm}^{-1}$  corresponds to Si-O stretching, and the bands at  $934$ , and  $915\text{ cm}^{-1}$  to Al-Mg-OH and Al-OH-Al deformation, respectively. These bands are associated with the minerals kaolinite, montmorillonite, illite, and muscovite. The greater peak intensity and resolution of these bands in the spectra of Yorkstone again suggested that this sandstone had the highest clay content, followed by Birchover, Stancliffe then Hollington Red.

The strong Si-O stretching band at  $1039\text{ cm}^{-1}$  was present in all four of these sandstones, and is associated with Na-Feldspar, so relatively high concentrations of Na-feldspar should be predicted. Another band present in the spectra and associated

with Na-feldspar was found at  $725\text{ cm}^{-1}$ . In the spectra of Hollington Red, however, a band was present at  $730\text{ cm}^{-1}$  instead, indicating that the K-feldspar content of this sandstone was higher than the Na-feldspar content.

The bands at  $800$  and  $781\text{ cm}^{-1}$  (due to Si-O-Si stretching), and the band at  $695\text{ cm}^{-1}$  (due to O-Si-O bending), are associated with quartz, and were strong and sharp in all the sandstones. The slight differences in peak intensity suggested that Hollington Red contained more quartz, followed by Birchover and Yorkstone, with Stancliffe containing the least.

The DRIFTS spectra of ball milled Berea, Clashach, and Castlegate sandstones and of ball milled pure Chelford sand are shown in Figures 7.3 and 7.4. Chelford sand was included because it was the quartz component of the training set and, since the sandstones were composed predominantly of quartz, their spectra were very similar to that of Chelford sand. Figure 7.3 shows the high wavenumber region of the DRIFTS spectra, while Figure 7.4 shows the low wavenumber region.

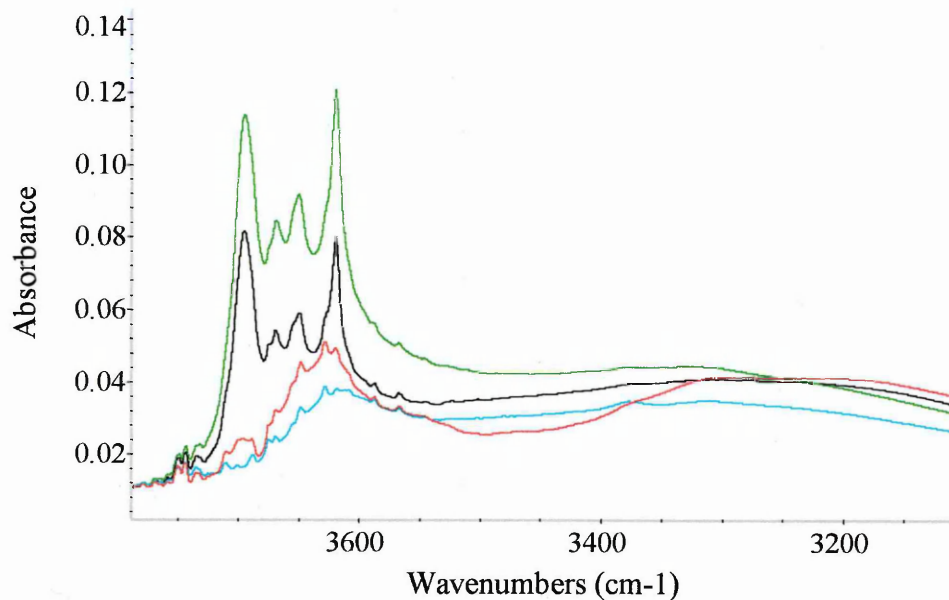


**Figure 7.3: The high wavenumber region of the DRIFTS spectra for ball milled Berea (dark green), Clashach (light blue), Castlegate (black) sandstones, and Chelford sand (red).**

The intensities of the four distinct OH stretching bands of kaolinite, present in the spectra of Berea and Castlegate, indicated that Berea contained a higher concentration of kaolinite than Castlegate although both sandstones contained less kaolinite than

Yorkstone, Birchover, Stancliffe and Hollington Red. It should also be noted that the spectrum of Castlegate was more similar to that of pure kaolinite since the band at  $3695\text{ cm}^{-1}$  was more intense than that at  $3620\text{ cm}^{-1}$ , indicating that while this sandstone contained kaolinite, it contained very little 2:1 layered minerals. It was clear from Figure 7.3 that the four OH stretching bands of kaolinite were not present in the spectra of pure Chelford sand or Clashach. This was to be expected in Chelford sand. However, Clashach was the only sandstone studied which did not contain kaolinite suggesting it was a “clean” sandstone.

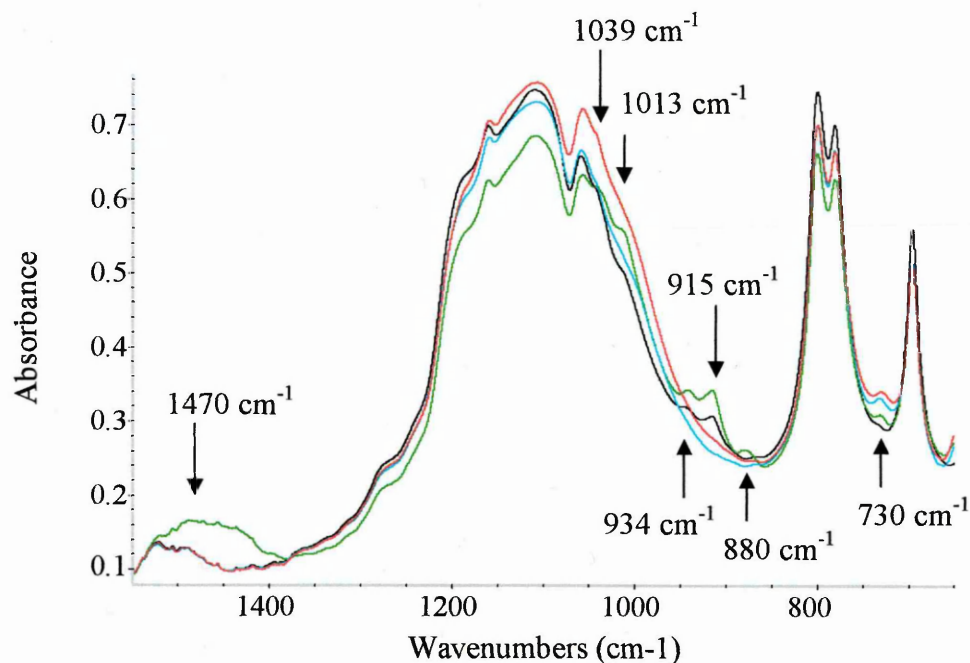


**Figure 7.4: The low wavenumber region of the DRIFTS spectra for ball milled Berea (dark green), Clashach (light blue), Castlegate (black) sandstones, and Chelford sand (red).**

Figure 7.4 shows a marked difference in the bands at  $1013$ ,  $934$  and  $915\text{ cm}^{-1}$ , associated with the clays; kaolinite, montmorillonite, illite, and muscovite, compared with those in Figure 7.2. The spectrum of Berea showed only a shoulder at  $1013\text{ cm}^{-1}$ , and the spectrum of Castlegate only a very slight shoulder. The bands at  $934$  and  $915\text{ cm}^{-1}$  were also more intense in the spectrum of Berea than in the spectrum of Castlegate indicating that Berea contained more clay. However, both sandstones contained less clay than Birchover, Yorkstone, Stancliffe, and Hollington Red

sandstones. The spectra of Chelford sand and Clashach did not display the 1013, 934, and 915  $\text{cm}^{-1}$  bands, again indicating that they did not contain much clay.

The band associated with Na-feldspar at 1039  $\text{cm}^{-1}$  was present as a shoulder in the spectrum of Berea, as a slight shoulder in the spectrum of Castlegate, and as a very slight shoulder in the spectrum of Clashach, indicating the order of decreasing Na-feldspar content. It should also be noted that a very slight shoulder was present in the spectrum of Chelford sand suggesting it may contain some impurity. This is discussed further in section 7.7.2. None of the spectra in Figure 7.4 showed a band at 725  $\text{cm}^{-1}$  (associated with Na-feldspar). However, some showed a band at 730  $\text{cm}^{-1}$  (associated with K-feldspar). The intensity of this band at 730  $\text{cm}^{-1}$  in the spectra, decreased in the order Chelford sand and Clashach, followed by Berea then Castlegate. This suggested that Berea, Clashach, Castlegate and Chelford sand contained a low concentration of Na-feldspar, and that Berea, Clashach and Chelford sand contained K-feldspar. Again, the possibility of impurities in Chelford sand is discussed in section 7.7.2.

The spectrum of Berea was unique due to the presence of a broad band at around 1470  $\text{cm}^{-1}$  and a band at 880  $\text{cm}^{-1}$ . These bands are associated with carbonate. This suggested that Berea contained more calcite and dolomite than the other sandstones.

The strong bands in the sandstone spectra of Figure 7.4, at 800, 781, and 695  $\text{cm}^{-1}$ , are associated with quartz and decreased in intensity in the order Castlegate, Chelford sand, Clashach, then Berea suggesting the order of decreasing quartz content.

Problems may arise in the prediction of the quartz component in the sandstones if, as the quartz band intensities suggested, Chelford sand contained a lower concentration of quartz than Castlegate. The implications of the quartz band intensities on quartz predictions are discussed further in section 7.7.1.

## **7.3 Predicting the Mineral Composition of Powders from Sandstone Rocks using the Absolute PLS Model**

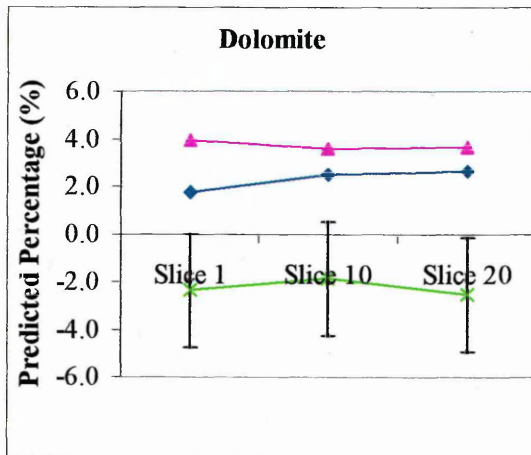
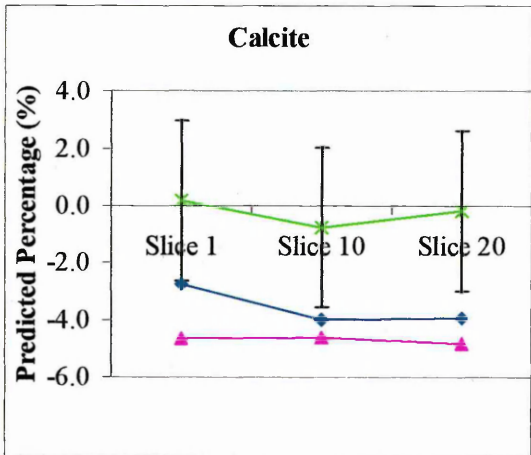
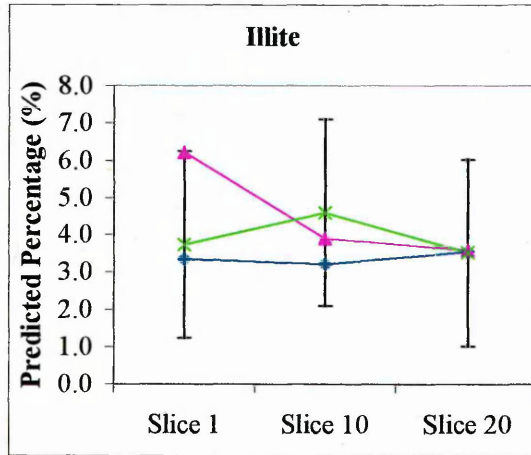
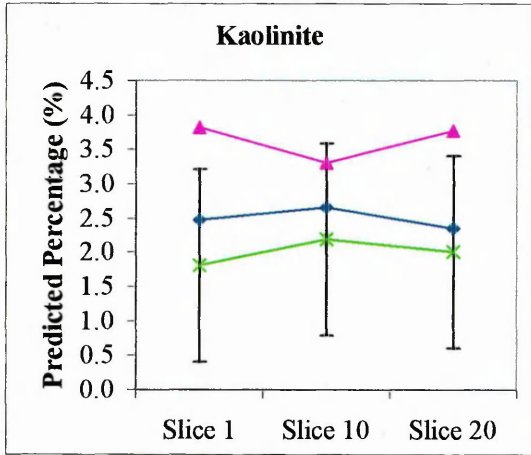
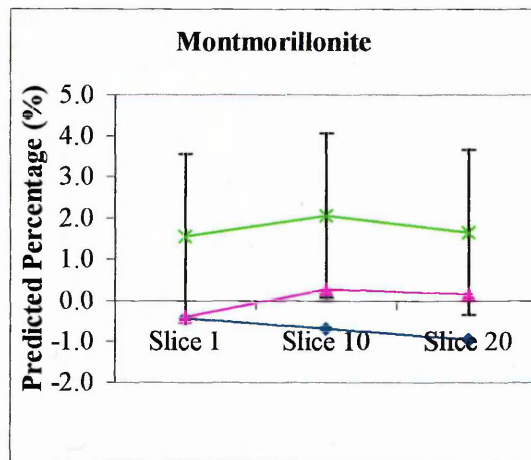
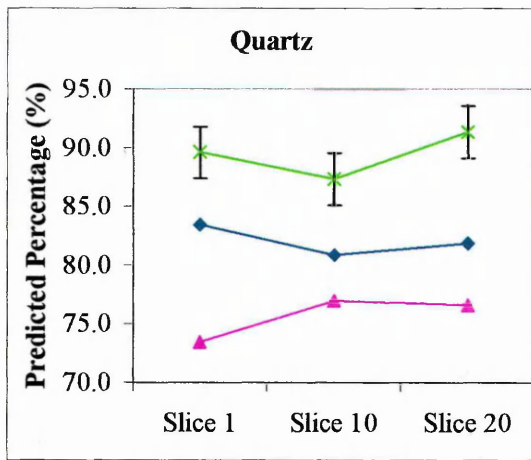
### **7.3.1 Introduction**

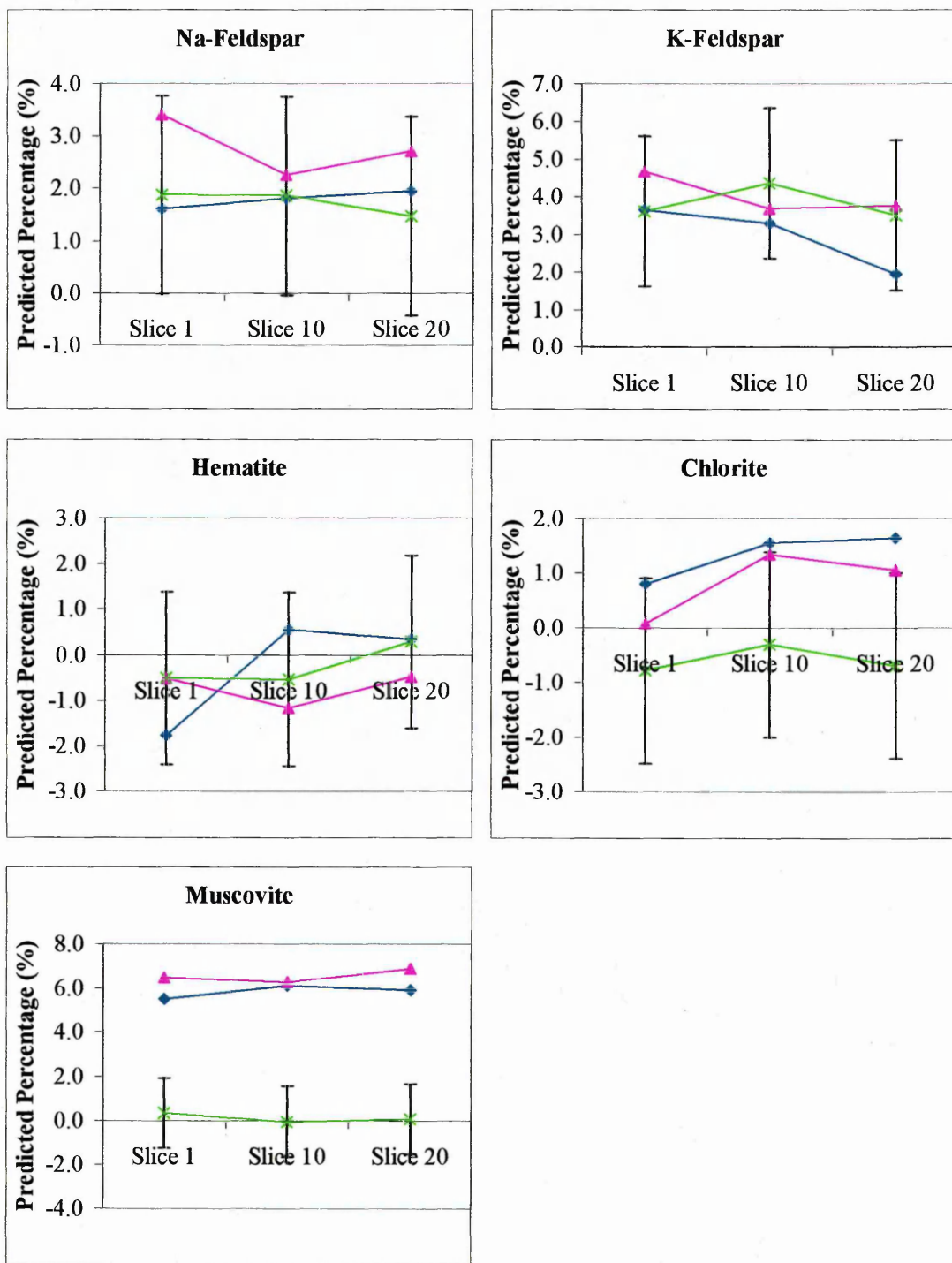
Spectra of the three different sets of sandstone powder samples; powder collected during cutting, ground slices, and ball milled slices, were collected. The wt% of different components present in the powders could then be predicted using the absolute PLS model described in chapter 6.

The components in the powder collected during cutting were predicted separately from the ground and ball milled slice halves so that the effect of the cutting process could be studied. It was thought that clay may be released during the cutting process and also that the friability of the rock may affect the amount of clay released during cutting.

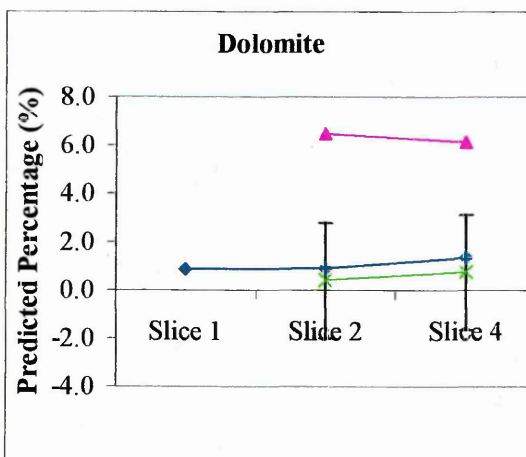
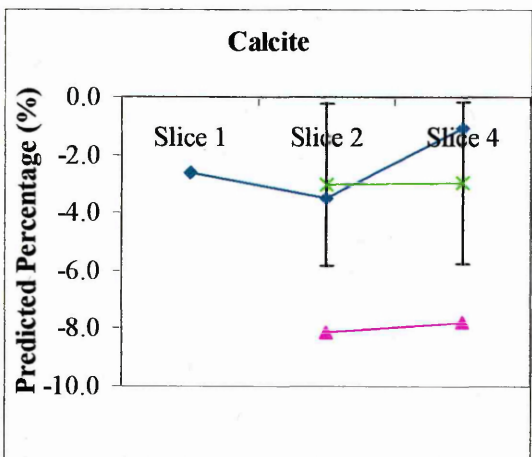
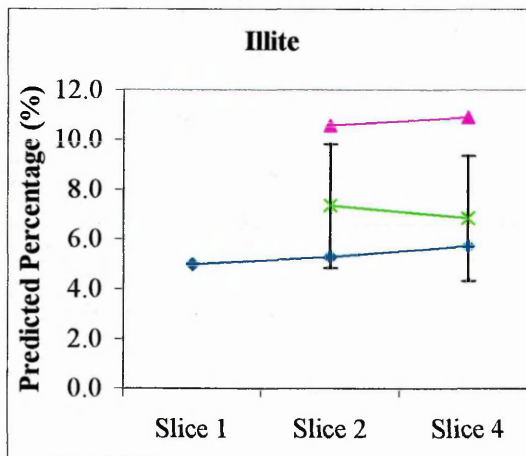
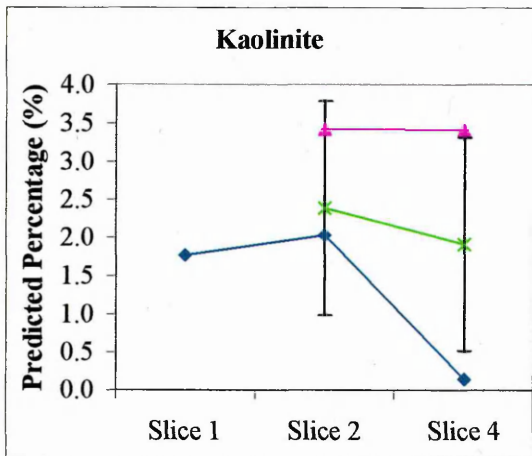
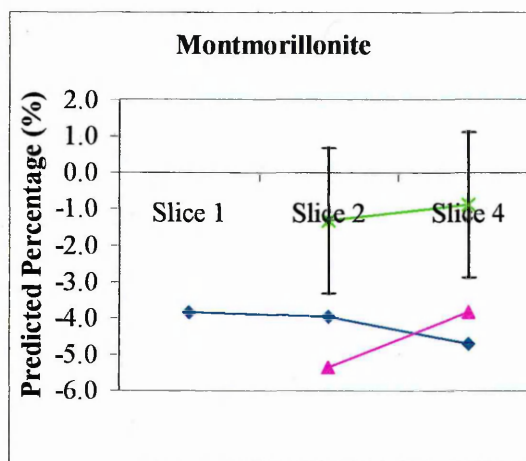
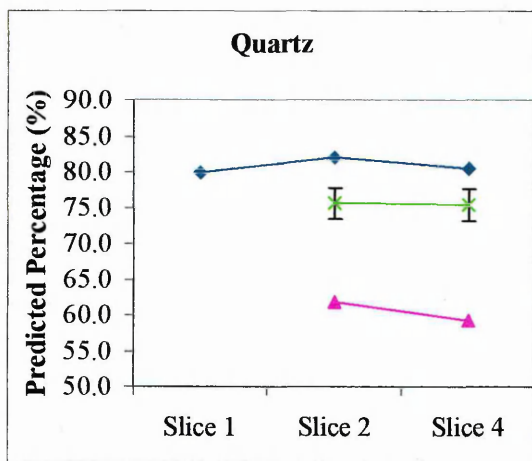
### **7.3.2 Comparing Predictions of Powder from Cutting, Ground Slices, and Ball milled Slices**

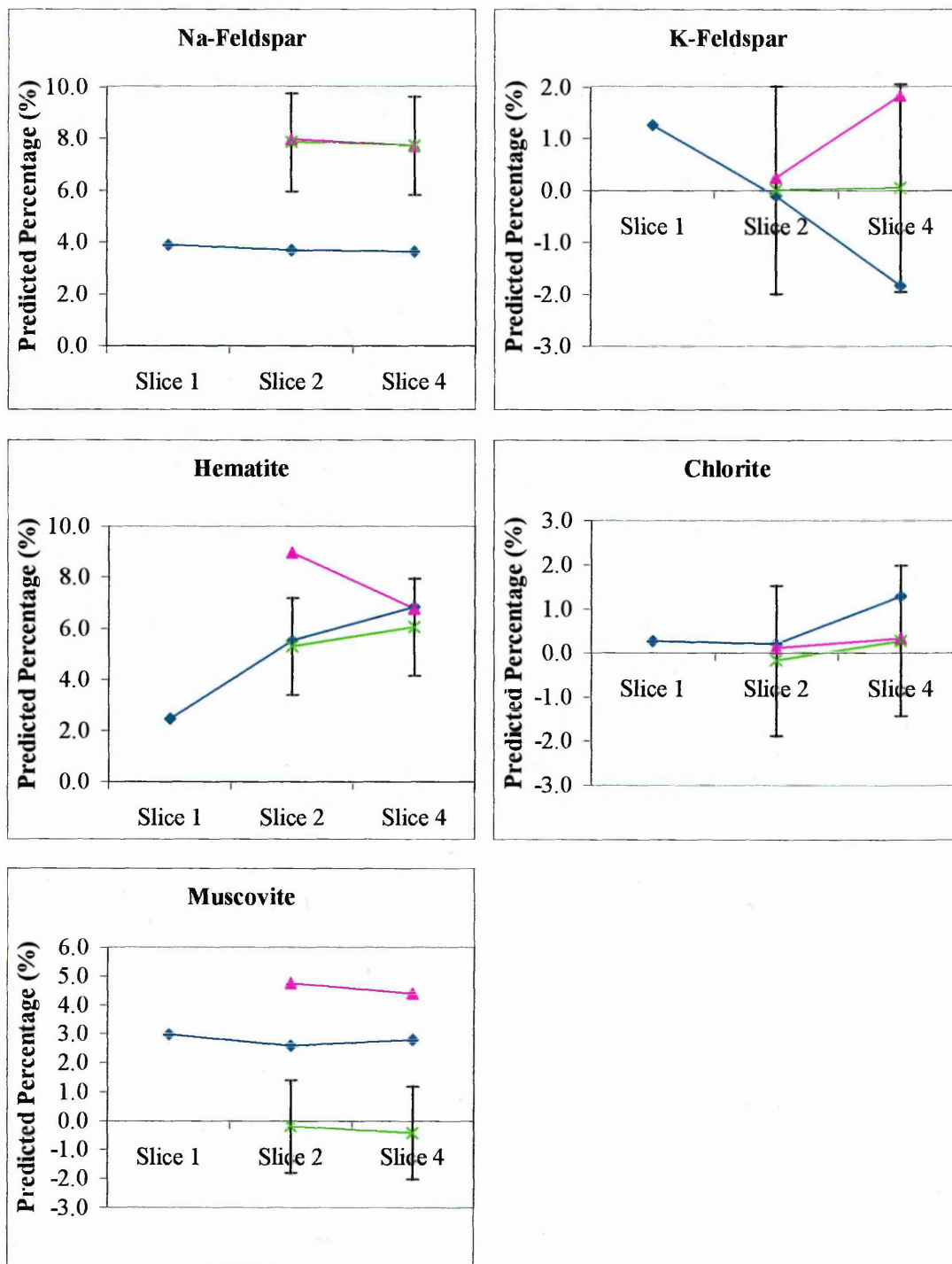
The predicted percentages for each component are shown in Figures 7.5-7.11 for the powders from the three slices of each of the sandstone cores; Hollington Red, Birchover, Yorkstone, Stancliffe, Berea, Clashach, Castlegate. Error bars are shown on the predictions for the ball milled slices of each sandstone. These show the maximum errors (largest difference between the actual and the predicted percentages) calculated for each training set component using the predictions of the independent standards by the absolute PLS model. For any given component, the maximum error for that component was the same for the predictions of the powders from cutting, the ground slices, and the ball milled slices, since all were predicted using the absolute PLS model.



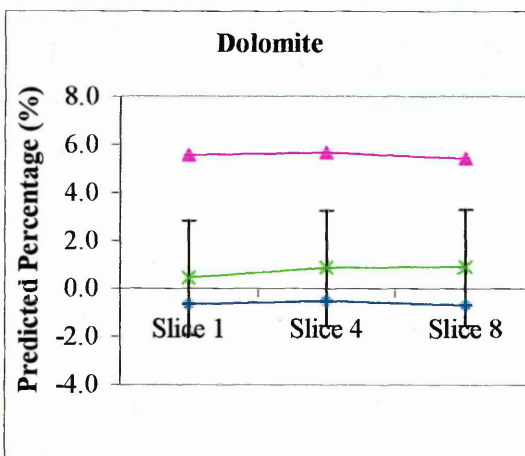
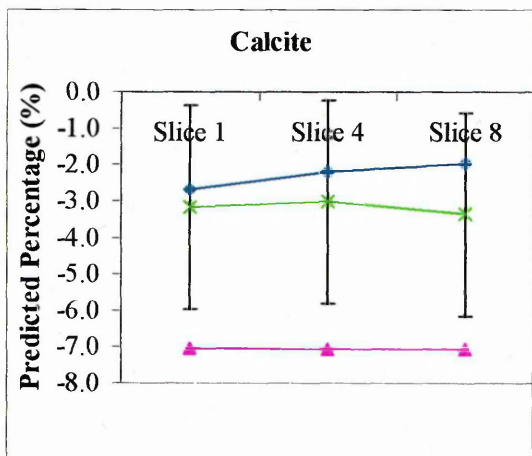
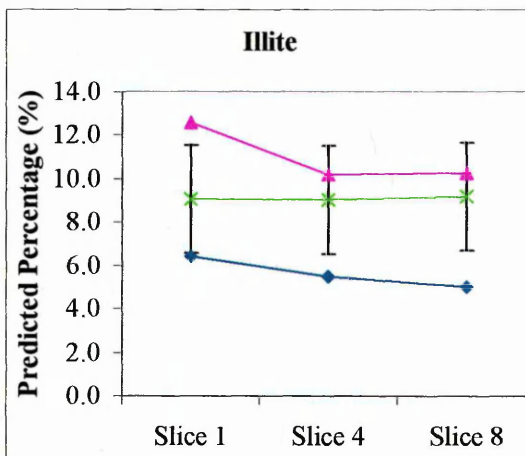
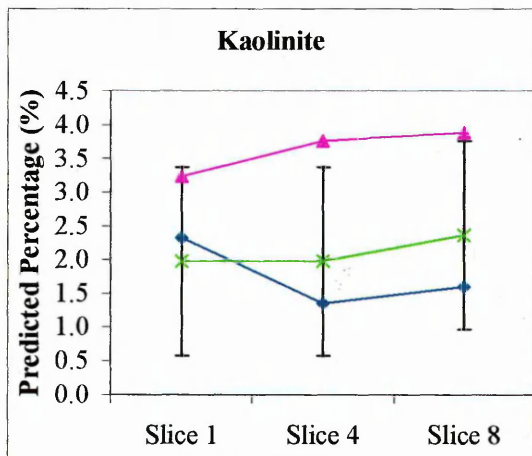
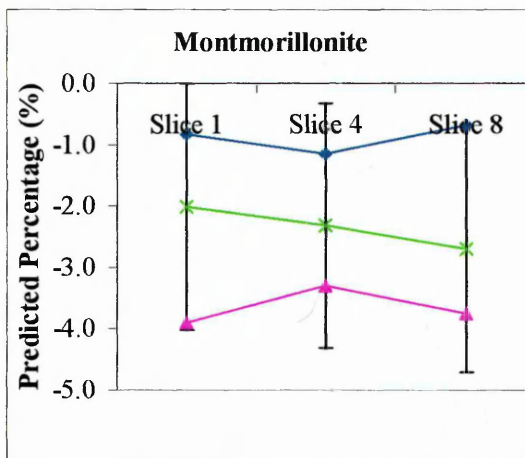
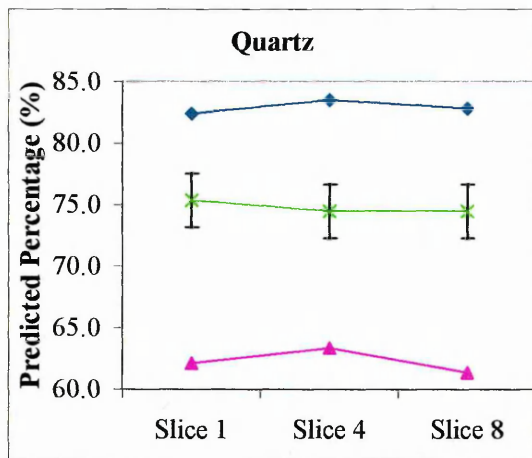


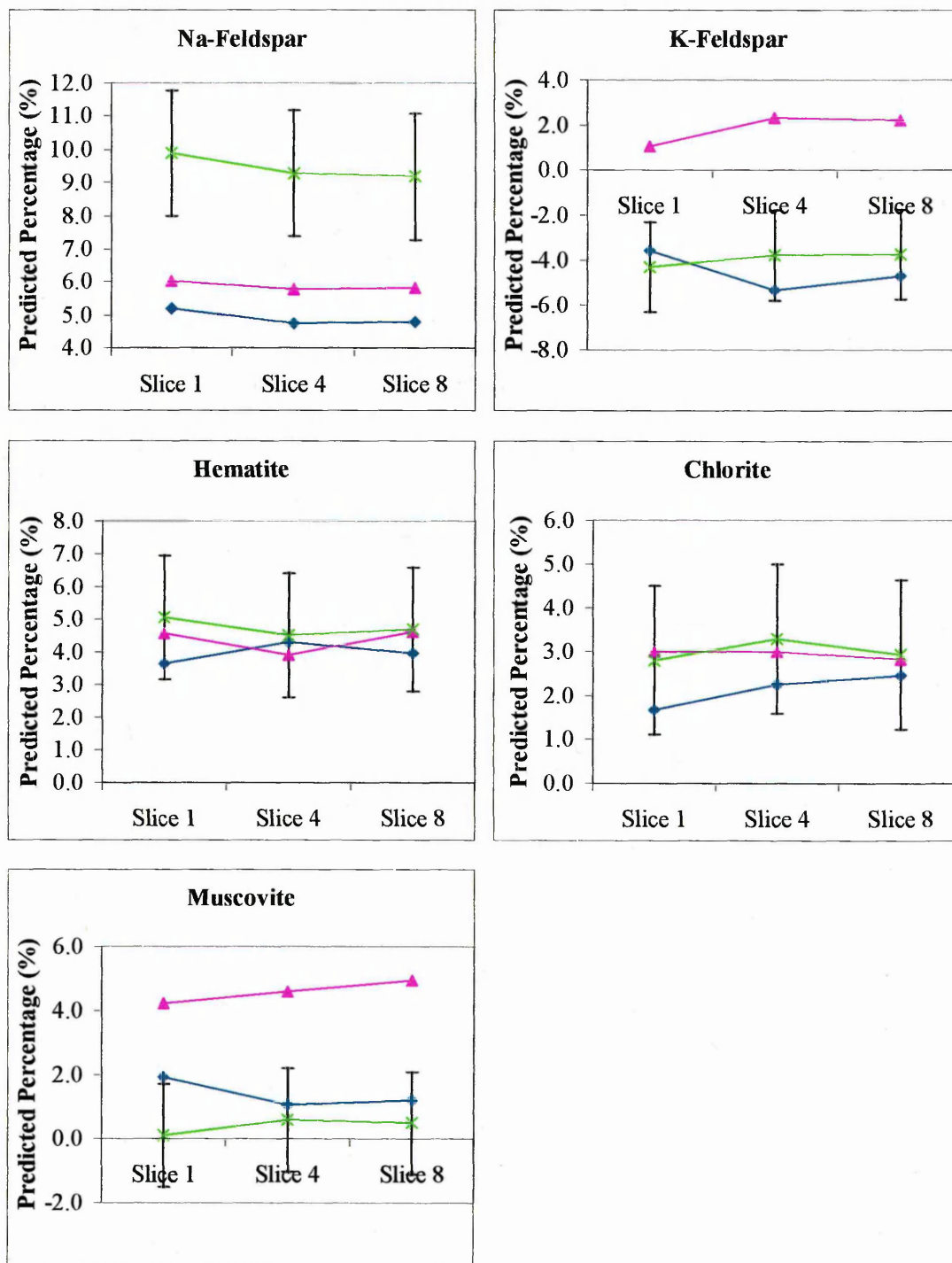
**Figure 7.5: Predicted percentages of each component (in the numbered slices identified) for the powder from cutting (blue), ground slices (pink), and ball milled slices (green) of a Hollington Red core using the absolute PLS model.**



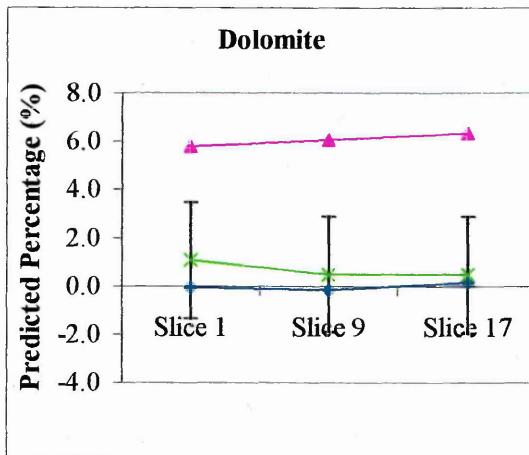
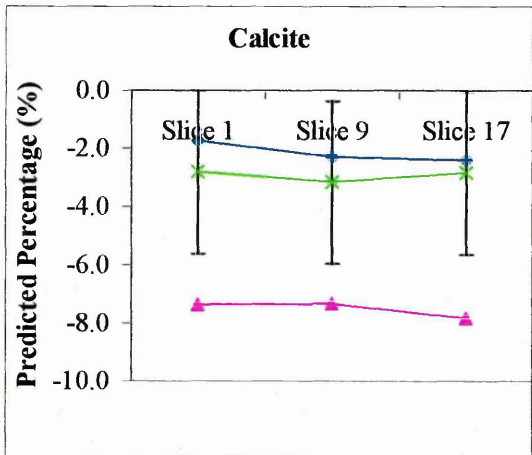
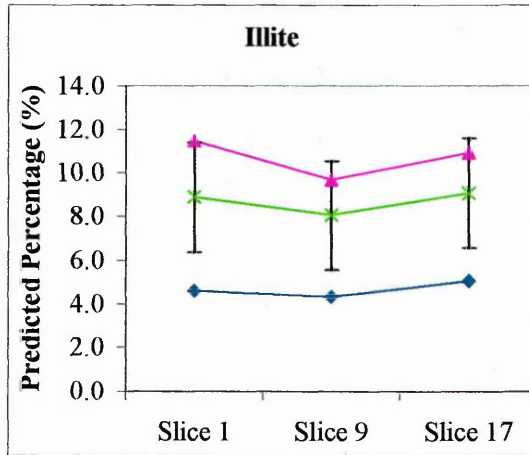
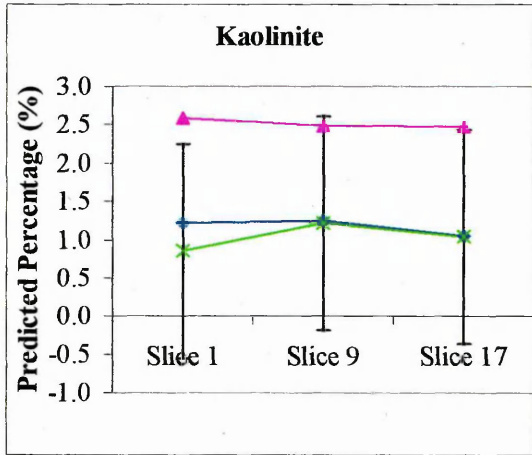
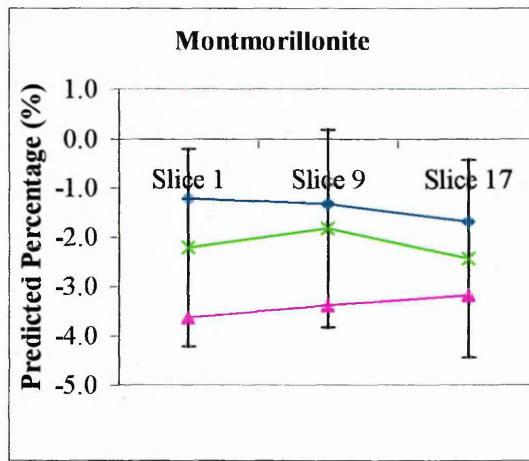
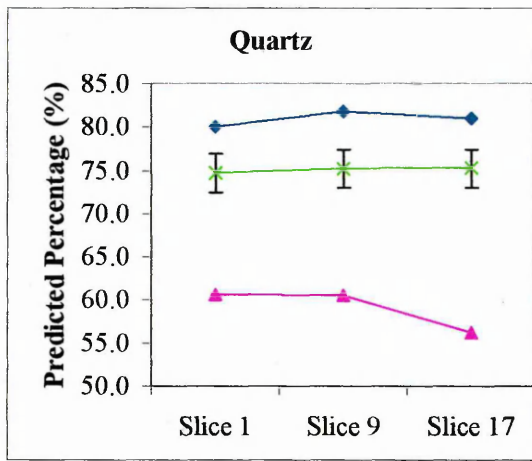


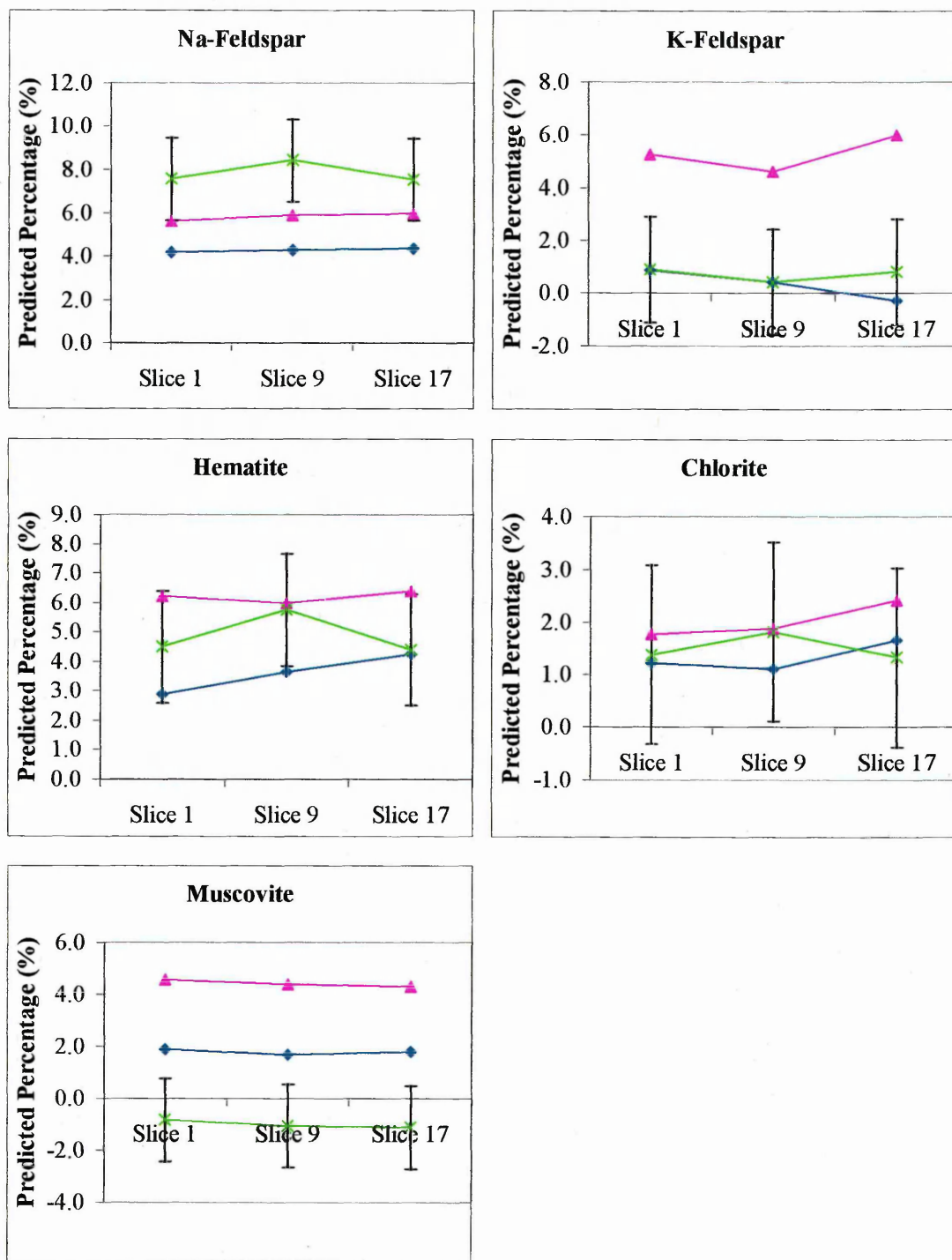
**Figure 7.6: Predicted percentages of each component (in the numbered slices identified) for the powder from cutting (blue), ground slices (pink), and ball milled slices (green) of a Birchover core using the absolute PLS model.**



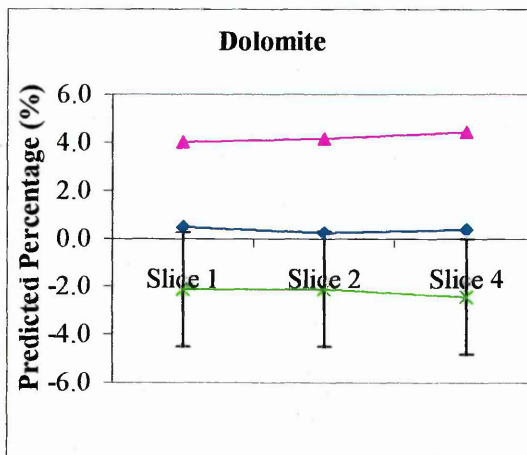
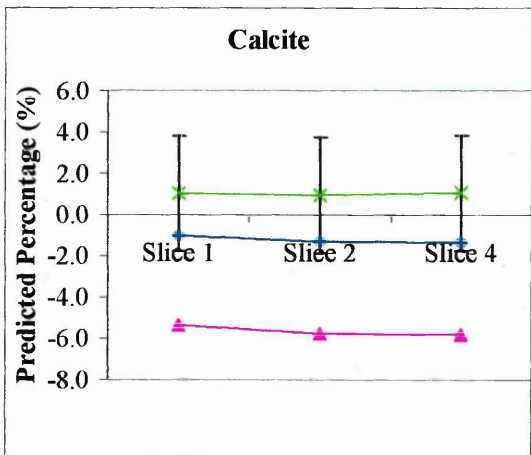
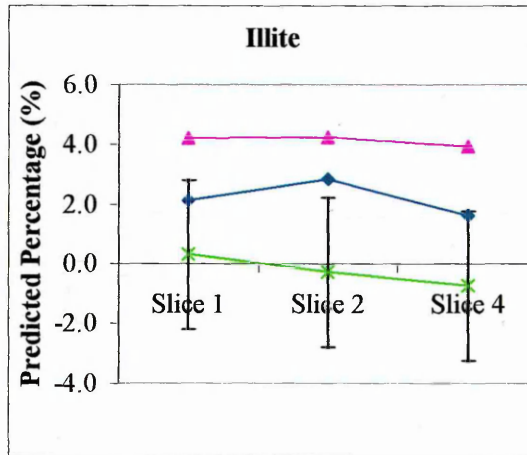
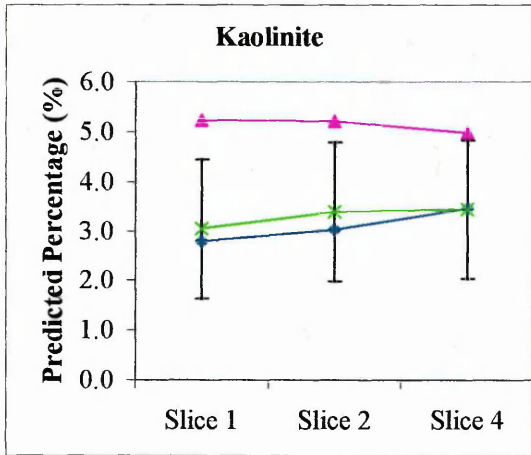
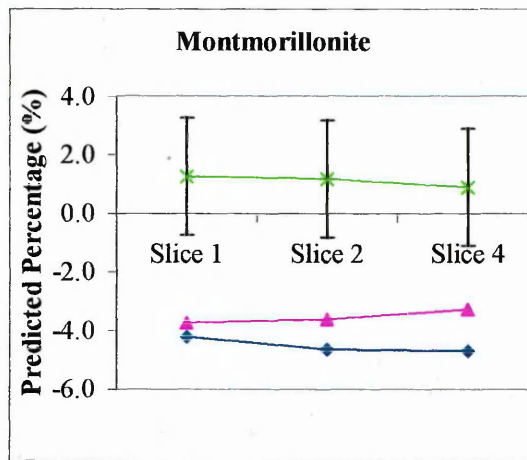
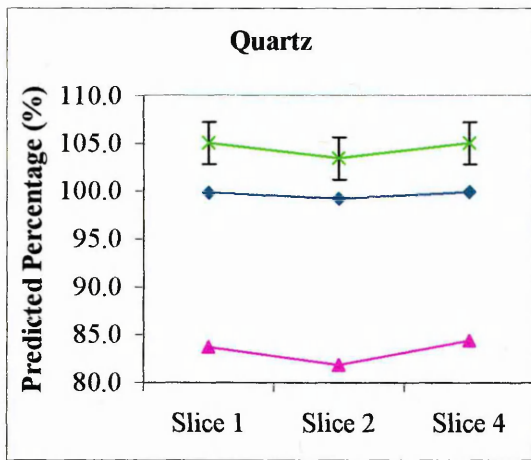


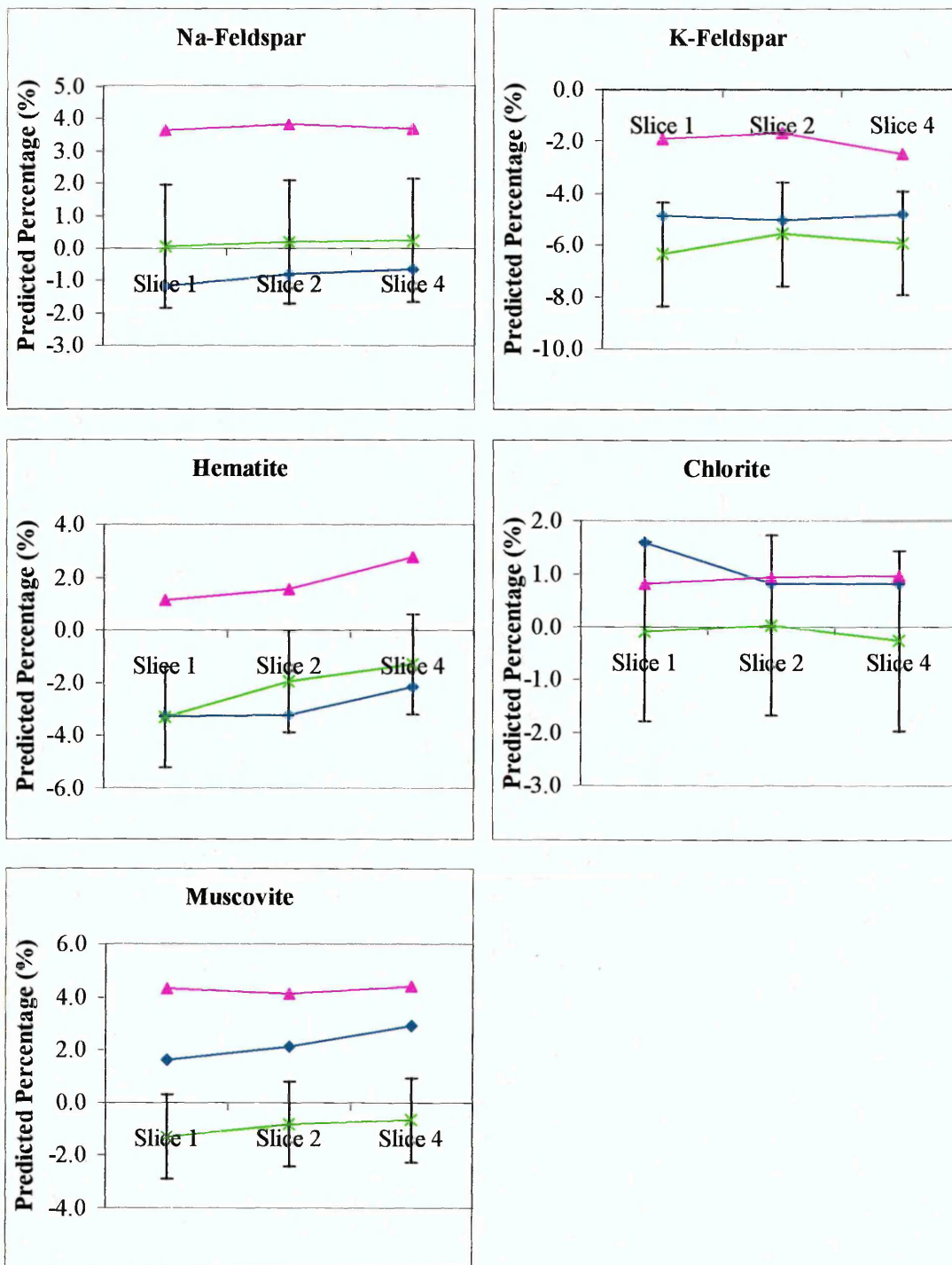
**Figure 7.7: Predicted percentages of each component (in the numbered slices identified) for the powder from cutting (blue), ground slices (pink), and ball milled slices (green) of a Yorkstone core using the absolute PLS model.**



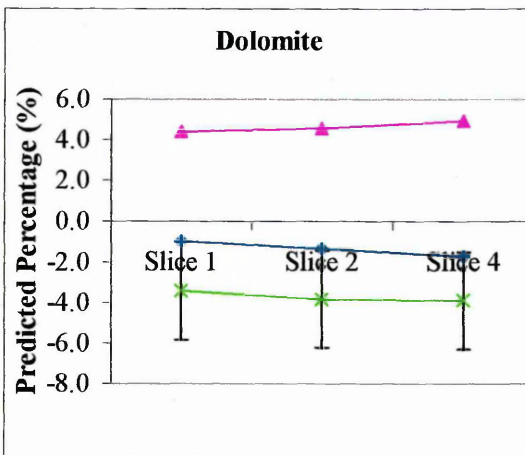
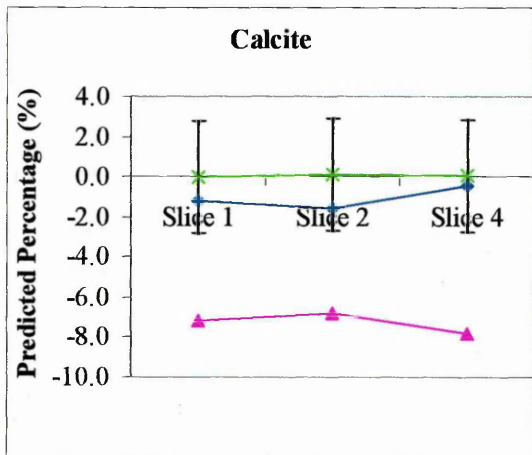
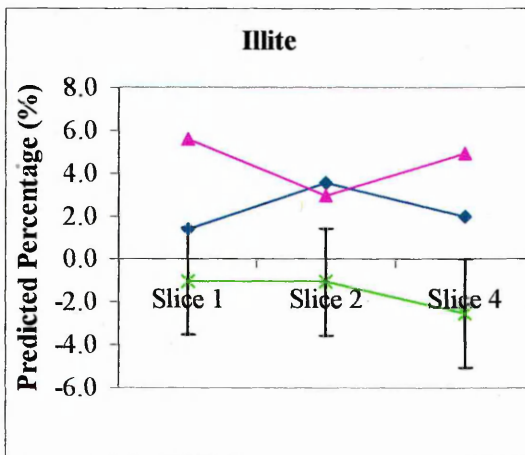
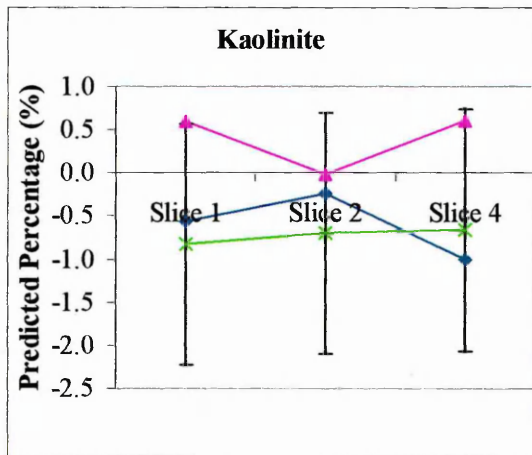
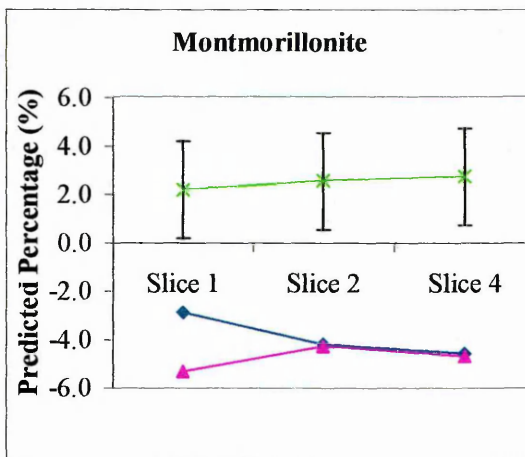
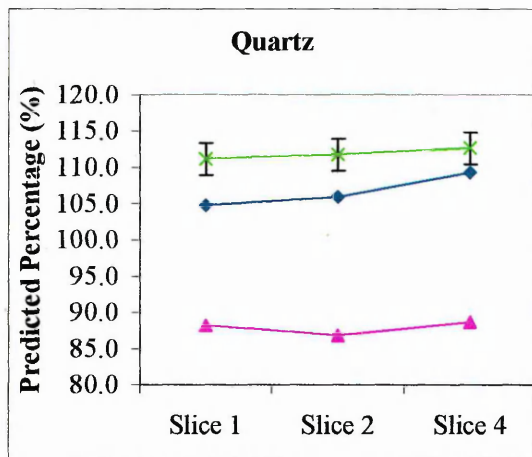


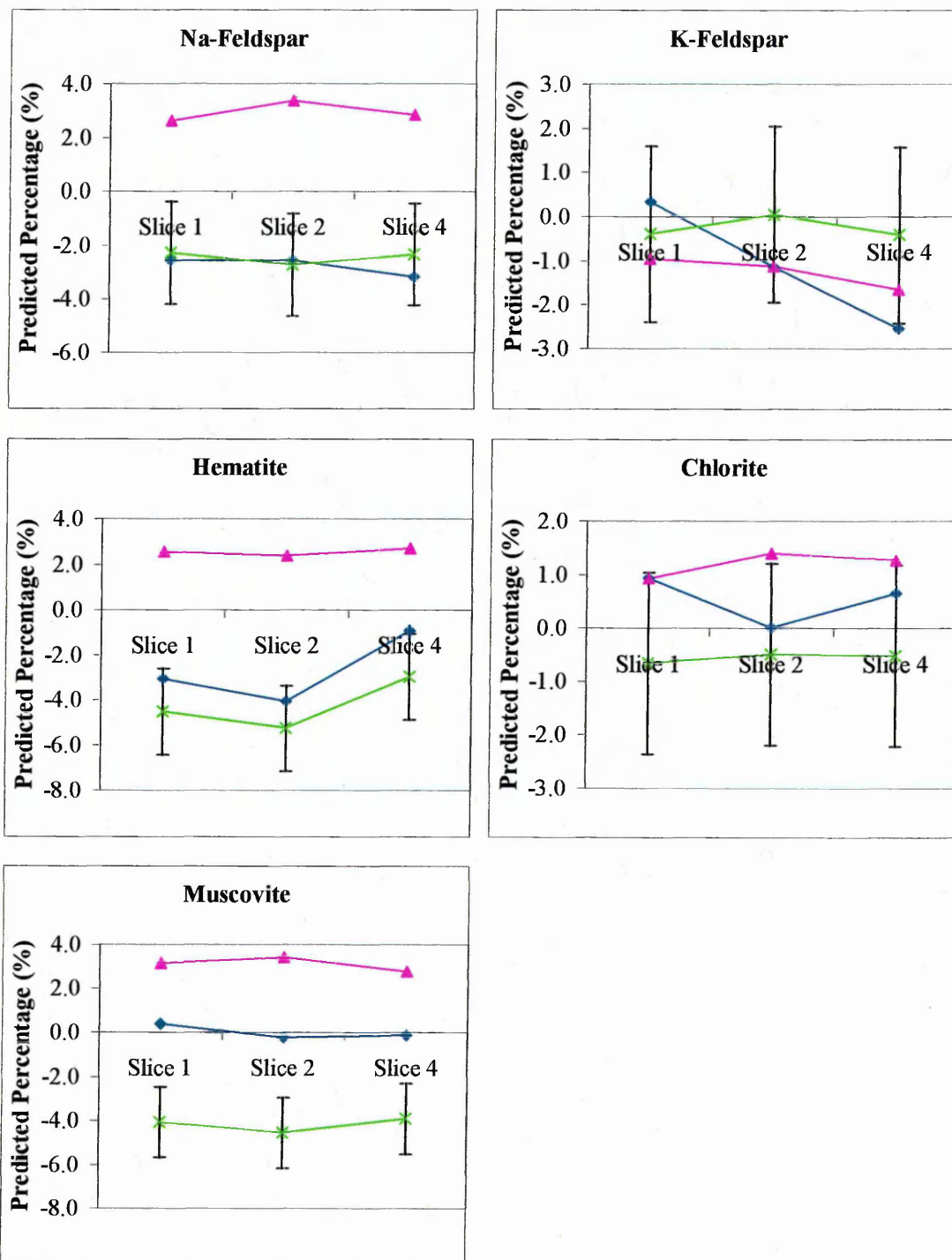
**Figure 7.8: Predicted percentages of each component (in the numbered slices identified) for the powder from cutting (blue), ground slices (pink), and ball milled slices (green) of a Stancliffe core using the absolute PLS model.**



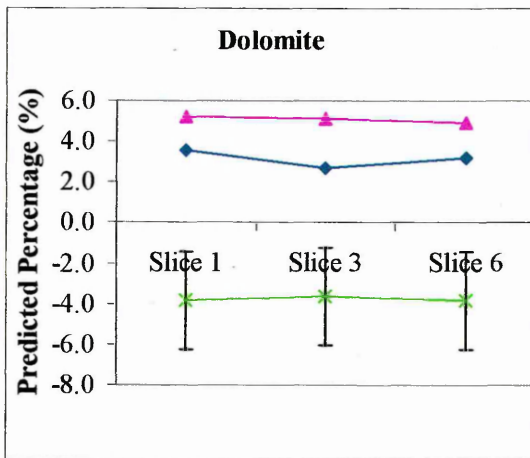
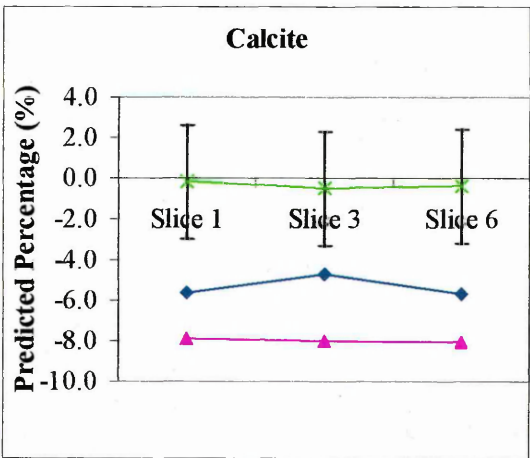
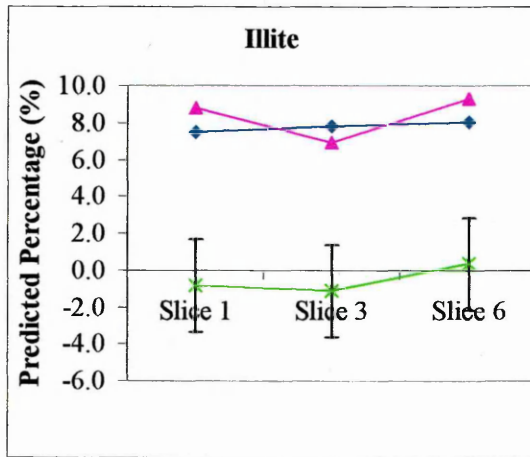
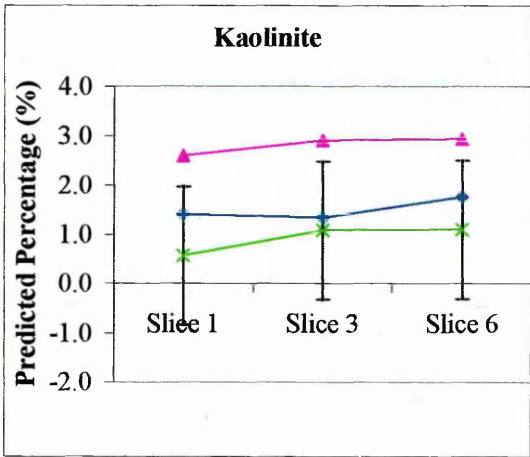
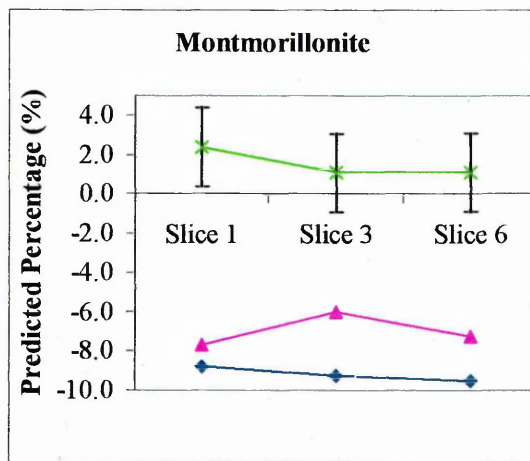
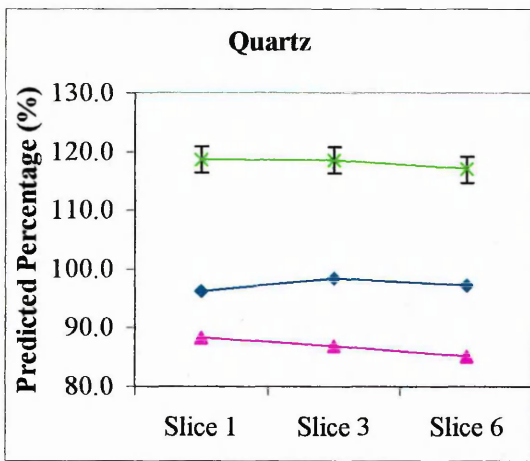


**Figure 7.9: Predicted percentages of each component (in the numbered slices identified) for the powder from cutting (blue), ground slices (pink), and ball milled slices (green) of a Berea core using the absolute PLS model.**





**Figure 7.10: Predicted percentages of each component (in the numbered slices identified) for the powder from cutting (blue), ground slices (pink), and ball milled slices (green) of a Clashach core using the absolute PLS model.**



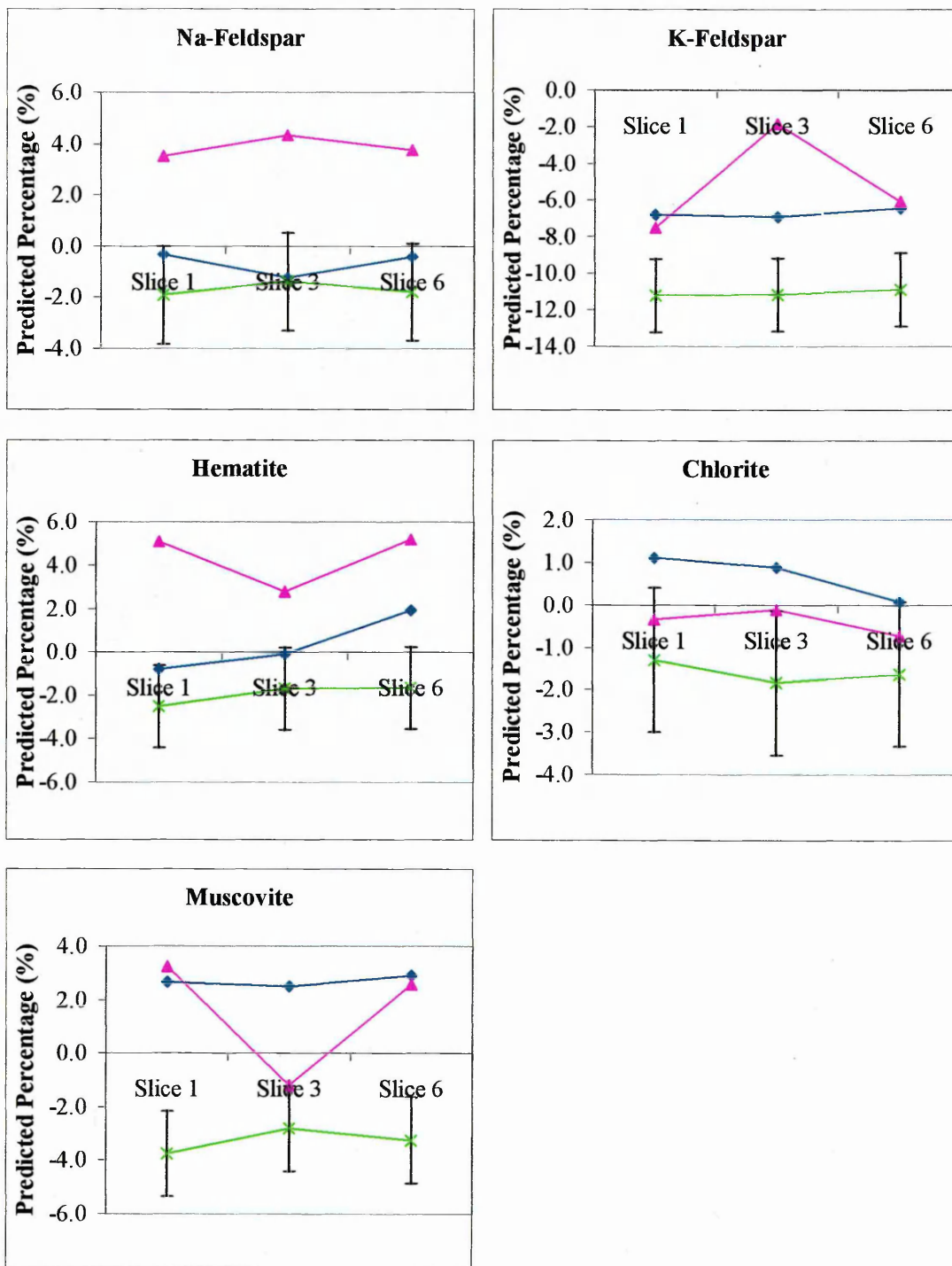


**Figure 7.11: Predicted percentages of each component (in the numbered slices identified) for the powder from cutting (blue), ground slices (pink), and ball milled slices (green) of a Castlegate core using the absolute PLS model.**

A point to note from Figures 7.5-7.11 is that some components were under predicted, giving negative values. This is a problem encountered in all PLS models and can

occur when the predicted concentration of a component is low. The predictions which were negative could either be ignored or assigned as meaning that the sample contained none of that component [21]. Chakrabarty *et al.* [110] also reported that the major drawback of the least squares technique was that it could predict unrealistic, negative, or over 100% values, and there was no way to prevent least squares models from doing this. The over prediction of quartz in the ball milled slices of the softer rocks Berea, Clashach, and Castlegate, by the absolute PLS model is discussed further in section 7.7.

Table 7.1 summaries the percentage of each component predicted for each sandstone. The predictions for the different powder samples were compared, where BM refers to the ball milled slices, PC refers to the powder from cutting, and HG refers to the hand ground slices. Where the predicted percentages were zero or are negative, the boxes are shaded, in order to draw attention to them.

Using Table 7.1 some general observations could be made regarding the predicted percentages of components in the sandstones. Except for the ball milled slices of Hollington Red, Berea, Clashach, and Castlegate, montmorillonite was predicted negatively or at zero. This suggested that there was no montmorillonite present in the sandstones, except in the rock slices of these softer rocks. Calcite, too, was predicted negatively or at zero in all but one sample; the ball milled slice of Berea. This indicated that calcite was not generally present in the sandstones, however, a low concentration may have been present in Berea. With the exception of some of the ground slice samples, no Na-feldspar or K-feldspar was predicted in the softer rocks; Berea, Clashach, and Castlegate. Neither was any K-feldspar present in Birchover and Yorkstone. The predictions for kaolinite and illite were mostly positive, with more illite than kaolinite, generally found in the sandstones. Exceptions to this were, Clashach, where no kaolinite was present, and in the rock slices of Berea, Clashach, and Castlegate, where no illite was present.

		Quartz (wt%)	Montmorillonite (wt%)	Kaolinite (wt%)	Illite (wt%)	Calcite (wt%)	Dolomite (wt%)	Na- Feldspar (wt%)	K- Feldspar (wt%)	Hematite (wt%)	Chlorite (wt%)	Muscovite (wt%)
Hollington Red	BM	90	2	2	4	0	-2	2	4	-0.5	-1	0
	PC	80	-0.5	2.5	3	-3	2	2	3	0	1	6
Birchover	HG	75	0	3.5	4.6	-4.5	3.7	2.5	4	-1	0.5	6
	BM	75	-1	2.5	7	-3	0.5	8	0	5.5	0	0
	PC	80	-4	1	5	-2.5	1	4	0	5	1	3
Yorkstone	HG	60	-4	3.5	10	-8	5.5	8	1	8	0	4.5
	BM	75	-2.5	2	9	-3	1	9.5	-4	4.5	3	0.5
Stancilffe	PC	83	-1	1.5	6	-2.5	-0.5	5	-5	4.5	2	1.5
	HG	63	-3.5	3.5	11	-7	6	6	2	4.5	3	4.5
Berea	BM	75	-2	1	8.5	-3	1	8	1	5	1.5	-1
	PC	80	-1.5	1	4.5	-2	0	4.5	0.5	3.5	1	2
	HG	58	-3.5	2.5	10	-7.5	6	6	5.5	6	2	4.5
Clashach	BM	105	1	3	0	1	-2	0	-6	-2	0	-1
	PC	100	-4.5	3	2	-1	0	-1	-5	-3	1	2
	HG	83	-3.5	5	4	-5.5	4	4	-2	2	1	4
Castlegate	BM	112	2.5	-1	-1	0	-3.5	-2.5	0	-4	-0.5	-4
	PC	107	-4	-0.5	3	-1	-1.5	-2.5	-1	-3	0.5	0
	HG	87	-4.5	0.25	4	-7	4.5	3	-1	2.5	1	3
Castlegate	BM	118	1.5	1	-0.5	-0.5	-4	-2	-11	-2	-1.5	-3
	PC	97	-9	1.5	8	-5.5	3	-1	-7	0	1	2.5
	HG	87	-7	3	8	-8	5	4	-5	4	-0.5	1

Table 7.1: Percentages of each named component predicted in the ball milled slices (BM), the powder from cutting (PC), and the hand ground slices (HG), of different sandstones.

The predictions of components in the powder from cutting, ground slices, and ball milled slices, were in many cases significantly different. One possible reason for this was that certain mineral components may have been preferentially released from the rock during cutting and were therefore more concentrated in the powder collected. Predictions for the harder rocks Birchover (Figure 7.6), Yorkstone (Figure 7.7), and Stancliffe (Figure 7.8), generally showed a lower concentration of quartz in the ball milled slices than in the powder from cutting, implying that more quartz was released as powder during the cutting of these rocks. The opposite trend was observed for the softer rocks, Hollington Red (Figure 7.5), Berea (Figure 7.9), Clashach (Figure 7.10), and Castlegate (Figure 7.11), where a higher concentration of quartz was predicted in the ball milled slices than in the powder from cutting, implying that more quartz remained in the rock slice during the cutting process. It should again be noted, however, that in the ball milled slices of Berea, Clashach, and Castlegate, the quartz was actually predicted at over 100 wt%. A possible reason for the location of the higher concentration of quartz is that in the harder, denser rocks, the grains could have been held in place by strong cement, so when cut, the saw actually cut through quartz grains, producing a relatively smooth rock slice surface and releasing a powder which was rich in quartz. When the softer, less dense, rocks were cut, however, the saw could have separated the quartz grains rather than cutting through them, producing a rougher rock slice surface, and the release of less powder. The powder that was released was lower in quartz content than that remaining in the rock slice.

The presence of clay in the ball milled slices, and in the powders from cutting the harder and softer rocks, appeared to follow an opposite trend to that of quartz. If the predicted percentages of the layer silicates; montmorillonite, kaolinite, illite, chlorite, and muscovite were added for each sample then it could be said that, generally, more of the layer silicates were present in the ball milled slices of the harder rocks than in the powder from cutting. For the softer rocks, very little layer silicate was generally found but, where it was present, more was found in the powder from cutting than in the ball milled slices. This implied that during the cutting of the harder rocks, more layer silicates remained in the rock, while during the cutting of the softer rocks more was released as powder. This could be because in the harder rocks, the layer silicates could have been pore-lining, so the cutting process would not damage them and more would remain in place. In the softer rocks, however, the little layer silicate present

may have acted as a weak cement so during the cutting process more was released as powder when the quartz grains were separated.

The location of clays after cutting was also investigated in chapter 5, in section 5.4.3.3, by visual interrogation of the XRD traces for the rock slices and for the powder from cutting each sandstone. From the intensity of the illite/muscovite peak at  $8.9^\circ 2\theta$  for the different sandstones it was thought that in all the sandstones, more illite/muscovite was present in the powder from cutting than in the rock slices. Although the predictions in Figures 7.5-7.11 suggested that more illite remained in the rock slice of the harder rocks, after cutting, it should be noted that for all sandstones more muscovite was predicted in the powder from cutting than in the rock slices, and it may be muscovite which dominated the XRD peak at  $8.9^\circ 2\theta$ . Enhanced intensity of the illite/muscovite peak in the XRD traces of the powders, however, may also be due to preferred orientation of the clays in the powder samples, as discussed in section 5.4.3.2 of chapter 5.

Most of the component predictions along the length of the core were within the model error bars, and in fact all the predictions for the ball milled slices were within the error bars. Predictions outside the error bars could be found for the powder from cutting Birchover (Figure 7.6), for components; kaolinite, K-feldspar, and hematite. The powder from cutting Clashach (Figure 7.10) also showed predictions outside the error bars for K-feldspar. For Castlegate (Figure 7.11), predictions for K-feldspar, hematite, and muscovite were again outside the error bars in the ground slices. While in these few cases, variation in mineralogy along the cores was indicated, the vast majority of the component predictions along the length of each core were within the model error bars suggesting that there were no significant differences in mineralogy along the length of the cores. This result was in contrast to the initial investigation in chapter 5, where it was thought from visual interrogation of the XRD traces of core slices that there may be significant differences in mineralogy along the length of a core.

Since both the ground slices and the ball milled slices originated from the rock slices themselves, the component predictions in each should be similar. The predictions for the ground slices and ball milled slices were, however, often significantly different. It

was thought that this was due to the difference in particle size and particle size distribution, of the powders. The effect of the large particle size, and large particle size distribution, of the slices ground by hand, on their DRIFTS spectra, may be too great to give the predictions any significant meaning. The particle size of the powders from cutting, hand ground slices, and ball milled slices, is discussed further in the following section 7.3.3.

### **7.3.3 Comparing the Particle Size of Powders**

#### **7.3.3.1 Introduction**

The difference in particle size of the different sets of powders; powder from cutting, ground slices, and ball milled slices, would have an effect on the percentages of components predicted in them. It was known that of the three sets of powders, the hand ground slices had the largest particle sizes and largest particle size distribution. The quartz grains were large and hard to crush, while the other mineral components had finer particle sizes. The powders ground manually in a mortar and pestle gave the lowest predicted percentages of quartz and this was because the large particle size of quartz in these samples produced spectra with lower intensity, differently shaped, Si-O stretching bands. Reig *et al.* [106] studied the effect of particle size on the spectra of ground silica samples. Absorbance ratios were used to quantify the amount of silica in a mixture, and it was found that the greatest influence on the accuracy of the quantification was the homogeneity of the particle size, and not the particle size itself. When the particle size distribution was small, quartz was quantified more accurately, even if the particle size was relatively large (around 40  $\mu\text{m}$ ).

#### **7.3.3.2 Comparing DRIFTS spectra of Powders**

The relationship between particle size and band intensity in the DRIFTS spectra has been discussed previously in sections 2.1.5.5.2 and 6.3.2. Figures 7.12-7.18 show the DRIFTS spectra of the powder from cutting, the ground slices, and the ball milled slices, for one slice of each sandstone core. The bands associated with antisymmetric Si-O-Si stretching (1200-1050  $\text{cm}^{-1}$  region), symmetric Si-O-Si stretching (800 and

781  $\text{cm}^{-1}$ ), and O-Si-O bending (695  $\text{cm}^{-1}$ ) were compared for each sample. The spectrum of ball milled pure Chelford sand was also included for comparison.

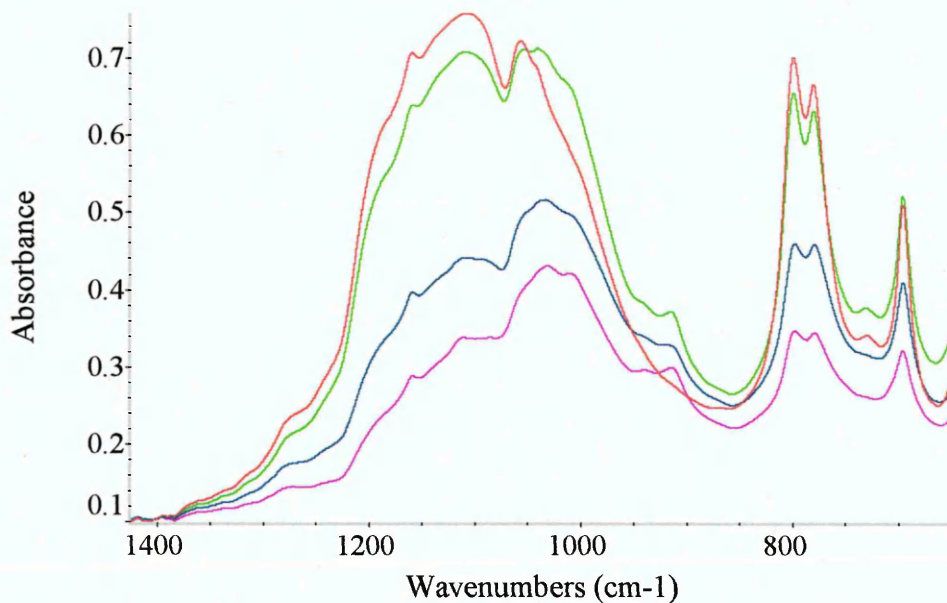


**Figure 7.12: DRIFTS spectra of ball milled Chelford sand (red), compared with the corresponding spectra for the ball milled slice 1 (green), powder from cutting slice 1 (blue), and ground slice 1 (pink) of Hollington Red.**

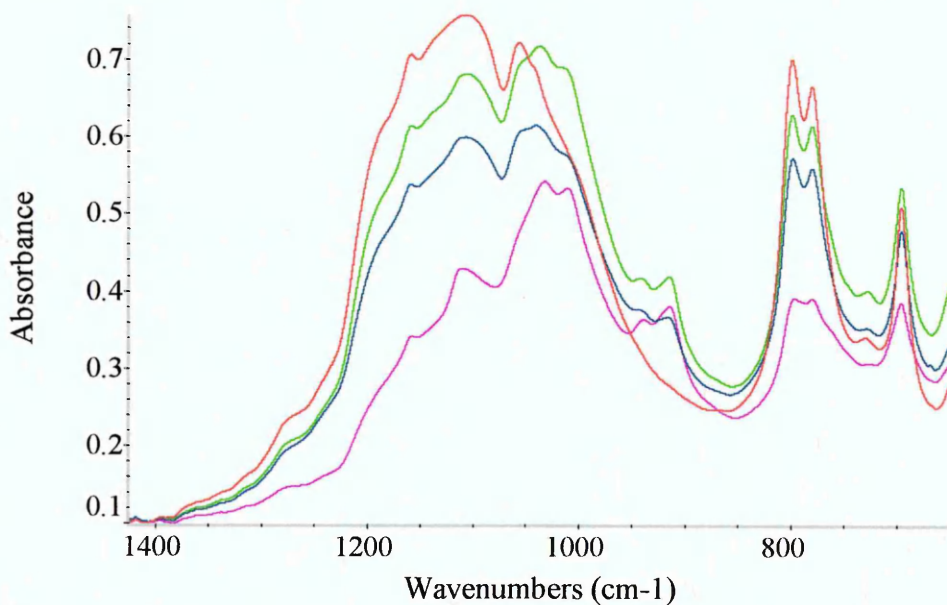


**Figure 7.13: DRIFTS spectra of ball milled Chelford sand (red), compared with the corresponding spectra for the ball milled slice 2 (green), powder from cutting slice 2 (blue), and ground slice 2 (pink) of Birchover.**

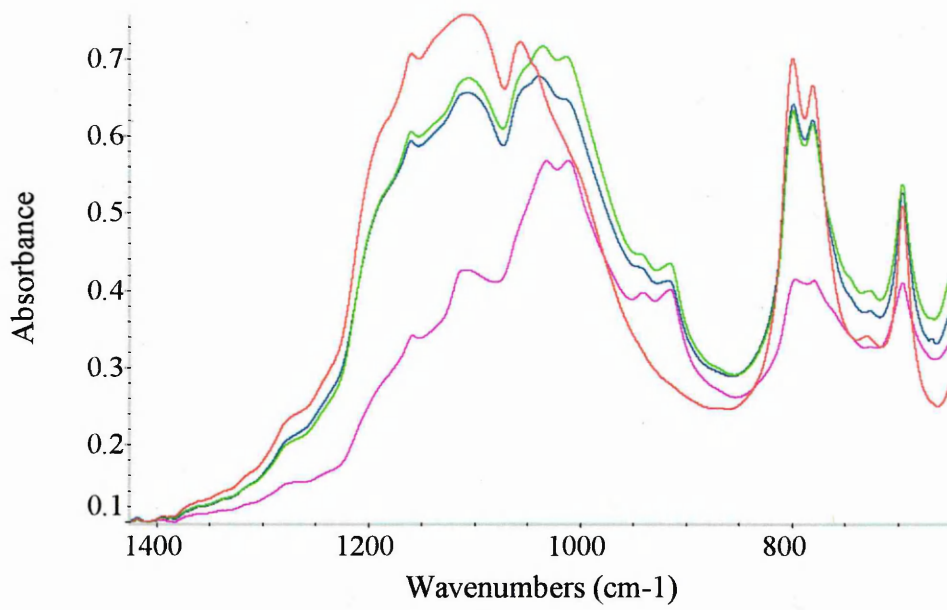


**Figure 7.14: DRIFTS spectra of ball milled Chelford sand (red), compared with the corresponding spectra for the ball milled slice 1 (green), powder from cutting slice 1 (blue), and ground slice 1 (pink) of Yorkstone.**

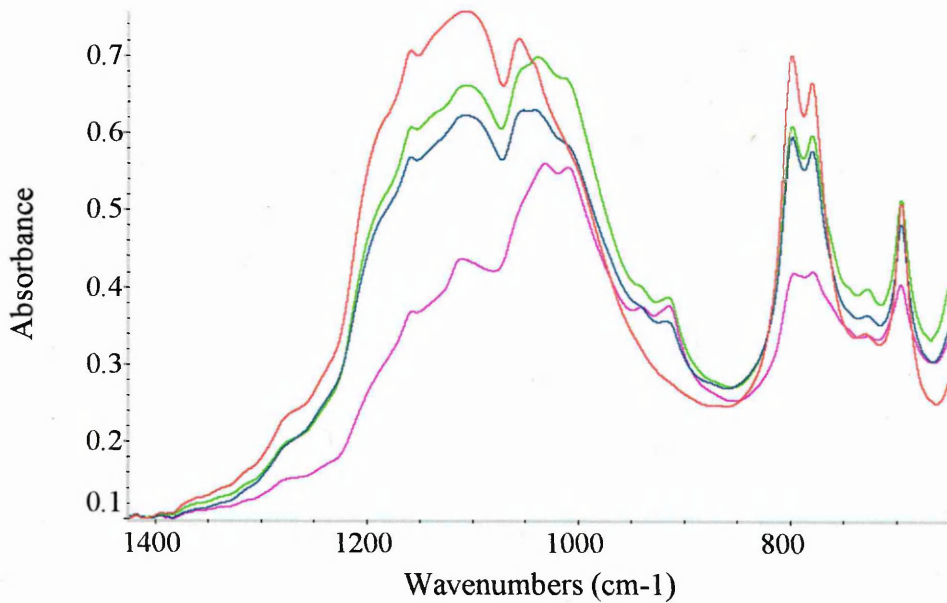


**Figure 7.15: DRIFTS spectra of ball milled Chelford sand (red), compared with the corresponding spectra for the ball milled slice 1 (green), powder from cutting slice 1 (blue), and ground slice 1 (pink) of Stancliffe.**

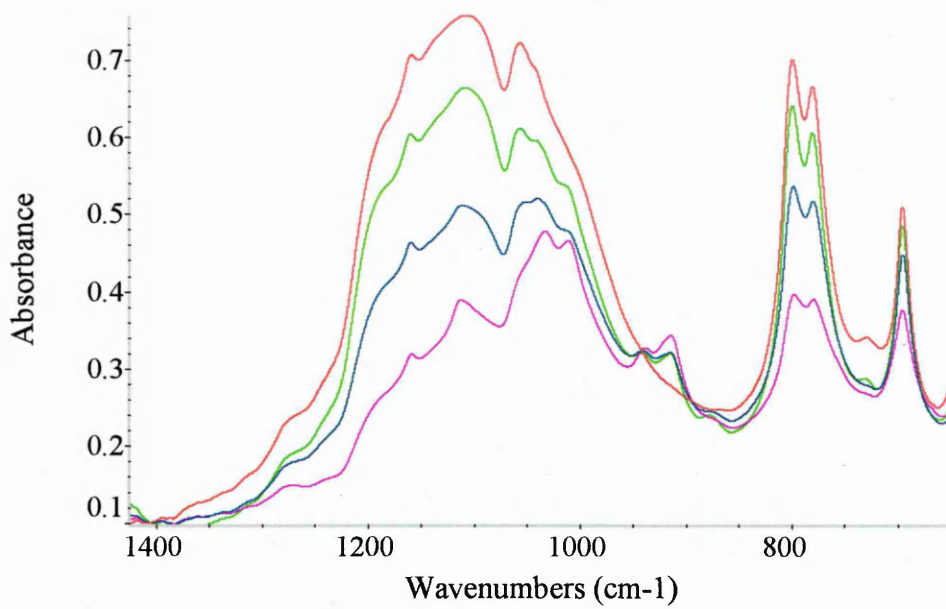


**Figure 7.16: DRIFTS spectra of ball milled Chelford sand (red), compared with the corresponding spectra for the ball milled slice 1 (green), powder from cutting slice 1 (blue), and ground slice 1 (pink) of Berea.**

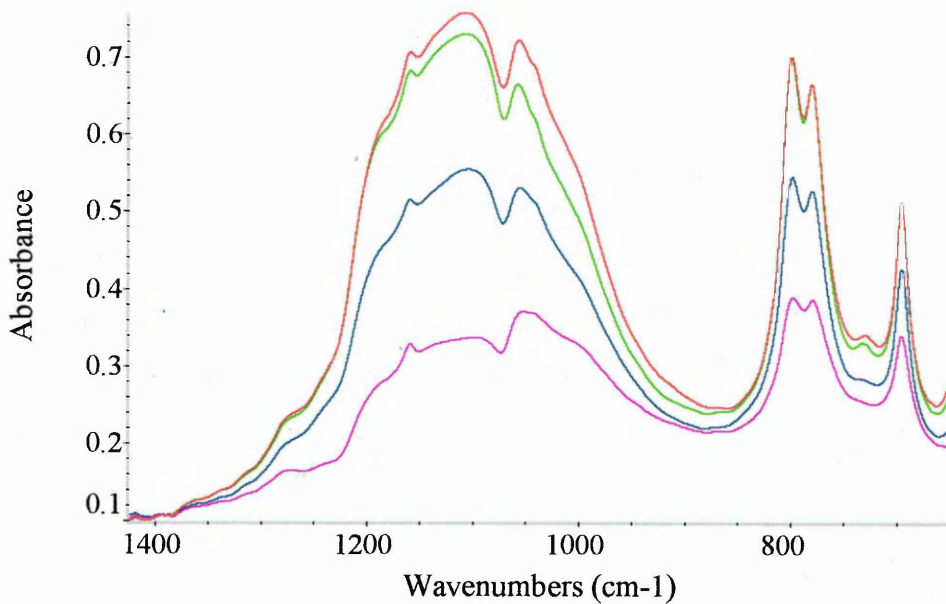


**Figure 7.17: DRIFTS spectra of ball milled Chelford sand (red), compared with the corresponding spectra for the ball milled slice 1 (green), powder from cutting slice 1 (blue), and ground slice 1 (pink) of Clashach.**

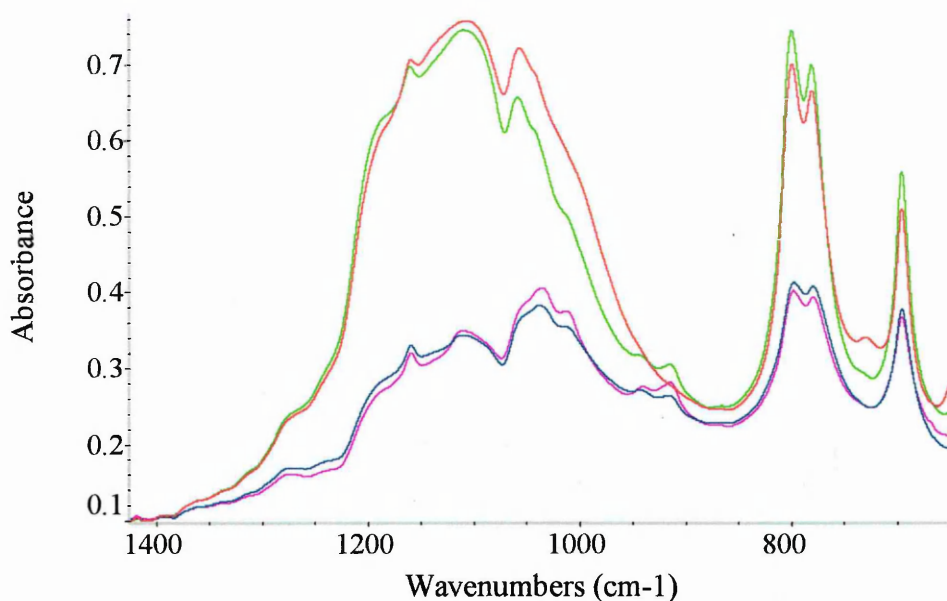


**Figure 7.18: DRIFTS spectra of ball milled Chelford sand (red), compared with the corresponding spectra for the ball milled slice 1 (green), powder from cutting slice 1 (blue), and ground slice 1 (pink) of Castlegate.**

The intensity of the bands gave some indication of the difference in particle size of the different powders. The most intense and well resolved bands at 800 and 781  $\text{cm}^{-1}$  were generally observed in the spectra of Chelford sand and the ball milled sandstone slices, suggesting that these samples had the smallest particle size. The spectra of the powder collected from cutting showed that generally these bands had a lower intensity than those in the ball milled slice spectra. This implied that the powders from cutting had a larger particle size than the ball milled slices. As predicted, the spectra of the ground slices exhibited less well resolved bands of lower intensities, since these powders contained the largest particles.

Not only were the intensities of the bands at 800 and 781  $\text{cm}^{-1}$ , in the powder from cutting, the ground slices, and the ball milled slices different, but also the ratio of the bands. The ratio of the 800 and 781  $\text{cm}^{-1}$  bands to the band at 695  $\text{cm}^{-1}$  also varied with the different powders. In the spectra of the ground slices, the intensities of the bands at 800 and 781  $\text{cm}^{-1}$  were very similar and there was only a slight difference in intensity between these bands and the band at 695  $\text{cm}^{-1}$ . In the spectra of the ball milled slices, the intensity ratios were more similar to those in the spectrum of Chelford sand, with the band at 800  $\text{cm}^{-1}$  more intense than that at 781  $\text{cm}^{-1}$ , and a larger intensity difference between these two bands, and the band at 695  $\text{cm}^{-1}$ . It was

thought to be the presence of more feldspar in the ground slices than in the ball milled slices that caused the bands at 800 and 781  $\text{cm}^{-1}$  to be of more similar intensity in the spectra of the ground slices, since both feldspars have spectra with bands near 780  $\text{cm}^{-1}$ . The bands at 800 and 781  $\text{cm}^{-1}$  in the spectra of Chelford sand, Na-, and K-feldspars are shown in more detail in Figure 7.56 in section 7.7.2.1.

It should be noted that in the spectrum of ball milled Clashach, the intensity of the 800 and 781  $\text{cm}^{-1}$  bands were very similar to the intensity of those in the spectrum of Chelford sand. Furthermore, in the spectrum of ball milled Castlegate, these bands were actually more intense than in the spectrum of Chelford sand. This may be the cause of the over prediction of quartz in these samples by the absolute PLS model. This is discussed further, in section 7.7.

Figures 7.12-7.18 also show that the shape of the antisymmetric Si-O-Si stretching bands in the region 1200-1050  $\text{cm}^{-1}$  were different in the spectra of the different powder samples. With the exception of Clashach (Figure 7.17), the shape of these bands in the spectra of the hand ground slices were significantly different to the shape of the bands in the spectra of the ball milled slices and of ball milled Chelford sand. The 1200-1050  $\text{cm}^{-1}$  region of the ground slice spectra appeared less like the 1200-1050  $\text{cm}^{-1}$  region of quartz, and was more similar in shape to the same region in the spectra of the feldspars and of kaolinite. The higher predicted percentages of the feldspars and kaolinite in the ground slices of the sandstones than in the ball milled slices, reflected this. In Clashach, the spectrum of the ground slice (Figure 7.17) showed similar band shape to the spectrum of the ball milled slice and to ball milled Chelford sand. The low predicted percentage of feldspars and kaolinite in Clashach also reflected this.

### 7.3.3.3 Comparing Peak Intensity of Powder and Rock XRD Traces

The opposite trend to that observed in DRIFTS spectra, with regards particle size and peak intensity, was observed in XRD traces. It has been well documented that DRIFTS spectra show more intense bands when the particle size is reduced. Bhaskar *et al.* [111] compared the particle size dependency of IR and XRD techniques for quartz analysis. It was found that while the DRIFTS spectra of quartz showed high intensity bands for samples with a smaller particle size, the XRD traces showed lower

intensity peaks for the same samples, and the XRD traces of quartz samples with a larger particle size showed more intense peaks.

Figures 7.19 and 7.20 show how the quartz peak height intensities, at  $20.9^\circ$  and  $26.7^\circ 2\theta$ , respectively, in XRD traces, differed with particle size for the different sandstones. Quartz peak intensities in XRD traces of the whole rock slices, powder from cutting, and the ball milled slices, were compared.

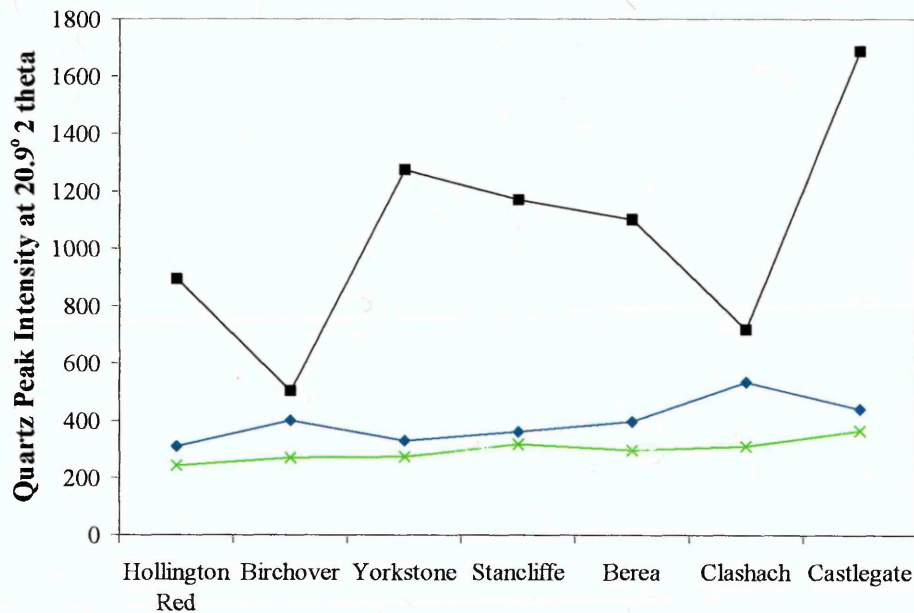


**Figure 7.19: XRD peak intensity (counts) at  $20.9^\circ 2\theta$  for whole rock slices (black), powder from cutting slices (blue), and ball milled slices (green), of the rocks identified.**

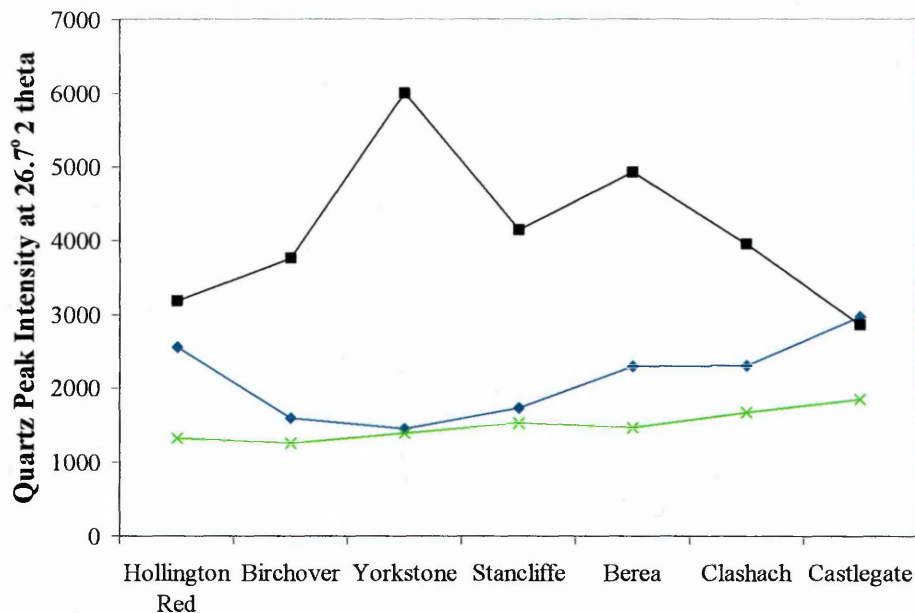


**Figure 7.20: XRD peak intensity (counts) at  $26.7^\circ 2\theta$  for whole rock slices (black), powder from cutting slices (blue), and ball milled slices (green), of the rocks identified.**

The quartz peaks were most intense in the whole rock sample, as would be expected, since these samples had the largest particle size, and also because the slit and mask sizes used were larger for collecting the XRD traces of the rock slices than used for collecting traces of the powder samples, as discussed in section 5.4.3.1 of chapter 5. The powder collected during the cutting process gave less intense quartz peaks, and ball milled slices, even less intense quartz peaks, again indicating the ball milled slices had the smallest particle size, although the peak intensities would also be influenced by the preferred orientation of clays in the powder samples, as discussed in section 5.4.3.2 of chapter 5.

A different trend in peak intensity variation for the sandstones was observed in the rock slice traces at  $20.9^\circ 2\theta$ , compared with that at  $26.7^\circ 2\theta$ . However, the same trend was observed for both peaks in the traces from the ball milled sandstone slices. This could be because the roughness of the natural sandstone rock surfaces were slightly different, causing the XRD traces of the rocks to show more peak intensity variation than shown in the traces of the homogeneous, packed, powder samples. It is interesting to note that despite the lower intensity of the quartz peaks in the traces of the powder from cutting, the trend in intensity for the different sandstones was the

opposite to that found in the rock slice traces. This was expected since, when less quartz was found in the powder from cutting, more quartz must have remained in the rock slice.

## **7.4 Comparing Absolute PLS Model and Other Model Predictions**

### **7.4.1 Introduction**

Since the standards of the training set in the absolute PLS model were ball milled, it was thought that the ball milled slices of the sandstones would give more accurate predictions of the rock components than the powder from cutting, and the ground slices. The percentages of components predicted in slice 1 of each sandstone, using the absolute PLS model were compared to predictions by models developed by different groups in independent studies.

The sandstones were studied by Schlumberger-Doll Research (SDR) using a least square fitting technique and FTIR transmission spectroscopy. Wavelet transform calculations were used to remove noise from useful information and a large collection of standards, including feldspars with Ca, Na, and K end members, was used. For complicated artificial mineral mixtures, SDR stated that the technique was 1% accurate. The model developed by SDR is referred to as LSF-SDR throughout this chapter. Dr. Stephen Hillier from the Macaulay Land Use Research Institute also studied these sandstones using detailed XRD analysis of crushed core samples. Both oriented clay fractions and whole rock random powders were studied. The minerals were quantified from whole rock data and the clay fraction was used to confirm and refine the identification of the clay minerals to provide complementary quantitative information. The errors found by Hillier for predicting different mineral components were typically within  $\pm 3\%$ . This model is referred to as XRD-Hillier throughout this chapter. As with the absolute PLS model described in chapter 6, Clegg [21] used DRIFTS spectra of artificial mineral mixtures to develop a PLS model that would quantify minerals in sandstones rocks. A seven component model was developed by Clegg, consisting of quartz, montmorillonite, kaolinite, illite, dolomite, feldspar, and chlorite, with the maximum error for quartz reported as  $\pm 3$  wt% and for the other

components, within  $\pm 1$  wt%. This model is referred to as PLS-Clegg throughout this chapter.

It should be noted that for each of the models compared, different areas of the cores or entirely different cores were studied, so some variation in predictions may be due to a different distribution of minerals within a core and between different cores.

Hollington Red rock must be discussed in more detail since it is a particularly non-uniform rock. It is considered a banded rock, i.e. there are regions of clay rich strata present between more silica rich regions. While SDR and Clegg predicted two sets of values for Hollington Red, one for the clay rich banded region and one for the silica rich region, an average value has been shown in Figures 7.21-7.29, for simplicity. The samples of Hollington Red quantified by the XRD-Hillier model, and the absolute PLS model, however, contained the clay rich and silica rich regions mixed together.

#### **7.4.2 Comparing Predictions by the Different Models**

A comparison of the predicted concentrations calculated by the four different models for different components of the sandstones are shown in Figures 7.21-7.30. It should be stated that SDR did not analyse the sandstones, Clashach, and Castlegate.

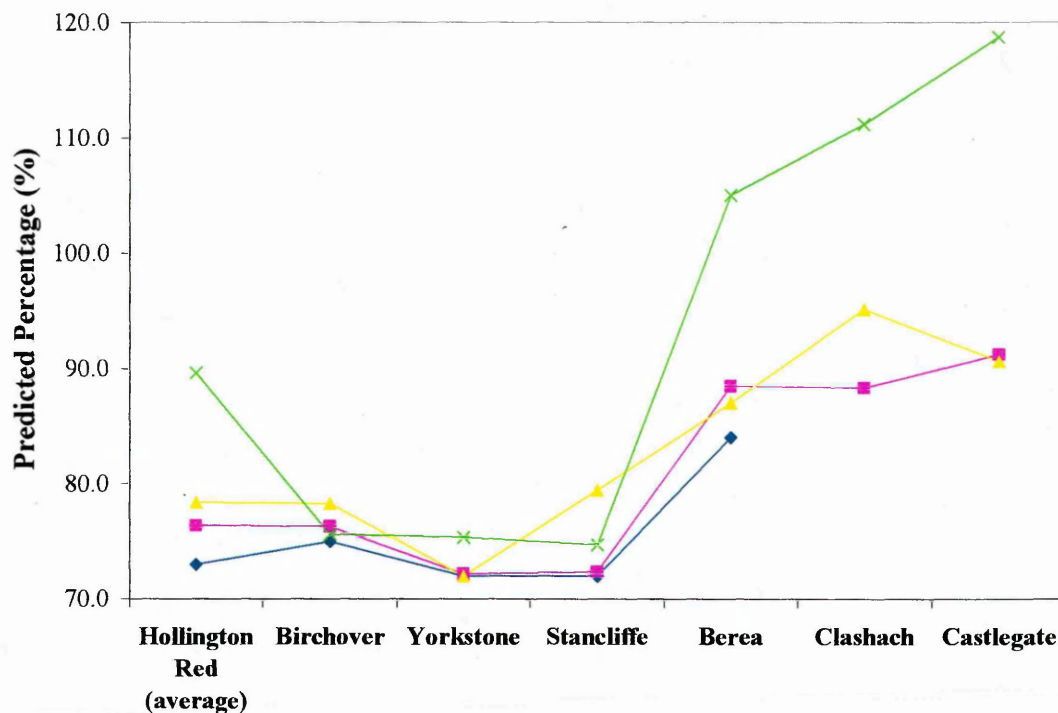


**Figure 7.21: Comparison of absolute PLS model (green) predictions of quartz in sandstones named, with predictions by LSF-SDR (blue), XRD-Hillier (pink), and PLS-Clegg (yellow). See section 7.4.1 for details of models.**

The predictions for quartz in the sandstones tended to follow the same trend for all the models. The predictions for quartz in the harder rocks; Birchover, Yorkstone, and Stancliffe, using the absolute PLS model, were very similar to those of the other models. It was immediately clear, however, that quartz in the softer rocks; Berea, Clashach, and Castlegate was vastly over predicted by the absolute PLS model. It should also be noted that the percentage of quartz predicted by the models followed the same trend as predicted from visual investigation of the Si-O-Si band in the DRIFTS spectra during the qualitative study in section 7.3.

Figure 7.22 compares predictions for combined montmorillonite and illite, in sandstones by the different models. These components were combined, since the XRD-Hillier model predicted these clays in this way. The PLS-Clegg model also reported combined predictions for montmorillonite and illite, since Clegg found that his model produced relatively poor predictions for the individual components. The absolute PLS model attempted to obtain predictions for these components

individually, and maximum errors for montmorillonite and illite were found to be 2.0 wt% and 2.5 wt% respectively. Table 7.1 showed that very little, if any, montmorillonite was present in the sandstones. However, for the purpose of comparing the models, the components were combined.

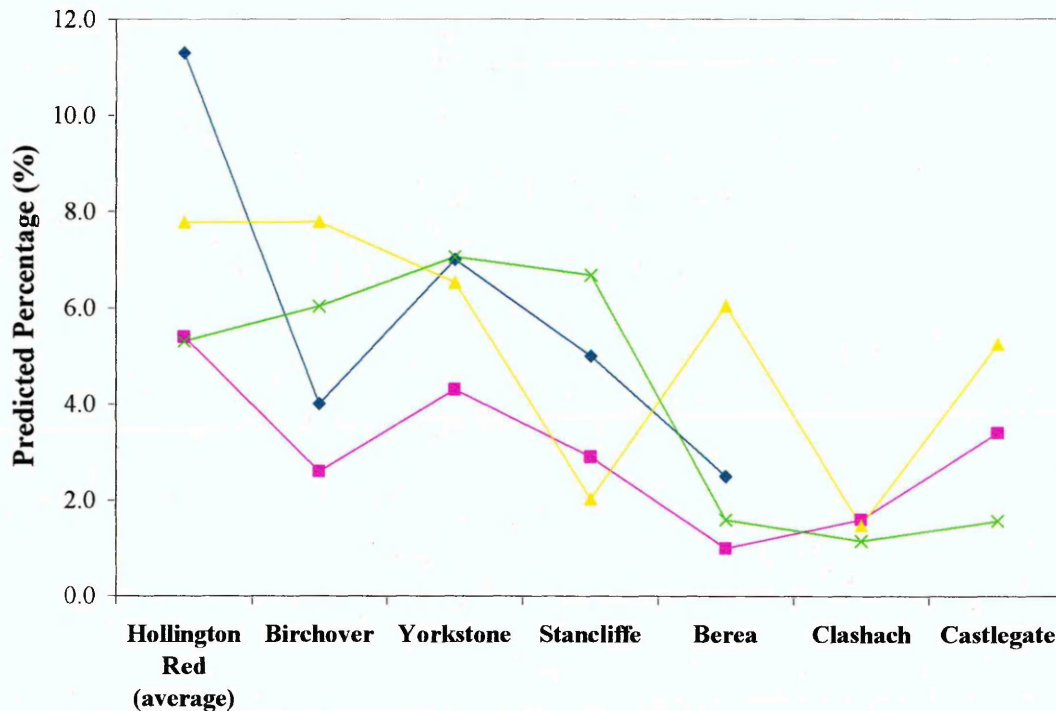


**Figure 7.22: Comparison of absolute PLS model (green) predictions of montmorillonite+illite in sandstones named, with predictions by LSF-SDR (blue), XRD-Hillier (pink), and PLS-Clegg (yellow). See section 7.4.1 for details of models.**

Since very little, if any, montmorillonite was found in the sandstones by the absolute PLS model, the predictions using the absolute PLS model, shown in Figure 7.22, were predominantly those of illite. With the exception of Hollington Red, the trend for montmorillonite and illite combined, in the different sandstones, was similar using the XRD-Hillier model, the LSF-SDR model, and the absolute PLS model. In fact, with errors for the different models ranging from  $\pm 1$  to  $\pm 3$  wt%, the predictions found using the models were very similar.

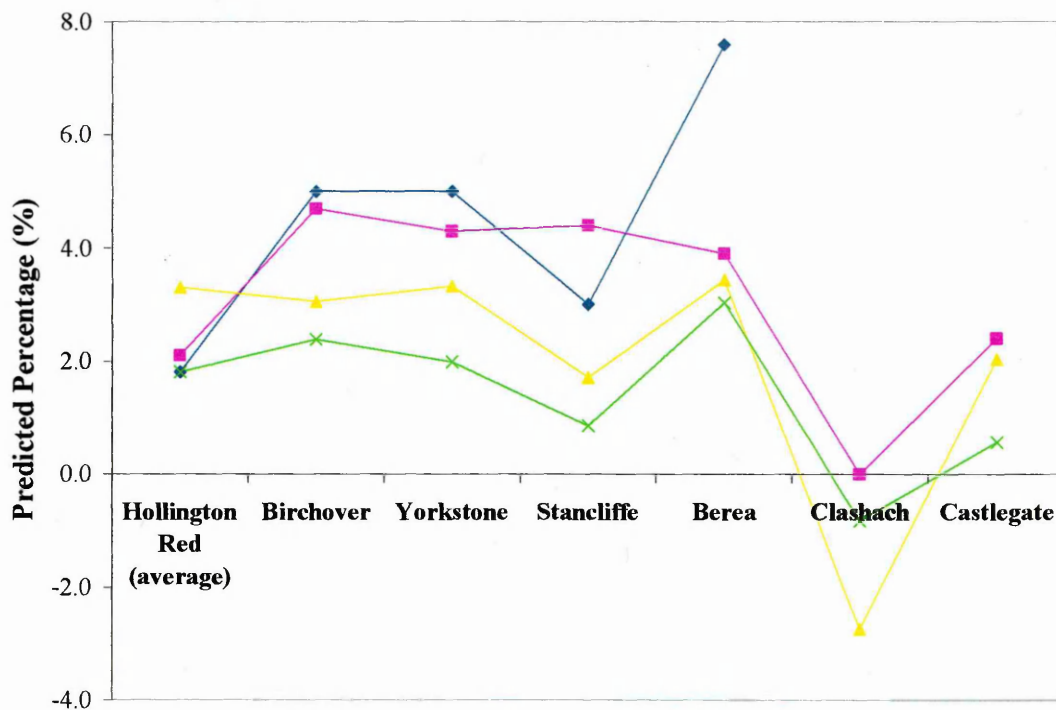


**Figure 7.23: Comparison of absolute PLS model (green) predictions of kaolinite in sandstones named, with predictions by LSF-SDR (blue), XRD-Hillier (pink), and PLS-Clegg (yellow). See section 7.4.1 for details of models.**

A similar trend was observed for the kaolinite predictions in the sandstones using all the models. However, the predictions calculated by the absolute PLS model appeared to be lower than those calculated by the other models. Taking into account the errors of the different models though, the predictions were similar.

Where there were negative predictions for components in the sandstones by the models, it was assumed that none of that component was present in the sandstone.

As with the predictions by the models, the qualitative study of the sandstone spectra in section 7.3, also indicated higher concentrations of kaolinite in Yorkstone, Birchover, and Stancliffe, and lower concentrations in Castlegate. Both the absence of the bands associated with kaolinite, in Figures 7.3 and 7.4 of section 7.3, and the prediction of no kaolinite by all the models in Figure 7.23, confirmed that Clashach contained no kaolinite.

The predictions for calcite by the different models are shown in Figure 7.24. In the PLS model developed by Clegg, dolomite was included as the only carbonate, so his model was not capable of quantifying calcite in the sandstones. The comparison of models in Figure 7.24 therefore does not include Clegg's PLS model.

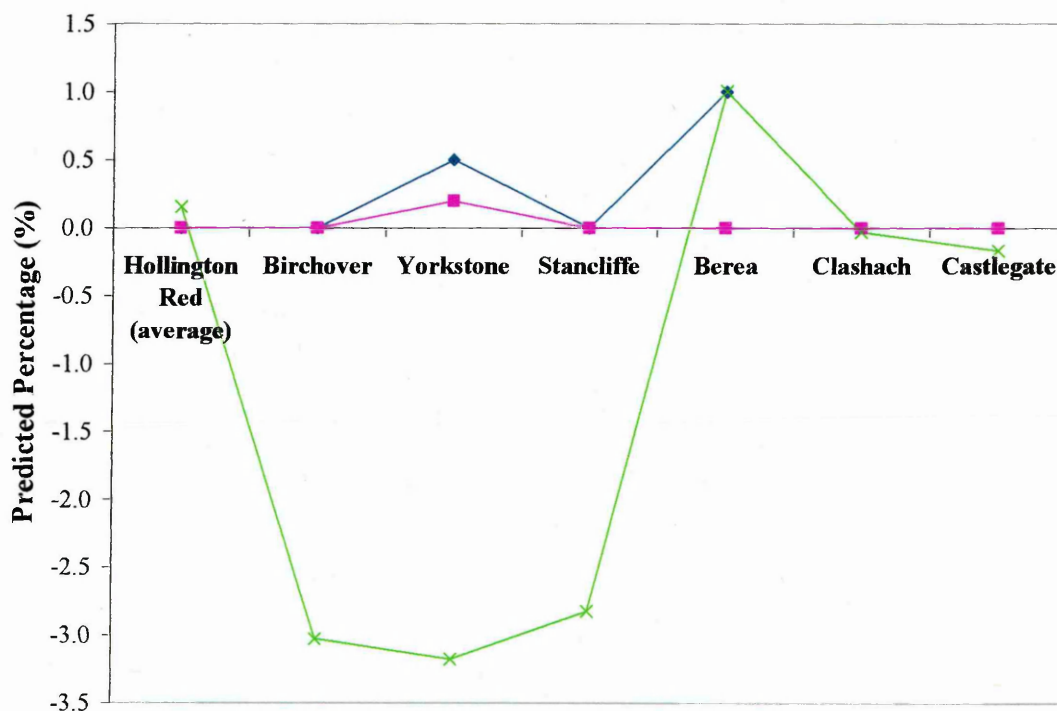


**Figure 7.24: Comparison of absolute PLS model (green) predictions of calcite in sandstones named, with predictions by LSF-SDR (blue), and XRD-Hillier (pink). See section 7.4.1 for details of models.**

A comparison of the model predictions of calcite in the sandstones was difficult since such small amounts, if any, were predicted. The LSF-SDR and XRD-Hillier models suggested that some calcite may have been present in Yorkstone, and the LSF-SDR model and absolute PLS model suggested some may have been present in Berea, although no models predicted high percentages of calcite. The absolute PLS model in fact calculated large negative values for calcite in Birchover, Yorkstone, and Stancliffe, indicating that they contained no calcite.

The predictions by the models, suggesting the presence of some calcite in Berea, was also confirmed in section 7.3, where visual investigation of the DRIFTS spectrum of Berea (Figure 7.4) suggested the presence of carbonate bands.

The XRD model developed by Hillier did not investigate the presence of dolomite in the sandstones so only the LSF-SDR model, the PLS-Clegg model and the absolute PLS model predictions are compared in Figure 7.25.

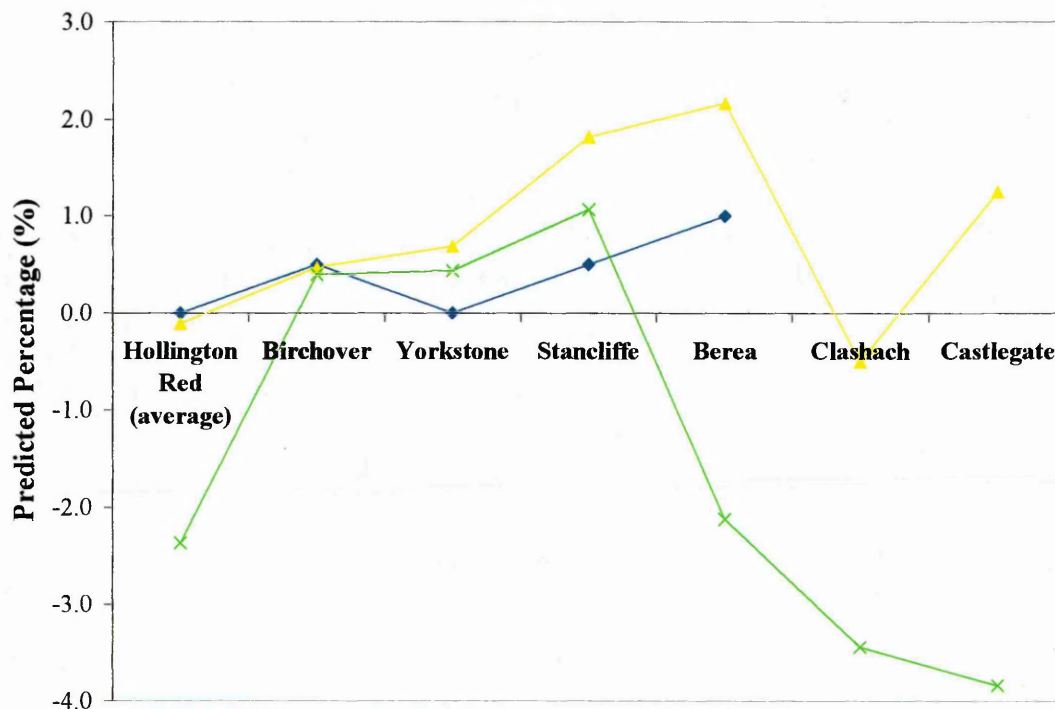


**Figure 7.25: Comparison of absolute PLS model (green) predictions of dolomite in sandstones named, with predictions by LSF-SDR (blue), and PLS-Clegg (yellow). See section 7.4.1 for details of models.**

The predictions of the absolute PLS model suggested a negative correlation between the concentration of calcite and dolomite in the sandstones. While large negative predictions were calculated for calcite in Birchover, Yorkstone, and Stancliffe, these same sandstones were the only ones which contained small amounts of dolomite.

Qualitative studies by Clegg [21] using Thermogravimetric-Mass Spectroscopy indicated that carbon dioxide did evolve from Stancliffe and Berea rocks, suggesting that carbonates were present in these sandstones at low concentrations. Interestingly, the highest percentages of calcite and dolomite predicted in the sandstones by the absolute PLS model were in Stancliffe and Berea.

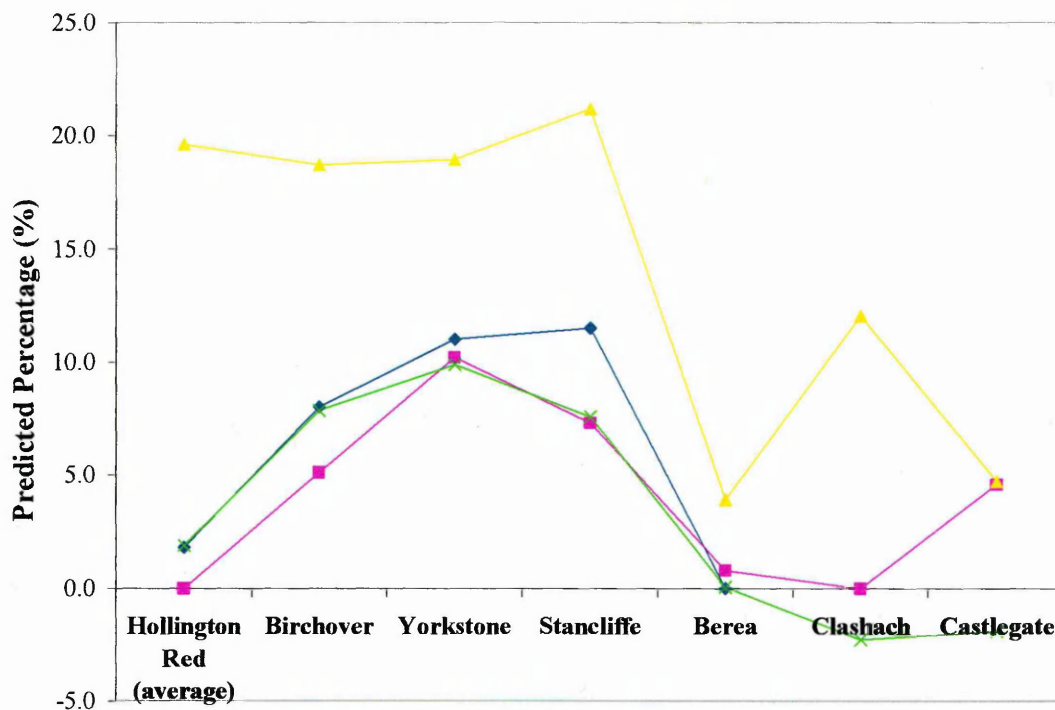


**Figure 7.26: Comparison of absolute PLS model (green) predictions of Na-feldspar in sandstones named, with predictions by LSF-SDR (blue), XRD-Hillier (pink), and PLS-Clegg (yellow). See section 7.4.1 for details of models.**

A similar trend was observed for the Na-feldspar predictions in the sandstones using the LSF-SDR model, XRD-Hillier model, and the absolute PLS model, while the PLS-Clegg model reported significantly higher Na-feldspar predictions in all the sandstones.

The same trend for the presence of Na-feldspar in the sandstones was also observed in the qualitative study of the sandstone DRIFTS spectra in section 7.3, where high concentrations of Na-feldspar in Birchover, Yorkstone, and Stancliffe, and low concentrations in the other sandstones, was suggested.

In the PLS model developed by Clegg, Na-feldspar was the only feldspar included and therefore the model was not capable of quantifying K-feldspar in the sandstones. Figure 7.27, comparing the predictions of K-feldspar by the models, therefore does not include the PLS-Clegg model.

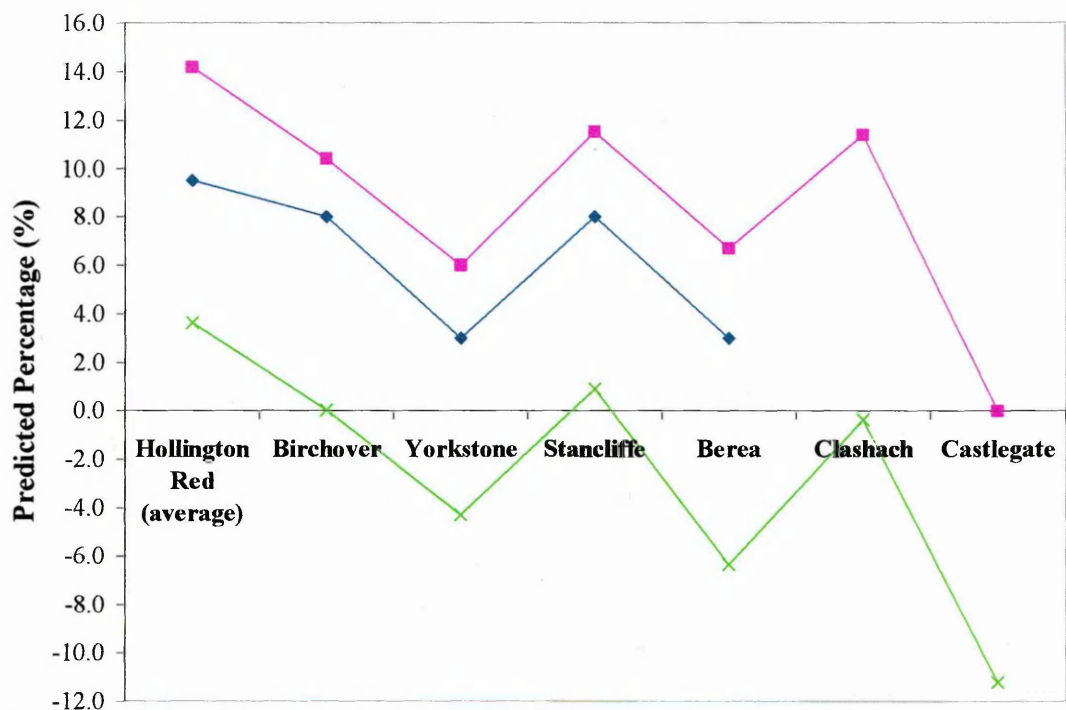


**Figure 7.27: Comparison of absolute PLS model (green) predictions of K-feldspar in sandstones named, with predictions by LSF-SDR (blue), and XRD-Hillier (pink). See section 7.4.1 for details of models.**

Although the same trend was observed for K-feldspar predictions by the LSF-SDR and the XRD-Hillier models, the values of the predicted percentages were quite different. The XRD-Hillier model predictions were up to 5 wt% higher than the LSF-SDR model predictions. The absolute PLS model predictions for K-feldspar were much lower than those predicted by the LSF-SDR and XRD-Hillier models, with K-feldspar only being predicted positively in Hollington Red, and Stancliffe.

The qualitative study of the sandstone DRIFTS spectra, in section 7.3, also suggested that higher concentrations of K-feldspar were found in Hollington Red and Clashach, and lower concentrations in Berea and Castlegate.

Again, the PLS-Clegg model is not included in the comparison of models shown in Figure 7.28 since hematite was not included in this model.

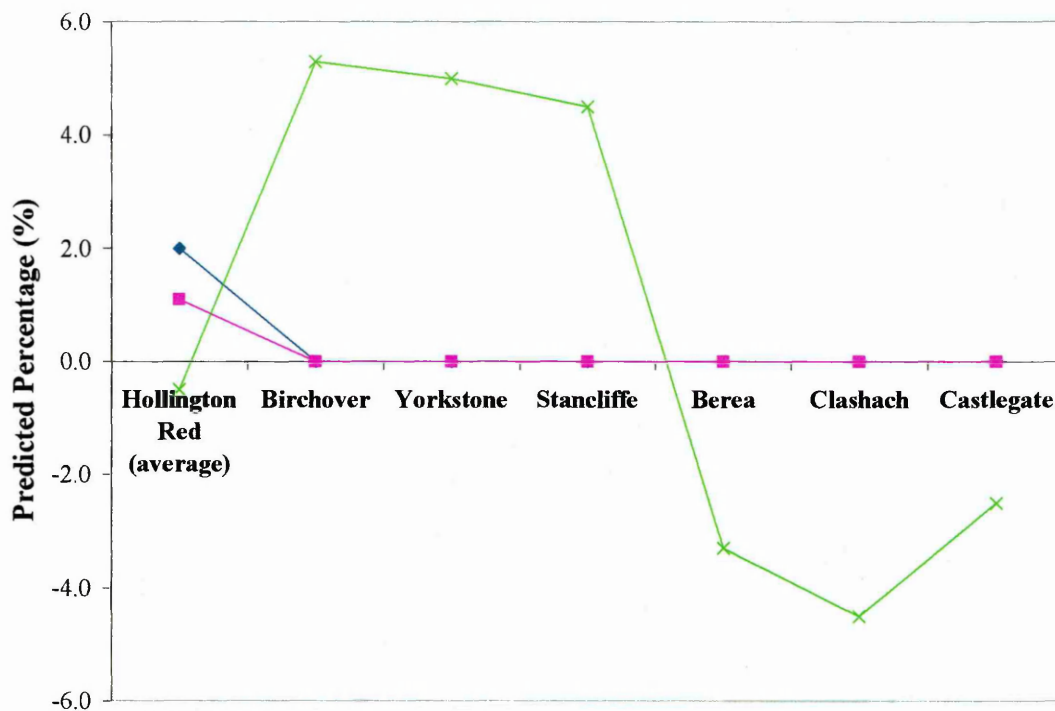


**Figure 7.28: Comparison of absolute PLS model (green) predictions of hematite in sandstones named, with predictions by LSF-SDR (blue), and XRD-Hillier (pink). See section 7.4.1 for details of models.**

It was clear that while SDR and Hillier predicted low amounts of hematite in Hollington Red, and none in the other sandstones, predictions by the absolute PLS model were quite different. This indicated that the absolute PLS model may not have been capable of predicting hematite. Hematite was the least precisely predicted component in the synthetic mixtures and required the most number of factors, and its poor prediction may be expected since the DRIFTS spectrum had few distinctive features and no strong bands.

It was only in the clay rich banded region of Hollington Red, that the LSF-SDR model predicted some hematite. Methven and Hughes [102] reported that the clay rich banded region of Hollington Red contained a high clay to feldspar ratio and a considerable quantity of hematite. The absolute PLS model predicted relatively high percentages of hematite in more clay rich, harder sandstones; Birchover, Stancliffe, and Yorkstone, and none in the other sandstones. This suggested that there may have been a positive correlation between the percentage of clay and the percentage of hematite present in sandstones.

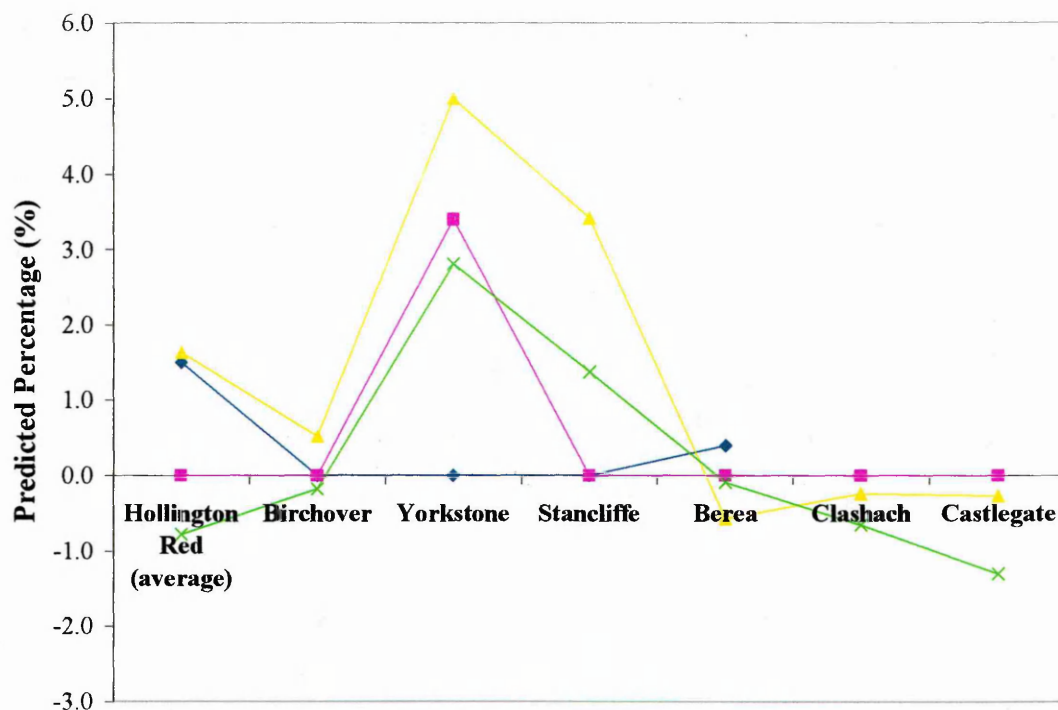


**Figure 7.29: Comparison of absolute PLS model (green) predictions of chlorite in sandstones named, with predictions by LSF-SDR (blue), and XRD-Hillier (pink), and PLS-Clegg (yellow). See section 7.4.1 for details of models.**

A similar trend in predictions for chlorite was observed for all the models except the LSF-SDR model. The XRD-Hillier model, PLS-Clegg model, and the absolute PLS model, all predicted the highest concentration of chlorite in Yorkstone.

Of the models used for comparison, only the least squares fitting model developed by SDR included muscovite. Figure 7.30 therefore compares only the predictions by the LSF-SDR model and the absolute PLS model.

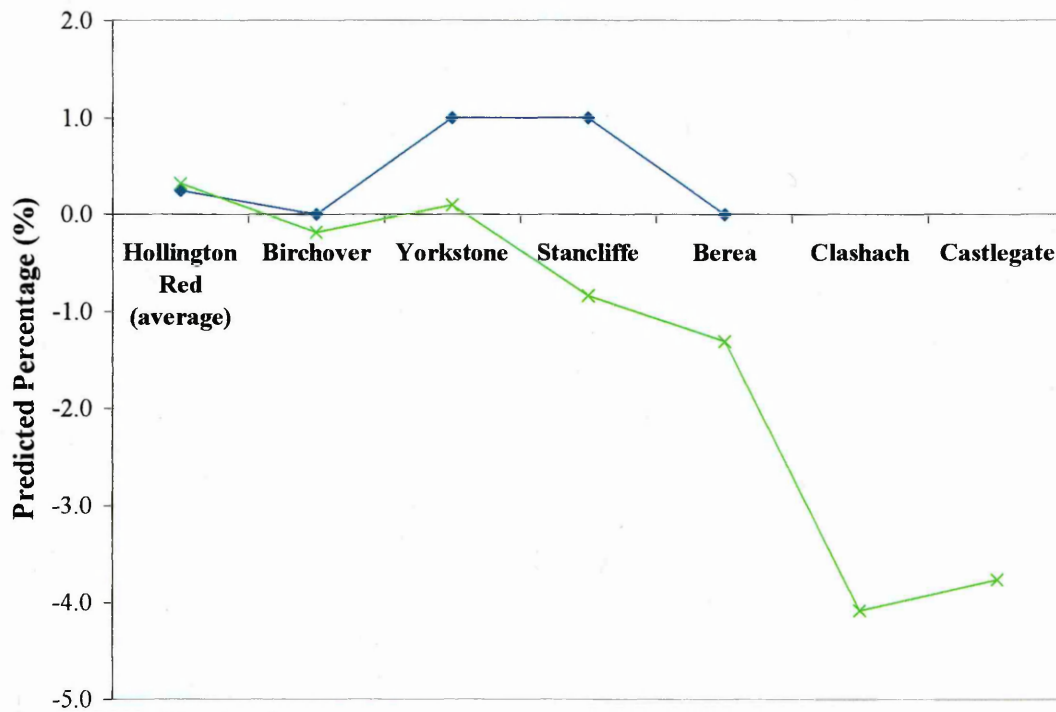


**Figure 7.30: Comparison of absolute PLS model (green) predictions of muscovite in sandstones named, with predictions by LSF-SDR (blue). See section 7.4.1 for details of models.**

As with calcite, it was difficult to compare the two sets of predictions of muscovite due to such low amounts being predicted.

Methven and Hughes [102] reported that the most significant variance in the mineralogy of Birchover, Stancliffe, and Yorkstone, was found in their feldspar and clay contents. This was also found to be the case for these sandstones using the absolute PLS model for prediction. The absolute PLS model predicted only 1 wt% difference between the quartz content of these sandstones, while the content of both total feldspar and total clay in these sandstones varied over 4 wt%. Methven and Hughes [102] also found an inverse correlation between the total feldspar and total clay content of the sandstones. This relationship was said to be related to the degree of alteration of feldspars to clay minerals, referred to as the textural maturity of the sandstone. Although this inverse correlation was unclear from the predictions of the individual feldspars and clays in this study, if the predictions of the two feldspars were combined and those of the clays combined, then this inverse correlation could be

seen to some extent. When comparing the harder sandstones; Birchover, Stancliffe, and Yorkstone, and the softer sandstones; Berea, Clashach, and Castlegate as two separate groups, this inverse correlation between feldspar and clay content was observed.

When making comparisons between the predictions calculated by the different models, the different analysis methods and model calculations should be taken into consideration. Hillier used XRD for analysis, while SDR used transmission infrared spectroscopy, so only the PLS model developed by Clegg used the same DRIFTS and PLS techniques as used in the absolute PLS model. Differences in the sampling should also be taken into consideration. As stated previously, all of the groups analysed different areas of the cores or entirely different cores to each other. Although component predictions along the core lengths in section 7.3.2 suggested that differences in mineralogy were minimal over a short core length, the core samples studied by the different investigators may have originated from more distant areas or from different cores. This may account for slight differences in the mineralogy of the sandstones calculated by each model.

It should also be noted that to produce the ball milled samples in this study, the cores were first cut into slices with a saw. During the cutting process, powder was produced, which was collected and analysed separately, and was therefore not included in the analysis of the ball milled samples. The samples used for analysis by Hillier and Clegg, on the other hand, were chipped off the core and crushed, so no powder had been removed during the process. If some minerals were preferentially released from the rock as powder during the cutting processes then this would account for some differences in the mineral predictions calculated by the absolute PLS model and the models developed by Hillier and Clegg.

#### **7.4.3 XRF of Ball milled Slices**

For further comparison, XRF analysis was carried out on one ball milled slice from each sandstone. The percentage of SiO<sub>2</sub> found in each sandstone is shown in Figure 7.31.

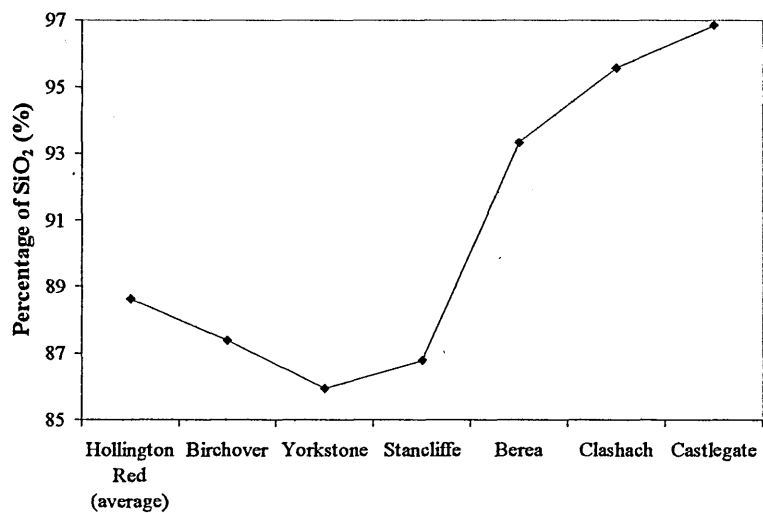


**Figure 7.31: Weight percentages of SiO<sub>2</sub>, from XRF analysis, for the quarry sandstones named.**

Although the SiO<sub>2</sub> percentage measured in the sandstones by XRF was due to quartz, the feldspars and the layer silicates, the sandstones contained predominantly quartz, so the percentage of SiO<sub>2</sub> measured was compared only with the prediction of quartz by the models. It was immediately clear that the trend for the percentage of SiO<sub>2</sub> found in the sandstones by XRF was the same as could be seen for the predictions of quartz using the models, in Figure 7.21. As with the quartz prediction, a higher percentage of SiO<sub>2</sub> was determined in Berea, Clashach, and Castlegate, than in the other sandstones.

The XRF analysis also included determining the percentages of Al<sub>2</sub>O<sub>3</sub>, Na<sub>2</sub>O, K<sub>2</sub>O, and CaO, and these are shown in Figure 7.32.

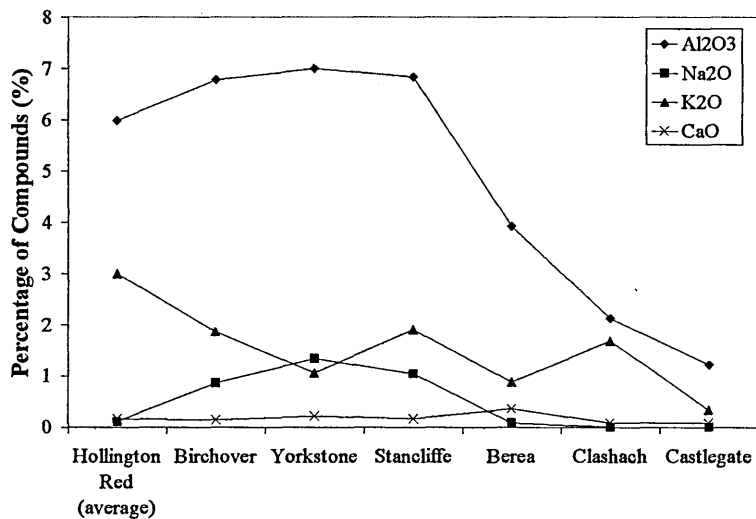


**Figure 7.32: Weight percentages of Al<sub>2</sub>O<sub>3</sub>, Na<sub>2</sub>O, K<sub>2</sub>O, and CaO, from XRF analysis, for the quarry sandstones named.**

Again the percentages of compounds measured by XRF could not be directly related to the predictions of single sandstones components, as Al<sub>2</sub>O<sub>3</sub> is found in all the layer silicates and in the feldspars, and K<sub>2</sub>O is found in illite, muscovite, and K-feldspar.

A trend can be seen in Figure 7.32 for the percentage of Al<sub>2</sub>O<sub>3</sub> measured by XRF and the predictions for illite and montmorillonite combined (Figure 7.22), and also for Na-feldspar (Figure 7.26). The higher percentages of illite + montmorillonite predicted by the absolute PLS model, in Hollington Red, Birchover, Yorkstone, and Stancliffe and the lower percentages predicted in Berea, Clashach, and Castlegate, correlated with the trend of the measured percentage of Al<sub>2</sub>O<sub>3</sub> found by XRF. The high percentages of Na-feldspar predicted in Birchover, Yorkstone, and Stancliffe, and low concentration of Na-feldspar predicted in Berea, Clashach, and Castlegate, by the absolute PLS model, also correlated well with the trend of the percentage of Al<sub>2</sub>O<sub>3</sub> measured by XRF.

The percentage of Na<sub>2</sub>O found in the sandstones by XRF also followed a very similar trend to the percentages of Na-feldspar predicted in the sandstones by the absolute PLS model and the XRD-Hillier model shown in Figure 7.26.

The percentage of  $K_2O$  found in the sandstones by XRF best followed the trend of the percentages of K-feldspar predicted by the models shown in Figure 7.27, with lower percentages of K-feldspar measured and predicted in Yorkstone, Berea, and Castlegate than in the other sandstones.

The percentage of CaO found in the sandstones by XRF was very low and the percentage of carbonate predicted by the models was also very low, as shown in Figure 7.24. Interestingly the percentage of CaO found in Berea by XRF was slightly higher than that found in the other sandstones, and both the LSF-SDR model, and the absolute PLS model predicted slightly higher percentages of calcite in Berea, than in the other sandstones.

## **7.5 Forming the Pragmatic PLS Model**

### **7.5.1 Introduction**

It was assumed that the XRD-Hillier model was the most accurate model since it is a well established technique. Although the absolute PLS model did generally give predicted percentages for components in the same trend for the sandstones as the XRD-Hillier model, some component percentages were over predicted by the absolute PLS model and some were under predicted. With the errors for the models considered, the absolute PLS model predicted all the components of the sandstones which contained more feldspars and clays (i.e. Birchover, Yorkstone, and Stancliffe) well, with respect to predictions by the XRD-Hillier model. The absolute PLS model, however, appeared to over predict the amount of quartz in the “cleaner” sandstones; Berea, Clashach, and Castlegate, and also under predicted the amount of K-feldspar in all the sandstones. Large negative predictions were also found for montmorillonite, calcite, dolomite, and muscovite in the sandstones using the absolute PLS model (Table 7.1). It was thought that the absolute PLS model needed to be optimised for predicting real sandstones, by trying to optimise the number of factors chosen for each component. It was especially important to try to improve on the predictions for quartz in the clean sandstones by the absolute PLS model, since this was where the greatest errors were observed. The model, with altered factors for optimised sandstone predictions, was named the pragmatic PLS model. It should be noted that the PLS-

Clegg model, compared with the absolute PLS model in section 7.4, was actually a pragmatic model, where Clegg optimised the number of factors chosen for components, based on obtaining the most accurate predictions for components in the sandstones.

### **7.5.2 Altering the Number of Factors**

During the formation of the absolute PLS model, it was found that altering the number of factors for a component exerts a huge influence on the prediction of that component. The factors in the absolute PLS model were chosen to give the most accurate predictions of the independent standards, which were synthetic mixtures of the components, similar to the calibration standards. The spectra of both the calibration and independent standards were collected on the same day. It was thought that real sandstone samples, with varying degrees of crystallinity, containing components not accounted for by the model, and having spectra collected on a different day, may require a different number of factors for particular components than those chosen for the synthetic independent standards. In an attempt to optimise the absolute PLS model for the suite of sandstone rocks studied, the number of factors for each component was altered to give predictions closest to the predictions of the XRD-Hillier model, since this was deemed the most accurate.

The Tables 7.2-7.8 show how the predicted percentage of each component varied as the number of factors was altered, for each sandstone. The green boxes indicate the percentage of each component predicted, using the number of factors chosen for the absolute PLS model, while the black boxes indicate the percentage of each component predicted, using the number of factors chosen for the pragmatic PLS model, i.e. the percentages of each component that were generally closest in value to those predicted by the XRD-Hillier model. For the components, Na-feldspar and chlorite, the number of factors chosen in the pragmatic PLS model were the same as those chosen in the absolute PLS model, since the percentages predicted by the absolute PLS model also gave the most accurate predictions in the sandstones.

The predictions of each component by the XRD-Hillier model are shown below the table, for each sandstone. No prediction is shown for montmorillonite using the XRD-Hillier model, since Hillier reported combined montmorillonite + illite predictions, and these are shown under the illite column. No predictions are shown

for dolomite and muscovite using the XRD-Hillier model since Hillier did not investigate the presence of these components in the sandstones. For some sandstones, the percentages of components predicted by the pragmatic PLS model were not the closest value to those predicted by the XRD-Hillier model. This was because the optimum number of factors chosen for a particular component had to take into consideration all the sandstones studied.

No. of Factors	Quartz	Montmorillonite	Kaolinite	Illite	Calcite	Dolomite	Na-Feldspar	K-Feldspar	Hematite	Chlorite	Muscovite
1	87.7	1.0	-1.2	6.0	-0.1	-1.3	5.0	3.6	-0.7	-0.8	1.2
2	86.9	-0.2	-0.2	5.6	-5.2	-7.2	5.4	5.1	-0.4	-2.5	1.2
3	87.1	1.4	1.6	2.4	0.2	-2.5	6.5	7.4	-0.2	-1.3	2.2
4	88.8	1.3	1.8	2.4	-0.9	-2.4	3.6	2.5	-0.3	-1.5	1.1
5	88.9	0.3	1.6	3.2	-1.1	-1.8	5.7	1.6	-0.2	-0.7	1.1
6	88.2	0.8	1.5	3.6	-0.5	-1.4	6.0	0.5	0.1	-0.8	1.2
7	88.9	1.5	1.6	3.2	-0.2	-1.4	4.5	0.7	-0.7	-0.8	-0.1
8	89.1	1.6	1.8	3.3	0.1	-0.7	5.2	-0.6	-0.1	-0.8	-0.3
9	89.4	1.8	1.7	3.0	0.4	-0.5	5.6	-0.2	-0.8	-0.8	-0.2
10	89.6	1.5	1.4	3.8	0.3	-0.2	4.5	1.6	-1.0	-0.7	0.2
11	89.3	1.0	1.4	4.3	0.2	-0.3	2.1	3.0	-0.9	-0.6	0.3
12	89.0	-0.5	1.5	4.0	0.2	-0.1	1.9	3.6	-0.1	-0.5	-0.1
13	89.7	-0.3	1.4	4.8	0.3	0.0	0.8	4.2	-0.2	-0.7	0.3
14	89.7	-0.5	1.5	3.7	0.6	0.0	0.5	4.8	-0.5	-0.3	1.1
15	89.0	-0.3	1.7	2.3	0.8	-0.2	-0.5	5.3	-0.5	-0.1	1.7
XRD-Hillier Predictions	76.4		2.1	5.4	0.0		0.0	14.2	1.1	0.0	

**Table 7.2: Predicted Percentages of each named component varying with number of factors, for Hollington Red. The green and black boxes indicate the percentage of each named component predicted using the number of factors chosen for the absolute and pragmatic PLS models, respectively.**

No. of Factors	Quartz	Montmorillonite	Kaolinite	Illite	Calcite	Dolomite	Na-Feldspar	K-Feldspar	Hematite	Chlorite	Muscovite
1	82.0	1.9	0.2	7.4	-1.8	-1.6	6.0	3.4	0.3	0.8	1.9
2	77.5	1.0	0.5	8.6	-6.5	-2.7	5.4	3.9	1.8	-0.4	1.5
3	77.9	2.4	2.2	6.5	-3.0	1.1	6.8	7.3	2.3	0.7	2.5
4	78.1	1.8	2.4	7.0	-3.0	0.4	4.4	4.1	3.5	-0.7	1.9
5	80.0	1.8	2.7	6.0	-2.8	0.4	4.2	2.6	4.4	-0.7	0.8
6	79.3	-0.2	3.1	6.2	-2.0	0.9	5.8	2.2	4.8	-0.2	0.8
7	79.0	-0.5	3.2	5.6	-1.6	0.9	5.4	2.9	5.9	-0.1	0.2
8	78.3	-1.3	3.4	4.9	-1.0	1.0	4.7	3.9	7.5	-0.4	-0.4
9	76.1	-1.1	3.8	6.0	-1.1	0.9	3.7	5.1	8.2	-1.0	-1.3
10	75.6	-1.0	3.3	7.0	-0.9	0.3	3.3	5.3	7.6	-1.1	-1.0
11	76.7	-0.7	3.2	8.6	-0.7	0.2	4.3	4.3	6.6	-1.2	-1.1
12	77.6	-1.0	3.2	7.4	-0.2	0.7	7.9	0.0	6.7	-0.5	-1.0
13	79.1	-0.8	3.0	7.0	0.0	0.6	7.6	0.4	5.7	-0.5	-0.2
14	79.2	-1.9	3.4	7.3	-0.6	0.2	6.8	0.8	5.9	-0.1	-0.6
15	80.0	-1.6	3.2	5.6	-1.0	0.3	6.3	1.2	5.3	0.1	0.1
XRD-Hillier Predictions	76.3		4.7	2.6	0.0		5.1	10.4	0.0	0.0	

**Table 7.3: Predicted Percentages of each named component varying with number of factors, for Birchover. The green and black boxes indicate the percentage of each named component predicted using the number of factors chosen for the absolute and pragmatic PLS models, respectively.**

No. of Factors	Quartz	Montmorillonite	Kaolinite	Illite	Calcite	Dolomite	Na-Feldspar	K-Feldspar	Hematite	Chlorite	Muscovite
1	78.1	2.5	1.1	8.0	-2.4	-1.8	6.7	3.0	0.8	2.0	2.4
2	74.6	1.7	0.6	8.8	-5.6	-1.0	5.8	2.4	2.1	1.5	1.6
3	75.4	2.7	2.0	7.5	-3.2	1.6	8.1	3.9	2.7	2.7	2.4
4	74.8	1.6	2.0	8.4	-2.7	0.4	6.5	0.1	4.1	2.0	2.0
5	77.6	1.5	2.3	7.1	-2.4	0.3	6.3	-2.2	5.0	2.1	0.7
6	77.7	-0.2	2.7	7.2	-1.7	0.5	7.1	-2.4	5.3	2.8	0.4
7	77.7	-0.7	2.8	7.0	-1.4	0.5	7.1	-2.5	6.4	2.9	-0.1
8	77.4	-2.0	3.0	7.1	-0.9	0.7	7.2	-1.8	7.2	2.4	-0.4
9	75.9	-1.9	3.1	7.9	-0.7	0.6	7.0	-1.3	7.3	2.0	-0.6
10	75.3	-1.7	2.6	8.9	-0.4	0.2	7.4	-1.0	6.7	1.9	-0.1
11	76.1	-1.9	2.6	10.6	-0.4	0.0	7.2	-1.4	5.9	1.9	-0.3
12	76.6	-2.0	2.5	9.4	0.0	0.6	9.9	-4.3	6.0	2.4	-0.5
13	77.8	-1.7	2.4	9.2	0.0	0.6	9.4	-3.8	5.2	2.2	0.1
14	77.9	-2.7	2.4	9.1	-0.4	0.4	8.6	-3.1	5.4	2.1	0.0
15	78.9	-3.0	2.3	8.3	-0.4	0.4	8.3	-2.7	5.0	1.9	0.9
XRD-Hillier Predictions	72.2		4.3	4.3	0.2		10.2	6.0	0.0	3.4	

**Table 7.4: Predicted Percentages of each named component varying with number of factors, for Yorkstone. The green and black boxes indicate the percentage of each named component predicted using the number of factors chosen for the absolute and pragmatic PLS models, respectively.**

No. of Factors	Quartz	Montmorillonite	Kaolinite	Illite	Calcite	Dolomite	Na-Feldspar	K-Feldspar	Hematite	Chlorite	Muscovite
1	84.0	1.5	-0.6	7.3	-1.5	-1.1	5.6	2.6	0.2	0.4	1.6
2	75.4	0.3	-0.7	10.8	-7.2	-2.0	5.8	3.2	2.6	-0.2	1.4
3	75.3	1.6	0.9	8.6	-2.8	2.6	9.8	6.8	3.1	1.3	2.6
4	74.7	0.5	0.9	9.2	-2.2	1.1	7.4	3.1	4.2	0.5	2.3
5	76.6	1.1	1.2	6.9	-1.7	0.6	6.7	0.5	5.2	0.6	0.8
6	76.6	-0.8	1.7	6.8	-0.9	1.0	7.8	1.2	5.6	1.4	0.4
7	76.5	-1.0	1.9	6.2	-0.5	1.0	7.4	1.7	6.7	1.6	-0.1
8	76.1	-2.2	2.2	5.5	-0.2	1.4	6.7	3.0	7.5	1.1	-0.5
9	75.0	-2.1	2.6	6.1	-0.4	1.3	5.5	3.9	7.9	0.5	-1.1
10	74.7	-1.7	2.1	7.1	-0.7	0.8	4.9	4.4	7.5	0.3	-1.1
11	76.1	-1.6	2.0	9.1	-0.6	0.7	4.5	4.3	6.7	0.2	-1.3
12	76.9	-2.7	2.0	8.3	-0.1	1.3	7.6	0.9	6.9	0.6	-1.6
13	78.5	-2.4	1.9	8.5	0.1	1.1	7.4	1.6	5.6	0.4	-0.8
14	78.7	-3.2	2.2	8.9	-0.2	0.8	6.7	1.9	5.4	0.7	-1.4
15	79.0	-2.4	2.0	7.3	-0.8	0.8	6.4	2.2	4.5	0.9	-0.9
XRD-Hillier Predictions	72.4		4.4	2.9	0.0		7.3	11.5	0.0	0.0	

**Table 7.5: Predicted Percentages of each named component varying with number of factors, for Stancliffe. The green and black boxes indicate the percentage of each named component predicted using the number of factors chosen for the absolute and pragmatic PLS models, respectively.**

No. of Factors	Quartz	Montmorillonite	Kaolinite	Illite	Calcite	Dolomite	Na-Feldspar	K-Feldspar	Hematite	Chlorite	Muscovite
1	93.5	0.5	-2.1	4.6	1.0	-0.1	3.4	0.6	-1.4	-1.7	0.0
2	99.0	0.4	0.8	0.9	-5.9	-6.1	1.2	1.7	-1.7	-2.7	-1.3
3	98.8	2.7	2.9	-2.9	1.0	-0.2	2.3	2.4	-1.6	-1.2	-0.3
4	100.7	2.0	3.0	-1.3	0.4	-2.1	-1.0	-4.2	-0.8	-2.4	-1.7
5	104.5	0.3	3.2	-0.5	-0.4	-1.0	2.1	-6.6	0.0	-0.9	-2.2
6	103.7	0.3	2.9	0.2	-0.1	-0.9	3.1	-8.9	-0.2	-0.1	-1.7
7	104.9	1.0	3.1	-0.3	0.3	-1.1	1.2	-8.5	-2.0	-0.2	-3.1
8	105.1	1.3	3.2	0.3	0.5	-0.4	3.3	-10.9	-1.7	-0.2	-2.4
9	105.4	1.9	2.9	-0.4	1.0	0.0	4.5	-10.2	-2.9	-0.3	-1.8
10	105.0	2.0	2.3	-0.6	1.5	0.4	4.9	-9.4	-3.2	-0.1	-1.1
11	104.8	1.1	2.4	0.6	1.2	0.3	0.9	-8.1	-2.2	0.0	-1.5
12	104.4	-0.8	2.3	0.8	1.3	0.4	0.1	-6.3	-1.7	-0.2	-1.7
13	105.2	-0.7	2.1	1.8	1.1	0.4	-1.1	-5.4	-2.1	-0.5	-1.3
14	106.6	-0.5	2.0	0.3	1.3	0.8	-1.9	-4.2	-3.0	-0.2	-0.1
15	106.2	-0.5	2.2	-1.1	0.5	0.8	-3.3	-3.3	-3.3	0.0	0.5
XRD-Hillier Predictions	88.5		3.9	1.0	0.0		0.8	6.7	0.0	0.0	

**Table 7.6: Predicted Percentages of each named component varying with number of factors, for Berea. The green and black boxes indicate the percentage of each named component predicted using the number of factors chosen for the absolute and pragmatic PLS models, respectively.**

No. of Factors	Quartz	Montmorillonite	Kaolinite	Illite	Calcite	Dolomite	Na-Feldspar	K-Feldspar	Hematite	Chlorite	Muscovite
1	103.1	-0.3	-4.4	4.6	-0.2	-1.6	2.9	0.0	-2.5	-3.1	-0.7
2	108.9	-1.1	-3.2	1.8	-9.4	-9.7	1.5	2.1	-2.9	-4.2	-2.1
3	108.2	1.7	-1.0	-3.2	0.0	-1.6	4.2	4.3	-2.8	-2.1	-0.7
4	109.6	0.9	-0.8	-1.6	-0.9	-3.4	0.0	-3.1	-2.4	-2.5	-2.4
5	110.0	-0.4	-0.8	-1.4	-1.5	-2.3	4.0	-3.1	-2.2	-1.2	-2.4
6	109.4	1.0	-1.0	-1.5	-0.5	-2.1	3.7	-4.6	-2.4	-0.7	-2.5
7	110.3	1.6	-0.7	-1.8	-0.2	-1.9	2.2	-3.7	-3.5	-0.8	-4.1
8	110.7	2.2	-0.5	-2.2	0.0	-1.0	2.6	-5.5	-3.5	-0.5	-4.4
9	111.1	2.8	-0.5	-3.1	0.5	-0.6	3.2	-5.1	-4.7	-0.5	-4.2
10	111.2	3.0	-0.9	-2.3	0.4	-0.1	1.8	-3.1	-4.8	-0.3	-4.2
11	111.2	2.5	-0.9	-1.2	0.3	-0.2	-2.0	-1.3	-4.4	-0.2	-4.4
12	110.6	0.2	-0.9	-1.1	0.4	0.0	-2.3	-0.4	-3.5	-0.2	-4.7
13	111.7	0.4	-1.0	0.1	0.2	-0.1	-3.2	0.6	-3.8	-0.5	-4.1
14	112.3	0.3	-0.8	-1.0	0.5	-0.1	-3.5	0.9	-4.1	-0.2	-3.0
15	111.5	0.5	-0.5	-2.7	0.1	-0.2	-4.6	1.5	-4.5	0.1	-2.5
XRD-Hillier Predictions	88.3		0.0	1.6	0.0		0.0	11.4	0.0	0.0	

**Table 7.7: Predicted Percentages of each named component varying with number of factors, for Clashach. The green and black boxes indicate the percentage of each named component predicted using the number of factors chosen for the absolute and pragmatic PLS models, respectively.**

No. of Factors	Quartz	Montmorillonite	Kaolinite	Illite	Calcite	Dolomite	Na-Feldspar	K-Feldspar	Hematite	Chlorite	Muscovite
1	100.4	0.2	-3.5	5.0	-0.7	-2.0	3.4	-0.1	-2.1	-2.4	-0.3
2	109.4	-0.2	-2.2	1.4	-8.6	-9.4	1.0	1.1	-2.5	-3.9	-2.1
3	109.5	2.6	0.0	-3.2	-0.2	-2.2	1.6	-0.1	-2.3	-2.2	-1.1
4	112.5	2.3	0.6	-1.5	-1.1	-3.8	-2.6	-9.6	0.3	-3.7	-3.3
5	117.4	1.0	1.1	-0.7	-1.7	-2.6	1.0	-11.9	0.7	-2.7	-4.6
6	117.6	1.0	1.1	-0.7	-0.4	-2.5	2.2	-15.4	0.5	-1.3	-4.6
7	118.2	1.0	1.4	-0.9	0.1	-2.3	2.0	-16.5	-1.2	-1.6	-5.8
8	118.4	2.4	1.5	-1.3	0.9	-1.3	2.4	-17.7	-1.5	-1.7	-5.8
9	119.4	3.3	1.5	-1.5	1.4	-0.6	3.1	-16.4	-2.7	-1.7	-5.5
10	118.7	3.6	0.6	-1.9	1.9	-0.5	3.1	-14.4	-3.7	-1.4	-3.9
11	118.4	2.4	0.8	0.0	1.4	-0.9	-2.4	-11.8	-3.4	-1.1	-4.1
12	117.3	0.6	0.7	-0.9	1.6	-0.6	-1.9	-11.2	-2.0	-1.1	-4.6
13	118.7	1.1	0.3	0.5	1.1	-0.7	-3.6	-10.0	-2.3	-1.6	-3.8
14	119.2	0.6	0.0	-0.8	1.1	-0.5	-4.0	-9.0	-2.4	-1.7	-2.4
15	119.6	0.1	0.3	-1.7	0.3	-0.7	-5.4	-7.9	-2.5	-1.8	-1.6
XRD-Hillier Predictions	91.2		2.4	3.4	0.0		4.6	0.0	0.0	0.0	

**Table 7.8: Predicted Percentages of each named component varying with number of factors, for Castlegate. The green and black boxes indicate the percentage of each named component predicted using the number of factors chosen for the absolute and pragmatic PLS models, respectively.**

It was useful to examine how the number of factors chosen altered the predicted percentages of components. For future studies it would be advantageous to study tables such as Table 7.2-7.8 at an earlier stage, to determine what number of factors to choose for each component. Unfortunately, however, although the predicted percentage of quartz could be reduced by reducing the number of factors, the over prediction of quartz in Clashach and Castlegate could not be prevented by altering the number of factors.

For the components, Na-feldspar and chlorite, the number of factors chosen in the absolute model which gave the most accurate predictions in the independent standards were also the factors which gave the most accurate predictions in the sandstones. In

these two components, therefore, the number of factors was not altered. For the other components, however, the percentages predicted in the sandstones by the pragmatic PLS model, were generally closer in value to those by Hillier, than the absolute PLS model predictions were.

### 7.5.3 Comparing Absolute PLS Model, Pragmatic PLS Model, and XRD-Hillier Model Predictions

Figures 7.33-7.40 compare the predicted percentages of components by the XRD-Hillier, absolute, and pragmatic PLS models.

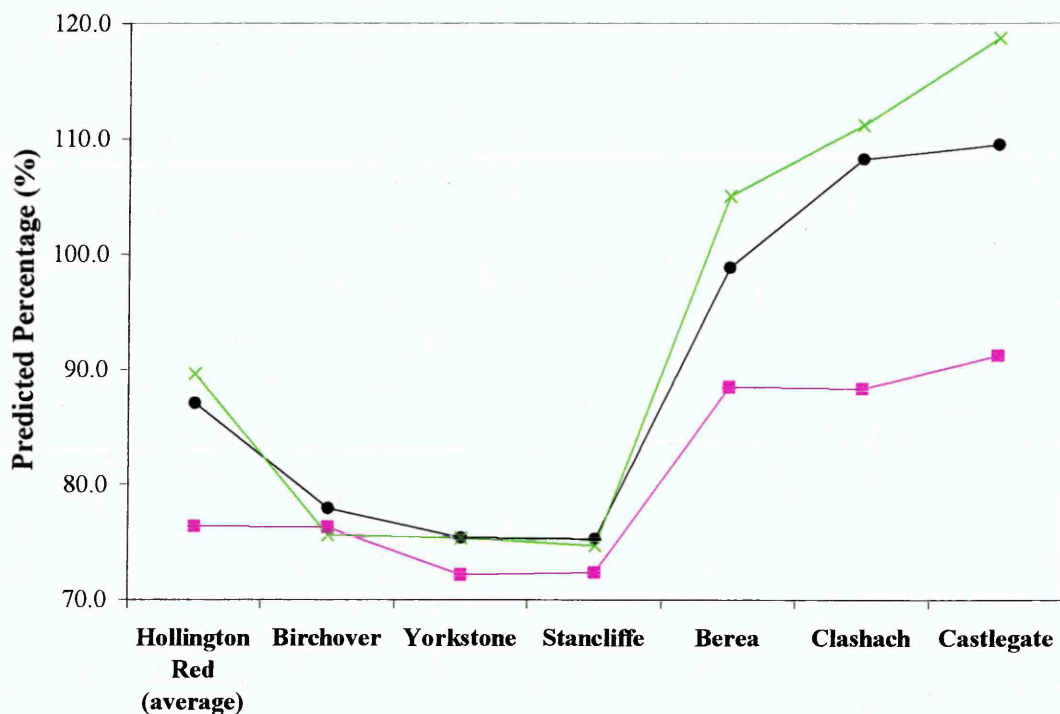


**Figure 7.33: Comparison of XRD-Hillier (pink) predictions of quartz in sandstones named, with predictions by the absolute (green), and the pragmatic (black) PLS models. See section 7.4.1 for details of models.**

Although the percentages of quartz predicted by the pragmatic PLS model were lower for Berea, Clashach, and Castlegate sandstones, than those predicted by the absolute PLS model, quartz was still over predicted. One possible reason as to why the PLS models predicted higher concentrations of quartz than the XRD model developed by Hillier is that DRIFTS spectroscopy can identify both amorphous and crystalline quartz, whereas XRD is only capable of identifying crystalline material. If the

sandstones contained both amorphous and crystalline quartz and, if the PLS models took account of both these forms, then the PLS models should give more true predictions for quartz. Percentages of quartz predicted in Clashach and Castlegate were over 100 wt% however, so other factors must have been involved, and these are discussed in section 7.7.

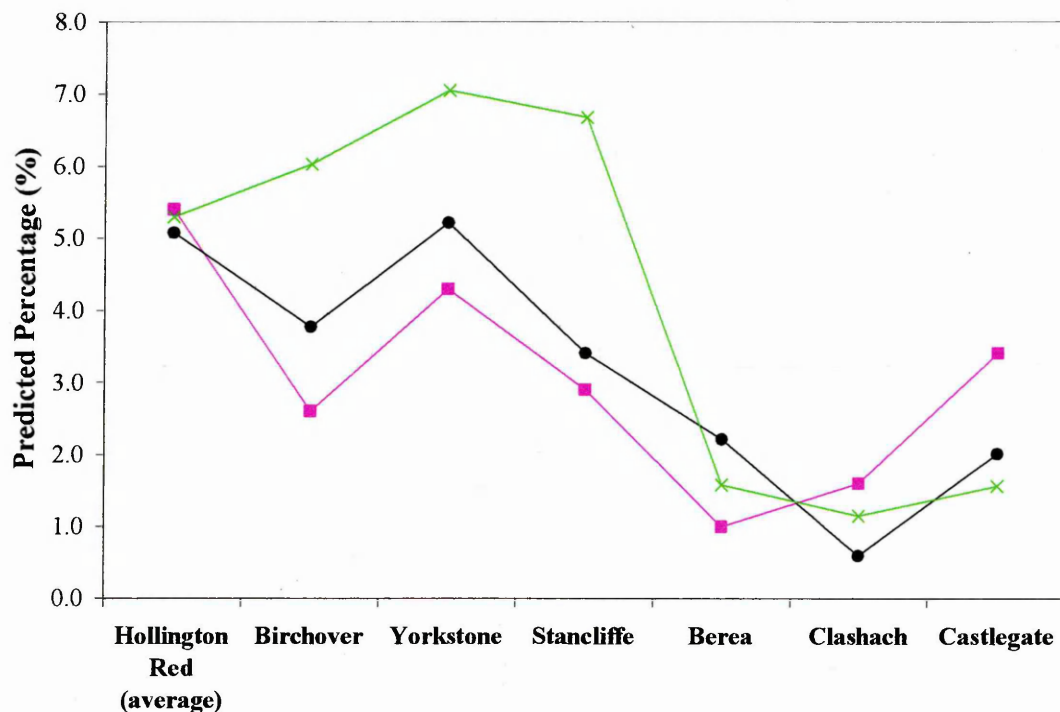


**Figure 7.34: Comparison of XRD-Hillier (pink) predictions of montmorillonite+illite in sandstones named, with predictions by the absolute (green), and the pragmatic (black) PLS models. See section 7.4.1 for details of models.**

The percentages of montmorillonite + illite predicted by the pragmatic PLS model were not only more similar in value to predictions by the XRD-Hillier model, but also followed the same trend more closely, than the absolute PLS model.

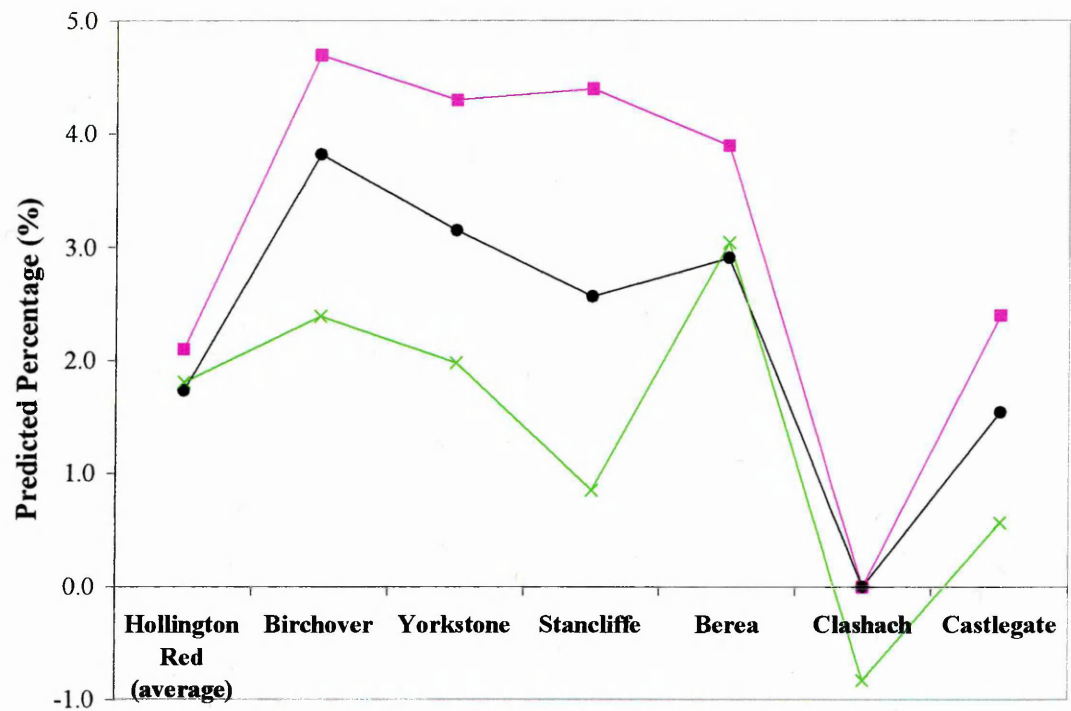


**Figure 7.35: Comparison of XRD-Hillier (pink) predictions of kaolinite in sandstones named, with predictions by the absolute (green), and the pragmatic (black) PLS models. See section 7.4.1 for details of models.**

Again, the percentages predicted by the pragmatic PLS model were closer in value to those of the XRD-Hillier model for kaolinite.

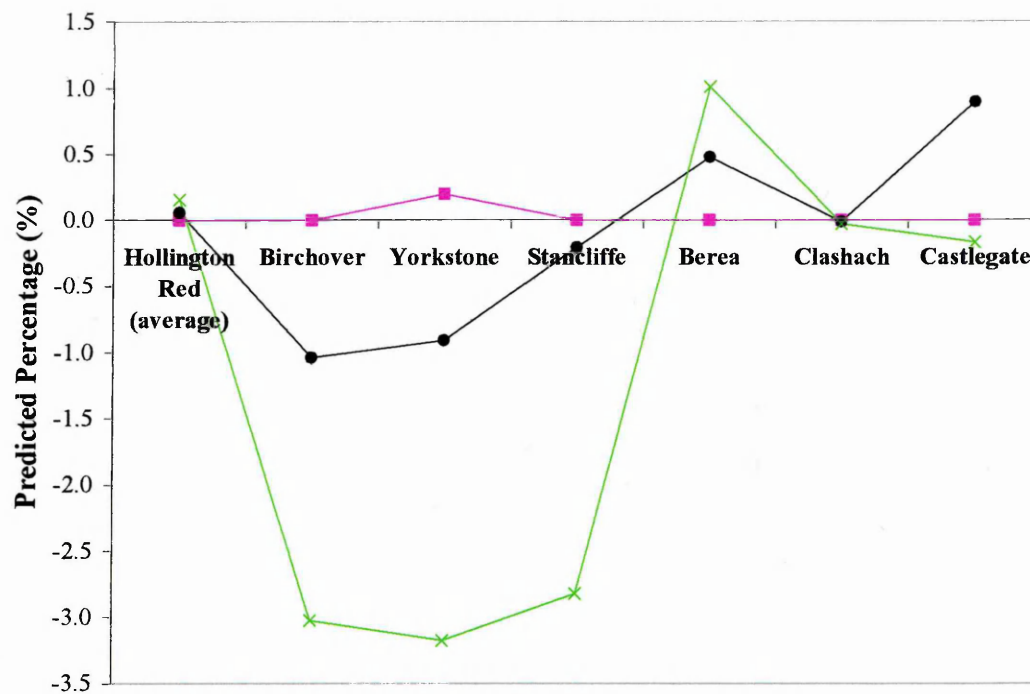


**Figure 7.36: Comparison of XRD-Hillier (pink) predictions of calcite in sandstones named, with predictions by the absolute (green), and the pragmatic (black) PLS models. See section 7.4.1 for details of models.**

Although negative percentages were still predicted for calcite in Birchover, Yorkstone, and Stancliffe using the pragmatic PLS model, the predictions were an improvement on the absolute PLS model.

As stated previously, the presence of dolomite in the sandstones was not investigated by Hillier, so in Figure 7.37, the absolute and pragmatic PLS model predictions are compared with the LSF-SDR model and the PLS-Clegg model.

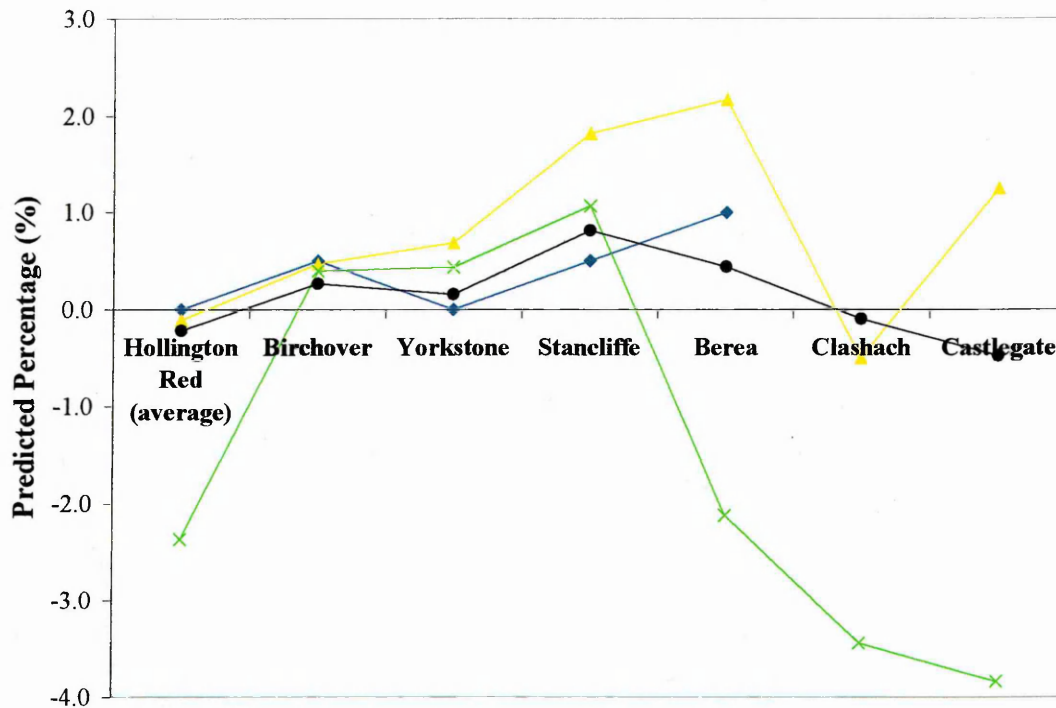


**Figure 7.37: Comparison of LSF-SDR (blue), and PLS-Clegg (yellow) predictions of dolomite in sandstones named, with predictions by the absolute (green) and the pragmatic (black) PLS models. See section 7.4.1 for details of models.**

The percentages of dolomite predicted by the pragmatic PLS model for the sandstones followed much more closely the trend of predictions by the LSF-SDR model, and the PLS-Clegg model, than the predictions by the absolute PLS model. The large negative percentages predicted by the absolute PLS model, were also absent in the pragmatic PLS model.

The predictions for Na-feldspar using the pragmatic model are not shown since the number of factors, and therefore the predicted percentages, for Na-feldspar were the same in both the absolute and the pragmatic PLS model. A comparison of these predicted percentages with predictions by the other models is shown in Figure 7.26.

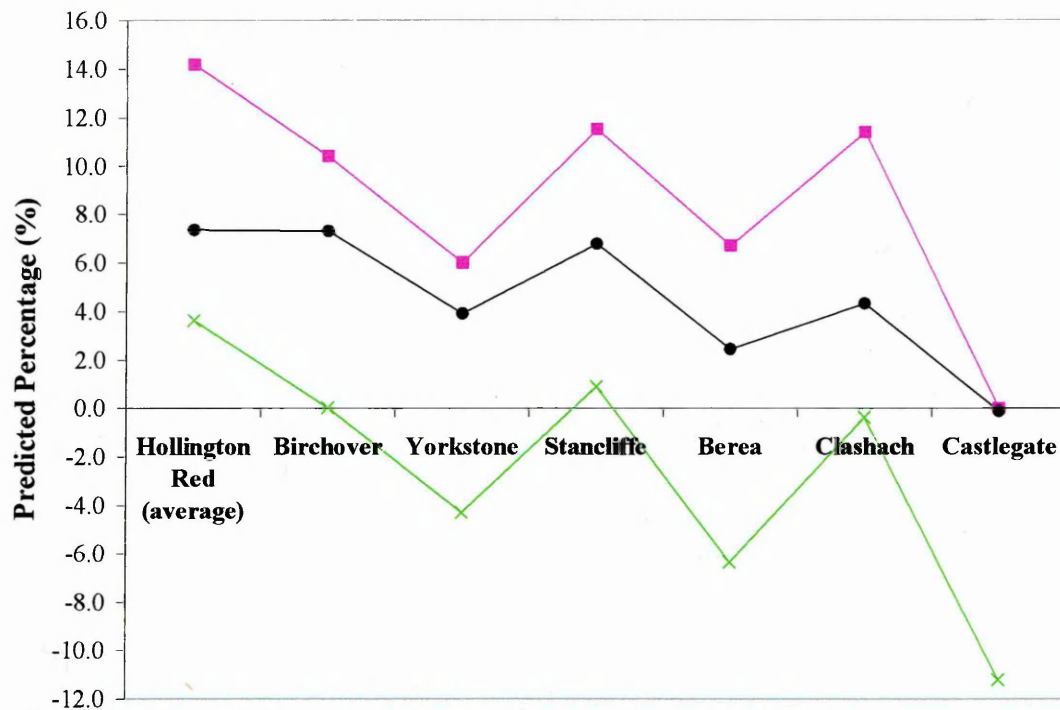


**Figure 7.38: Comparison of XRD-Hillier (pink) predictions of K-feldspar in sandstones named, with predictions by the absolute (green), and the pragmatic (black) PLS models. See section 7.4.1 for details of models.**

The percentages of K-feldspar predicted by the pragmatic PLS model followed the same trend for the sandstones as both the absolute PLS model and the XRD-Hillier model, but were closer in value to the predictions by the XRD-Hillier model than were the absolute PLS model predictions.

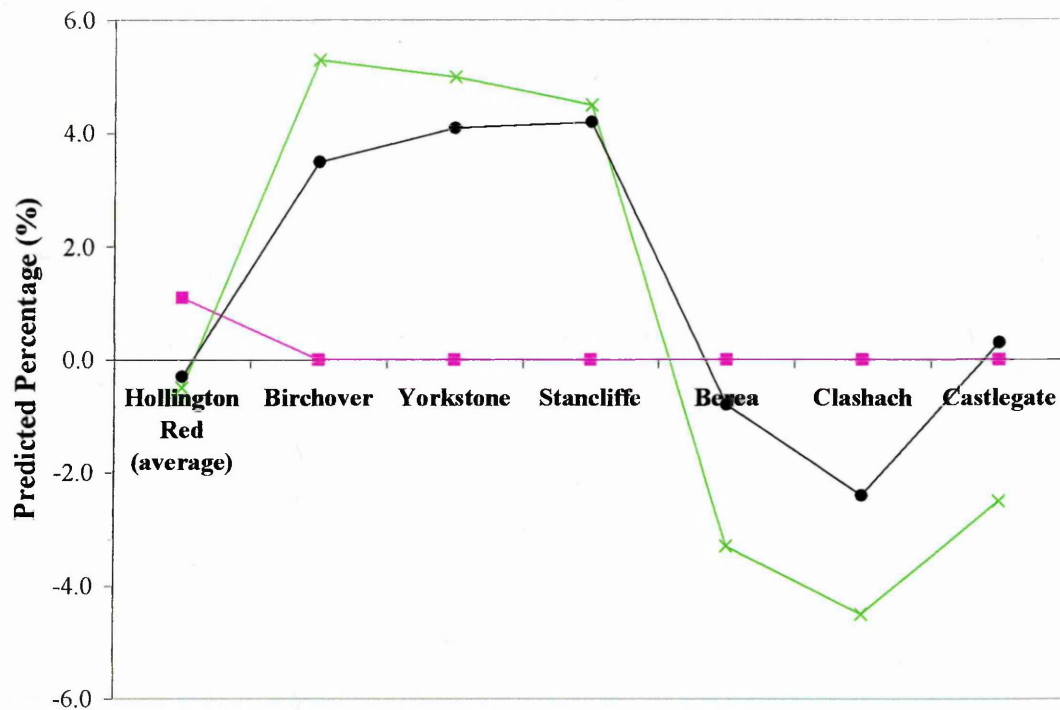


**Figure 7.39: Comparison of XRD-Hillier (pink) predictions of hematite in sandstones named, with predictions by the absolute (green), and the pragmatic (black) PLS models. See section 7.4.1 for details of models.**

Despite the slight improvement in predictions of hematite using the pragmatic PLS model, the predictions remained quite different to those by the XRD-Hillier model.

As with Na-feldspar, the predictions for chlorite using the pragmatic model are not shown since the number of factors chosen for chlorite was the same in both the absolute and the pragmatic PLS models. Comparisons of these predicted percentages with predictions by the other models, is shown in Figure 7.29.

Neither Hillier nor Clegg investigated the presence of muscovite in the sandstones. In Figure 7.40, the absolute and pragmatic PLS model predictions for muscovite are therefore compared with predictions by the LSF-SDR model.

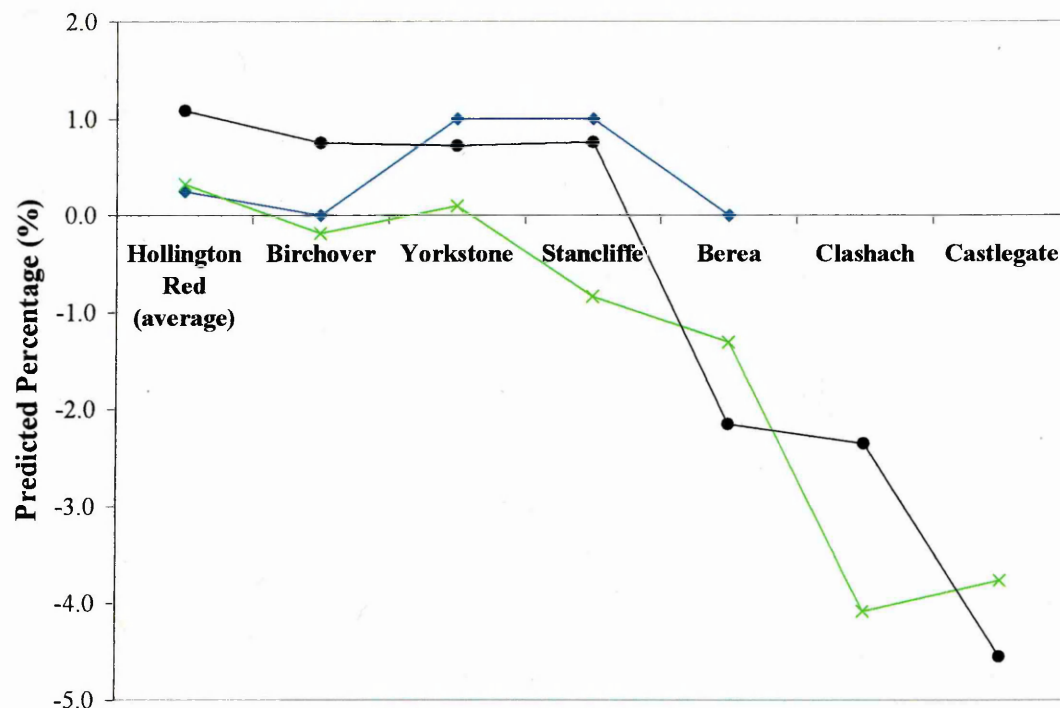


**Figure 7.40: Comparison of LSF-SDR (blue) predictions of muscovite in sandstones named, with predictions by the absolute (green), and the pragmatic (black) PLS models. See section 7.4.1 for details of models.**

In the sandstones where some muscovite was predicted, the percentages predicted were so low that comparison between different models was difficult since the low predictions were within the individual errors for the different models. The percentages of muscovite predicted in Yorkstone and Stancliffe by the pragmatic PLS model were closer to predictions of muscovite by the LSF-SDR model than by absolute PLS model predictions. The large negative predicted percentages in Berea, Clashach, and Castlegate, by the absolute PLS model, were not improved, however, by using the pragmatic PLS model.

## 7.6 Absolute and Pragmatic PLS Model Errors

### 7.6.1 Maximum Errors of Absolute and Pragmatic PLS Models

The maximum errors (largest difference between the actual and the predicted percentages of the independent standards) for each training set component, in the absolute and pragmatic PLS models are shown in Table 7.9. The corresponding number of factors chosen for each component in each model is also included.

Component	No. of Factors for Absolute PLS model	Max. error for Absolute PLS model (wt%)	No. of Factors for Pragmatic PLS model	Max. error for Pragmatic PLS model (wt%)
Quartz	10	±2.2	3	±3.7
Montmorillonite	8	±2.0	9	±3.1
Kaolinite	4	±1.4	9	±1.2
Illite	14	±2.5	8	±4.7
Calcite	3	±2.8	8	±4.0
Dolomite	4	±2.4	10	±1.5
Na-Feldspar	12	±1.9	12	±1.9
K-Feldspar	12	±2.0	3	±6.8
Hematite	15	±1.9	4	±4.2
Chlorite	6	±1.7	6	±1.7
Muscovite	13	±1.6	5	±3.5

**Table 7.9: Comparisons of the number of factors chosen and maximum errors for the absolute and pragmatic PLS models, for each of the named components.**

As stated previously, the number of factors chosen for components, Na-feldspar and chlorite, was the same for the absolute and the pragmatic PLS models. The maximum error for these components was therefore the same for both models. For components where the number of factors in the absolute and pragmatic PLS models were different, the components predicted by the pragmatic PLS model generally had a greater maximum error than when predicted by the absolute PLS model. This was especially true for K-feldspar, where the maximum error had increased from ±2 wt% in the

absolute PLS model to  $\pm 6.8$  wt% in the pragmatic PLS model. This suggested that while the pragmatic PLS model may have predicted percentages of K-feldspar closer in value to those predicted by the XRD-Hillier model, compared with predictions by the absolute PLS model, the accuracy of those predictions had decreased. Dolomite was an exception to the trend of increased maximum errors in the pragmatic PLS model, since the maximum error was less when predicted by the pragmatic PLS model. This may be expected since the pragmatic PLS model included more factors than the absolute PLS model for dolomite prediction.

## **7.6.2 Maximum Reproducibility Errors**

### **7.6.2.1 Introduction**

The reproducibility of component predictions in three sets of powders; the powder from cutting, the ground slices, and the ball milled slices, was studied. The reproducibility errors were calculated by first collecting three spectra of the same sample from each of the sets of powders, with the sample cup being emptied and re-packed between collections. Percentages of components were then predicted for each spectra and the lowest value for each component subtracted from the highest value of each component to give reproducibility errors for each set of powders.

### **7.6.2.2 Results**

Figures 7.41-7.51 show the reproducibility errors for each set of powders and each sandstone component, using the absolute PLS model. For comparison, the reproducibility errors for predictions of ball milled powders using the pragmatic PLS model are also shown. In Figures 7.41-7.51, the two horizontal dashed lines indicate the maximum error, as shown in Table 7.9, for the absolute PLS model (red) and for the pragmatic PLS model (black).

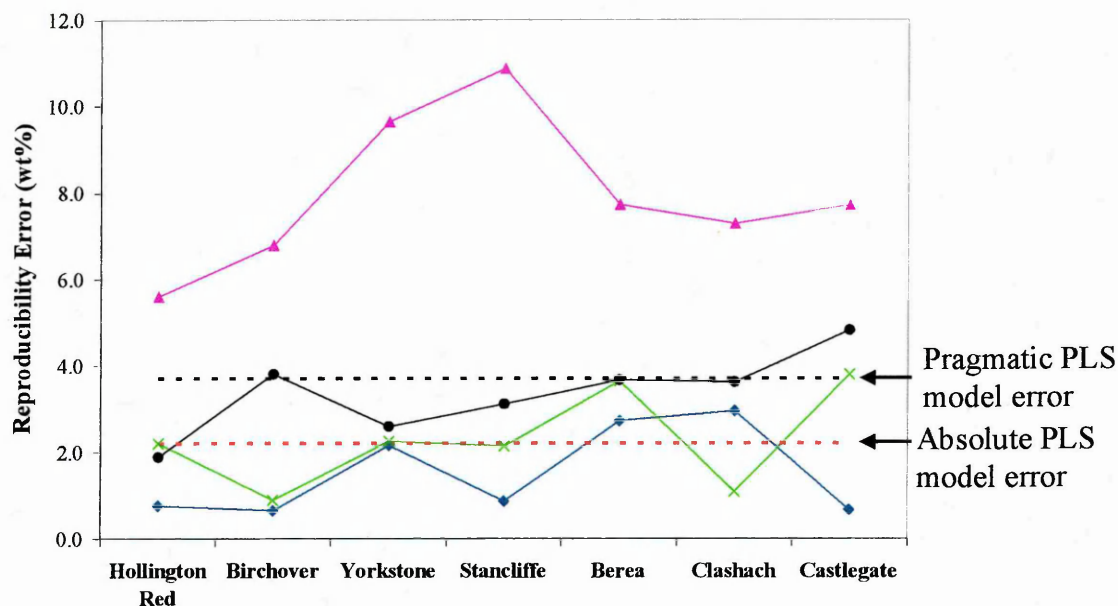


**Figure 7.41: Reproducibility errors for quartz in powder from cutting (blue), ground slice (pink), and ball milled slice (green) using the absolute PLS model, and ball milled slice (black) using the pragmatic PLS model, in the sandstones named. The red and black dashed lines indicate the maximum errors for the absolute and pragmatic PLS models, respectively.**

The largest reproducibility error for quartz was clearly found for the ground slices (Figure 7.41), which was expected since this powder had the largest particle size and particle size distribution. The reproducibility errors for the powder from cutting and for the ball milled slices using the absolute PLS model were similar and generally fell below the maximum error for the absolute PLS model. The errors found for the ball milled slices using the pragmatic PLS model were, however, slightly greater, which was expected since the maximum error for the pragmatic PLS model was greater than it was for the absolute PLS model.

Clegg reported a reproducibility error range for predictions of quartz in sandstones at  $\pm 1.0$ - $2.2$  wt%, using the PLS-Clegg model (a pragmatic model), while the error range of predictions found using the absolute and the pragmatic PLS models were  $\pm 0.9$ - $3.8$  wt% and  $\pm 1.9$ - $4.8$  wt%, respectively. The PLS-Clegg model therefore predicted quartz with more precision than the absolute and pragmatic PLS models. This may be because the sandstones studied by Clegg had been ball milled for longer than those studied in this thesis. The 20 minutes ball milling time, used by Clegg, compared to

the 5 minutes ball milling time used in this thesis, perhaps reduced errors caused by different particle sizes and particle size distributions of the different sandstones and therefore reduced the reproducibility error in the PLS-Clegg model.

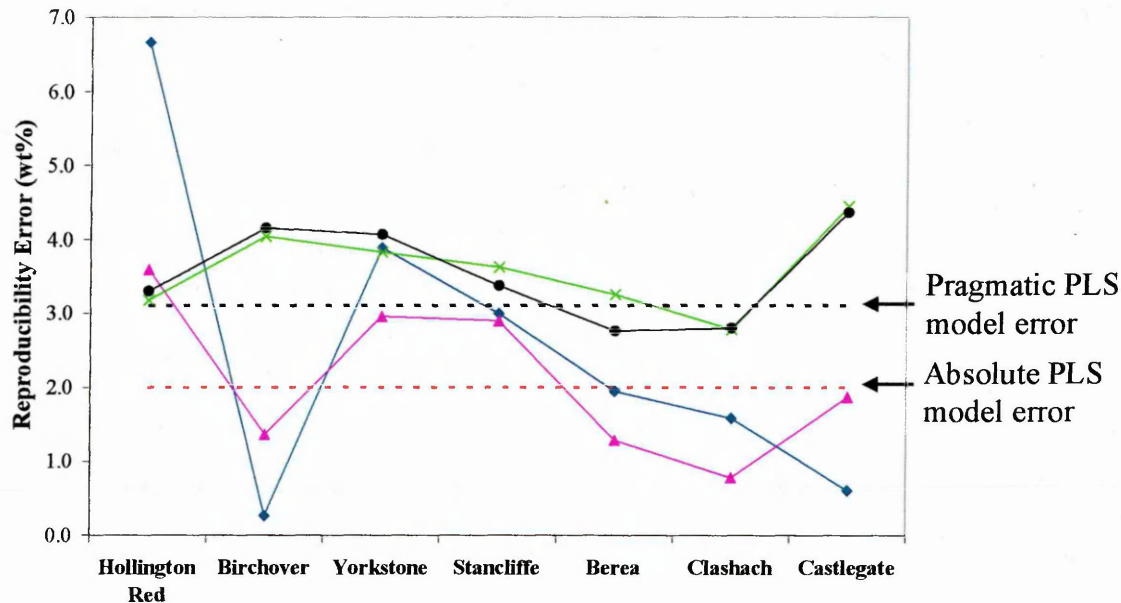


**Figure 7.42: Reproducibility errors for montmorillonite in powder from cutting (blue), ground slice (pink), and ball milled slice (green) using the absolute PLS model, and ball milled slice (black) using the pragmatic PLS model, in the sandstones named. The red and black dashed lines indicate the maximum errors for the absolute and pragmatic PLS models, respectively.**

The reproducibility errors for the predictions of montmorillonite in the hand ground slices (Figure 7.42) appeared to be less than for the ball milled slices. The reproducibility errors using the absolute and pragmatic PLS model were very similar despite the maximum errors for the two models being different. Interestingly, the reproducibility errors for montmorillonite in all the sandstones using the absolute PLS model were greater than the absolute PLS model maximum error so it must have been the lack of reproducibility of detecting montmorillonite in the sandstones that caused the greater error.

For predictions of montmorillonite and illite combined, the reproducibility error for predictions of sandstones using the PLS-Clegg model ranged from  $\pm 0.8$ - $1.2$  wt%. The reproducibility error for predictions of sandstones using the pragmatic PLS model ranged from  $\pm 2.8$ - $4.4$  wt% for montmorillonite, and from  $\pm 1.8$ - $3.7$  wt% in illite. If

the components were combined, as they were in the PLS-Clegg model, the range of reproducibility errors for the sandstones, using the pragmatic PLS model, would be  $\pm 0.6-1.5$  wt%, indicating greater precision. The PLS-Clegg model and the pragmatic PLS model, therefore, predicted the combined percentage of montmorillonite and illite in sandstones, with the same degree of precision.

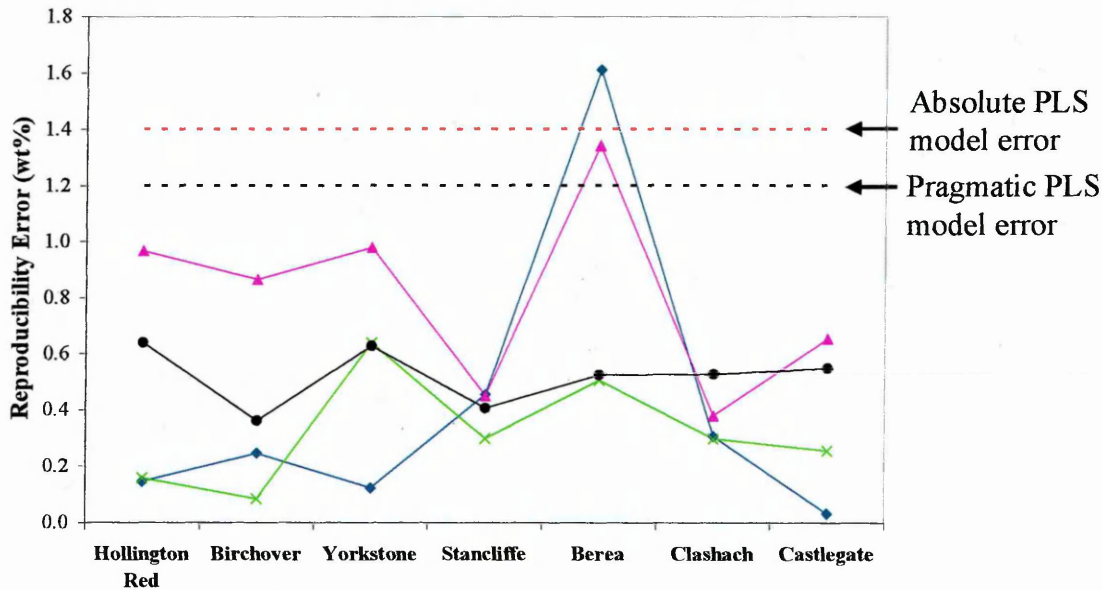


**Figure 7.43: Reproducibility errors for kaolinite in powder from cutting (blue), ground slice (pink), and ball milled slice (green) using the absolute PLS model, and ball milled slice (black) using the pragmatic model, in the sandstones named. The red and black dashed lines indicate the maximum errors for the absolute and pragmatic PLS models, respectively.**

The reproducibility errors for the predictions of kaolinite were very low for all the powders studied (Figure 7.43), especially for the ball milled slices, using the absolute and pragmatic PLS models, where the reproducibility errors were always less than  $\pm 0.7$  wt%. The predictions for the ball milled slices by the absolute PLS model were the most reproducible, but both the absolute and the pragmatic PLS models had reproducibility errors lower than the maximum error for each model, so detection and prediction of kaolinite from the sandstone spectra was very reproducible. It was unclear as to why the reproducibility errors for the hand ground slice and powder from cutting Berea were greater than for the other sandstones, though it does further confirm that samples should be ball milled to obtain reproducible results.

The reproducibility error range for predicting kaolinite in the sandstones using the PLS-Clegg model was found to be  $\pm 0.8$ -3.0 wt%. The absolute and pragmatic PLS models could predict kaolinite with more precision, with an error range of  $\pm 0.2$ -0.6 wt% using the absolute PLS model, and of  $\pm 0.4$ -0.6 wt% using the pragmatic PLS model.

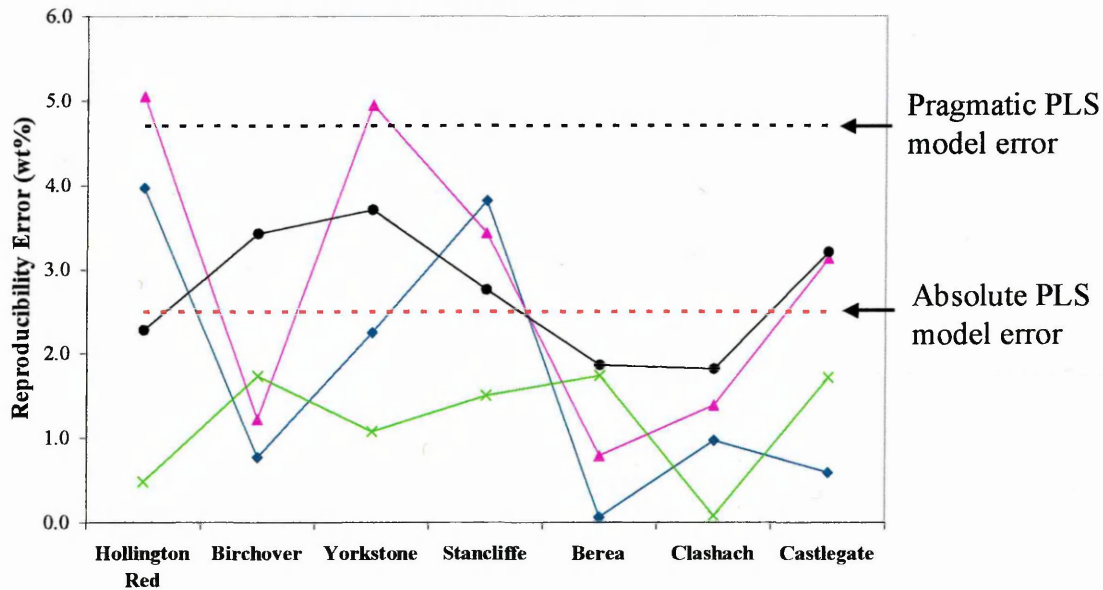


**Figure 7.44: Reproducibility errors for illite in powder from cutting (blue), ground slice (pink), and ball milled slice (green) using the absolute PLS model, and ball milled slice (black) using the pragmatic model, in the sandstones named. The red and black dashed lines indicate the maximum errors for the absolute and pragmatic PLS models, respectively.**

The reproducibility errors for predicting illite alone (Figure 7.44) were far greater than for predicting kaolinite. The most reproducible predictions were found for the ball milled slices using the absolute PLS model, and the reproducibility errors were also less than the error of the absolute PLS model. Although the predictions for the ball milled slices using the pragmatic PLS model were less reproducible than those using the absolute PLS model, the reproducibility errors were again less than the maximum error of the pragmatic PLS model.

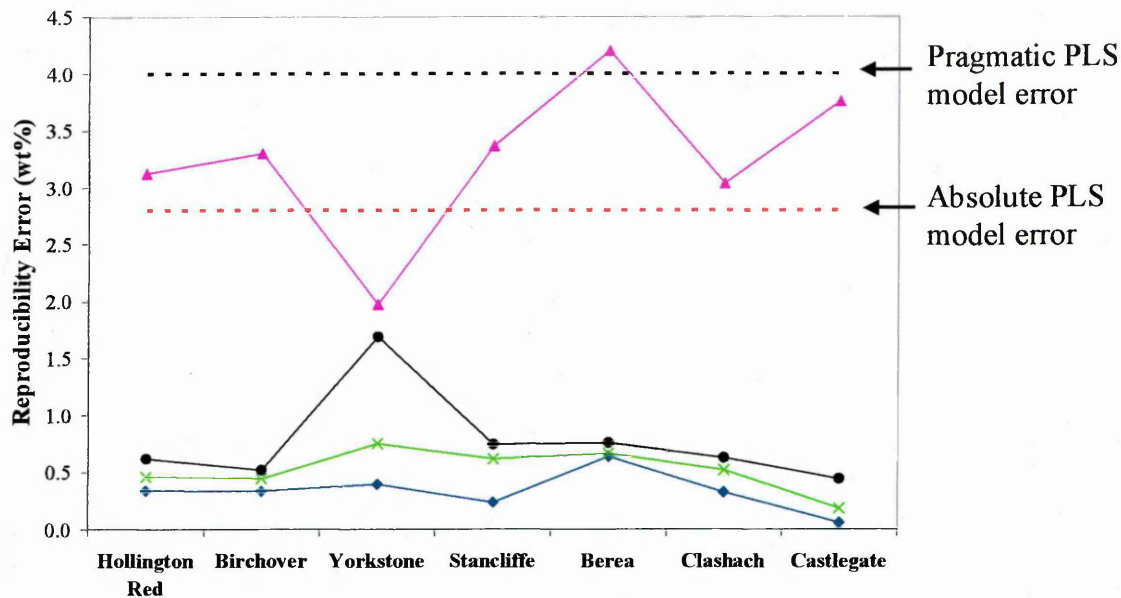


**Figure 7.45: Reproducibility errors for calcite in powder from cutting (blue), ground slice (pink), and ball milled slice (green) using the absolute PLS model, and ball milled slice (black) using the pragmatic model, in the sandstones named. The red and black dashed lines indicate the maximum errors for the absolute and pragmatic PLS models, respectively.**

It was clear that the reproducibility of calcite predictions for the ground slices was worse than for the ball milled slices and for the powder from cutting (Figure 7.45). The reproducibility of the predictions for the ball milled slices using the absolute PLS model was again better than for the pragmatic PLS model. However, for both models, the reproducibility errors were far lower than the maximum error for the models. The detection of calcite in the spectra of ball milled sandstones and its subsequent percentage prediction by the models, was therefore, very reproducible. Despite the reproducibility, it should be noted that predictions for calcite were generally negative, suggesting that, except for Berea perhaps, the sandstones did not contain calcite.

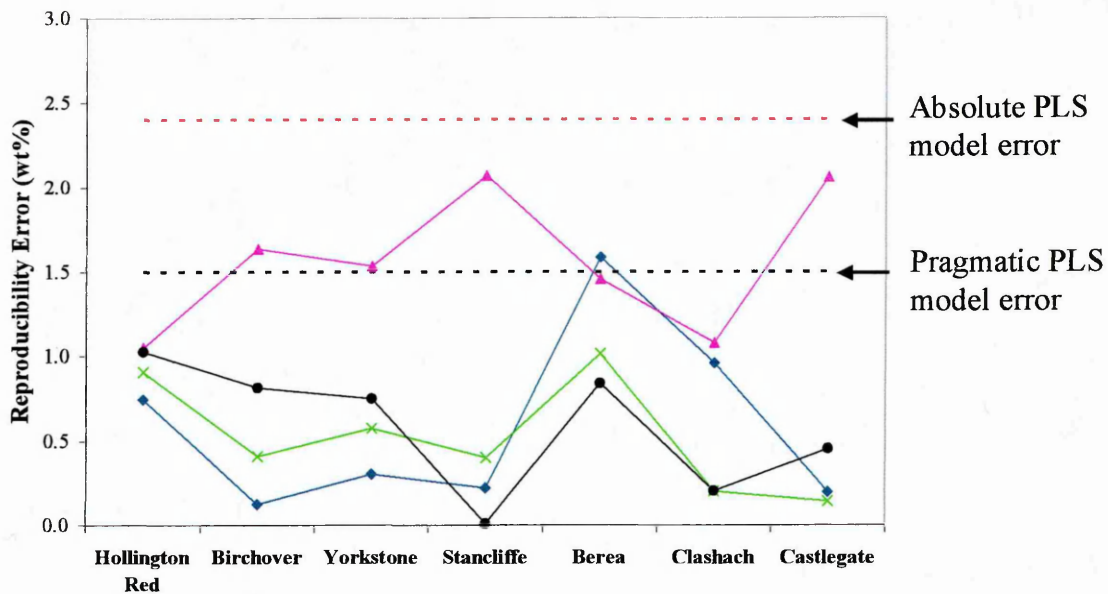


**Figure 7.46: Reproducibility errors for dolomite in powder from cutting (blue), ground slice (pink), and ball milled slice (green) using the absolute PLS model, and ball milled slice (black) using the pragmatic model, in the sandstones named. The red and black dashed lines indicate the maximum errors for the absolute and pragmatic PLS models, respectively.**

Again for the prediction of dolomite (Figure 7.46), the reproducibility was worse in the ground slices and better in the powder from cutting and in the ball milled slices. The reproducibility errors for predicting dolomite in the hand ground slices were, however, generally lower than for predicting calcite in the hand ground slices. The reproducibility errors of the predictions for the ball milled slices using both the absolute and the pragmatic PLS models, were again lower than the maximum error for the models.

The PLS-Clegg model, the absolute and the pragmatic PLS models, all predicted dolomite in the sandstones with the same degree of precision. The reproducibility error range for predicting dolomite in the sandstones, found by the PLS-Clegg model, was  $\pm 1.0$ - $1.1$  wt%, while using the absolute and the pragmatic models it was  $\pm 0.1$ - $1.0$  wt% and  $\pm 0.0$ - $1.0$  wt% respectively.

Only one set of reproducibility errors for the ball milled slices and one model error, is shown in Figure 7.47 for the prediction of Na-feldspar, since the number of factors for

this component in both the absolute and the pragmatic PLS models was the same, so predictions and therefore errors for this component were the same using both models.

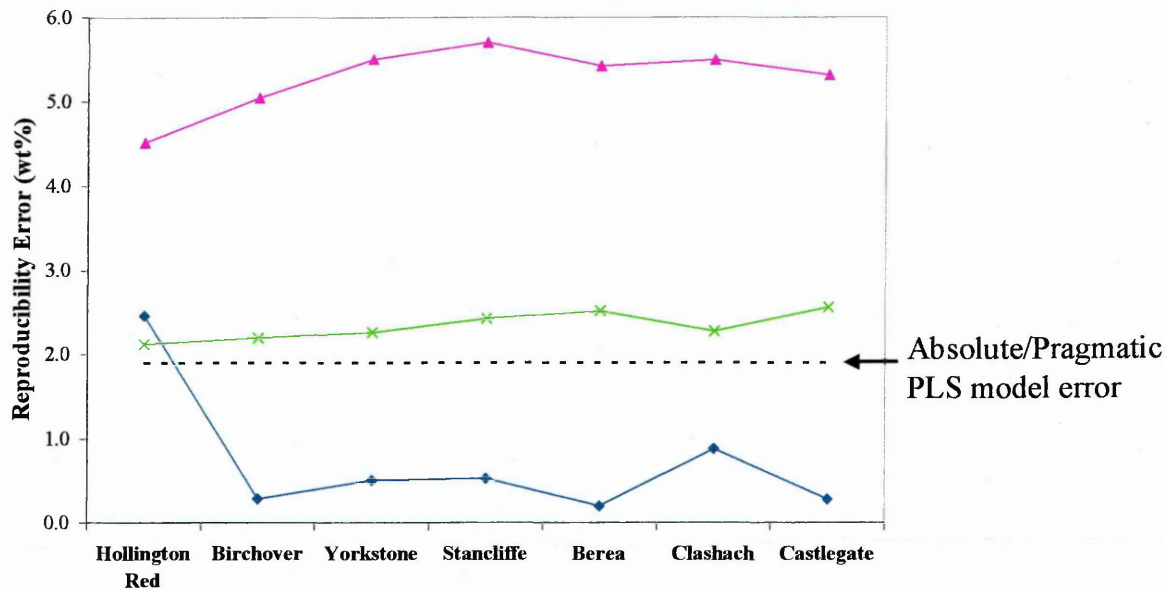


**Figure 7.47: Reproducibility errors for Na-feldspar in powder from cutting (blue), ground slice (pink), and ball milled slice (green) using the absolute/pragmatic PLS model, in the sandstones named. The black dashed line indicates the maximum error for the absolute/pragmatic PLS model.**

For the prediction of Na-feldspar, the reproducibility was notably worse for the ground slices than for the other powders (Figure 7.47). The predictions for the ball milled slices were more reproducible than for the ground slices. However, it was the prediction of Na-feldspar in the powder from cutting that was the most reproducible. It should be noted that the reproducibility errors were actually slightly greater than the model error suggesting that reproducible detection of Na-feldspar in the sandstone spectra may have been difficult.

Slightly greater precision was found in predicting Na-feldspar in the sandstones by the absolute/pragmatic PLS model than by predictions found using the PLS-Clegg model. The reproducibility error range for the sandstones was  $\pm 2.1$ - $2.5$  wt% using the absolute/pragmatic PLS model and was reported as  $\pm 1.1$ - $3.9$  wt% by the PLS-Clegg model.

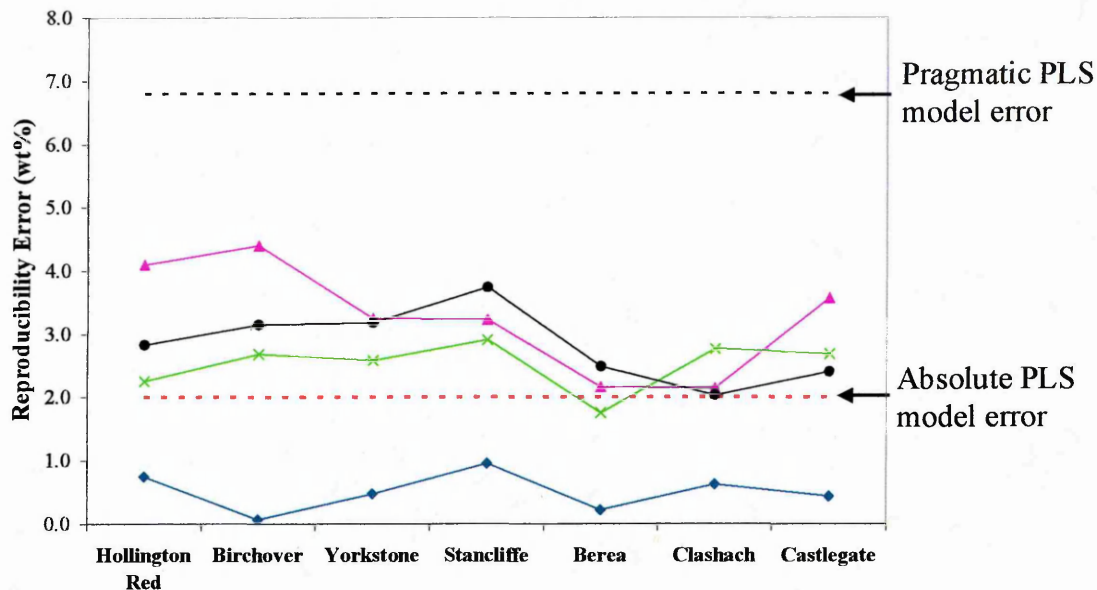


**Figure 7.48: Reproducibility errors for K-feldspar in powder from cutting (blue), ground slice (pink), and ball milled slice (green) using the absolute PLS model, and ball milled slice (black) using the pragmatic model, in the sandstones named. The red and black dashed lines indicate the maximum errors for the absolute and pragmatic PLS models, respectively.**

As with Na-feldspar it was the prediction of K-feldspar in the powder from cutting that was the most reproducible (Figure 7.48). The reproducibility errors of the ball milled slices using the absolute PLS model were slightly greater than the maximum error of the model, suggesting that the absolute PLS model had difficulty detecting K-feldspar reproducibly from the spectra of the sandstones. While the large maximum error for the pragmatic PLS model suggested that the model predicted K-feldspar with less accuracy, the reproducibility of K-feldspar predictions using the pragmatic PLS model were similar to those using the absolute PLS model.

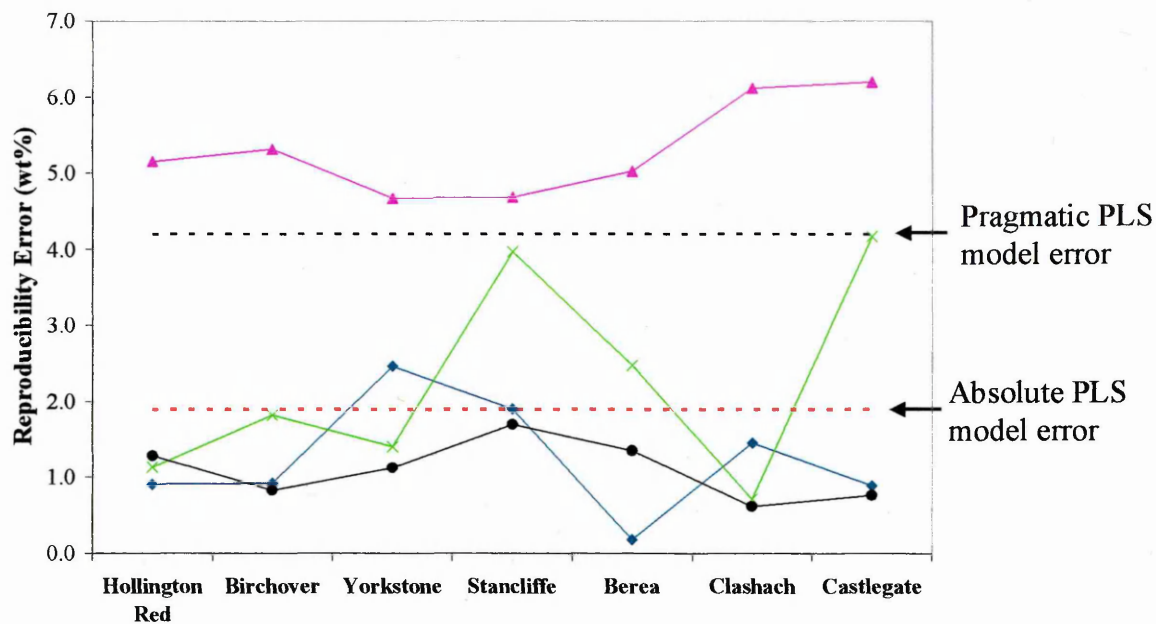


**Figure 7.49: Reproducibility errors for hematite in powder from cutting (blue), ground slice (pink), and ball milled slice (green) using the absolute PLS model, and ball milled slice (black) using the pragmatic model, in the sandstones named. The red and black dashed lines indicate the maximum errors for the absolute and pragmatic PLS models, respectively.**

As was the case for most of the components, the reproducibility errors for predicting hematite in the sandstones were also greater for the ground slices than for the other powders (Figure 7.49). The greater maximum error in the pragmatic PLS model was not reflected in the low reproducibility error for predicting hematite in the ball milled slices of the sandstones.

As with Na-feldspar, only one set of reproducibility errors for the ball milled slices, and one model error, is shown in Figure 7.50 for the prediction of chlorite since the number of factors for this component was the same in both the absolute and the pragmatic PLS models.

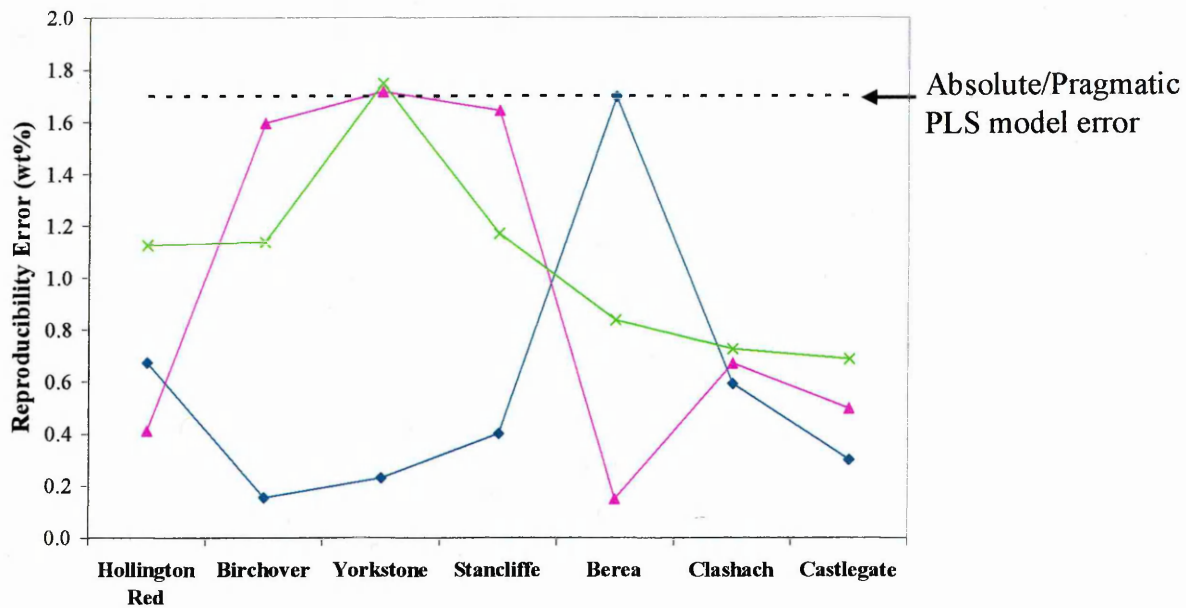


**Figure 7.50: Reproducibility errors for chlorite in powder from cutting (blue), ground slice (pink), and ball milled slice (green) using the absolute/pragmatic PLS model, in the sandstones named. The black dashed line indicates the maximum error for the absolute/pragmatic PLS models.**

Both the maximum error for the model and the reproducibility errors for predicting chlorite in the powder from cutting, ground slices, and ball milled slices, were very low indicating that the model detected and predicted chlorite in the independent standard spectra accurately and in the sandstone spectra very reproducibly.

The absolute/pragmatic PLS model was found to predict chlorite with slightly greater precision than the PLS-Clegg model. The reproducibility error range for predicting chlorite in the sandstones using the PLS-Clegg model, was found to be  $\pm 0.5$ - $2.5$  wt%, while the reproducibility error range found using the absolute/pragmatic PLS model was  $\pm 0.7$ - $1.7$  wt%.

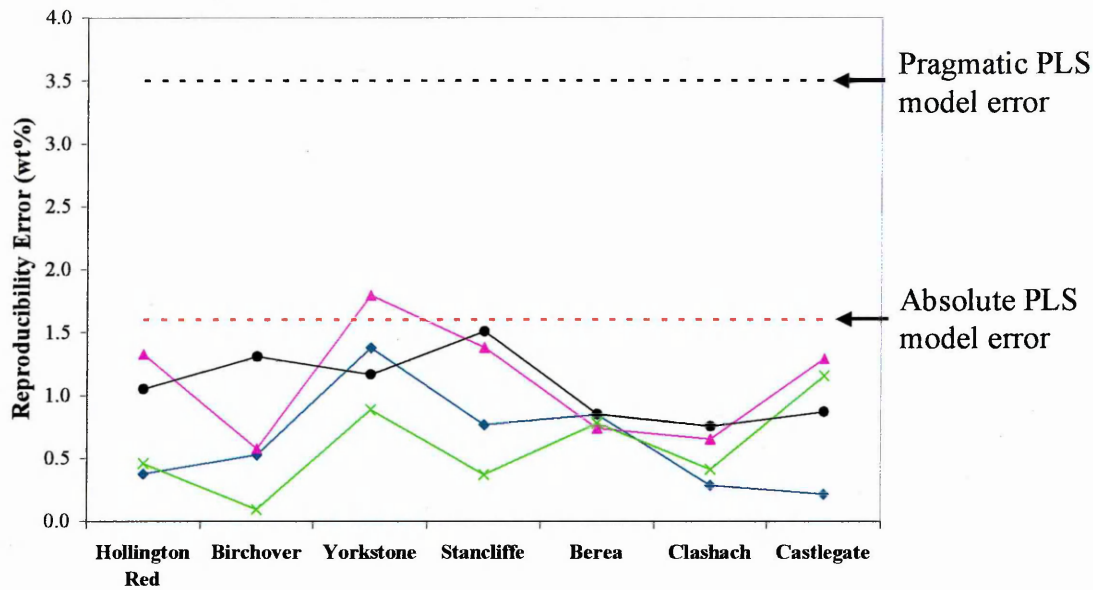


**Figure 7.51: Reproducibility errors for muscovite in powder from cutting (blue), ground slice (pink), and ball milled slice (green) using the absolute PLS model, and ball milled slice (black) using the pragmatic model, in the sandstones named. The red and black dashed lines indicate the maximum errors for the absolute and pragmatic PLS models, respectively.**

Again, the reproducibility errors for predicting muscovite in the powder from cutting, ground slices, and ball milled slices, were all very low. The reproducibility errors for predictions of muscovite in the ball milled slices using the absolute PLS model were, however, slightly lower than predictions using the pragmatic PLS model.

### 7.6.2.3 Conclusion

Table 7.10 shows a summary of the errors associated with the absolute and pragmatic PLS models and also the PLS-Clegg model. The maximum errors for each component of each model are shown, and the average errors for each component using the absolute and pragmatic PLS models also. The reproducibility errors for predicting ball milled sandstone slices are also shown for the three models.

		Quartz	Mont.	Kaolinite	Illite	Illite + Mont.	Calcite	Dolomite	Na- Feldspar	K- Feldspar	Hematite	Chlorite	Muscovite
Max. Errors (±wt%)	Absolute	2.2	2.0	1.4	2.5	-	2.8	2.4	1.9	2.0	1.9	1.7	1.6
	Pragmatic	3.7	3.1	1.2	4.7	-	4.0	1.5	1.9	6.8	4.2	1.7	3.5
Average Errors (±wt%)	PLS- Clegg	3	-	1	-	1	-	1	1	-	-	1	-
	Absolute	1.1	0.7	0.7	0.7		0.9	0.8	0.9	0.8	0.7	0.9	0.7
Reprod. Errors (±wt%)	Pragmatic	1.9	1.3	0.3	1.5		0.9	0.6	0.9	3.0	2.2	0.9	1.7
	Absolute	0.9- 3.8	2.8- 4.4	0.2-0.6	0.1- 1.7		0.2-0.8	0.1-1.0	2.1-2.5	1.7-2.9	0.7-4.2	0.7-1.7	0.1-1.2
Errors (±wt%)	Pragmatic	1.9- 4.8	2.8- 4.4	0.4-0.6	1.8- 3.7	0.6-1.5	0.4-1.7	0.0-1.0	2.1-2.5	2.0-3.7	0.6-1.7	0.7-1.7	0.8-1.5
	PLS- Clegg	1.0- 2.2	-	0.8-3.0	-	0.8-1.2	-	1.0-1.1	1.1-3.9	-	-	0.5-2.5	-

Table 7.10: Summary of Errors in the Absolute and Pragmatic PLS Models, and in the PLS-Clegg Model together with a comparison of the reproducibility and average errors for predicting the named components in the ball milled sandstone slices.

The highest reproducibility error for prediction of components was most often found for the ground slices. This was expected since the particle size distribution was greatest in the ground slices, making the samples less homogeneous. The reproducibility errors for the hand ground slices were also generally higher than the maximum error for the absolute PLS model, suggesting that it was difficult to collect reproducible spectra of the hand ground slices, and therefore the predictions of components were not very reproducible. In contrast, the reproducibility errors for the powder from cutting, and for the ball milled slices, were generally less than the absolute PLS model errors in most components. This suggested that for these powders, the spectra were more reproducible, and so it was the error of the model, rather than the reproducibility of the spectra, that caused the greater error.

For most components, the reproducibility of the predictions from the absolute PLS model was better than those from the pragmatic PLS model. This indicated that although the predictions of components using the pragmatic PLS model were closer to those of Hillier than those using the absolute PLS model, the pragmatic PLS model had more difficulty in detecting components from the sandstone spectra reproducibly than the absolute PLS model.

The reproducibility errors found by using the absolute and pragmatic PLS models were compared with those reported by Clegg [21] using the PLS-Clegg model, as shown in Table 7.10. The ranges in errors found for the different sandstones suggested that the PLS-Clegg model predicted quartz with more precision, predicted combined montmorillonite + illite, and also dolomite, with the same precision, and predicted kaolinite, chlorite, and Na-feldspar, with less precision than the pragmatic PLS model.

## **7.7 Reasons for Quartz Predictions**

### **7.7.1 Over-Prediction of Quartz in Sandstones**

#### **7.7.1.1 Introduction**

Changing the number of factors of the absolute PLS model to produce the pragmatic PLS model improved predictions of some components in the sandstones, i.e. brought predictions closer to those calculated by the XRD-Hillier model. The prediction of

quartz in Clashach and Castlegate sandstones by both the PLS models, however, was still over 100 wt% regardless of the number of factors chosen. In attempting to find reasons for these poor predictions, the DRIFTS spectra and XRD traces of training set components, and of the sandstones were examined more closely.

### 7.7.1.2 Silica Band Intensity in DRIFTS spectra of Sandstones

The intensity of the symmetric Si-O-Si stretching bands, at 800 and 781  $\text{cm}^{-1}$ , in DRIFTS spectra of the sandstones and of pure Chelford sand were examined to help explain the reason for the over prediction of quartz in Clashach, and Castlegate sandstones. The spectra are shown in Figure 7.52.

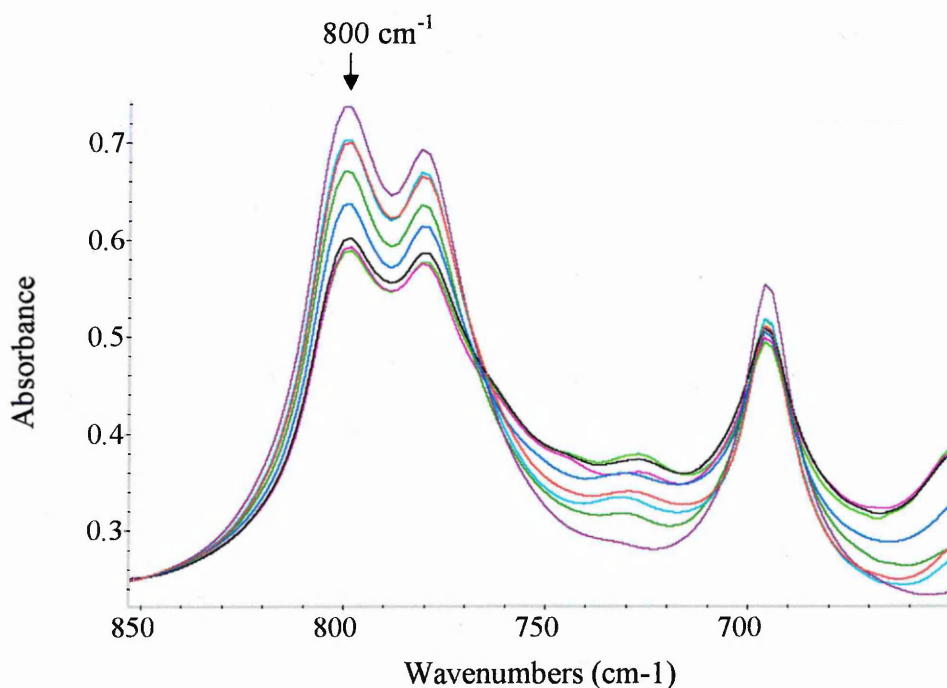


**Figure 7.52: The low wavenumber region of the DRIFTS spectra for ball milled Hollington Red (blue), Birchover (black), Yorkstone (pink), Stancliffe (green), Berea (dark green), Clashach (light blue), Castlegate (yellow) sandstones, and Chelford sand (red).**

Figure 7.52 shows intensity differences of the bands at 781 and 800  $\text{cm}^{-1}$  in spectra of the different sandstones. The intensity ratio of these bands was mentioned previously, in section 7.3.3, with regards to differences observed in the spectra of the powder from cutting, hand ground slices, and ball milled slices. When comparing the intensity ratio of these bands in spectra of the different sandstones, it could be seen

that the spectra of the sandstones which contained more clay and feldspar; Hollington Red, Birchover, Yorkstone, and Stancliffe, showed the intensity of the  $781\text{ cm}^{-1}$  band at a similar intensity to that at  $800\text{ cm}^{-1}$ . The spectra of the “cleaner” sandstones; Berea, Clashach, and Castlegate, however, showed the band at  $800\text{ cm}^{-1}$  at a higher intensity relative to that at  $781\text{ cm}^{-1}$ . The spectra of both Na- and K-feldspars showed bands at around  $780\text{ cm}^{-1}$ , and so it was thought to be the presence of more feldspar in Hollington Red, Birchover, Yorkstone, and Stancliffe, than in Berea, Clashach, and Castlegate that caused the difference in intensity ratios.

The intensity ratio of the  $781$  and  $800\text{ cm}^{-1}$  bands in the spectrum of Chelford sand was actually less than that observed in the spectrum of Castlegate, i.e. the bands were of more similar intensity in the spectrum of Chelford sand. This suggested the possibility that Chelford sand may have contained more feldspar than Castlegate.

The overall intensity difference of the bands at  $781$  and  $800\text{ cm}^{-1}$  in the different sandstones was also clear. These bands appeared generally less intense in the spectra of Birchover, Yorkstone, and Stancliffe, and more intense in the spectra of Berea, Clashach, and Castlegate sandstones. The predictions of quartz in these sandstones using the PLS models also followed a similar trend, with less quartz predicted in Birchover, Yorkstone, and Stancliffe, and more in Berea, Clashach, and Castlegate. Significantly, it was also clear from Figure 7.52 that the  $781$  and  $800\text{ cm}^{-1}$  bands were less intense in the spectrum of Chelford sand than in the spectra of Castlegate and Clashach and this may have been the cause of the over prediction of quartz in these samples by the absolute and pragmatic PLS models.

Similar trends were observed for the quartz peak intensities in the XRD traces of the sandstones and Chelford sand.

### **7.7.1.3 Quartz Peak Intensity in XRD traces of Sandstones**

The quartz peak near  $26.7^\circ 2\theta$  in XRD traces of the sandstones and of pure Chelford sand is shown in Figure 7.53.

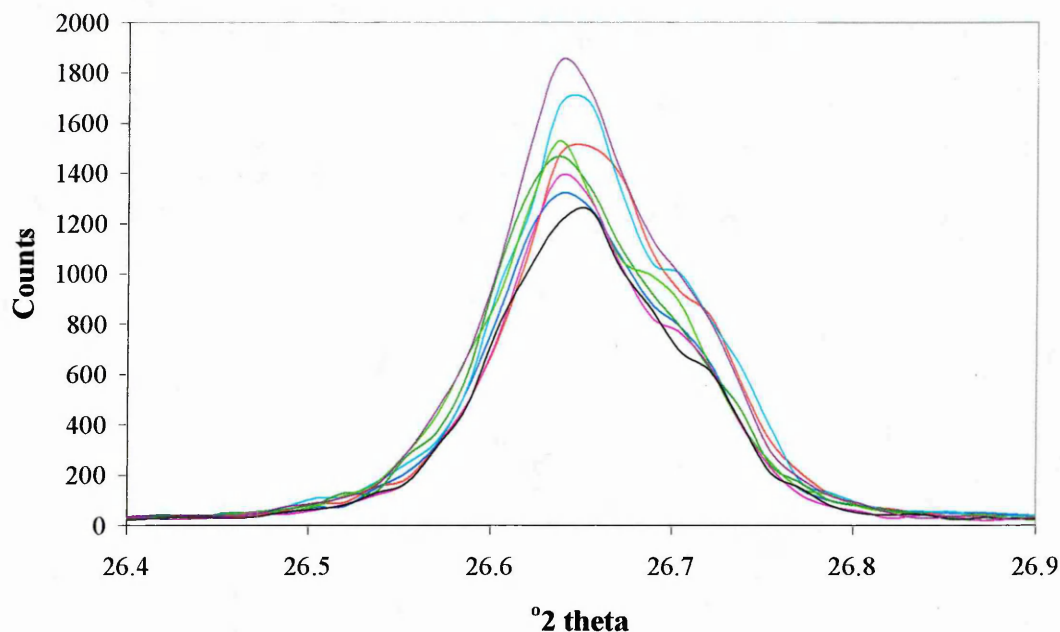


**Figure 7.53: XRD traces, illustrating the difference in quartz peak shapes and intensities, for ball milled Hollington Red (blue), Birchover (black), Yorkstone (pink), Stancliffe (green), Berea (dark green), Clashach (light blue), Castlegate (purple) sandstones, and Chelford sand (red).**

As for the bands at  $781$  and  $800\text{ cm}^{-1}$  in the DRIFTS spectra shown in Figure 7.52, a more intense quartz peak at  $26.7^\circ 2\theta$  in XRD traces shown in Figure 7.53 was observed for the sandstones, Castlegate, and Clashach, than for pure Chelford sand.

Another important observation from Figure 7.53 was the slight difference in peak shape and position of the quartz peak for the different sandstones. While the quartz peak was at  $26.65^\circ 2\theta$  for Castlegate, Clashach, and Chelford sand, it was at  $26.64^\circ 2\theta$  for the other sandstones. A shoulder was also observed in the XRD traces of the sandstones, at positions ranging from  $26.69$  to  $26.72^\circ 2\theta$  for the different sandstones. The shoulder appeared more pronounced in the XRD traces of Clashach, Stancliffe, and Yorkstone, than in the other sandstones, although the reason for this was unclear. The difference in the peak intensities for different sandstones could indicate that they contained quartz from different sources, with slightly different elemental compositions. Differences in the size of the unit cell of the quartz in the sandstones may account for the differences in the position of the quartz peaks. If the sandstones studied contained quartz from different sources and with different crystallinities, the

predicted amount of Chelford sand in each would not be a true representation of the amount of quartz in each.

#### 7.7.1.4 Conclusion

Figure 7.54 shows how the quartz band intensity in the DRIFTS spectra, and the percentage of SiO<sub>2</sub> found by XRF, varied for the different sandstones, while Figure 7.55 shows how the quartz peak intensity in the XRD traces varied for the different sandstones. The absorbance at 800 cm<sup>-1</sup> in the DRIFTS spectrum of Chelford sand, and the percentage of SiO<sub>2</sub> found in Chelford sand by XRF, are included in Figure 7.54, and the intensity of the peak at 26.7° 2θ in the XRD trace of Chelford sand included in Figure 7.55, for comparison.

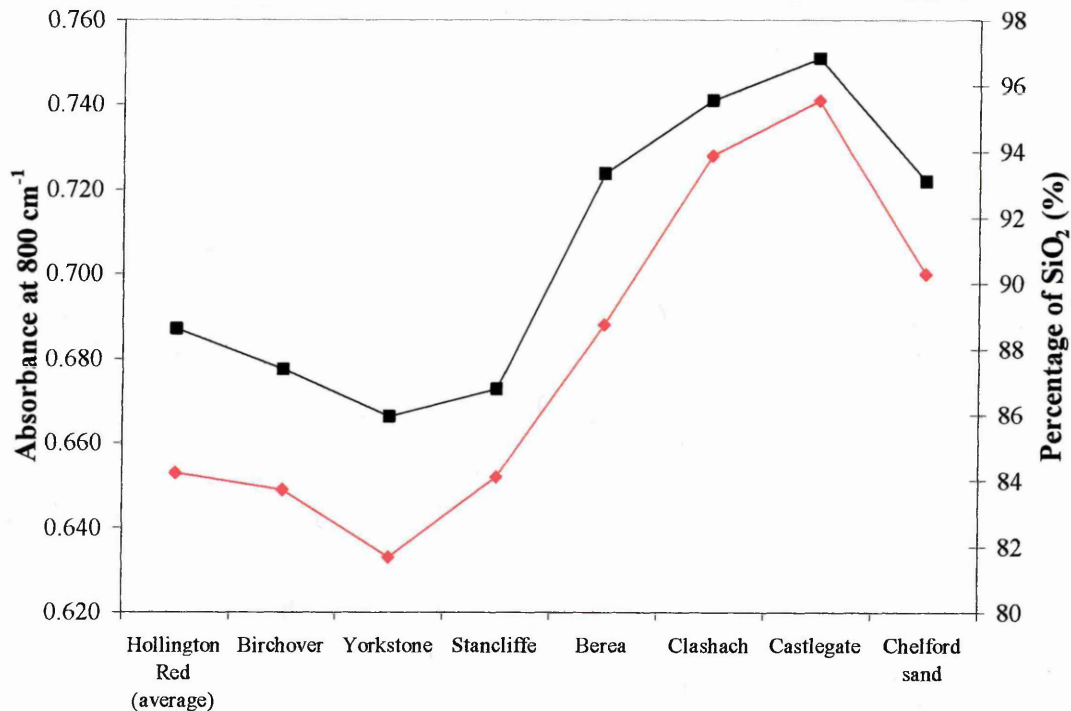


**Figure 7.54: Absorbance at 800 cm<sup>-1</sup> (associated with quartz) in the DRIFTS spectra (red) compared with the percentage of SiO<sub>2</sub> found by XRF (black) for the named sandstones and pure Chelford sand.**

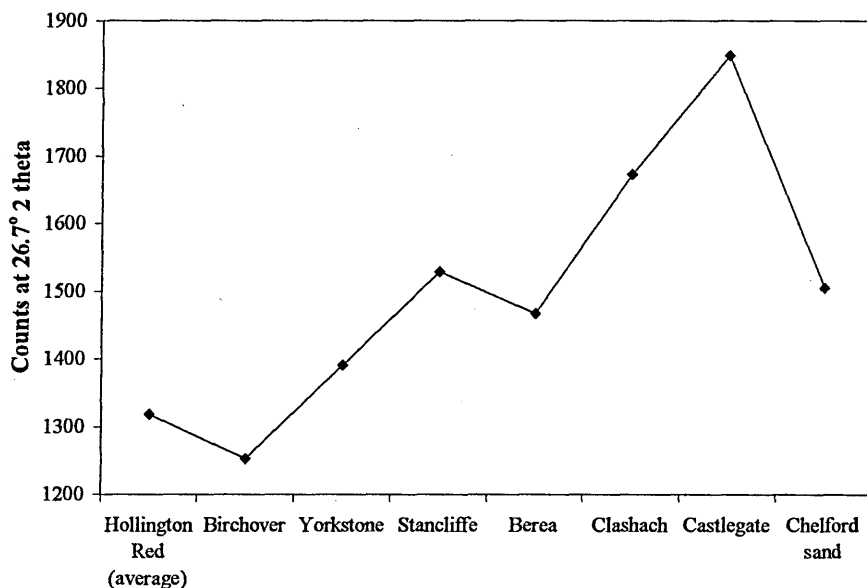


**Figure 7.55: Intensity of 26.7° 2θ quartz peak in XRD traces of the named sandstones and of pure Chelford sand.**

The intensity of the band at 800 cm<sup>-1</sup> in the DRIFTS spectra, the percentage of SiO<sub>2</sub> found by XRF, and also the percentage of quartz in the sandstones predicted by the PLS models, all followed a similar trend. A slightly different trend was observed for the 26.7° 2θ quartz peak intensity in XRD traces of the sandstones, although the highest intensities were still observed for Clashach and Castlegate.

Notably, the absorbance of the band at 800 cm<sup>-1</sup> in the DRIFTS spectrum of pure Chelford sand, the percentage of SiO<sub>2</sub> found in pure Chelford sand by XRF, and the intensity of the peak near 26.7° 2θ in the XRD trace of pure Chelford sand, were lower than that in DRIFTS spectra, XRF analysis, and XRD traces of Clashach and Castlegate sandstones. This may suggest that the pure quartz component of the training set contained less quartz than the two sandstones. This would obviously create a problem for quartz predictions by the PLS models, if the models used bands such as the Si-O-Si stretching band at 800 cm<sup>-1</sup> to calculate the predictions.

## 7.7.2 Impurities in the Training Set Components

### 7.7.2.1 Presence of Feldspars in Chelford Sand

During the qualitative DRIFTS study of the different sandstones and Chelford sand, in section 7.3, it was noticed, when studying the low wavenumber region, that Chelford sand exhibited bands not associated with quartz. The low wavenumber region of the DRIFTS spectra of quartz, Na-feldspar, and K-feldspar are shown in Figure 7.56 in order to determine the assignment of these bands.

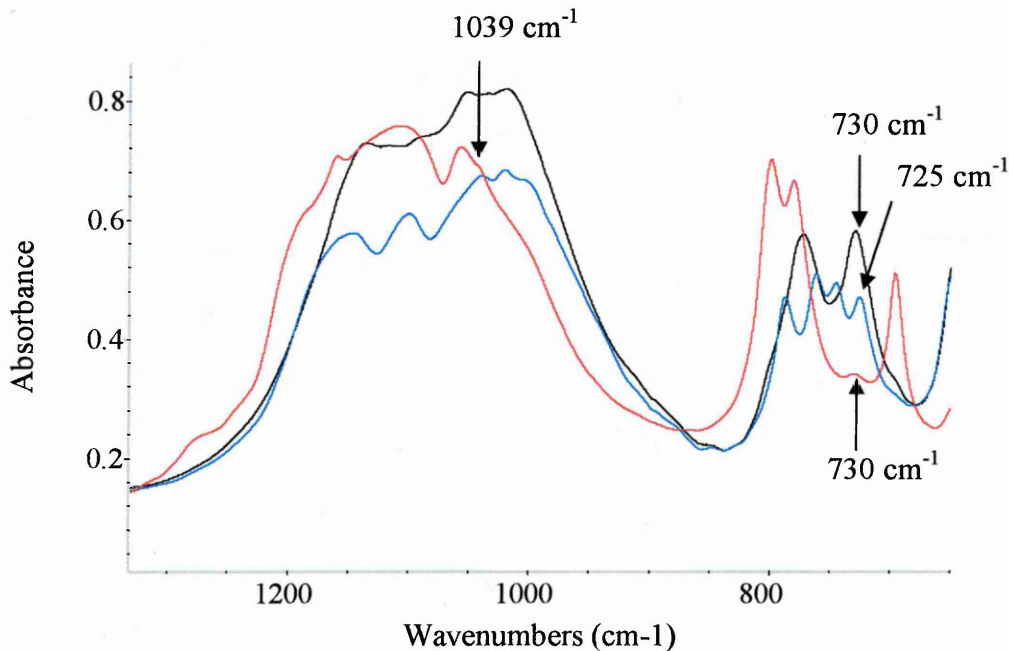


**Figure 7.56: The low wavenumber region of the DRIFTS spectra for Na-feldspar (blue), K-feldspar (black), and ball milled Chelford sand (red).**

The spectrum of Chelford sand exhibited a slight shoulder at  $1039\text{ cm}^{-1}$  and a low intensity band at  $730\text{ cm}^{-1}$  neither of which were associated with quartz. After examining the spectra of the other components, it was discovered that bands at  $1039\text{ cm}^{-1}$  and  $730\text{ cm}^{-1}$  were associated with Na-feldspar and K-feldspar, respectively. This suggested that Chelford sand may have contained both feldspars as impurities. The position of the band at  $730\text{ cm}^{-1}$  (associated with K-feldspar) instead of at  $725\text{ cm}^{-1}$  (associated with Na-feldspar) and also the presence of only a weak shoulder at  $1039\text{ cm}^{-1}$  (associated with Na-feldspar), suggested that there was more K-feldspar than Na-feldspar present in Chelford sand. The XRF analysis of Chelford sand and Castlegate are shown in Chart 7.1.

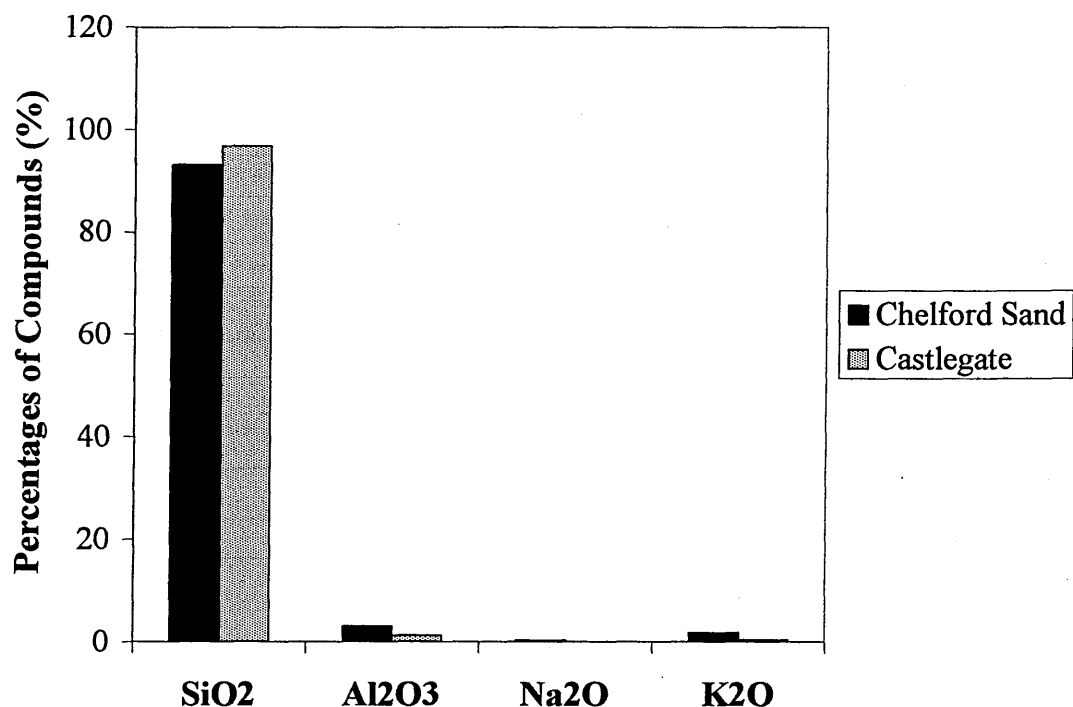


**Chart 7.1: Comparison of metal oxide content (wt%), from XRF, for Chelford sand and Castlegate.**

The presence of more K<sub>2</sub>O than Na<sub>2</sub>O in Chelford sand, may again suggest that Chelford sand contained more K-feldspar, than Na-Feldspar.

Interestingly, the presence of a more pronounced band at 730 cm<sup>-1</sup> in the DRIFTS spectrum of Chelford sand than in the spectrum of Castlegate (Figure 7.52), and the presence of a higher percentage of K<sub>2</sub>O found by XRF in Chelford sand than in Castlegate, suggested that Chelford sand contained more K-feldspar than Castlegate sandstone. This was also implied in section 7.7.1.2 since the bands at 781 and 800 cm<sup>-1</sup> in the spectrum of Chelford sand were of a more similar intensity than the same bands in the spectrum of Castlegate, suggesting the possibility that Chelford sand may have contained more feldspar than Castlegate.

The XRD traces of Na- and K-feldspar and of pure ball milled Chelford sand were also investigated for the presence of feldspars in the Chelford sand, and the region 26-29° 2θ is shown in Figure 7.57.

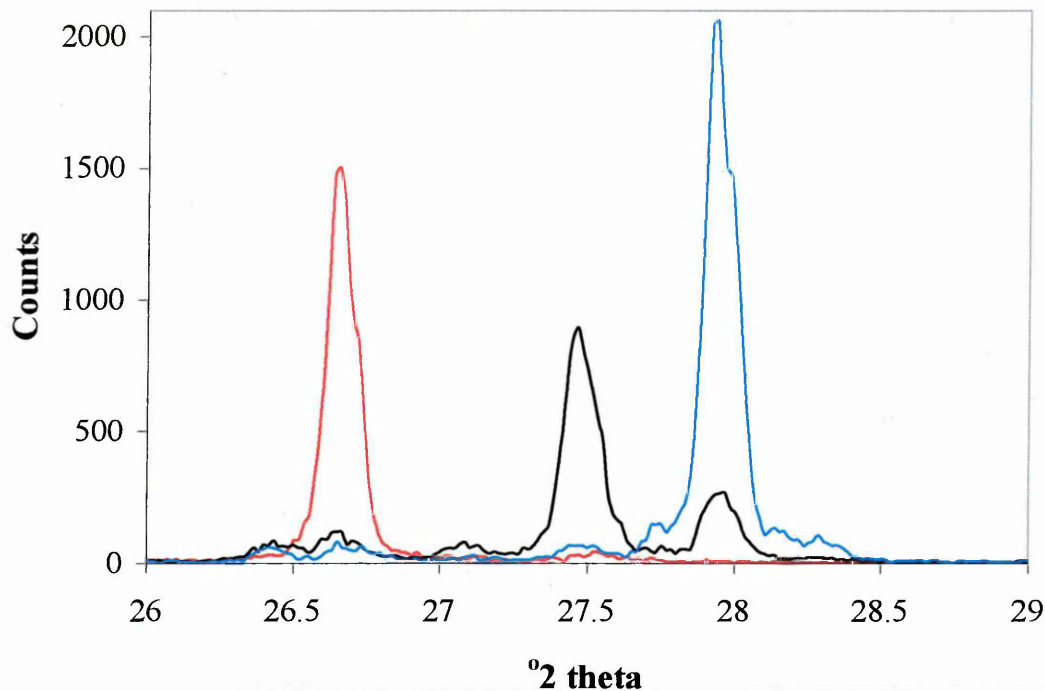


**Figure 7.57: XRD traces of Na-feldspar (blue), K-feldspar (black), and ball milled Chelford sand (red).**

The peak at  $26.7^\circ 2\theta$  is indicative of quartz, while the peaks at  $27.5^\circ 2\theta$  and  $27.9^\circ 2\theta$  are indicative of K- and Na-feldspar, respectively. The XRD trace of Chelford sand did not appear to show the presence of the feldspar peaks. However, investigation of this region of the XRD traces of the three training set components highlighted another possible reason for the over predictions of quartz in some sandstones. The traces of K- and Na-feldspar may both contain a weak peak at  $26.7^\circ 2\theta$ , suggesting that both feldspars may have contained some quartz.

#### 7.7.2.2 Presence of Quartz in the Feldspars

After a weak quartz peak, at  $26.7^\circ 2\theta$ , was found in the XRD traces of the feldspars, shown in Figure 7.57, indicating a quartz impurity, the feldspars were further investigated for impurities using XRF. The XRF analysis of K- and Na-feldspar is shown in Chart 7.2.

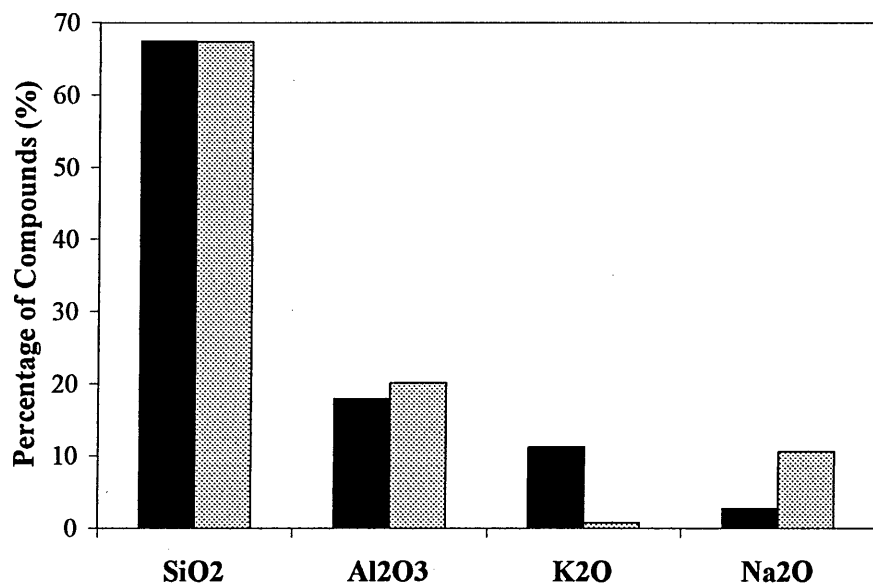


**Chart 7.2: Comparison of metal oxide content (wt%), from XRF, for K-feldspar (black bars) and Na-feldspar (shaded bars).**

The SiO<sub>2</sub> content of the two feldspars was similar, as was Al<sub>2</sub>O<sub>3</sub> content. However, as expected, there were larger differences in the K<sub>2</sub>O and Na<sub>2</sub>O contents. K-feldspar obviously contained a much greater percentage of K<sub>2</sub>O than was present in Na-feldspar and Na-feldspar contained a greater percentage of Na<sub>2</sub>O than was present in K-feldspar. It could be seen from the XRD traces of the feldspars shown in Figure 7.57 that K-feldspar showed a peak at 27.9° 2θ which was associated with Na-feldspar. The XRF analysis also showed that while both feldspars contained K<sub>2</sub>O and Na<sub>2</sub>O, the amount of Na<sub>2</sub>O that K-feldspar contained was significantly greater than the amount of K<sub>2</sub>O that Na-feldspar contained. Studies of the XRD traces and XRF analysis of the feldspars therefore indicated that both feldspars contained quartz, and K-feldspar also contained some Na-feldspar impurity. These impurities would again affect the predictions of quartz and feldspar calculated by the PLS models.

### 7.7.2.3 Presence of Quartz in the Clays

The impurities found in the Chelford sand, and feldspar components, led to further studies of the XRD traces of all the training set components, in order to determine if other “pure” components contained impurities. XRD traces of the clays,

montmorillonite, and illite, are shown in Figure 7.58, along with the trace of Chelford sand.

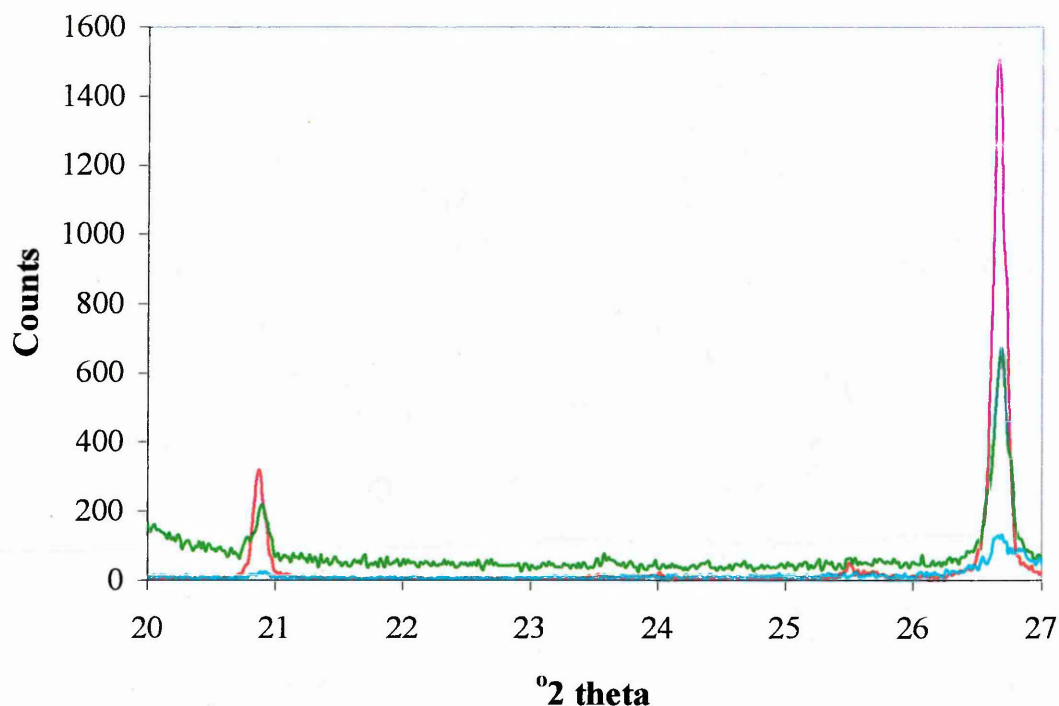


**Figure 7.58: XRD traces of montmorillonite (green), illite (light blue), and Chelford sand (red).**

The characteristic quartz peaks at  $20.9$  and  $26.7^\circ 2\theta$  could be seen clearly in the XRD trace of Chelford sand. The same peaks, however were present in the traces of montmorillonite and illite clays, and were especially pronounced in the trace of montmorillonite. This suggested that not only did Na- and K-feldspar contain quartz, but the montmorillonite and illite clays also contained quartz.

Vogt *et al.* [108] investigated the presence of impurities in some Clay Mineral Society clays, by measuring both the bulk material and the  $<2 \mu\text{m}$  fraction by XRD and by using XRF. Vogt *et al.* found that the main impurities in SWy-2 were quartz and kaolinite, at 5.2 wt% and 1.3 wt%, respectively.

The purity of some Clay Mineral Society clays were also studied by Chipera and Bish [109] using XRD. The clay minerals were studied as obtained directly from the Clay Mineral Repository and then the  $<2 \mu\text{m}$  fraction was removed and studied. The improvement in purity when the  $<2 \mu\text{m}$  fraction was removed was reported. The

mineral abundances were found using the RIR (reference intensity ratios) method, also used by Hillier [70], and described in section 5.4.3.2. KGa-2 obtained directly from the Clay Mineral Repository was found to contain 96% kaolinite, 3% anatase (TiO<sub>2</sub>) plus mica and /or illite. SWy-2 obtained directly from the Clay Mineral Repository was found to contain 75% smectite, 8% quartz, 16% feldspar, 1% gypsum plus mica and/or illite. No improvement in the purity was found when studying the <2 μm fraction of KGa-2, however, a large improvement was found in the purity of SWy-2 when the <2 μm fraction was studied. In the <2 μm fraction of SWy-2, 95% was smectite, 4% quartz, 1% feldspar plus gypsum and mica and/or illite. It should be noted that in the studies described in this thesis, the clay minerals obtained from the Clay Mineral Repository were used without removal of the <2 μm fraction. In future work, the <2 μm fractions of the Clay Mineral Repository clays should be used as components in the training set.

Graham *et al.* [75] quantified the quartz content of clays and found that the normal range for quartz content in the aluminosilicates was between 20 and 40 wt%, indicating that the quartz content of most clays was second in abundance in concentration only to the clay minerals themselves.

The presence of quartz in montmorillonite and illite, however, would have little effect on predictions by the PLS models since very little montmorillonite was present in the sandstones, and although more illite was present, illite contained very little quartz.

### 7.7.3 Summary

The over prediction of quartz in Clashach and Castlegate sandstones was not surprising after studying their DRIFTS spectra, their percentage of SiO<sub>2</sub> found by XRF, and XRD traces, in comparison to those of Chelford sand. The DRIFTS spectra and XRD traces of the two sandstones showed higher intensity quartz peaks than those in Chelford sand and they both also contained more SiO<sub>2</sub> than Chelford sand. One possible reason for this could be that the clay present in the training set standards was smeared on the surface of the quartz particles, masking the spectrum from the underlying quartz particle. The PLS model would then consider the diminished spectrum of quartz to be the true spectrum. In a sandstone where little or no clay was present, such as in Clashach and Castlegate, the silica particles would be exposed,

causing enhancement of the silica infrared absorbance bands. This could then lead to the model predicting percentages of quartz over 100%. A difference in shape of the quartz peak at  $26.7^\circ 2\theta$ , and presence of a shoulder in the XRD traces of sandstones also suggested differences in the sandstones associated with the quartz component. Differences in the quartz peak intensity and shape in DRIFTS spectra and XRD traces of the different sandstones and Chelford sand may mean that the predicted concentration of Chelford sand in the sandstones was not truly representative of the quantity of quartz they contained.

Another possible reason for the over prediction of quartz in the two sandstones is that the particle size distribution of all the sandstones may not have been the same. The effect of particle size on band intensity and resolution in DRIFTS spectra of samples is immense, as could be seen from the spectra of Chelford sand ground by hand and ball milled (Figure 6.1 in section 6.3.2). All the training set standards, and also all the sandstones, were ball milled for the same length of time in the hope that the particle size distribution in each would be the same and so the DRIFTS spectra would not be influenced by particle size. Differences in particle size may, however, have occurred between different sandstones after ball milling, due to the difference in hardness of the sandstone rocks. The harder sandstone rocks; Birchover, Yorkstone, and Stancliffe may have required longer grinding times in order to get the same particle size distribution as that obtained in the softer sandstones; Clashach and Castlegate, after a shorter time. The terms “harder” and “softer”, refer to the ease with which the rocks were cut, with harder rocks taking a longer time to cut through. The sandstones were all ball milled for the same length of time but the grains of the softer rock may have been released earlier than those of the harder rocks, causing them to be ground for longer. This may have caused the softer rocks; Clashach and Castlegate, to have spectra with higher intensity bands. Since the sandstones studied by Clegg [21] were ball milled for 20 minutes, rather than 5 minutes as in the studies of this thesis, any effect due to differences in particle size would be much reduced.

Differences in particle size may also, however, have occurred between different standards and different sandstones due to the difference in their composition. The particles of quartz were the largest and hardest particles in the sandstones and could have acted, along with the tungsten carbide pot and balls of the ball mill, as an

additional aid to grinding. In samples which contained a high concentration of quartz, the particles would be ground with more friction and therefore the particle size may have been smaller than in samples which contained a lower concentration of quartz, and a higher concentration of softer particles. The particle size of ball milled Clashach and Castlegate sandstones, which contained high quantities of quartz and low quantities of clays, may have been smaller than the other sandstones, which contained more clay. A  $\text{SiO}_2$  sample with smaller particle size is known to give DRIFTS spectra with higher intensity bands, and this could be another reason for the high intensity of quartz bands in the DRIFTS spectra of Clashach and Castlegate sandstones. Since pure Chelford sand also contained a high concentration of quartz, it should also have had a smaller particle size after milling, and therefore have had higher intensity quartz bands in its DRIFTS spectrum than those present in the DRIFTS spectra of the other sandstones. The intensity of quartz bands in the DRIFTS spectra of Clashach and Castlegate, however, were slightly higher than those in the spectrum of Chelford sand.

Bhaskar *et al.* [112] used infrared spectroscopy to determine the quartz content in dust samples from coal mines. It was found that infrared absorbance varied with particle size, with a maximum absorbance found when the particles were about 2  $\mu\text{m}$  in diameter, with decreasing absorbance found when the particle size deviated from 2  $\mu\text{m}$ . Bhaskar *et al.* reported that the particle size of quartz should be reduced to <4  $\mu\text{m}$  in order to correctly determine the content of quartz. Graham *et al.* [75] used infrared spectroscopy and the peak fitting technique, using the quartz band near 691  $\text{cm}^{-1}$  to quantify the quartz content of clays. It was reported that a particle size range of 1.5-14.5  $\mu\text{m}$  was required for the analysis of quartz.

It is evident from the results in section 7.7.2 that some of the training set components were not “pure” and they contained other components as impurities. The quartz component, Chelford sand, appeared to contain K-feldspar, and possibly Na-feldspar also. Both the feldspars, and also the clays; montmorillonite and illite, appeared to contain quartz. In addition, K-feldspar was found to contain some Na-feldspar impurity. These impurities in the training set components complicate the PLS model, since, during preparation of the model, known concentrations of the components in the calibration standards were included. However, the addition of impurities was not accounted for, so the composition of the calibration standards included would be

incorrect. A higher number of factors for some components may be required due to the complication of impurities and a larger maximum error found. The impurities would also affect the predictions of the independent standards and sandstone samples. It was expected that the impurities in Chelford sand would have the greatest effect on the PLS models since Chelford sand was the dominant component in all the standards and samples, with concentration ranges between 50 and 100 wt%.

## 7.8 Comparing Results with Literature

Comparisons were made throughout this chapter between different models developed to quantify minerals in quarried sandstones.

Schlumberger-Doll Research (SDR) used a least square fitting technique and FTIR transmission spectroscopy to quantify minerals in Hollington Red, Birchover, Yorkstone, Stancliffe and Berea sandstones. Wavelet transform calculations were used to remove noise from useful information and a large collection of standards, including feldspars with Ca, Na, and K end members, were used. The full composition of the standards and the procedure used, however, was unknown. For complicated artificial mineral mixtures, SDR stated that their technique was 1% accurate.

Dr. Stephen Hillier from the Macaulay Land Use Research Institute studied the same sandstones as SDR, and also Clashach and Castlegate sandstones, using detailed XRD analysis of crushed core samples. Both oriented clay fractions and whole rock random powders were studied. The minerals were quantified from whole rock data and the clay fraction was used to confirm and refine the identification of the clay minerals to provide complementary quantitative information. The maximum errors for the components were typically within  $\pm 3$  %.

Of the models compared in this chapter, the model most similar to the pragmatic PLS model was one developed by Clegg [21]. Clegg [21] used DRIFTS spectra of artificial mineral mixtures to develop a PLS model to quantify minerals in sandstone rocks. A seven component model was developed by Clegg, consisting of quartz, montmorillonite, kaolinite, illite, dolomite, feldspar, and chlorite. The PLS-Clegg model quantified quartz in independent synthetic mixtures with 3 wt% accuracy, and the other minerals within 1 wt% accuracy, while the absolute PLS model, described in this thesis, quantified all minerals with a maximum error of less than  $\pm 2.8$  wt%. The

accuracy of the pragmatic PLS model was reduced with all minerals having a maximum error of less than  $\pm 4.7$  wt% except for K-feldspar which had a maximum error of  $\pm 6.8$  wt%.

X-ray powder diffraction is the most commonly used technique for quantification of minerals in sandstones. Środoń *et al.* [78] used XRD to quantitatively determine the mineral content of both synthetic mineral mixtures and natural shale samples and the method used was described in section 3.4 of chapter 3. The mineral content of the samples was calculated using an equation that related wt% of mineral to the intensity of a reflection corresponding to that mineral, in the XRD pattern of a mixture. Środoń *et al.* reported the mineral component errors as the average errors i.e. an average of the differences between the actual and the predicted percentages. In this chapter, the errors for predictions of the components were generally reported as maximum errors, but for comparison, the average errors were calculated. The average errors for the prediction of different mineral components found by Środoń *et al.* using XRD were very similar to those found using the absolute PLS models described in this chapter. Środoń *et al.* found that all components had an average prediction error of less than  $\pm 1.8$  wt%, while the absolute PLS model predicted all components with an average error of less than  $\pm 1.1$  wt%. The average errors for predictions of components, using the pragmatic PLS model were slightly higher, with all components predicted within  $\pm 3.0$  wt%. The results for real shale rock samples indicated a variation in quartz content. Środoń *et al.* found that rocks with low quartz content were kaolinite rich or rich in 2:1 Fe clays, while rocks with high quartz content were rich in 2:1 Al clays.

Chakrabarty *et al.* [110] used XRD and a modified matrix algebra-based method to quantify minerals in synthetic mineral mixtures and in real rock samples. The matrix algebra method used least-squares or linear regression to quantify minerals but was thought to be unstable due to the possibility of predicting negative values or values greater than 100%. The modified matrix algebra-based method was designed to overcome these instabilities by incorporating initial guesses for the mineral quantities, found by studying the XRD pattern of the unknown sample. Errors for the predictions were expressed as percentage relative errors. The absolute errors were calculated for the prediction of components by Chakrabarty *et al.*, and the accuracy compared with that of the absolute and pragmatic PLS models in this chapter. The absolute error for

predicting quartz was greatest for the method used by Chakrabarty *et al.* at  $\pm 23.7\%$ , followed by the error for predicting smectite, at  $\pm 7.7\%$ . Predictions for the other components using the method, were all within  $\pm 1\%$  accuracy. The errors for predicting smectite, and especially quartz, using this method, were far greater than the errors for predicting these components using both the absolute and pragmatic PLS models. When predicting minerals in real rock samples, Chakrabarty *et al.* found that the predicted mineral fractions added to 1.00, indicating that all the minerals present in the rock had been accounted for. As was reported by Clegg [21], Chakrabarty *et al.* found that more accurate predictions were determined when the smectite and illite minerals were combined.

The Rietveld (1969) quantitative XRD method was used by Ward *et al.* [77] to quantitatively predict the mineral content in powdered samples. SIROQUANT is a software system which can quantify up to 25 minerals in a mixture from a powder XRD pattern using the Rietveld method. Normative analysis can also be used to obtain quantitative results by determining normative mineral percentages from a rock's chemical composition. The use of a multi-option computation method, called SEDNORM, allows more flexibility, with elemental allocations varied to suit the material under study. These methods were described in more detail in section 3.3.2 of chapter 3. Ward *et al.* [77] compared the results of predicting mineral components of sandstone rocks using point counting, SIROQUANT, and SEDNORM, and found relatively poor correlations. However, they suggested that SIROQUANT offered the most direct method for quantification. Using SIROQUANT, the absolute errors for predicting mineral components were all within  $\pm 4.8\%$ . The accuracy of the predictions was therefore very similar to that found using the pragmatic PLS model, where all components were predicted within  $\pm 4.7$  wt%, except K-feldspar which was predicted with  $\pm 6.8$  wt% accuracy.

## 7.9 Conclusion

The absolute PLS model was used to predict the concentrations of minerals in real sandstone rocks from the DRIFTS spectra of powdered samples. The mineralogy along the length of the sandstones; Hollington Red, Birchover, Yorkstone, Stancliffe, Berea, Clashach, and Castlegate, was investigated. The predictions calculated for different core slices suggested that there were no significant differences in mineralogy along the length of the cores. The mineral components in three different sets of sandstone powder samples; powder from cutting, ground slices, and ball milled slices, were quantified using the absolute PLS model. Differences in the predictions of components for the different sets of powders were thought to be caused by the release of minerals during cutting and also because the particle size of the sets of powders was different. During the cutting of the harder rocks, more quartz was released as powder, while in the softer rocks, more quartz remained in the rock during cutting. The opposite was true for the location of layer silicates after cutting, i.e. after cutting of the harder rocks, more remained in the rock, while in the softer rock very little of the layer silicates were generally found, but where they were present, more was released during cutting. The powders ground manually in a mortar and pestle gave the lowest predicted percentages of quartz and this was because the large particle size of quartz in these samples produced spectra with lower intensity, differently shaped, Si-O-Si stretching bands. Since the training set standards used in the PLS model were ball milled, it was thought that the ball milled slices of sandstones would give the most accurate predictions.

The predictions of components in the different sandstones, calculated by the absolute PLS model, were compared. The predictions were also compared with those calculated by models developed by others, including an XRD model by Dr. Stephen Hillier from the Macaulay Land Use Research Institute, a least square fitting technique with FTIR transmission spectroscopy by Schlumberger-Doll Research, and a PLS with DRIFTS model developed by Clegg. The predicted concentrations of calcite, dolomite, and hematite were too low to be able to compare the models, and mica was not investigated by Hillier. The predictions of the other components by the absolute PLS model, however, followed the same trend for the sandstones as the predictions by the XRD-Hillier model. However, the values of the predictions by the

different models were quite different for some components. Overall the absolute PLS model predicted the components in the sandstones; Birchover, Yorkstone, and Stancliffe very well, but over predicted the quartz content in sandstones; Berea, Clashach, and Castlegate.

In order to improve the accuracy of the predictions by the absolute PLS model, the number of factors was altered and the pragmatic PLS model was created. The XRD-Hillier model was thought to be the most accurate since it is a well established technique. The sandstone component concentrations predicted by the pragmatic PLS model were closer in value to those predicted by the XRD-Hillier model and were therefore considered to be more accurate. For components quantified by the XRD-Hillier model, the PLS-Clegg model, and the absolute and pragmatic PLS models, the pragmatic PLS model predicted the components with more accuracy (i.e. closer values to those by the XRD-Hillier model) than both the PLS-Clegg model and the absolute PLS model. The pragmatic PLS model contained more components than the PLS-Clegg model and, with the exception of the quartz component, produced predictions closer to those of the XRD-Hillier model. Predictions for the quartz component by the PLS-Clegg model were closer to those of the XRD-Hillier model than the predictions using the absolute and pragmatic PLS models due to the over prediction of quartz in Clashach and Castlegate sandstones by the PLS models derived in this thesis.

One possible reason for the over prediction of quartz could be that the clay present in the training set standards was smeared on the surface of the quartz particles, masking the spectrum from the underlying quartz particle. The PLS model would then consider the diminished spectrum of quartz to be the true spectrum. In a sandstone where little or no clay was present, such as in Clashach and Castlegate, the silica particles would be exposed, causing enhancement of the silica infrared absorbance bands. This could then lead to the model predicting percentages of quartz over 100%. Another reason may be that the sandstones contained quartz from different sources, i.e. they did not all contain Chelford sand. If this were the case then the predicted concentrations of Chelford sand in the sandstones would not be truly representative of the quantity of quartz they contained.

Difference in particle size between different sandstones after ball milling would also affect the DRIFTS spectra and therefore the predictions of components in the sandstones. After ball milling, sandstones may have had different particle sizes due to the difference in hardness of the sandstone rocks. Difference in particle size may also have occurred between different standards and different sandstones due to the differences in their composition. In samples which contained a high concentration of quartz, the quartz would act as an additional aid to grinding causing smaller particle sizes than in samples which contained a low concentration of quartz.

Inaccuracies in predicted percentages of some components may be due to impurities. The quartz component, Chelford sand, was found to contain some K-feldspar, and possibly some Na-feldspar also, as impurities. Both the feldspars, and also the clays; montmorillonite and illite, were found to contain quartz. In addition, K-feldspar was found to contain some Na-feldspar impurity. These impurities in the training set components complicate the PLS model, and would affect the predictions.

The errors found for predicting different mineral components in rocks using the absolute and pragmatic PLS models were comparable with those found by groups using XRD techniques. The absolute PLS model predicted all components within  $\pm 2.8$  wt%, while the pragmatic PLS model predicted all components, except K-feldspar, with  $\pm 4.7$  wt% accuracy. K-feldspar was predicted with  $\pm 6.8$  wt% accuracy. The errors found by Hillier for predicting different mineral components in rocks, using XRD, were typically within  $\pm 3\%$ . Ward *et al.* [77] used XRD and SIROQUANT and predicted all mineral components within  $\pm 4.8\%$ . Środoń *et al.* [78] also used XRD to predict mineral components in rock and found errors very similar to those found using the absolute PLS model. Środoń *et al.* found that all components had an average prediction error of less than 1.8 wt%, while the absolute PLS model predicted all components with an average error of less than 1.1 wt%.

## 8. Conclusions

### 8.1 Use of DRIFTS and PLS to quantify small amounts of swelling mineral, smectite, in synthetic mixtures.

Successful quantification of small amounts (0.1-30 wt%) of smectite in mixtures with kaolinite has been achieved using DRIFTS and PLS. Determining the concentration of small amounts of swelling mineral, smectite, in mixtures with non-swelling mineral, kaolinite, is important because small amounts of smectite can sequester all the treatment chemicals introduced to a reservoir rock if its presence remains undetected. Traditionally, clay minerals are most commonly studied using XRD as it has been found to be a powerful technique for mineral quantification [70]. However, DRIFTS was used in this study since it requires only a small amount of sample, is fast, and is relatively inexpensive compared with XRD.

Other groups [98, 73] have attempted to quantify the amount of smectite in mixtures with kaolinite, using peak fitting with infrared spectroscopy. Since the visual detection of smectite and kaolinite was required from the infrared spectra, overlapping of bands caused the technique to be only semi-quantitative. For example, Madejová *et al.* [73] found that kaolinite could be detected at concentrations as low as 0.5 wt%, while smectite could not be detected below 40 wt%.

The power of PLS for improving the detection limit of minerals in a mixture was demonstrated in this study. A set of synthetically prepared mixtures of smectite, kaolinite, and an additional mineral, calcite, were used to prepare a calibration, from which concentrations of the minerals in unknown samples could be determined.

The potential use of a chemical probe, DMF, to improve the accuracy of the smectite predictions was investigated. However, the presence of the strongest DMF peak in the spectra of both smectite and kaolinite after the mixture was exposed meant its presence did not improve the accuracy or precision of predictions.

The most precise and accurate predictions were found for the model which included spectra collected from samples where the KBr diluent had been ball milled, and the sample compacted into the cup with a compaction device, prior to spectral collection. This was thought to be due to the smaller particle size distribution and homogeneous compaction of the samples. The maximum error for predictions of kaolinite, smectite,

and calcite were  $\pm 2.2$  wt%,  $\pm 3.8$  wt%, and  $\pm 4.9$  wt%, respectively. In conclusion, it has been found that smectite could be detected at lower concentrations using PLS than could be detected by peak fitting infrared bands, with an error of  $\pm 3.8$  wt%.

## 8.2 Heterogeneity of Sandstone Rock Cores

The heterogeneity of sandstone rock cores was studied by visual inspection of XRD patterns of sandstone core slices and the powder produced during cutting, in order to gain knowledge on the length scale over which the rock mineralogy varies and also to help determine what a representative sample size was. Seven quarried sandstones were studied; Hollington Red, Birchover, Yorkstone, Stancliffe, Berea, Clashach, and Castlegate.

Visual inspection of the rock surfaces, the amount of powder collected during the cutting process, and studies by Methven and Hughes [102] on the chemical and physical properties of sandstones, indicated that Birchover, Yorkstone, and Stancliffe were harder rocks, with small pores ( $< 1-10 \mu\text{m}$ ) and a lower porosity (11-16%), while Berea was slightly softer. Hollington Red, Clashach, and Castlegate sandstones were softer still, i.e. they were the easiest to cut, contained a larger number of large pores (10-100  $\mu\text{m}$ ) and had a higher porosity (22-25%).

The peak intensity ratios between clay and quartz peaks in the XRD traces, indicated varying amounts of clay in each slice of sandstone. Less kaolinite, illite and muscovite was generally found in the softer sandstones, Clashach and Castlegate, than in the other sandstones, suggesting that these were “clean” sandstones. The intensity of the illite/muscovite peak in XRD traces of the powder from cutting and of the rock slices implied that in all the sandstones, more illite and muscovite was removed from the emerging rock surface in the cutting process than remained in the rock slices. Since mineralogical heterogeneity was found along the length of the different sandstone cores investigated, it was thought that ideally a representative sample would be one collected from a ball milled sample of a large portion of a core.

## 8.3 Sandstone Absolute PLS Model

While the XRD traces and DRIFTS spectra of sandstone rocks could be investigated visually to provide qualitative information with regards their mineral content, the

power of PLS for providing quantitative predictions of mineral concentrations within a sample has been proven when studying the three component system of kaolinite, smectite, and calcite.

The sandstone absolute PLS model was constructed with a synthetic mineral training set comprising eleven mineral components chosen to resemble the composition of a real sandstone rock. Studies using different wavenumber regions, and pre-processing in models, indicated that the most precise and accurate predictions were found when using the full (4000-655  $\text{cm}^{-1}$ ) region, no pathlength correction, but automatic baseline correction for the pre-processing. The model was further optimised by altering the number of factors.

For the absolute PLS model, the  $R^2$  values of the calibrations and predictions for all components, except for montmorillonite and hematite, were above 0.9. Hematite was the least precisely predicted component. However, this was expected since the DRIFTS spectrum had few distinctive features and no strong bands. Montmorillonite had the lowest  $R^2$  of calibration value, at 0.73. However, the  $R^2$  value of the predictions of montmorillonite was 0.91, so it was still precisely predicted.

The results for the absolute PLS model were comparable with those for the seven component PLS model developed by Clegg. The correlation coefficients of all the components in Clegg's PLS model were over 0.92, and the number of factors chosen ranged from 5 to 10. In the absolute PLS model, all the components had  $R^2$  values of calibrations over 0.89, except for montmorillonite, at 0.73, and the number of factors chosen ranged from 3 to 15. Although initially, this implied that the model developed by Clegg was more accurate, it tended to be the components, not included in Clegg's model, that required the high number of factors in the absolute PLS model, such as hematite and muscovite.

The maximum errors found for components in the absolute PLS model and in the PLS model developed by Clegg were of the same order. Clegg reported that the accuracy of quartz prediction in the independent synthetic mixtures was  $\pm 3$  wt%, and the other minerals  $\pm 1$  wt%, while the absolute PLS model quantified all minerals within  $\pm 2.8$  wt%. The error found for predicting components using the absolute PLS model was similar to that found by Hillier [70] for predicting samples containing clay and non-clay minerals using X-ray powder diffraction. The maximum errors reported by Hillier were typically  $\pm 3$  wt% for each component.

## 8.4 Quantification of Sandstone Rocks

The absolute PLS model was used to predict the concentrations of minerals in real sandstone rocks from the DRIFTS spectra of powdered samples. The mineralogy along the length of the sandstones; Hollington Red, Birchover, Yorkstone, Stancliffe, Berea, Clashach, and Castlegate, was investigated and the predictions suggested that there were no significant differences in mineralogy along the length of the individual cores.

The mineral components in three different sets of sandstone powder samples; powder from cutting, ground slices, and ball milled slices, were quantified. Differences in the predictions were considered to be caused by the release of minerals during cutting and also because the particle size of the sets of powders was different. Predictions for the harder rocks Birchover, Yorkstone, and Stancliffe, implied that more quartz was released as powder during the cutting process than remained in the rock slices, while the opposite trend was true for the softer rocks, Hollington Red, Berea, Clashach, and Castlegate. This was thought to be due to quartz grains possibly being cut through during the cutting of the harder rocks, while in the softer rocks the different quartz grains may have been separated during the cutting process.

The powders ground manually in a mortar and pestle gave the lowest predicted percentages of quartz due to the large particle size of quartz in these samples producing spectra with lower intensity, differently shaped, Si-O-Si stretching bands. Since the training set standards used in the PLS model were ball milled, it was thought that the ball milled slices of sandstones gave the most accurate predictions.

The predictions of components in the different sandstones, calculated by the absolute PLS model, could be compared with predictions calculated by models developed by others, including an XRD model by Dr. Stephen Hillier from the Macaulay Land Use Research Institute, a least square fitting technique with FTIR transmission spectroscopy by Schlumberger-Doll Research, and a PLS with DRIFTS model developed by Clegg. The predictions of most components by the absolute PLS model followed the same trend for the sandstones as the predictions by the XRD-Hillier model. However, some component percentages were over predicted by the absolute PLS model and some under predicted. With the errors for the models considered, the

absolute PLS model generally predicted the components of the harder sandstones, Birchover, Yorkstone, and Stancliffe very well, with respect to predictions by the XRD-Hillier model, however, it appeared to over predict the amount of quartz in Berea, Clashach, and Castlegate.

In order to improve the accuracy of the predictions by the absolute PLS model, the number of factors was optimised and the pragmatic PLS model was created. The XRD-Hillier model was thought to be the most accurate because it is a well established technique and, since the sandstone component concentrations predicted by the pragmatic PLS model were closer in value to those predicted by the XRD-Hillier model, they were considered to be more accurate. The pragmatic PLS model contained more components than the PLS-Clegg model and, with the exception of the quartz component, produced predictions closer to those of the XRD-Hillier model. Predictions for quartz in Clashach and Castlegate, using the pragmatic PLS model, remained over predicted. Therefore, while the PLS models derived in this thesis successfully predicted components in harder sandstones which contained more clay and feldspars, they were not as capable at quantifying minerals in “cleaner” sandstones, which contained high concentrations of quartz. This may be because the PLS models derived in this thesis did not include standards with high concentrations of quartz and very low concentrations of clay. The models may therefore be optimised for predicting components in sandstones containing clay, but not be optimised for predicting “clean” sandstones.

Other possible reasons for the over prediction of quartz in clean sandstones are that since they contained little clay, more silica particles could have been exposed, causing possible enhancement of the silica infrared absorbance bands and also they may have contained quartz from different sources, causing poor predictions for Chelford sand.

Inaccuracies in predicted percentages of some components may have been due to impurities. The quartz component, Chelford sand, was found to contain some K-feldspar, and possibly some Na-feldspar as impurities. Both the feldspars, and also the clays; montmorillonite and illite, were found to contain quartz. In addition, K-feldspar was found to contain some Na-feldspar impurity. These impurities in the training set components would complicate the PLS model, and would affect the predictions.

The maximum errors found for predicting different mineral components in sandstones, using the absolute and pragmatic PLS models, were similar to those found by groups using XRD techniques. The absolute PLS model predicted all components within  $\pm 2.8$  wt%, while the pragmatic PLS model predicted all components, except K-feldspar, with  $\pm 4.7$  wt% accuracy. K-feldspar was predicted with  $\pm 6.8$  wt% accuracy.

## 8.5 Considerations for Future Work

### 8.5.1 Improving the Training Set and PLS Models

For the “less clean” sandstones, which contained more clay and feldspar, it may be possible to extend the training set further by including more minor minerals. Some investigators found small amounts of the Ca-feldspar, anorthite, small amounts of other carbonates, such as magnesite and siderite, and also small amounts of sulphate, in the sandstones. The possible addition of alumina ( $\text{Al}(\text{OH})_3$ ) into the training set was investigated during the work in this thesis. However, it was found to contain a high amount of aluminium carbonate impurity, so was not included. If it were possible to remove the impurity from alumina, or obtain a more pure sample, and add this along with the minor minerals mentioned into the training set, then quantification of minerals in the “less clean” sandstones, may be more complete.

Some of the clay minerals included in the training set were found to contain a quartz impurity. The impurities present in some clays obtained from the Clay Mineral Society have been studied by different workers [108, 109]. Generally, it was found that using the  $< 2$   $\mu\text{m}$  fraction of the clays produced more pure samples. In future preparation of a training set, the standards should contain the  $< 2$   $\mu\text{m}$  fraction of the clays.

The DRIFTS spectrum of hematite contained few distinctive features and no strong bands, which may be the reason it was the least precisely predicted component. The addition of hematite in the training set standards may have worsened the predictive ability of the model since PLS could not assign any particular features of the DRIFTS

spectrum of an unknown, to hematite. The predictive ability of the sandstone PLS models may, therefore, improve if a training set was prepared without hematite.

There was some variation in the DRIFTS spectra of training set standards and sandstones at around  $3430\text{ cm}^{-1}$ . This broad band was due to the H-O-H vibrations of water and in future studies, the variation in intensity of this band may be reduced if all samples were dried prior to spectral collection.

The tables which showed how the predictions for components varied as the number of factors was increased for each sandstone were vital for determining the correct number of factors to choose for each component. In future PLS models, these tables should be studied earlier, for each different model prepared, so that a more thorough investigation of the effect of different pre-processing techniques and wavenumber regions on predictions is carried out.

The PLS models derived in this thesis successfully predicted components in sandstones which contained higher concentrations of clays and feldspars, and were less successful at predicting quartz concentrations in “cleaner” sandstones which contained high concentrations of quartz. This may be because the PLS models derived in this thesis did not include standards with high concentrations of quartz and very low concentrations of clay. The highest percentage of quartz in the standards was 90 wt%. However, the actual percentage of quartz in clean sandstones may be greater than this. Also, all of the standards which contained higher percentages of quartz also contained clay. The PLS models may, therefore, have been optimised for predicting components in sandstones which contained clay, but were not optimised for predicting “clean” sandstones.

It may therefore be advantageous to extend the training set to include standards containing high concentrations of quartz and no clay. Accurate quantification of minerals in sandstones, with a wider range of compositions, may then be possible.

The Chelford sand quartz component used in the PLS models derived in this thesis, was found to contain some impurities, which may have caused some inaccuracies in the predictions. If it were possible to clean Chelford sand with acid or alkali

treatment, without damaging the structure, the resulting “purer” quartz component may cause an improvement in the accuracy of predictions.

Chelford sand may also, however, not be the optimum quartz component for the sandstones studied. The training set could also be altered by using a different quartz component. Since Clashach has been found to be a clean sandstone, it could be used as the quartz component in a model used to quantify minerals in other clean sandstones.

It is thought that one possible reason for the over prediction of quartz could be that the clay present in the training set standards was smeared on the surface of the quartz particles, masking the spectrum from the underlying quartz particle. The PLS model would then consider the diminished spectrum of quartz to be the true spectrum. In a sandstone where little or no clay was present, such as in Clashach and Castlegate, the silica particles would be exposed, causing enhancement of the silica infrared absorbance bands. This may then lead to the model predicting percentages of quartz over 100%. Investigation into the smearing of clay on the surface of silica particles could be carried out using scanning electron microscopy (SEM).

Difference in particle size between different sandstones after ball milling was also thought to affect the DRIFTS spectra and therefore the predictions of components in the sandstones. After ball milling, sandstones may have had different particle sizes due to the difference in hardness of the sandstone rocks. Differences in particle size may also have occurred between different standards and different sandstones due to the difference in their composition. In samples which contained a high concentration of quartz, the quartz would act as an additional aid to grinding causing smaller particle sizes than in samples which contained a low concentration of quartz. Future studies could include investigating the optimum ball milling time in order to ensure a small and reproducible particle size distribution for every sample. The actual particle sizes of the different standards and sandstones should also be found using SEM or by suspending the samples in water and using the gravitational settling method.

### **8.5.2 Other Techniques**

The use of attenuated total reflectance (ATR) spectrometry using the Golden Gate diamond ATR accessory (manufactured by Thermo Electron Corporation Ltd.), for spectral collection of the training set standards and sandstone powders could be investigated. The Golden Gate accessory can exert a measured amount of pressure on a powdered sample to ensure the crystal surface is covered, and the high strength of the diamond can allow pressures of up to 250 pounds to be applied. The relative band intensities of ATR-IR spectra may be different to those in DRIFTS spectra. However, preparing a PLS model with ATR-IR spectra would be possible. A very small amount of sample would be required to cover the ATR crystal surface, and very little sample preparation required, since the powders could be studied neat, without mixing with KBr diluent. This would make ATR-IR spectra collection faster than using DRIFTS. Problems may arise with using ATR, due to the requirement of close sample contact with the crystal. It would be difficult to ensure that exactly the same amount of sample was on the crystal for each measurement, and that exactly the same load of pressure was applied. The pressure applied may also cause a preferred orientation of the clay minerals onto the crystal surface, but not cause the same effect on other minerals, resulting in a possible enhancement of the clay absorbance bands in a spectrum of a mixture. Since the diamond crystal is so small also, it may not be possible to ensure that a representative sample would be measured.

### **8.5.3 Quantification of Carbonate Rocks**

Better understanding of carbonate reservoirs is becoming more important since these reservoirs hold vast oil reserves and hydrocarbon production from carbonate reservoirs is expected to increase through the next century [5]. The complexity and heterogeneity of carbonate rocks would make mineral quantification difficult and determining a representative sample size would be vital for bulk quantitative analysis. The carbonate training set would have to include very high concentrations of calcite and dolomite, and very low concentrations of quartz, feldspars, clays and other minerals such as pyrite ( $\text{FeS}_2$ ). On the smaller scale, the use of RAMAN or the IR microscope to collect spectra from the carbonate rock surface at different positions may make it possible to semi-quantitatively investigate the location of the minerals present with regards to features such as large pores.

## 9. Conferences Attended

Infrared and Raman Discussion Group (IRDG) Christmas Meeting.

Location: King's College, London. Date: 18<sup>th</sup> December 2002.

Infrared and Raman Discussion Group (IRDG) University Research Meeting.

Location: UMIST, Manchester. Date: 15<sup>th</sup> October 2003.

Infrared and Raman Discussion Group (IRDG) Christmas Meeting.

Location: King's College, London. Date: 15<sup>th</sup> December 2003.

Materials Research Day

Location: Sheffield Hallam University. Date: 10<sup>th</sup> September 2004

Current Knowledge on the Layer Charge of Clay Minerals

Location: Smolenice castle, Slovakia. Date: 18<sup>th</sup>-19<sup>th</sup> September 2004

Presented poster: **'Influence of Layer Charge on the Desorption of Dimethylformamide from Smectite'**.

2<sup>nd</sup> Mid-European Clay Conference

Location: Miskolc, Hungary. Date: 20<sup>th</sup>-24<sup>th</sup> September 2004

Presented poster: **'Spectral Analysis using Statistical Methods - Quantification of small amounts of swelling mineral, smectite, in synthetic mixtures with kaolinite using diffuse reflectance infrared spectroscopy (DRIFTS)'**.

## 10. References

- [1] M. E. Tucker, *Sedimentary Petrology An Introduction*, Blackwell Scientific Publications (London), Geoscience Texts, Ed. A. Hallam, Vol. 3 (1981).
- [2] R. C. Selley, *An Introduction to Sedimentology*, Academic Press Inc. (London) (1976).
- [3] M. D. Wilson, E. D. Pittman, *Journal of Sedimentary Petrology*, 1977, **47**, 3-31.
- [4] J. W. Neasham, *Society of Petroleum Engineers 6858*, 1977, 1-7.
- [5] D. Jardine, J. W. Wilshart, 'Carbonate Reservoir Description', International Petroleum Exhibition and Technical Symposium, Society of Petroleum Engineers (1982).
- [6] N. R. Morrow and J. Buckley, web site abstract, 'Wettability and Oil Recovery by Imbibition and viscous displacement from fractured and heterogeneous carbonates', 2002, <http://baervan.nmt.edu/Petrophysics/co3-sow.doc>, date of access: 10/10/2005.
- [7] M. Akbar, 'A Snapshot of Carbonate Reservoir Evaluation', *Oilfield Review* (Winter 2000/2001), 20-41.
- [8] M. E. Tucker, V. P. Wright, *Carbonate Sedimentology*, Blackwell Scientific Publications (1990).
- [9] H. Elshahawi, T. Kimentos, 'Enhanced Productivity in a Heavy Oil Reefal Reservoir as a Result of Improved Reservoir Characterisation', Society of Petroleum Engineers (2000).
- [10] J. T. Greensmith, *Petrology of the Sedimentary Rocks*, 6<sup>th</sup> Edition, Vol. 2, George Allen and Unwin (1978).
- [11] F. David, L. Walker, M. R. Lee, I. Parsons, *Mineralogical Magazine*, 1995, **59**, 505-534.
- [12] web site – COREX, 'Amott Wettability', <http://www.corex.co.uk/97-019.htm>, date of access: 10/10/2005.
- [13] web site - 'Basic Properties and Data Management', [http://www.pttc.org/pwm/pw\\_s1.htm](http://www.pttc.org/pwm/pw_s1.htm), date of access: 10/10/2005.
- [14] C. Legens, T. Palermo, H. Toulhoat, A. Fafet, P. Koutsoukos, *Journal of Petroleum Science and Engineering*, 1998, **20**, 277-282.
- [15] G. C. Frye, M. M. Thomas, *Chemical Geology*, 1993, **109**, 215-226.

- [16] J. O. Buckman, 'Wettability Studies of Petroleum Reservoir Rocks', ESEM application note for FEI COMPANY, web site:  
<http://www.pet.hw.ac.uk/cesem/pdfbin/feinote.pdf>, date of access: 10/10/2005.
- [17] S. W. Bailey, Structures of Layer Silicates, in: *Chemistry of Clays and Clay Minerals*, Mineralogical Society Monograph No. 6, Edited by A. C. D. Newman (1987).
- [18] J. M. Adams, 'The Swelling of Clay', *Education in Chemistry*, **12**, (1975).
- [19] D. Moore and R. Reynolds Jr., *X-ray Diffraction and the Identification and Analysis of Clay Minerals*, 2<sup>nd</sup> Edition, Oxford University Press (1997).
- [20] J. Madejová, *Vibrational Spectroscopy*, 2002, **944**, 1-10.
- [21] F. Clegg, PhD Thesis, Sheffield Hallam University, 1998, 'Thermo-analytical and Spectroscopic Characterisation of Pore lining Minerals in Reservoir Rocks'.
- [22] G. J. Churchman, J. S. Whitton, G. G. C. Claridge, B. K. G. Theng, *Clays and Clay Minerals*, 1984, **32**, 241-248.
- [23] R. L. Ledoux, J. L. White, *Journal of Colloid and Interface Science*, 1966, **21**, 127-152.
- [24] R. Frost, J. Kristof, E. Horvath, J. T. Kloprogge, *Spectrochimica Acta Part A*, 2000, **56**, 1191-1204.
- [25] CMS Workshop Lectures Vol. 8, *Organic Pollutants in the environment*; Sawhney, B. L., Ed.; The Clay Minerals Society: Boulder, CO, 1996.
- [26] web site – <http://mineral.galleries.com/minerals/>, date of access: 03/02/2006.
- [27] T. A. Shigorova, N. V. Kotov, Ye. N. Kotel'nikova, B. M. Shmakin, V. A. Frank-Kamenetskiy, *Geochemistry International*, 1981, **5**, 76-82.
- [28] C.-P. Sherman Hsu, Infrared spectroscopy, in: *Handbook of Instrumental Techniques for Analytical Chemistry*, Edited by F. Settle, Pearson Education Inc., Upper Saddle River, New Jersey, (2000), 247-283.
- [29] J. M. Hollas, *Modern Spectroscopy*, 2<sup>nd</sup> Edition, John Wiley and Sons Ltd, 1995.
- [30] web site - Introduction to Fourier Transform Infrared Spectroscopy, [http://mmrc.caltech.edu/mmrc\\_html/FTIR/FTIRintro.pdf](http://mmrc.caltech.edu/mmrc_html/FTIR/FTIRintro.pdf), Thermo Nicolet, date of access: 29/01/2006.
- [31] D. E. Leyden, R. S. S. Murthy, 'Diffuse reflectance Fourier transform IR spectroscopy', *Trends in analytical chemistry*, 1988, **7**(5), 164-169.
- [32] R. W. Parker, R. L. Frost, *Clays and Clay Minerals*, 1996, **44**, 32-40.

- [33] M. Fuller, 'Diffuse Reflectance Infrared Analysis: A Brief Review of Theory and Applications', Nicolet FT-IR technical note.
- [34] B. Azambre, O. Heintz, M. Schneider, A. Krzton, J. V. Weber, *Talanta*, 1999, **50**, 359-365.
- [35] M. L. E. TeVrucht, P. R. Griffiths, *Applied Spectroscopy*, 1989, **43**, 1293-1294.
- [36] Z. Krivácsy, J. Hlavay, *Talanta*, 1994, **41**, 1143-1149.
- [37] T. Hughes, C. Methven, T. Jones, S. Pelham, *Advanced Cement Based Materials*, 1995, **2**, 91-104.
- [38] Z. Krivácsy, J. Hlavay, *Journal of Molecular Structure*, 1995, **349**, 289-292.
- [39] M. Fuller, P. Griffiths, 'Infrared analysis by diffuse reflectance spectrometry', American Laboratory, 1978, 69-80.
- [40] M. Fuller, P. Griffiths, *Analytical Chemistry*, 1978, **50**, 1906-1910.
- [41] Z. Xu, B. C. Cornilsen, D. C. Popko, W. D. Pennington, J. R. Wood, J. Hwang, *The Internet Journal of Vibrational Spectroscopy*, Vol 5, Ed 1, 2001.
- [42] R. L. Frost, É. Makó, J. Kristóf, E. Horváth, J. Theo Kloprogge, *Langmuir*, 2001, **17**, 4731-4738.
- [43] S. Yariv, I. Lapidés, *Journal of Materials Synthesis and Processing*, 2000, **8**, 223-233.
- [44] E. F. Aglietti, *Applied Clay Science*, 1994, **9**, 139-147.
- [45] P. J Sánchez-soto, A. Justo, J. L. Pérez-rodriguez, *Journal of Materials Science*, 1994, **29**, 1276-1283.
- [46] A. La Iglesia, A. J. Aznar, *Journal of Materials Science*, 1996, **31**, 4671-4677.
- [47] S. A. Yeboah, S. Wang, P. R. Griffiths, *Applied Spectroscopy*, 1984, **38**, 259-264.
- [48] M. Hřebičík, G. Budínová, T. Godarská, D. Vláčil, S. B. Vogenseh, K. Volka, *Journal of Molecular Structure*, 1997, **410-411**, 527-530.
- [49] R. A. Velapoldi, J. E. Tvedt, 'Sample rotation in diffuse reflectance Fourier transform infrared spectroscopy', *Review of Scientific Instruments*, 1987, **58**, 1126-1128.
- [50] P. Kubelka, F. Munk, *Z. Tech., Phys.*, 1931, **12**, 593.
- [51] P. Kubelka, *J. Opt. Soc. Am.*, 1948, **38**, 448.
- [52] Griffiths, De Hasser, *Fourier Transform Infrared Spectroscopy*, John Wiley and Sons (New York), 1986, 332-333.

- [53] D. Bish, C. Duffy, *CMS Workshop Lectures Vol 3, Thermal Analysis in Clay Science - Thermogravimetric Analysis of Minerals*, The Clay Minerals Society; Boulder: CO, 1990.
- [54] L. J. Janik, J. O. Skjemstand, M. D. Raven, *Australian Journal of Soil Research*, 1995, **33**, 621-36.
- [55] Grams32-PLS-PLUS IQ chemometric manuals, Galactic Industries Corporation, 395 Main Street, Salem, NHO 3079, USA, (1991).
- [56] P. Geladi, B. R. Kowalski, *Analytica Chimica Acta*, 1986, **185**, 1-17.
- [57] J. Forsyth, PhD thesis, Sheffield Hallam University, 2001, 'Characterisation of Minerals using Evolved Gas Analysis and Infrared Spectroscopy'.
- [58] C. T. Johnston, D. A. Stone, *Clays and Clay Minerals*, 1990, **38**, 121-128.
- [59] R. Ledoux, J. White, '*Infrared Studies of the Hydroxyl groups in Intercalated Kaolinite Complexes*', Thirteenth national Conference on Clays and Clay Minerals, 1976.
- [60] J. Kristóf, J. Mink, E. Horváth, M. Gábor, *Vibrational Spectroscopy*, 1993, **5**, 61-67.
- [61] J. Madejová, I. Kraus, P. Komadel, *Geologica Carpathica – Series Clays*, 1995, **4**, 23-32.
- [62] W. B. White, The carbonate minerals, in: *The infrared Spectra of Minerals*, Mineralogical Society Monograph 4, Edited by V. C. Farmer (1974), 227-283.
- [63] C. Sheldon Thompson, M. E. Wadsworth, *American Mineralogist*, 1957, **42**(5), 334-341.
- [64] A. Matteson, M. M. Herron, Schlumberger-Doll Research Note, ISD-004 91 52, 1991.
- [65] C. Breen, F. Clegg, T. L. Hughes, J. Yarwood, *Journal of Physical Chemistry*, B. 2001, **105**, 4872-4878.
- [66] C. Breen, F. Clegg, T. L. Hughes, J. Yarwood, *Langmuir*, 2000, **16**, 6648-6656.
- [67] J. R. Sohn, S. I. Lee, *Langmuir*, 2000, **16**, 5024-5028.
- [68] A. Bloodworth, A. Hurst, D. Morgan, *Detection and estimation of low levels of kaolinite by evolved water vapour analysis, Proceedings of the 9<sup>th</sup> International Clay Conference*, Strasbourg, 1989, V.C Farmer and Y. Tardy (Eds) Sci. Geol, Mem., 1990, **89**, 143-148.
- [69] G. W. Brindley, G. Brown, '*Crystal Structures of Clay Minerals and their X-ray Identification*', Mineralogical Society Monograph No. 5, 1980.

- [70] S. Hillier, *International Association of Sedimentologists Special Publication*, 2003, **34**, 213-251.
- [71] J. Kristóf, R. L. Frost, W. N. Martens, E. Horváth, *Langmuir*, 2002, **18**, 1244-1249.
- [72] C. T. Johnston, M. F. de Oiveira, B. J. Teppen, G. Sheng, S. A. Boyd, *Environmental Science and Technology*, 2001, **35**, 4767-4772.
- [73] J. Madejová, J. Keckes, H. Palkova, P. Komadel, *Clay Minerals*, 2002, **37**, 377-388.
- [74] S. de la Fuente, J. Cuadros, J. Linares, *Clays and Clay Minerals*, 2000, **48**(2), 299-303.
- [75] J. A. Graham, J. M. Walker, *Applied Spectroscopy*, 1983, **37**(4), 342-347.
- [76] B. M. Moudgil, S. Mathur, S. Behl, *Colloids and Surfaces A: Physicochemical and Engineering Aspects*, 1994, **92**, 183-188.
- [77] C. Ward, J. Taylor, D. Cohen, *Journal of Sedimentary Research*, 1999, **69**, 1050-1062.
- [78] J. Środoń, V. A. Drits, D. K. McCarty, J. C. C. Hsieh, D. D. Eberl, *Clays and Clay Minerals*, 2001, **49**, 514-528.
- [79] M. Kahle, M. Kleber, R. Jahn, *Geoderma*, 2002, **109**, 191-205.
- [80] V. R. Ouhadi, R. N. Yong, *Applied Clay Science*, 2003, **23**, 141-148.
- [81] S. Hillier, *Clay Minerals*, 1999, **34**, 127-135.
- [82] Editors- D. Bish, J. Post, *'Modern Powder Diffraction' Reviews in Mineralogy*, Mineralogical Society of America, BookCrafters Inc., Chelsea, Michigan, Vol. 20 (1989).
- [83] C. Ruan, C. Ward, *Applied Clay Science*, 2002, **21**, 227-240.
- [84] X. Jianhong, T. R. Astin, and P. Mao, *Science in China (Series D)*, 2001, **44**, 307-317.
- [85] D. J. Morgan, *Journal of Thermal Analysis*, 1977, **12**, 245-263.
- [86] J. Środoń, *Mineralogical Magazine*, 2002, **66**(5), 677-687.
- [87] D. M. Thornley and T. J. Primmer, *Clay Minerals*, 1995, **30**, 27-38
- [88] A. K. Özer, M. Gülaboğlu, S. Bayrakçeken, *Industrial and Engineering Chemistry Research*, 2000, **39**, 679-683.
- [89] R. C. Reynolds, Jr, *NEWMOD, a computer program for the calculation of one-dimensional diffraction patterns of mixed-layered clays*, Hannover, NH (1985).

- [90] R. C. Reynolds, Jr, Principles and techniques of quantitative analysis of clay minerals by X-ray powder diffraction, in: *Quantitative Mineral Analysis of Clays*, Clay Mineral Society Workshop Lectures Vol. 1, Edited by D. R. Pevear and F. A. Mumpton, Clay Minerals Society, Evergreen, CO, (1989), pp4-36.
- [91] A. Mandile, A. Hutton, *International Journal of Coal Geology*, 1995, **28**, 51-69.
- [92] Morad, AlDahan, *Clay Minerals*, 1987, **22**, 237-243.
- [93] A. Matteson, and M. M. Herron, Mineralogy from FTIR: Results for Two Carbonate Case Studies, Schlumberger Research Note, ISD-006 90 45, 1990.
- [94] J. Jiang, R. J. Berry, H. W. Siesler, Y. Ozaki, *Analytical Chemistry*, 2002, **74**, 3555-3565.
- [95] H. J. Luinge, J. H. van der Maas, T. Visser, *Chemometrics and Intelligent Laboratory Systems*, 1995, **28**, 129-138.
- [96] P. Fletcher, P. V. Coveney, T. L. Hughes, C. M. Methven, 'Predicting the quality and performance of oilfield cements using artificial neural networks and FTIR spectroscopy', Schlumberger Cambridge Research - External Paper, 1995.
- [97] H. Yang, P. R. Griffiths, J. D. Tate, *Analytica Chimica Acta*, 2003, **489**, 125-136.
- [98] T. Visser, H. J. Luinge, J. H. van der Maas, *Analytica Chimica Acta*, 1994, **296**, 141-154.
- [99] K. Pearson, *On lines and Planes of closest fit to systems of points in space*. Phil Mag, 1901, **2**, 559-572 in "Introduction to WIN-DAS", K. Kelmsley, Wiley, 1998.
- [100] E. Joussein, S. Petit, A. Decarreau, *Earth and Planetary Sciences*, 2001, **332**, 83-89.
- [101] J. J. Berzas, J. Rodríguez Flores, M. J. Villaseñor Llerena, N. Rodríguez Fariñas, *Analytica Chimica Acta*, 1999, **391**, 353-364.
- [102] C. M. Methven, T. L. Hughes, 'Chemical and Physical Properties of Sandstones used in Core Flood Experiments for Conformance Control', Schlumberger Cambridge Research departmental note, 1995.
- [103] E. Leary, 'The Building Sandstones of the British Isles', Building Research Establishment Report, 1992.
- [104] M. E. Crocker, E. C. Donaldson, L. M. Marchin, *Society of Petroleum Engineers 11973*, 1983, 1-10.
- [105] Z. Krivácsy, J. Hlavay, *Talanta*, 1995, **42**(4), 613-620.
- [106] F. Bosch Reig, J. V. Gimeno Adelantado, M. C. M. Moya Moreno, *Talanta*, 2002, **58**, 811-821.

- [107] N. V. Vagenas, A. Gatsouli, C. G. Kontoyannis, *Talanta*, 2003, **59**, 831-836.
- [108] C. Vogt, J. Lauterjung, R. X. Fischer, *Clays and Clay Minerals*, 2002, **50**(3), 388-400.
- [109] S. J. Chipera, D. L. Bish, *Clays and Clay Minerals*, 2001, **49**(5), 398-409.
- [110] T. Chakrabarty, J. M. Longo, *The Journal of Canadian Petroleum Technology*, 1997, **36**(11), 15-21.
- [111] R. Bhaskar, J. Li, L. Xu, *American Industrial Hygiene Association Journal*, 1994, **55**(7), 605-609.
- [112] R. Bhaskar, L. Xu, Society for Mining, Metallurgy, and Exploration, Inc., *Transactions*, 1994, **294**, 1801-1806.